UNIVERSITY OF SOUTHAMPTON

FACULTY OF ENGINEERING AND THE ENVIRONMENT

Civil, Maritime and Environmental Engineering Sciences

ASSESSMENT OF STEEL ENDPLATE MOMENT CONNECTIONS WITH STAINLESS STEEL BOLTS SUBJECTED TO RAPID LOADING RATES

by

George Culache

Thesis for the degree of Doctor of Philosophy

June 2017

Abstract

Past field investigations into the collapse of steel-framed buildings have shown that buildings are particularly vulnerable to progressive or disproportionate collapse.

It was found that in the event of a high-explosive blast in the proximity of a building or of an airplane impact, failure initially occurred in the connections of the structural members resulting in loss of load carrying capacity of some of these members. This failure propagated and eventually caused partial or total collapse of the structures. Failure occurred first in the connections, because the strength or moment capacity of the connections were usually lower than the strength of the member itself. Plastic deformation became localized in the weakest components of the connections causing these to fracture rapidly. These events usually led to the loading and failure of the connections in time periods of less than 100 milliseconds.

In this research, steel moment connections were designed and subjected to quasi-static and high-rate tests, subsequently failing the latter within 50 milliseconds. Similarly, carbon steel black bolts and stainless steel bolts were tested under both high and low loading rates to explore the effect of loading rate on both the strength and ductility of the bolts used in connection tests.

The ductility of common industry standard connections was quantified and improved through the use of stainless steel bolts. This work shows that connections with stainless steel bolts show a fourfold increase in rotation capacity and strain energy absorbed, compared to the same connections having carbon steel bolts.

Advanced material models, that include the strain rate dependence of both yield stress and fracture strain, were used in order to provide a good characterization of the material behaviour for different strain rates. Finite element models were developed in order to predict the strength and capacity of moment connections for different sizes and with different end-plate thicknesses. Conclusions were obtained with respect to the effect of bolt types, their position and end-plate thickness on the moment and rotation capacities of the connections.

This work ultimately provides a method for modelling the nonlinear static and dynamic behaviour of connections using either bolt type. The method has been used to produce results of a parametric study where relevant connection properties were varied. It provides engineers the tools to model connections and access to results that can inform them on possible solutions to improve connection robustness and ultimately the resilience of steel frames.

Table of Contents

List of Tables

List of Figures

List of Accompanying Materials

A disc is provided with this Thesis containing:

1. The thesis in electronic format;
2. Two of the latest presentations summarising this research;
3. Videos with (1) experimental tests, (2) comparing experimental tests with modelling results and (3) other modelling videos;
4. Photos and data log from of all tests;
5. Material models spreadsheets as Abaqus input data for steels of grades S355, A4-70 (SS) and grade 8.8 (CS) used in the finite element models;
6. Tested connections Abaqus selected models;
7. Full scale connections Abaqus selected models;
8. Experimental data – bolts and coupons tests;
9. Experimental data – connections tests.

DECLARATION OF AUTHORSHIP

I, George Culache, declare that this thesis and the work presented in it are my own and has been generated by me as the result of my own original research.

ASSESSMENT OF STEEL ENDPLATE MOMENT CONNECTIONS WITH STAINLESS STEEL BOLTS SUBJECTED TO HIGH LOADING RATES

I confirm that:

1. This work was done wholly or mainly while in candidature for a research degree at this University;
2. Where any part of this thesis has previously been submitted for a degree or any other qualification at this University or any other institution, this has been clearly stated;
3. Where I have consulted the published work of others, this is always clearly attributed;
4. Where I have quoted from the work of others, the source is always given. With the exception of such quotations, this thesis is entirely my own work;
5. I have acknowledged all main sources of help;
6. Where the thesis is based on work done by myself jointly with others, I have made clear exactly what was done by others and what I have contributed myself;
7. Parts of this work have been published as:

   Culache G., Byfield M.P., Ferguson N.S., Tyas A., 2016. Robustness of beam to column moment connections with stainless steel bolts subjected to high rates of loading. *Journal of Structural Engineering of the American Society of Civil Engineers*. In press; accepted for publication.

Signed: .....

Date: .....

Acknowledgements

I would like to thank:

Dr. Neil Ferguson for his patience, guidance and supervision;

Dr. Andy Chipperfield for helping me finish this Thesis;

Dr. Michael Byfield for his technical input;

Dr. Andy Robinson for providing support in the TSRL laboratory at the University of Southampton;

Alan Hindle, Dr. Andy Tyas, Dr. Jim Warren and the technical staff at the laboratory of the University of Sheffield Civil Engineering Department in Buxton; without their help the experimental side of this research would not have been possible;

Joao Ribeiro from the University of Coimbra for helping me with the Finite Element modelling in Abaqus; without his help the modelling side of this research might not have been possible;

Other staff at the University of Coimbra for allowing me to visit for two weeks in the summer of 2015.

Definitions and Abbreviations

Chapter 1	
NIST	National Institute of Standards and Technology
FEMA	Federal Emergency Management Agency
FE or FEA	Finite elements or finite element analysis
WTC	World Trade Center
Chapter 2	
BCSA	British Constructional Steelwork Association
CEN	European Committee for Standardization
SCI	Steel Construction Institute
OFHC copper	oxygen-free high thermal conductivity copper
Chapter 3	
CEDUS	Civil Engineering Department of University of Sheffield
CS	carbon steel, referring to carbon steel of grade 8.8
DIF	dynamic increase factor – for yield and ultimate stress
DRF	dynamic reduction factor – for fracture strain
SS	stainless steel, referring to stainless steel of grade A4-70
TSRL	Testing and Structures Research Laboratory
Chapter 4	
C3D8R	linear brick element with reduced integration
CONN2D2	2D connector element
CPUs	central processing units
GPGPUs	general-purpose graphics processing units
ER	strain rate
PEEQ	equivalent plastic strain
TRIAX	stress triaxiality

Chapter 1: Introduction

1.1 Historic background

During World War II considerable research was carried out into the effect that weapons produced on buildings by Lord John Baker and Sir Dermot Christopherson (Byfield 2006). Their forensic investigations identified a distinct weakness in the beam-column connections used during that time in multi-storey steel framed buildings. Figure 1.1 is an example of documented evidence of connection failure. They concluded that the majority of the collapses caused by bombs could be traced back to connection failures, and one of their recommendations was that full moment-resisting joints should be provided when blast resistance is required (Byfield 2006; Smith et al. 2010; Carper & Smilowitz 2006).

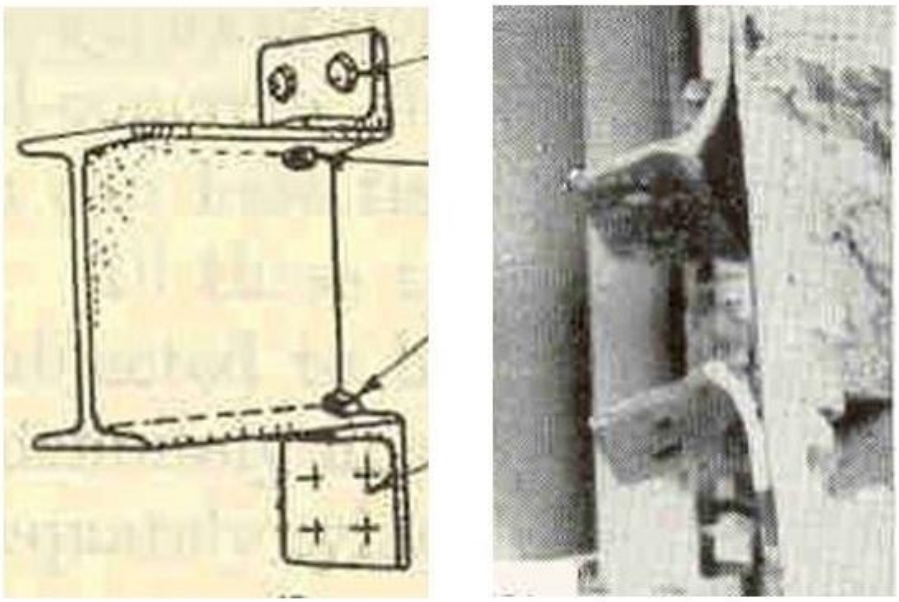

Figure 1.1: WWII Connection damage investigated by Lord Baker in 1948 (Byfield 2006)

The first historic event that led to changes in building regulations was the partial collapse of Ronan Point in London in 1968. Ronan Point was a 22-floor block of flats constructed from precast modular walls. As a result of the explosion, the external load bearing wall was separated from the flooring system initiating a progressive collapse of a whole corner of the block.

An amendment was made to regulations to account for the possibility of disproportionate collapse: "*The building shall be constructed so that in the event of an accident the building will not suffer collapse to an extent disproportionate to the cause."* (Department for Communities and Local Government 2013). The Building Regulations 2000 document is

presented briefly in Appendix A.1 as an example of national guidelines for the assessment of risk and tolerable risk of collapse. Similar guidelines were introduced at European level through the Eurocode, in the US, in Canada and in other countries throughout the world.

In 1995, a truck bomb caused the progressive collapse of Alfred P. Murrah Federal Office Building in Oklahoma City. The blast caused the failure of four columns which led to failure of the transfer girder above these subsequently triggering a progressive collapse.

More recently, the collapse of the World Trade Centre buildings in New York in 2001 led to a renewed interest into improving the robustness of buildings. The two aircrafts penetrated far enough in the cores of the two towers that they adversely affected the emergency exits, trapping people in the upper levels of the towers before they collapsed (FEMA 2002; Shyam-Sunder 2005; National Commission on Terrorist Attacks 2004). Failure of the exterior columns occurred both at the bolted connections between column ends and at various locations in the column, depending on the local severity of the impact load and the proximity of the bolted connection to the impact (Sadek 2005).

These events and others in the past two decades led to reports summarising that one of the key safety issues in tall buildings is vulnerability to progressive collapse and the following major conclusion was consistently reiterated:

> *"This vulnerability is directly related to the strength, ductility and hence the energy absorption capacity of the connections between the main structural elements."* (Institution of Structural Engineers 2002)

These events also led to an intensification of research papers on progressive collapse from 20 papers between 1992 and 2000 to over 450 papers between 2002 and 2012 (El-Tawil, S., Li, H., Kunnath 2014). As there is significant risk, cost and effort associated with high-quality experimental testing and the fact that it is often carried out by military organizations that restrict publication of the data, computational modelling and simulation represent the primary tools in this research area. Et-Tawil et al. (2014) emphasize that "One of the greatest needs at the moment is for high-quality test data at the component and sub-assembly levels. Tests provide the necessary data for validation of modelling tools and development of design guidelines" (El-Tawil, S., Li, H., Kunnath 2014).

1.2 The World Trade Center Towers

On the morning of 11 September 2001 a Boeing 767-200ER aircraft was flown into the north face of the World Trade Centre 1 tower at 8:46am. Soon after, another aircraft of the same type was flown into the south face of the World Trade Centre 2 tower at 9:03am. Both planes, scheduled to arrive in Los Angeles, were loaded with sufficient fuel for transcontinental flights. Figure 1.2 shows the impact locations and the plane orientation to the towers.

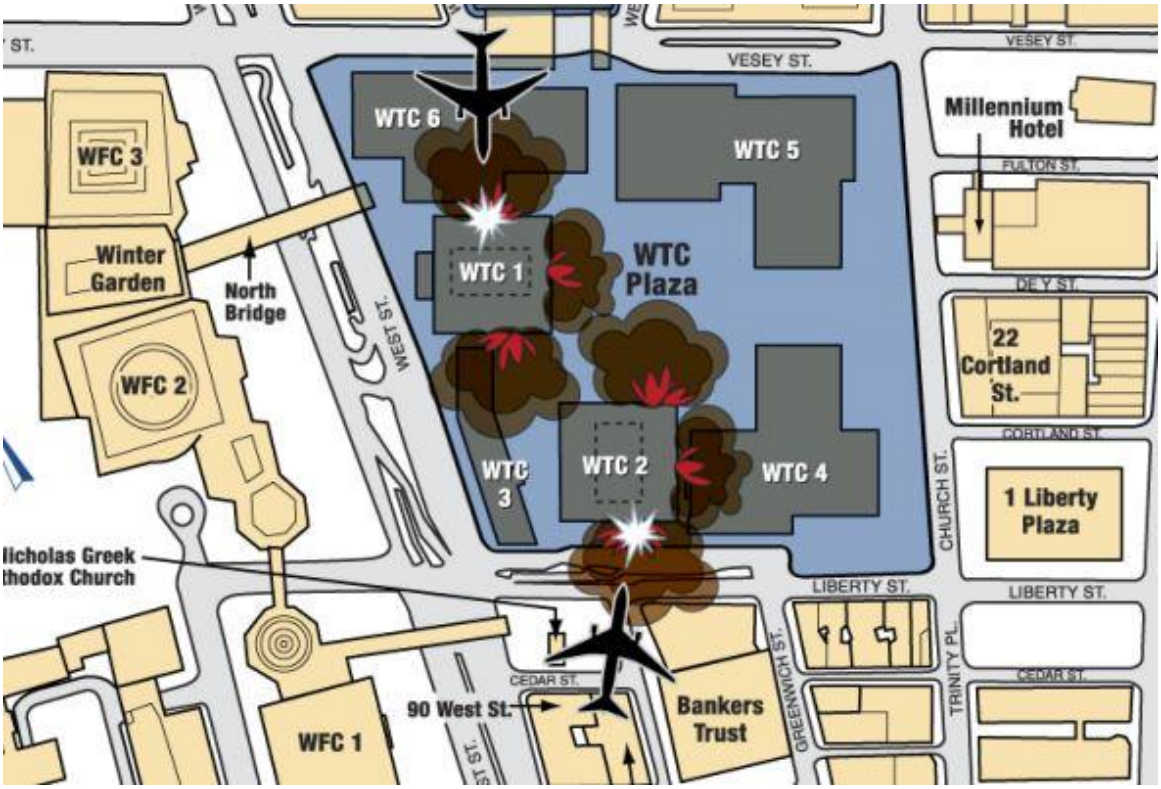

Figure 1.2: WTC impact locations and resulting fireballs (FEMA 2002)

Failure of the exterior columns occurred, both at the bolted connections between the column ends and at various locations in the column depending on the local severity of the impact load and the proximity of the bolted connection to the impact. Figure 1.3 (a) shows the staggered failure pattern in the columns caused by the fact that column splices were staggered mid-height at each floor. Figure 1.3 (b) shows the failure mechanism of the columns at their column splices. The simple moment capacity was calculated to be 20 to 30% of the plastic moment capacity of a column fabricated from steels with yield points of 340N/mm^2 up to 670 N/mm^2, assuming no axial load in the columns. Figure 1.3 (c) shows a photograph of a failed connection and a failed bolt. The planes banked steeply as they went into the building causing damage across multiple floors.

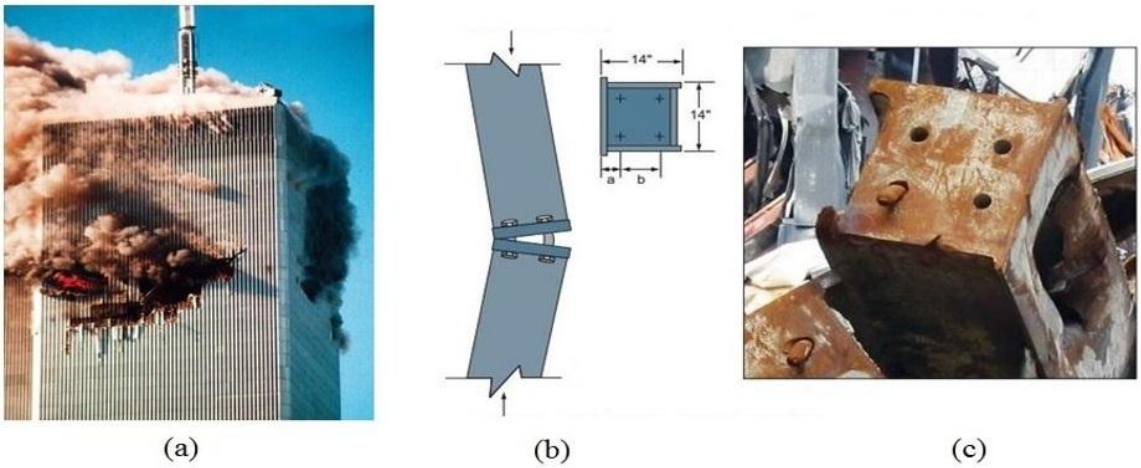

Figure 1.3: (a) Staggered failure pattern where column splices were located, (b) failure mechanism of column and (c) failed connection showing failed bolt (FEMA 2002)

The north tower, WTC 1, was struck between floors 94 and 98, with the impact centred on the north face and the aircraft destroyed all escape routes. Most of the occupants of the tower escaped before the tower collapsed 1 hour and 43 minutes later. However, 1,355 people were trapped in the floors above the impact level and were unable to escape.

Figure 1.4 shows the relative location and orientation of the three stairwells.

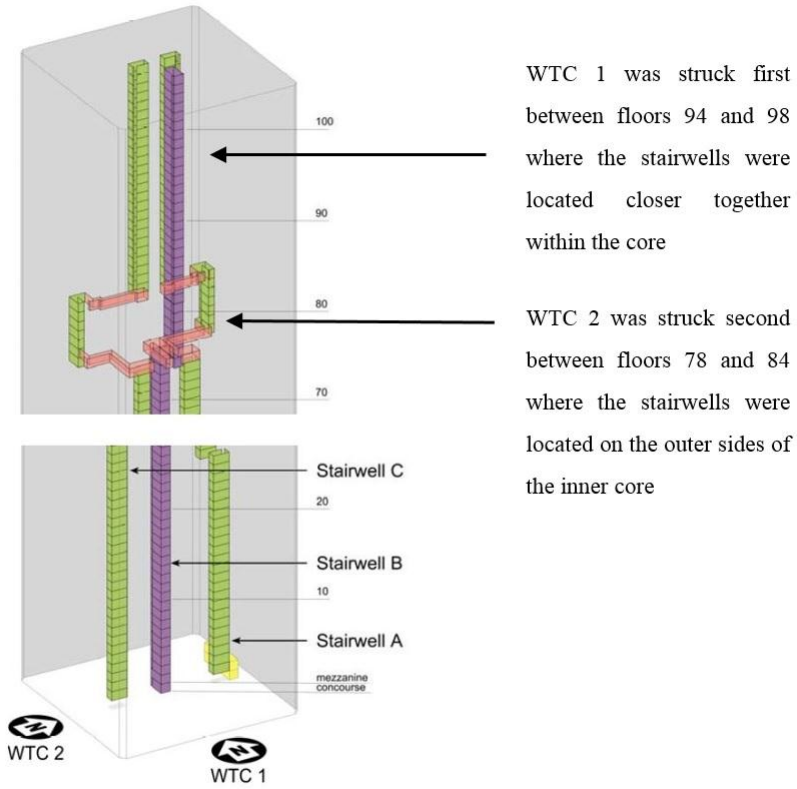

Figure 1.4: Location and orientation of the three stairwells (NIST NCSTAR 1 2005)

The south tower, WTC 2, was struck between floors 78 and 84 toward the east side of the south face. By the time the second aircraft struck many people had descended low enough to be able to escape by self-evacuation and using elevators. The aircraft destroyed the operation of the elevators and two out of three stairways. Eighteen people from above the impact zone found a passage through the damaged Stairwell A and escaped before the tower collapsed 56 minutes later. A total of 619 people did not escape, the majority of which were in or above the impact zone.

NIST carried out the structural performance and aircraft impact damage analysis of the WTC towers. Figure 1.5 shows the top view of the WTC 1 global impact model. The entire aircraft fully penetrated the tower in approximately 250ms. The fuselage was severely damaged, both from the penetration through the columns and the penetration of the 96th floor slab that sliced the structure of the fuselage in half.

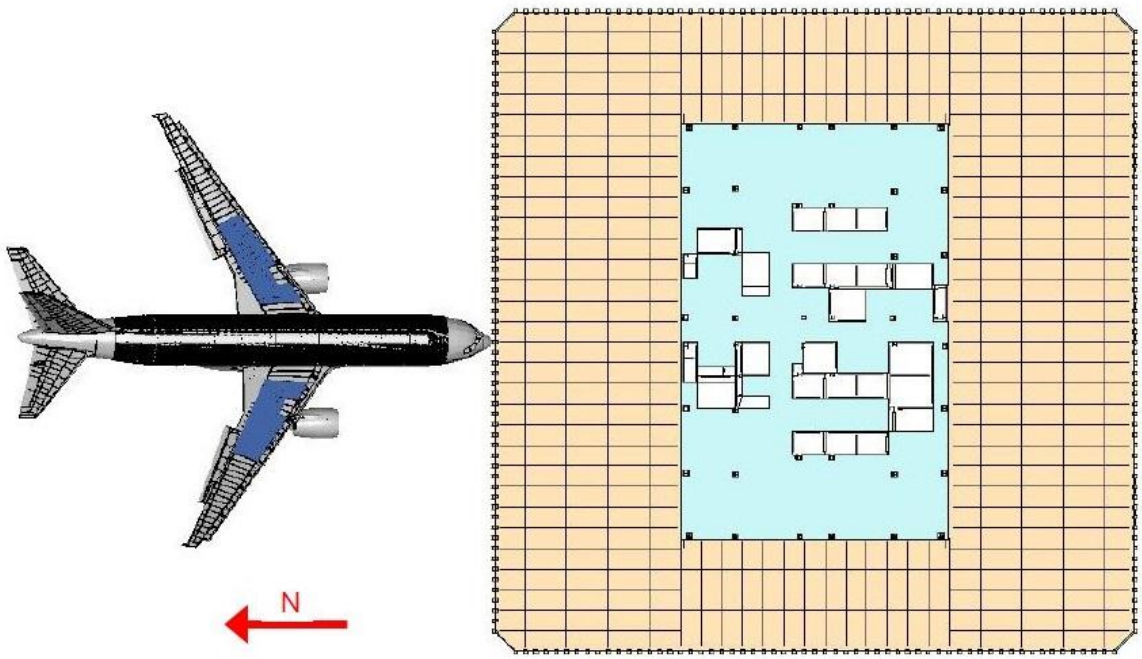

Figure 1.5: Top view of the WTC 1 global impact model (NIST NCSTAR 1 2005)

The tower steels and aircraft fuselage aluminum alloys exhibited significant nonlinear rate-dependent deformation and failure behaviour that they had to be represented in the model by the constitutive relationships. Tests were carried out on ASTM 370 mild steel used in the tower and the various 2024 and 7075 aluminum alloys used in the construction of the Boeing 767 airframe structure. Finite element analysis of these was used to find the true stress-strain data and the constitutive model parameters used in the analysis.

The analysis of aircraft impacts into the WTC was subject to uncertainties in the input parameters such as:

- Material properties: high strain rate material constitutive behaviour and failure criteria for the towers and the aircraft
- Tower parameters: structural strength and mass distribution, connection and joint position relative to impact and joint failure behaviour
- Aircraft parameters: aircraft speed, angle of incidence and location of impact

Since the event is subjected to the above uncertainties, three modelling scenarios were created. The Base Case Impact Analysis was based on reasonable estimates of all input parameters, some of which were estimated from material tests.

The More Severe Impact Analysis included variations in certain key parameters. First of all, the failure strain of the aircraft materials was varied to be 125% of the baseline value to inflict more damage to the towers. For the tower model, the failure strains were reduced to 80% of the baseline value. In addition the mass of the aircraft was increased by 5% and the mass of the building contents was reduced. These variations contributed to more severe damage to the tower structure, since they made the tower structure weaker and the aircraft stronger.

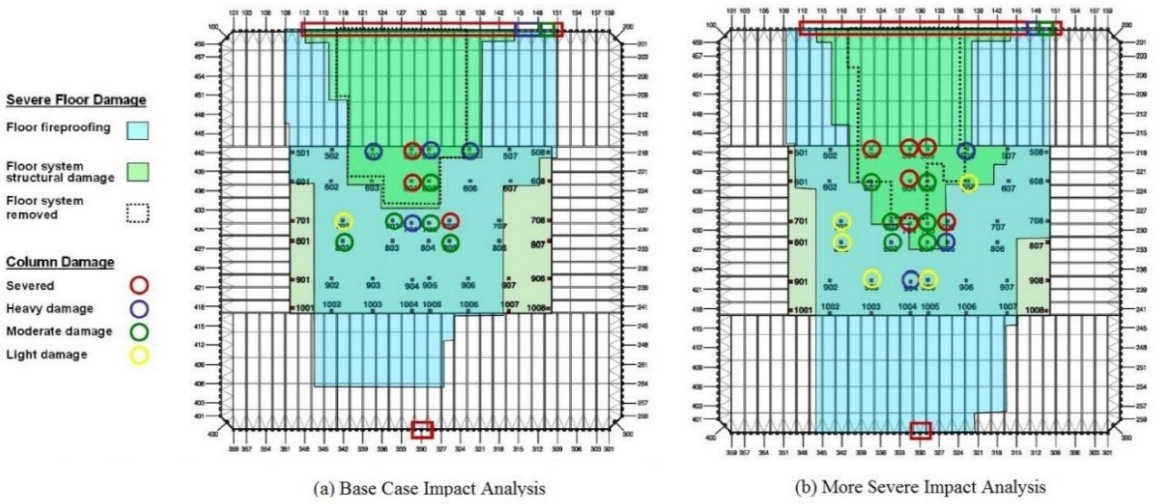

Figure 1.6: Damage in (a) the base case and (b) more severe case (Sadek 2005)

Figure 1.6 (a) shows the extent of column damage in the tower in the base case analysis. The three columns circled in red are severed and the other circled columns are significantly damaged. Figure 1.6 (b) shows that in the more severe case the number of severed columns increases to six and more columns are significantly damaged. Since the extent of damage is

greater in the more severe case, it was more likely that the emergency exits were completely blocked or destroyed in that case.

The Less Severe Impact Analysis included variations which achieved the opposite to the severe case, making the tower steels stronger and the plane weaker. The less severe case did not meet two key observables: (1) no debris was calculated to exit the side opposite to impact, in contradiction to what was observed in photographs and (2) the subsequent structural response analysis shows that the towers would not have collapsed had the less severe damage results been used.

The modelling presented by the NIST reports leads to a very important finding. One of the most important conclusions that can be deduced from that modelling is that there was a direct correlation between failure strain of the materials and the extent of aircraft penetration into the building. The case studies show that if tower steels are assumed to have a greater failure strain, making these more ductile, there is less damage to the inner core of the building.

Since the emergency exits were generally located within the inner core, more ductile tower materials would have increased the likelihood that one or more emergency exits would have remained operational in the case of WTC 1. Evidence from WTC 2 suggests that had at least one emergency exit remained operational people could have escaped from the upper levels of the towers since 1 hour and 43 minutes were sufficient for people to evacuate the building.

Appendix A.2 presents a comparison of typical high-rise buildings and aircraft sizes.

1.3 Aims and objectives of this research

The overall aims of this research were to quantify and improve the performance of industry standard semi-rigid steel connections of beams to columns when subjected to high rate loading.

The first objective was therefore to quantify and if necessary find a way to improve this robustness. In order to achieve this objective the following steps were taken:

1. The difference in behaviour between carbon steel and stainless steel bolts was established through tensile testing under different loading rates.
2. Typical industry-standard moment resisting connections were tested under both quasi-static and dynamic loading. The connections used both types of bolts.
3. The difference in performance was established by processing the experimental data to obtain relationships between the applied moment, rotation, time and the energy absorption of the connections.

The second objective of this research was to create numerical models that would accurately predict the behaviour of connections under both quasi-static and high-rate loading. As part of this objective, different modelling methods were explored that would help reduce computational time. In order to achieve the modelling objectives the following steps were taken:

1. Full 3D finite element models of the bolt, steel coupon and T-stub were created and analysed at different loading rates. These were validated using experimental tests.
2. Full 3D finite element models of the connections were created in order to replicate the connection behaviour under both low and high loading rates. These models were validated against experimental tests.
3. Simplified component models were developed for the tested connections. Three dimensional components were replaced with simple two dimensional elements, in order to save computing resources and reduce computational time while still producing accurate results for the connection behaviour.

Finally, models were produced of scaled-up versions of essentially the same type of connections. These were double in size and with a greater moment capacity. A parametric study was carried out by varying the plate thickness to find its effect on the strength and ductility of the connection. Other connection properties were also varied such as geometrical properties, bolt type and bolt position.

1.4 Main contributions

The outcome was an improvement in the robustness of the connections through the use of more ductile stainless steel bolts instead of carbon steel bolts. Although a difference in the ductility of these bolts is reported in the literature, no connection tests with stainless steel bolts have been reported previously. This work shows for the first time that the behaviour of the connection can be significantly improved with this simple modification.

Different finite element models were created and compared. Conclusions were drawn to establish the design steps needed to achieve an improvement in the ductility and strength of the connection. The outcome was that numerical models can be created to accurately predict the behaviour. Simplified component models must be carefully developed. They must capture the behaviour of all the active components before they can adequately represent the connection in a frame model. The rotation capacity of the connection is directly related to the amount of plastic deformation that can occur in the connection and to the type of failure mechanism of the components of the connection.

This work provides for the first time a high rate analysis of the failure of these types of flush and extended endplate connections with stainless steel bolts. It provides for the first time graphs of endplate thickness versus connection rotation for different bolt types and the modelling method for obtaining such graphs for any type of connection. This allows engineers to easily obtain concrete reliable values of rotation and moment capacity for the scaled-up connections presented in this work.

Conclusions are drawn about the steps needed to improve the robustness of typical moment resisting connections, accurately model their behaviour under different types of loading and model sub-assemblies that adequately represent the behaviour of connections in order to improve their resilience under extreme loading conditions.

Fully welded connections represent a realistic alternative to providing bolted connections in a building. However, fully welding a connection requires the presence of specialist labour on site, welding equipment and takes longer than bolting the connection. Furthermore, their brittleness is likely comparable to that of connections with carbon steel bolts. For this reason, bolted connections are the most common connections. They are preferred by the construction industry, particularly by contractors, because of the ease of erection and assembly of the frame. This work focuses on these.

1.5 Thesis layout

To assist the reader, the following section describes the layout of the thesis, comprising seven chapters, and identifies where the key research questions have been addressed and answered.

Chapter 2 contains a literature review with a general introduction to building connections and recent experimental and numerical work with connections subjected to different loading rates. The review also includes recent work on the behaviour of bolts; threaded assemblies and beam-to-column assemblies; and recently developed modelling methods. Finally, a short review of popular material models that describe the plastic and fracture behaviour of steel at different rates is presented.

Chapter 3 presents the existing design methodology for bolts and connections and how this was applied to design the connections in this work. It then describes the experimental methodologies for testing bolts in tension and connections under different loading rates. A series of tests were conducted on grade 8.8 carbon steel bolts and grade A4-70 stainless steel bolts. The strain rate dependence of the stress and fracture strain for stainless steel bolts is quantified. Tests on flush and extended endplate moment connections were conducted with both bolt types. The dynamic failure phenomenon is described in detail and a discussion follows on when the dynamic increase in strength at the component level is reflected in the strength of the connection. Connection test results are compared with results from the University at Coimbra and general conclusion are drawn.

Chapter 4 introduces essential theoretical and finite element analysis concepts needed in understanding and modelling the behaviour of the material under large deformations, high strain rates and at fracture. Two important element types are introduced: the solid brick element and the connector element. Components of the connection are modelled in 3D at different loading rates and the results are validated with experimental tests. The concept of connectors is introduced and explained in detail and how this provides a practical method of reducing computational time.

Chapter 5 presents the development of finite element analysis models with the use of concepts and material models presented in Chapter 4. The moment connections tested were modelled under both quasi-static and dynamic loading conditions. Very good agreement was obtained for quasi-static models. Modelling the dynamic failure of the connections was more challenging for a number of reasons. More detail is given in the case of dynamic modelling of the connections. Modelling and test results are discussed. Numerical predictions and

experimental observations are compared to draw conclusions on what causes the differences in the results.

Chapter 6 presents models of full-scale connections and a parametric study into the effect of type of plate, plate thickness, bolt position and bolt type on the rotation and ultimate moment capacities of the connection. Graphs are plotted that allow engineers to easily make an estimate of the capacities of some standard industry connections and how these may be influenced by the aforementioned properties.

Chapter 7 includes the general conclusions of the research project, a summary of findings and recommendations for future work.

Chapter 2: Literature review

2.1 Introduction

This chapter contains a literature review with a general introduction to building connections and recent experimental and numerical work carried out on connections subjected to different loading rates. The review also includes recent experimental and numerical work on the behaviour of bolts, threaded assemblies and beam-to-column assemblies. Also, recently developed modelling methods are described. Finally, a short review of popular material models that describe the plastic deformation and fracture behaviour of steel at different rates is presented.

2.2 Steel connections

Structural steel frames consist of steel beams and columns assembled together at their joints. The joint configuration is the type or layout of the joint in a zone within which the axes of two or more inter-connected members intersect. Figure 2.1 shows common major-axis joint configurations.

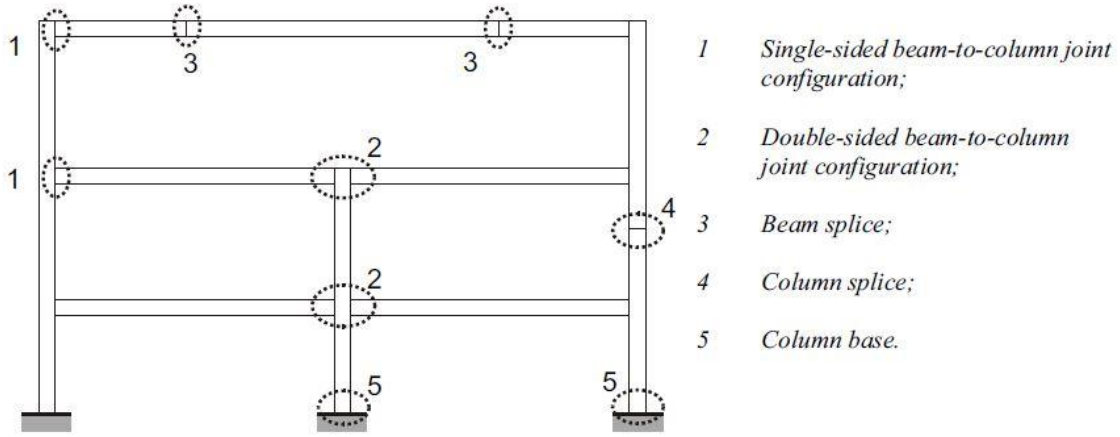

Figure 2.1: Major-axis joint configurations (CEN 2005)

The connection is a location at which two elements meet. It is the assembly of the basic components required to represent the behaviour during the transfer of the relevant internal forces and moments at the connection (CEN 2005). The joint represents the connection plus the surrounding zone of interaction such as the web panel zone. For example, a beam-to-column joint consists of a web panel and one connection if it is one sided, Figure 2.2.

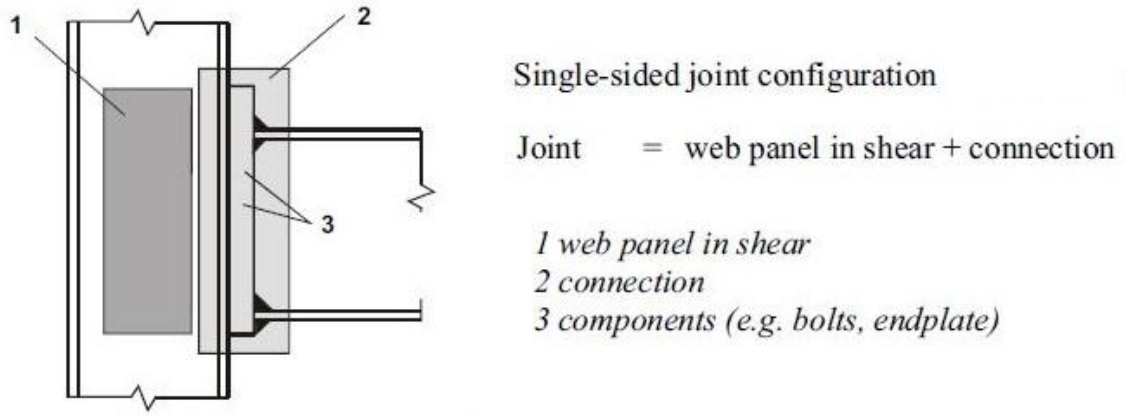

Figure 2.2: Parts of a beam-to-column joint configuration (CEN 2005)

BS EN 1993-1-8 requires that joints are classified by stiffness (rigid, semi-rigid or nominally pinned) and by strength (full strength, partial strength or nominally pinned). Depending on stiffness and strength, in order to identify the effect of the joint on the analysis of the frame, BS EN 1993-1-8 makes a distinction between three joint models:

- Simple: the joint may be assumed not to transmit bending moments;
- Continuous: the joint behaviour may be assumed to have no effect on the analysis;
- Semi-continuous: the joint behaviour needs to be taken into account in the analysis;

Beam to column joints that are designed to transfer moments between the members in addition to forces are moment-resisting. Moment-resisting joints will usually be rigid and either full or partial strength; thus the joints are either continuous or semi-continuous. Partial strength connections are connections that have a design moment resistance smaller than the design plastic moment resistance of any connecting member.

This thesis is concerned with experimental testing and numerical modelling of one-sided partial-strength moment-resisting joints with two types of connections: flush end-plate and extended end-plate connections. According to the models above, these connections are classified as semi-continuous.

2.3 Connection design and rotational stiffness

A moment-resisting joint is made of components: the bolts in tension, the end plate in bending, the beam flange in compression, etc. Figure 2.3 shows all the relevant components that must be checked in the design process of a moment-resisting joint (SCI/BCSA 2013). In the case in Figure 2.3 the top of the beam is in tension and the bottom is in compression. There are two bolt rows in tension and each row is represented by a tensile resistance force. If a moment is applied to the connection a couple is formed between the two forces in tension and the compression force acting in the bottom flange of the beam. Here, the centre of compression is defined for simplicity as the middle of the bottom flange. The moment capacity is derived by taking the weakest of the tensile components and multiplying them with their lever arms, taken from the centre of compression. For example, if the weakest tensile component is the bolt in tension then this will govern the tensile resistance, failure mode, moment capacity and rotation capacity.

The design implies an iterative process where the component dimensions are modified until the weakest components have the resistance that would be able to form a couple large enough to resist the applied moment.

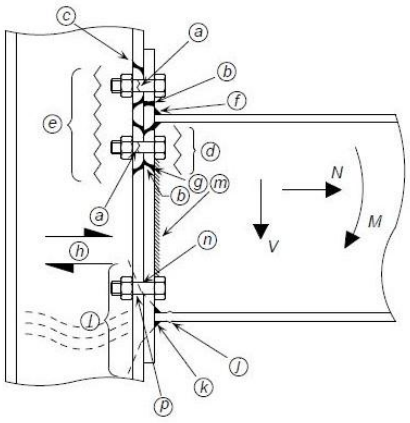

ZONE	REF	COMPONENT	Procedure
TENSION	a	Bolt tension	STEP IA
	b	End plate bending	STEP IA
	c	Column flange bending	STEP IA
	d	Beam web tension	STEP IB
	e	Column web tension	STEP IB
	f	Flange to end plate weld	STEP 7
	g	Web to end plate weld	STEP 7
HORIZONTAL SHEAR	h	Column web panel shear	STEP 3
COMPRESSION	j	Beam flange compression	STEP 2
	k	Beam flange weld	STEP 7
	l	Column web	STEP 2
VERTICAL SHEAR	m	Web to end plate weld	STEP 7
	n	Bolt shear	STEP 5
	p	Bolt bearing (plate or flange)	STEP 5

Figure 2.3: Components to be evaluated in a moment-resisting joint (SCI/BCSA 2013); V, N, M are the applied shear force, axial force and moment respectively

A moment-resisting joint can be represented by a rotational spring connecting the centre line of the connected members at the point of intersection, Figure 2.4 (a) and (b). The properties of the joint model can be expressed in the form of a design moment-characteristic that describes the relationship between the bending moment $M_{j,Ed}$ applied to the joint and the corresponding rotation φ_{Ed} between the connecting members. The moment-rotation characteristic is generally non-linear as indicated in Figure 2.4 (c).

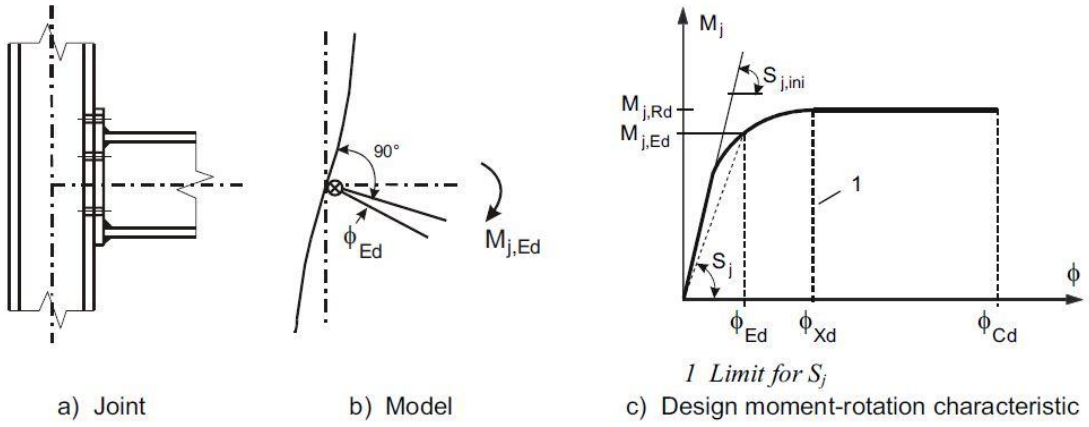

Figure 2.4: Design moment-rotation characteristic for a joint (CEN 2005)

In order to determine the moment-rotation characteristic presented in Figure 2.4 for partial-strength moment connections the following methods may be used. These methods were developed in time through testing and research into connection behaviour.

The experimental method. The connection is tested and the moment-rotation characteristic is obtained from load and displacement measurements. The limitations of this method are the significant risk, cost and effort associated with high-quality experimental testing.

The mathematical formulation method. Once the connection is tested, curve fitting is performed on the data and the parameters of polynomial or other functions are found. The mathematical function will be dependent on the geometrical characteristics of the connection. Reuse of one particular function becomes problematic when a different connection geometry is employed or designed.

The mechanical models method. The connection is split into its component and each component is represented by a nonlinear spring, such as a bilinear or trilinear spring. The properties of each component can be determined experimentally or analytically. The springs are then assembled in a mechanical model and this model is used to find the moment-rotation characteristic.

The Eurocode component method (CEN 2005). The component method is based on the mechanical model method. Expressions are given in the Eurocode for the elastic stiffness of each particular component depending on its dimensions.

The Finite Element method. The joint is modelled in three dimensions and meshed with very small finite elements. The stress-strain relationship for each material type is input into the model. Each material only requires one set of data that describes the elastic-plastic and

fracture behaviour of the material. A force or displacement is applied and a moment-rotation characteristic is obtained.

Del Savio et al. (2009) proposed a generalised component-based model for beam-to-column connections that also includes axial versus moment interaction. Del Savio et al. use a trilinear model to describe each component as a non-linear spring, see Figure 2.5. The component has an elastic stiffness k_{cp}^{e} which is obtained from the Eurocode. The plastic stiffness is $k_{cp}^{p} = \mu^{p} k_{cp}^{e}$ and the ultimate stiffness $k_{cp}^{u} = \mu^{u} k_{cp}^{e}$ are obtained by multiplying the elastic stiffness with the strain hardening coefficients μ^{p} and μ^{u}.

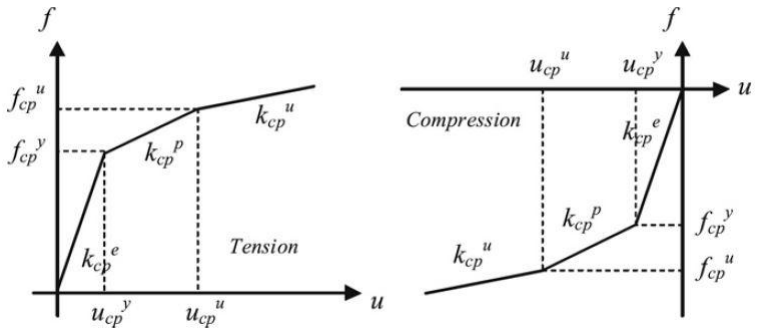

Figure 2.5: Force-displacement characteristic for components in tension and compression

Del Savio et al. used these trilinear springs to develop a model for an extended end-plate connection. The following two figures illustrate an example of the application of the component method in order to find the moment-rotation characteristic. Figure 2.6 shows a drawing of the connection and the mechanical model used by Del Savio et al. to represent it. Figure 2.7 shows the comparison of Del Savio's model with test EE3 which is given in Lima et al. (2004).

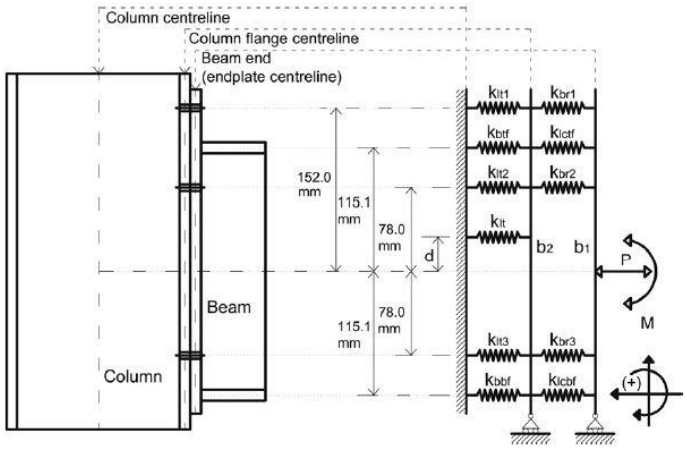

Figure 2.6: Proposed mechanical model for connection with tri-linear springs studied by Del Savio et al. (2009)

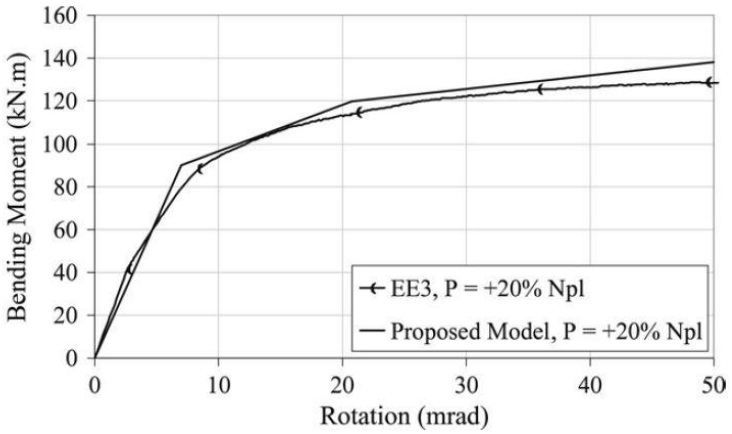

Figure 2.7: Proposed model by Del Savio et al. (2009) versus test EE3 by Lima et al. (2004)

Reasonable agreement was obtained by Del Savio et al. with their proposed model. The same approach was used by Al-Jabri et al. (2005) to model flexible end-plate bare-steel joints in fire. Again, the same approach was used more recently by Stoddart (2012) and by Fang et al. (2013) to model the behaviour of partial depth end-plate connections under high strain rates and flush end-plate connections under elevated temperatures respectively.

The end-plate in bending is a particular component in the connection whose behaviour can be modelled using a trilinear spring as described by Del Savio. The strain hardening coefficients from the research papers mentioned above were selected for this purpose. Table 2.1 shows the plastic and ultimate coefficients adopted by these researchers for the end-plate in bending component of the connection.

Table 2.1: Plastic and ultimate strain hardening coefficients

Author:	Del Savio et al. 2009	Al-Jabri et al. 2005	Stoddart et al. 2013	Fang et al. 2013
μ^p	0.100	0.05	0.08	0.01-0.03
μ^u	0.043	0.01	0.03	0.01-0.03

An examination of the table above leads to the conclusion that there are as many strain hardening coefficients for end-plate in bending as there are researchers studying the post-elastic behaviour of connections.

It is important to note that the connections studied by these researchers were all geometrically different. There were differences in the number of bolt rows, whether the end-plate was partial or full-depth and in the distance between the bolts and the web of the beam

or the column. In addition, the connections were loaded under different conditions such as different loading rates and different temperatures. These some of the reasons why each researcher uses different strain hardening coefficients. The coefficients were chosen or modified so that agreement is obtained between the tests and the component method.

It can be concluded that, just as the mathematical formulation method has functions dependent on connection geometry and loading conditions, so too the mechanical model or component method has strain hardening coefficients which may be highly dependent on geometry and loading conditions such as loading rates and loading temperatures.

2.4 Behaviour of threaded assemblies

2.4.1 Stress distributions and concentrations in bolts and nuts

According to Bickford (2007), the bolt or group of bolts in joints must create a clamping force between joint members in order to prevent these from separating. For a given diameter and thread configuration, this force will depend mainly on the tensile and shear strengths of the material. There are three types of strength that the design engineer will be concerned with when dealing with bolts:

1. The tensile strength of the body of the bolt;
2. The thread-stripping strength;
3. The shear strength.

If a symmetrical bolt is placed in a joint and loaded in pure tension, an ideal stress distribution would look as depicted by Figure 2.8, with the main body in tension and the bolt head, nut, and joint members in compression.

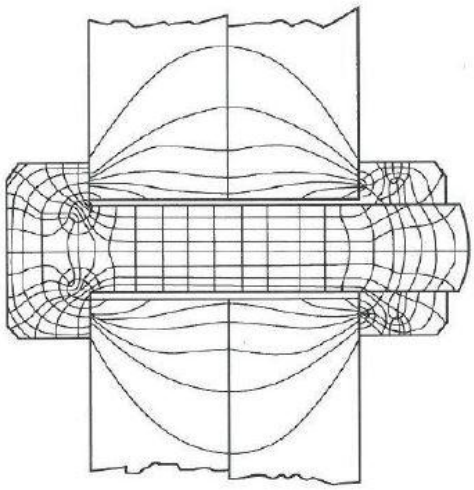

Figure 2.8: Lines of principal tension and compression in a bolt loaded in tension (Bickford 2007)

An analysis of stress magnitudes reveals three stress concentration areas that create stress levels beyond the average. According to Bickford (2007), these stress concentration areas are:

1. The fillet, where the head joins the body;
2. The thread run-out point, where the threads meet the body;
3. The first thread to engage the nut.

These are the points at which the fastener will usually fail. Due to the variation in the area of the bolt under tension caused by the presence of the thread and also due to the presence of the concentration areas shown above, the stress distribution is not constant in the bolt.

Sopwith (1948) studied the distribution of stress along the length of the nut. He took into account bending deflections of the threads, axial recession due to radial compression in the threads, and axial recession due to radial contraction of the bolt and expansion of the nut caused by the radial pressure. He carried out a detailed mathematical analysis of the problem extending and refining the theories developed by Den Hartog, Goodier and other researchers. He developed a theoretical model which could be used to predict the non-uniform load distribution along the length of the nut and the influence of various geometrical parameters that depend on the thread profile. Comparison of his theoretical model with experimental results from other researchers showed a good agreement. He concluded that, for a conventional nut, the stress magnitude in the nut peaks at the first thread with the first three threads carrying most of the load. The peak stress can be reduced slightly by increasing the length of the nut up to a point beyond which increasing the length of the nut has no effect on the peak. Although increasing the length may slightly reduce the peak, the distribution is less uniform with increasing lengths. The most popular way to improve the stress distribution is to use a nut which is partially in tension. This is achieved through designing nuts with special geometry as suggested by Sopwith (1947) or illustrated more clearly by Bickford (2007).

There are three possible failure modes of a fastener assembly in case of tensile overload:

1. *Bolt body breaking* occurs when the length of thread engagement is long and the nut or internal thread material is of compatible strength with the bolt;
2. *Bolt – external thread stripping* occurs when the length of engagement is short and the internal thread material is relatively strong;
3. *Nut – internal thread stripping* occurs when the length of engagement is short and the internal thread material is relatively weak.

Alexander (1977) developed a practical method to predict the failure mechanism of the bolt under quasi-statically applied loads, whether fracture or thread stripping, and the ultimate capacity of bolt-nut assemblies. His method relies on several strength reduction coefficients which take into account numerous factors affecting the strength: dimensions e.g. length of thread engagement, strength, strength ratios, volumetric nut expansion, thread bending, friction and torque. This method has become the basis on which some standards and codes were developed and is commonly called the Alexander model. The following equations were developed by Alexander to predict the ultimate static strength and mode of failure of the assembly in the event of overloading with a purely tensile load.

For bolt breaking, the ultimate load F_{br} is:

$$F_{br} = \sigma_s A_{si} \tag{2.1}$$

where σ_s is the material ultimate tensile strength of the externally threaded member, A_{si} is the tensile stress area of the externally threaded member.

For bolt thread stripping, the ultimate load F_{sb} is:

$$F_{sb} = 0.6\, C_1\, C_2\, \sigma_s\, AS_{si} \tag{2.2}$$

where 0.6 is the shear strength to ultimate tensile strength ratio, C_1 is the nut dilation factor, C_2 is the bolt thread bending factor, σ_s is the material ultimate tensile strength of the externally threaded member and AS_{si} is the shear area of the external thread.

For nut thread stripping, the ultimate load F_{sn} is:

$$F_{sn} = 0.6\, C_1\, C_3\, \sigma_n\, AS_{si} \tag{2.3}$$

where 0.6 is the shear strength to ultimate tensile strength ratio, C_1 is the nut dilation factor, C_3 is the nut thread bending factor, σ_n is the material ultimate tensile strength of the internally threaded member and AS_{si} is the shear area of the internal thread. The coefficients given in the equations above can be calculated using the figures or the empirical relationships presented by Alexander (1977).

Bickford (2007) provides the equations above with a slightly simplified appearance, but the factors influencing the strength are the same. Therefore the process of finding the strength reduction factors that the design engineer has to go through is the same. Instead of

coefficients C_1 and C_2/C_3. Bickford (2007) gives four coefficients which have the following meaning:

- SR1 is a strength reduction factor for nut dilation (similar to C_1)
- SR2 is a strength reduction factor for thread bending depending on ratio R_s (similar to C_2/C_3)
- SR3 is a coefficient of friction factor
- SR4 is a rotary motion factor or factor accounting for the effect of applied torque

If all these factors are taken into account, the final ultimate load for thread stripping could be in some, possibly more extreme, cases reduced to 50% of its initial value. Tables of factors for different bolt grades, lengths of thread engagement and other conditions are provided by Bickford (2007).

2.4.2 Testing and modelling of bolts under different rates

Mouritz (1994) was one of the first to conduct investigations in the behaviour of threaded assemblies at higher rates of loading. The bolts he tested were mild steel M6 bolts with property class 4.6. He used three experimental methods to load the bolt/nut combinations in tension with strain rates varying from 10^{-5} to $10^{3}\ s^{-1}$. For each method he tested 6mm diameter bolts in order to find the thread stripping strength. He also tested bolts that were machined in the shank region to approximately 3mm in order to make the capacity of the shank lower than that of the threads. This allowed prediction of the strength of the shank. The methods he used were:

1. Tensile testing ($\dot{\varepsilon} = 2.5 \cdot 10^{-5}\ s^{-1}$)
2. Drop tower impact testing ($\dot{\varepsilon} \sim 1 - 10\ s^{-1}$)
3. Underwater explosion shock testing ($\dot{\varepsilon} \sim 10^{2}\ s^{-1}$)

In the underwater explosion shock testing it was found that threads failed at loads which were only 8-15% of the failure load of the shank. The bolt threads were examined by optical and scanning electron microscopy after being tested through the three testing methods. Mouritz (1994) found that the deformation and failure behaviour of the threads when tested with the three techniques were similar. Figure 2.9 shows micrographs from examination by optical and scanning microscopy.

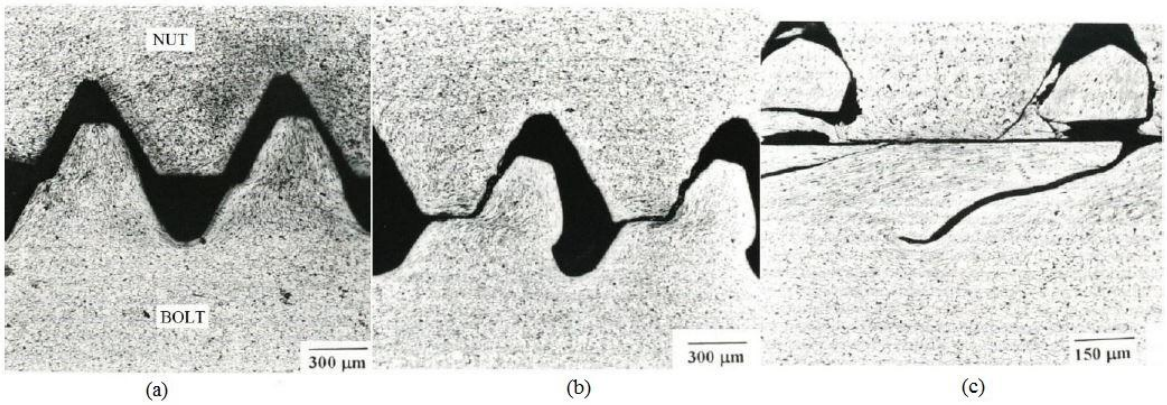

Figure 2.9: Examples of the deformation and damage from increasing pressures of (a) 25 MPa (b) 49 MPa (c) Thread stripping at impact energy of 120 J (Mouritz 1994)

At the lowest tensile loads the tips of the bolt thread were plastically deformed as shown in Figure 2.9 (a) and the nut was not deformed. Figure 2.9 (b) shows the tips being deformed more under higher pressure. Figure 2.9 (c) shows the thread after much higher loading, with the tips of the bolt thread having been sheared off and become wedged into the opposing thread of the nut. The nut threads show no significant damage.

Mouritz (1994) indicates that in the tensile testing technique the load was applied to the bolt at a constant rate for the duration of the test. However, in the drop tower impact technique and in the underwater explosion shock test, the bolts were not loaded at a constant strain rate, but were subjected to a transient pressure pulse. These different testing techniques may produce changes in strength measurement. He found that threads are significantly weaker than the shank and that they fail by a two stage process: firstly, the tips of the threads are plastically deformed and sheared off at high loads; secondly, the remaining thread is plastically deformed into the pitch of the thread. The failure mechanism of the thread does not appear to be influenced by the strain rate.

Mouritz (1994) concludes that the strength of the threads relative to the strength of the shank shows a gradual decrease with increasing strain rate. In other words, as the strain rate increases the threads are increasingly likely to fail at lower fractions of the shank strength.

Munoz-Garcia et al. (2005) performed tests on M12 mild steel bolts of grades 8.8 and 10.9, stainless steel bolts of grade A4-70 and galvanized steel bolts. They used two testing methods in order to subject the bolts to different strain rates:

1. Tensile testing with a universal testing machine ($\dot{\varepsilon} \sim 1 - 10 \cdot 10^{-5}\ s^{-1}$)
2. Drop hammer impact testing ($\dot{\varepsilon} \sim 2.5 \cdot 10^{0} - 1.5 \cdot 10^{2}\ s^{-1}$)

They found that in both quasi-static tests and dynamic tests of mild steel bolts, on 8.8 or 10.9 bolts with one nut, thread stripping was always the critical failure mechanism, see Figure 2.10 (a). Failure through bolt body breaking in both the quasi-static and dynamic tests occurred only when two nuts where used. The fracture occurred in the threaded portion between the underside of the nut and the unthreaded part of the bolt, while the shank remained elastic, see Figure 2.10 (b).

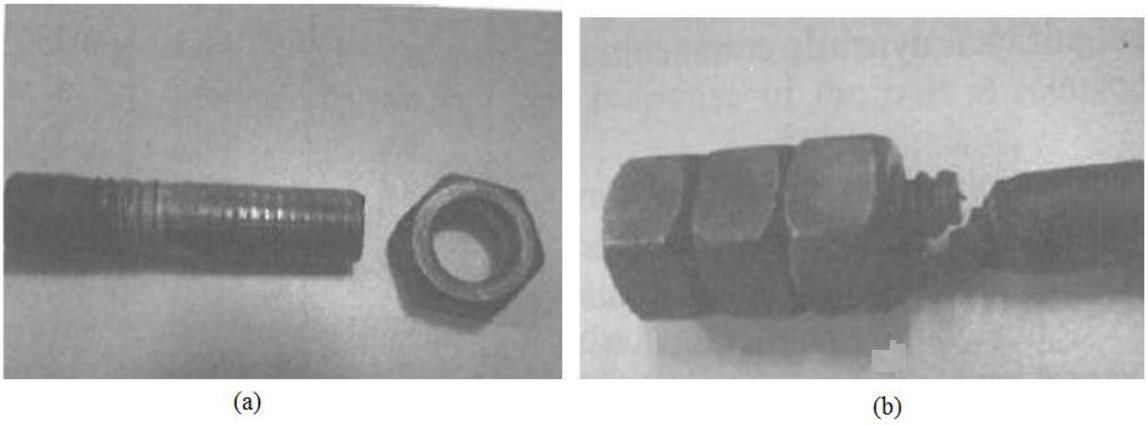

Figure 2.10: (a) Thread stripping failure and (b) bolt body failure (Munoz-Garcia et al. 2005)

It is interesting to notice that the crack in Figure 2.10 (b) runs between the first thread to engage the nut and the thread run-out point, where the threads meet the shank, the locations indicated by Bickford (2007) as the points where fasteners usually fail.

The resistance of the bolt failing through body breaking was found to be approximately 16% higher than the resistance of the bolt failing through thread stripping. Munoz-Garcia et al. (2005) concluded that both failure mechanisms show low ductility with a maximum strain value of 4.6% and that the quasi-static ultimate strength of the bolts was higher than the dynamic ultimate strength.

An important conclusion of their research was that stainless steel bolts showed a different behaviour from mild steel. As opposed to mild steel bolts, stainless steel bolts never failed through thread stripping but only through shank breaking and the ultimate quasi-static strength was lower than the ultimate dynamic strength. This means that the increase in material strength at dynamic rates is also reflected in the strength increase of the bolt-nut assembly as a whole.

This failure mode is counter-intuitive since the tensile area in the threaded region is smaller than the tensile area of the bolt body. This behaviour is explained by the local increase in the strength levels for austenitic grades by cold working of the thread during manufacture (SCI/EuroInox 2006). This reference (SCI/EuroInox 2006) reported that the 0.2% proof strength is typically enhanced by a factor of 50% in the corners of the thread by cold forming.

It is possible that shank failure was obtained due to the high local strength of the threaded region of austenitic stainless steel.

A significant increase in ductility was also observed with strains ranging from 16% in quasi-static tests to 19%-22% for dynamic tests, see Figure 2.11. They conclude that stainless steel could potentially be used in the bolts and in the cleats of connections thus increasing the robustness to progressive collapse of structures.

Figure 2.11: (i) Original stainless bolt (ii) bolt loaded at a low strain rate, (iii) medium strain rate and (iv) high strain rate (Munoz-Garcia et al. 2005)

Fransplass et al. (2011) tested M5 threaded rods of property class 4.6 at strain-rates ranging from 10^{-5} to $10^{3}\ s^{-1}$ using two methods:

1. Tensile tests at low ($10^{-4} - 10^{-1}\ s^{-1}$) and medium strain rates ($10^{-1} - 10^{1}\ s^{-1}$) in a servo-hydraulic testing machine;
2. High strain rates ($10^{1} - 1.9 \cdot 10^{3}\ s^{-1}$) in a split-Hopkinson tension bar (SHTB) using a purpose-made fixture.

As opposed to previous researchers, Fransplass et al. used a model set-up that would simplify the stress distributions and avoid the stress concentration areas caused by the bolt head fillet, the thread run-out and the compressed nut or the first thread to engage the nut. The purpose-made fixture, as opposed to a usual nut, was made of quenched Arne tool-steel in order to control the location where the failure could take place and to ensure no plastic deformation, fracture or dilation occurred in the fixture. They measured the Vickers hardness of the external thread and found it had an average of between 200-220 VH depending in which region of the cross section it was measured. Although they imply that it is significantly higher, they did not indicate the Vickers hardness for the purpose-made fixtures.

The main difference in the assembly tested by Fransplass is the absence of a nut and therefore of a nut/bolt combination. The main focus of the paper by Mouritz (1994) is the testing of bolt/nut combinations under different loading rates, whereas the main focus of the paper of Fransplass et al. (2001) is the testing of a threaded rod under different loading rates.

As opposed to other researchers, Fransplass used the Alexander model in order to predict the failure mode and ultimate load and proposed that the Alexander model would be more accurate if it included the rate-dependent tensile strength of the material.

Fransplass et al. concluded in 2011 that this modified model gave good agreement with experimental results. The material and threaded assembly tests indicated an increased tensile strength and ductility with increase in strain-rate. They have also found that the parameters that have an influence on the failure mode include: the length of thread engagement, the grip length and the strain-rate. They also conclude that the number of threads in the grip length changed the failure mode.

More recently, Fransplass et al. (2013) carried out numerical simulations of tests on threaded assemblies adopting a thermoelastic-thermoviscoplastic constitutive model and a ductile failure criterion. The simulations captured the overall physical behaviour, the maximum force and mode of failure. They included the effect of adiabatic heating which was found to give a lower force level as well as an earlier occurrence of fracture compared to simulations where adiabatic heating is neglected. See Figure 2.12 and note the predicted stress concentration and the path of the highest stresses in red, where a crack usually forms at failure of carbon steel bolts.

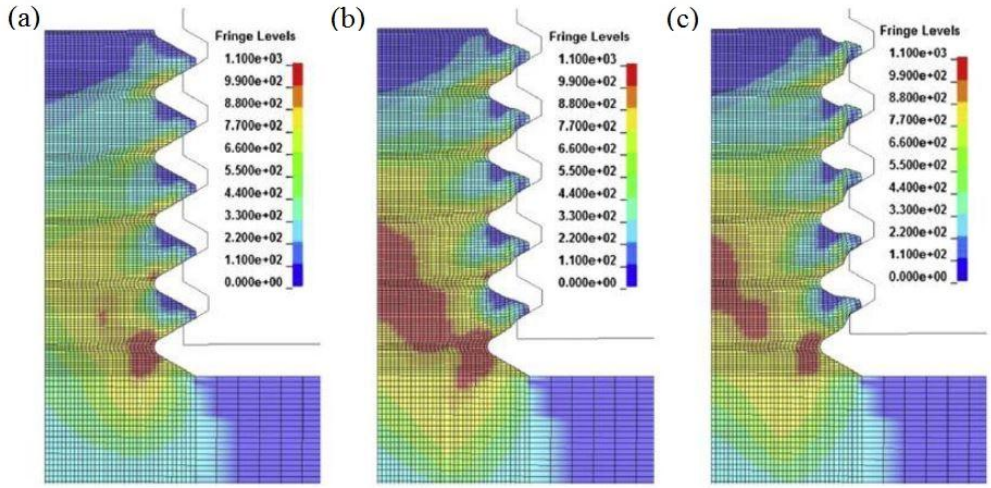

Figure 2.12: Stress distribution in a bolt-nut connection representing maximum principal stress during (a) elastic behaviour, (b) at maximum force, and (c) at beginning of failure (Fransplass et al. 2013)

2.5 Behaviour of steel connections and beam-column assemblies

The need for the adequate tying of load bearing members was highlighted by the partial collapse of the Ronan Point apartment building in 1968, after which regulations were introduced in the UK which defined the tying forces which beam connections must be able to resist without fracture. The objective was two-fold: to help keep members tied together when subjected to lateral loads; and to enable columns to be supported by catenary action in the event of column damage. Catenary action supposedly occurs in double joints where two beams are connected to a damaged column. If the column is damaged at lower levels it should theoretically be supported by the tensile action in the beams provided the connections are ductile enough. The importance of providing adequate tying was well known to World War 2 investigators, who often observed beam column connection failures occurred due to the suction pressures which develop when bombs detonate near buildings (near misses).

Owens and Moore (1992) carried out a series of tests subjecting double web cleat and flexible end plate connections to purely tensile tying forces and large displacements. The research showed that common connection types can resist the tying forces as specified by the codes at that time although plastic deformation was required. The tie force regulation did not, however, stipulate rotation requirements and it was subsequently demonstrated that the industry standard connections used in most UK steel framed buildings lack the rotation capacity to support columns through catenary action (Byfield and Paramasivam, 2007). Despite this short-coming the tie force method remains popular with regulators and has been incorporated into Eurocode 1.

Munoz-Garcia (2005) used the non-linear explicit finite element analysis software LS-DYNA to model a number of connections tested by Owens and Moore (1992) under high rates of loading. The geometrical properties were the same as in the work of Owens and Moore (1992). Munoz-Garcia (2005) performed finite element analysis on three types of connections that include the following elements and variables studied:

1. Partial depth endplate connection models consisting of: column, beam, endplate, bolt rows. Variables studied: number of bolt rows;

2. Web cleat connection model consisting of: column, beam, angles, bolts. Variables studied: gauge distance of the bolts

3. Flush endplate connections: column, beam, flush endplate, bolt rows. Variables studied: plate thickness.

The material was modelled as kinematic/isotropic elastic-plastic which behaves as an elastic-plastic material that includes linear strain hardening and material failure. In order to take into account the dynamic increase in strength of the steel due to higher strain rates, the Cowper-Symonds equation was used. This equation is given by:

$$\frac{\sigma_d}{\sigma_s} = 1 + \left(\frac{\dot{\varepsilon}}{C}\right)^{\frac{1}{q}} \tag{2.4}$$

where σ_d is the dynamic flow stress, σ_s is the static flow stress, $\dot{\varepsilon}$ is the strain rate, C and q are material parameters which are derived from experimental tests at higher strain rates. In the literature review, Munoz-Garcia (2005) found a large number of values for the Cowper-Symonds coefficients for mild steel and listed several values. The difference in the values given in the literature for these parameters comes from the fact that their values are strain dependent. The values chosen in his work were as suggested in the LS-DYNA user manual, $C = 1300\ m/s$ and $q = 5$. No dynamic enhancement was used for the structural bolts.

Munoz-Garcia (2005) performed 3D finite element analysis on three types of connections: partial end plate, web cleat and flush end plate connections. He applied no dynamic increase factor to the strength of bolts as he observed none in their experimental testing. His conclusions are that there is a decrease in the strength of connections at higher rates of loading.

Izzuddin et al. (2008) proposed a new framework for progressive collapse assessment of multi-storey buildings that considers sudden column loss as a design scenario and according to the authors is the first paper that quantifies the factors influencing robustness. This proposed framework was applied to the assessment of real steel-framed composite multi-storey buildings by Vlassis et al. (2008) . The proposed assessment framework can be applied at the overall structural level or at various sub-structural levels, see Figure 2.13.

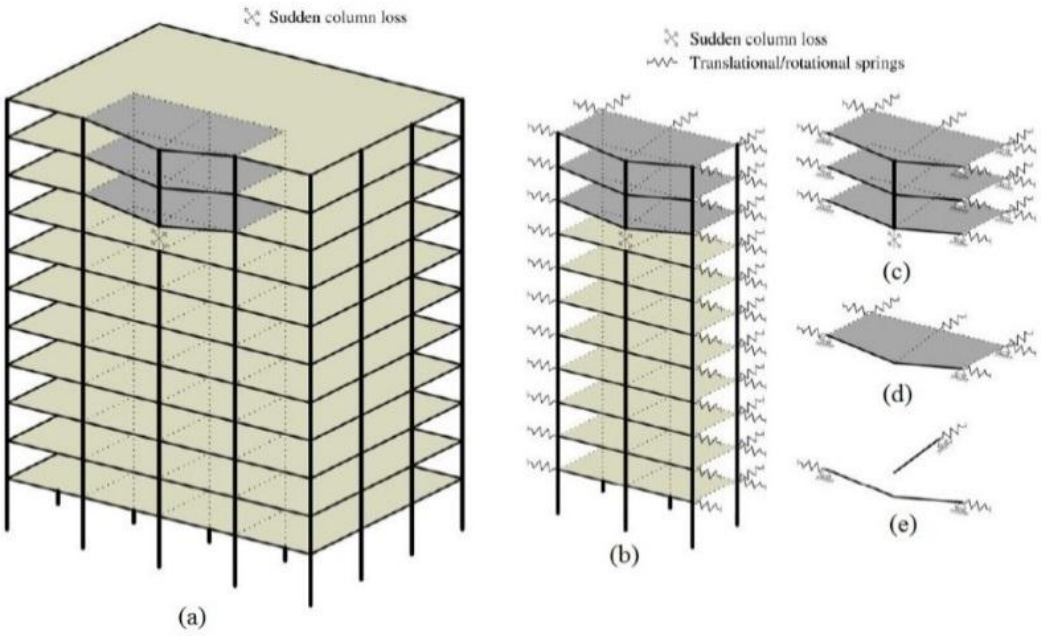

Figure 2.13: Building subjected to column loss and sub-structural levels for progressive collapse assessment (Izzuddin et al. 2008)

Detailed modelling of the nonlinear static response can be considered at various levels of structural idealisation in order to obtain a characteristic nonlinear static response under various loads, see Figure 2.14. This typically involves the use of advanced nonlinear finite element models.

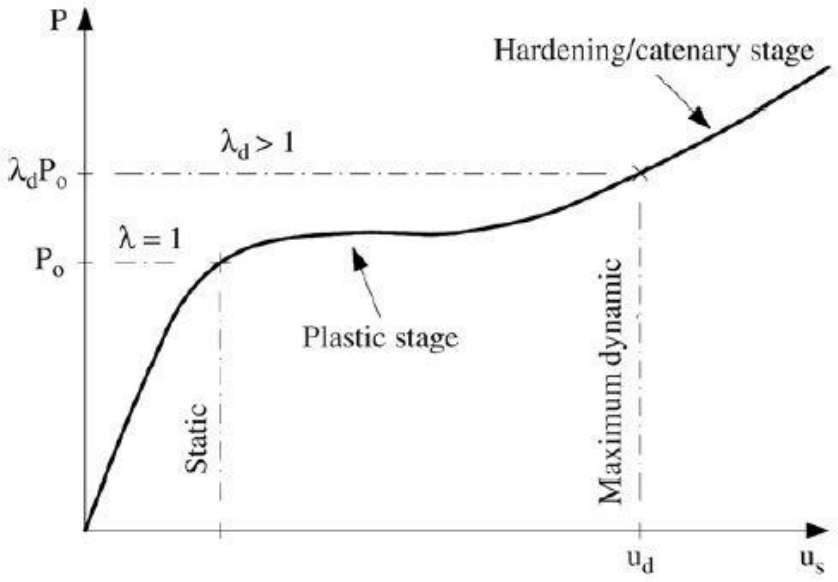

Figure 2.14: Characteristic nonlinear static response under proportional load ($\boldsymbol{P = \lambda P_0}$) (Izzuddin et al. 2008)

Izzuddin et al. (2008) suggest that energy absorption, redundancy and ductility supply do not provide a complete system to measure structural robustness. They proposed that for sudden column loss scenarios, the single measure of structural robustness should be the system pseudo-static capacity (P_f), the comparison of which against the applied gravity loading (P_0) established the required limit state, see Figure 2.15.

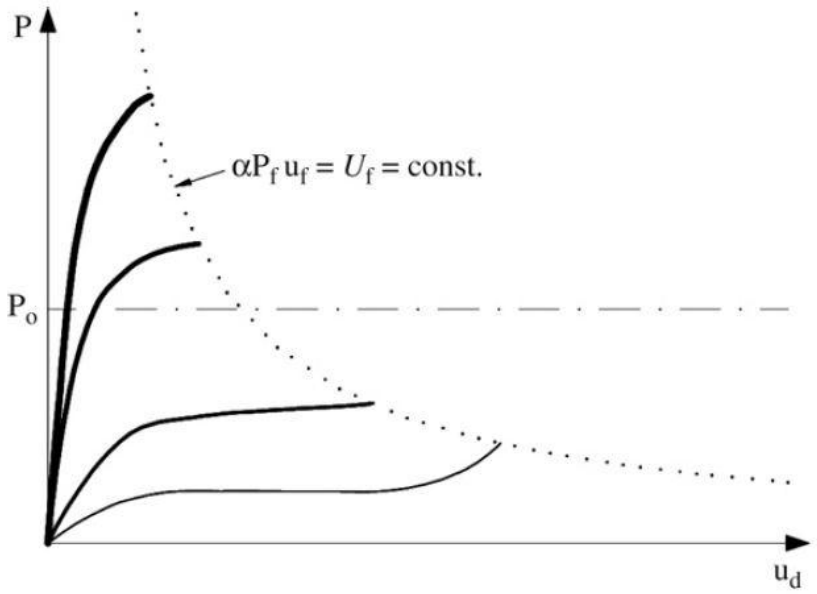

Figure 2.15: Different pseudo-static responses with identical energy absorption capacity (Izzuddin et al. 2008)

In a companion paper, Vlassis et al. (2008) demonstrated the application of the proposed progressive collapse assessment framework to steel-framed composite buildings with simple/partial-strength connections subject to sudden loss of a vertical support member. The case study demonstrated that steel-framed composite buildings with typical structural configurations can be prone to progressive collapse initiated by local failure of a vertical support member.

Izzuddin et al. (2008) and Vlassis et al. (2008) also mention the need for further development in simplified modelling of connections and for the realistic representation of the nonlinear response of various connection types under dynamic loading conditions.

The National Institute of Standards and Technology (NIST), in the United States, conducted a comprehensive research program to study the behaviour of structures that might experience disproportionate collapse if subjected to abnormal loads (Sadek et al. 2010). Lew et al. (2013) describe the test setup and results, loading apparatus, test sequence and instrumentation in more detail. Sadek et al. (2013) describe the analysis in more detail

including: the steel material models used, the detailed model approach, the reduced model approach and comparison with experimental results. See Figure 2.16 for illustrations of the detailed and reduced models.

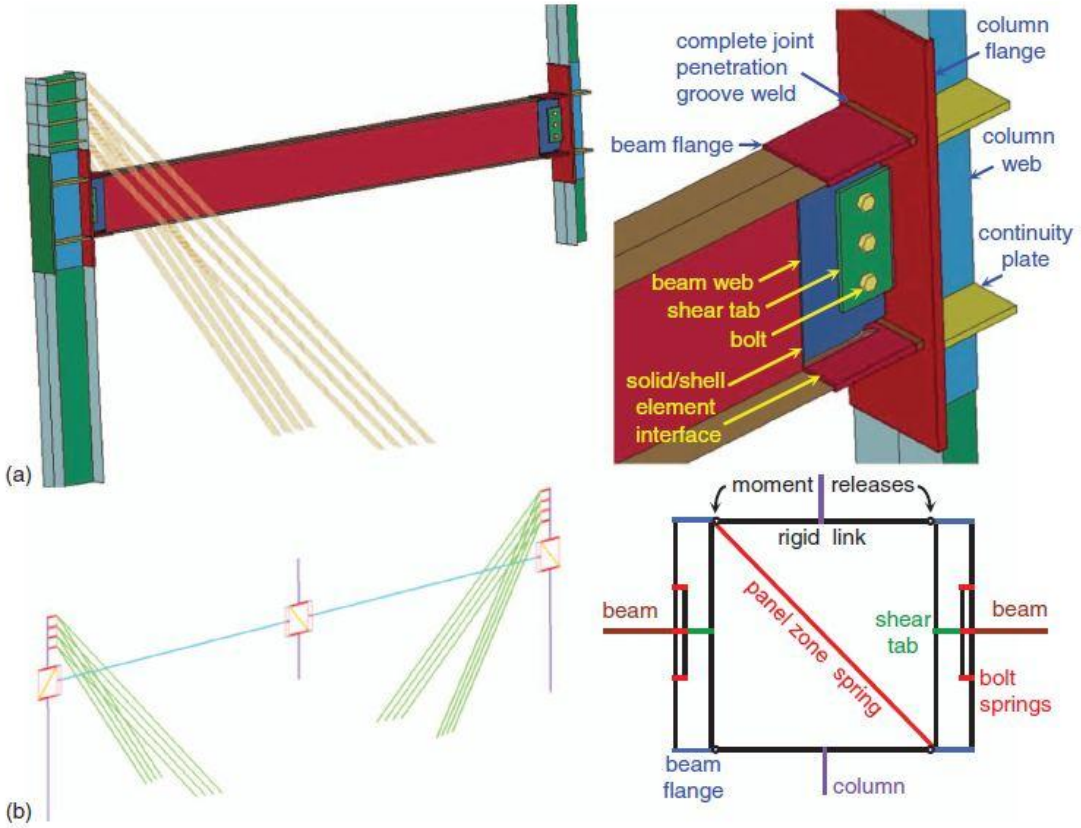

Figure 2.16: Steel assembly models with connection: (a) detailed; (b) reduced (Sadek et al. 2011)

These tests simulated column removal scenarios, with each assembly consisting of three columns and two beams. Each was subject to vertical displacement of the centre column until failure, with column displacement rate set at 25 mm/min. Tests were carried out with two different types of connections, welded unreinforced flange-bolted web (WUF-B) connections and reduced beam section (RBS) connections. Figure 2.17 shows how the "dog bone" connection experiences more plastic deformation and the failure location is more predictable. These tests however are quasi-static tests for a dynamic failure mechanism. They may inaccurately reflect what happens in a real column loss scenario or other scenarios, such as aircraft impact or explosions.

Figure 2.17: Failure mode of (a) WUF-B specimen and (b) RBS specimen (Lew et al. 2013)

Sadek et al. (2013) concluded that comparison of the computational results with experimental measurements showed good agreement. Both the detailed and reduced models were capable of capturing the primary response characteristics and failure modes, providing validation of the modelling approaches. They indicate that the reduced models developed will be valuable in the analysis of complete structural systems for assessing the reserve capacity and robustness of structures. Figure 2.18 show the detailed models for the connections.

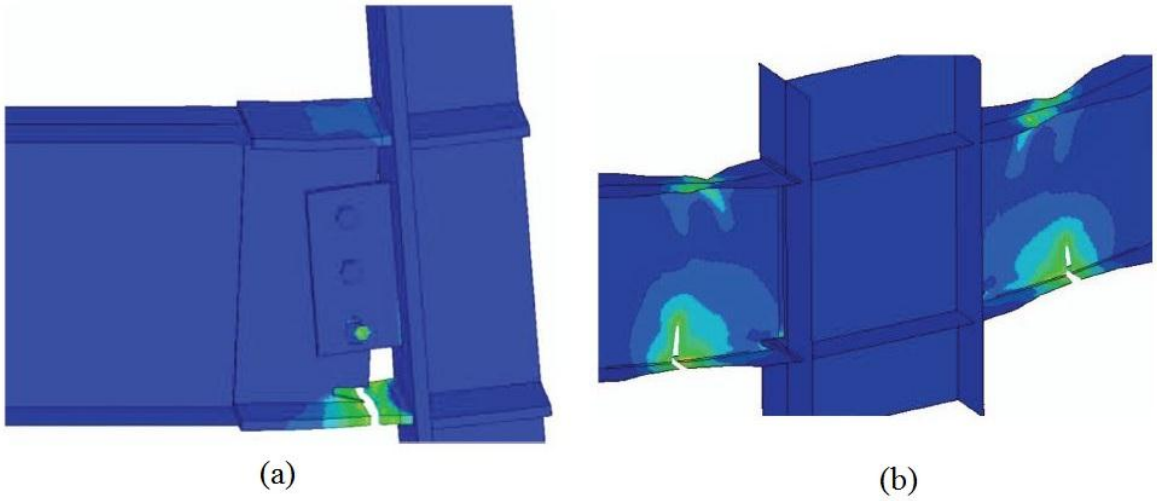

Figure 2.18: Failure mode from detailed model of (a) WUF-B connection and (b) RBS ("dog bone") connection (Sadek et al. 2013)

As stated earlier, Et-Tawil et al. (2014) emphasize that *"One of the greatest needs at the moment is for high-quality test data at the component and subassembly levels. […] These tests will provide the necessary data for validation of modelling tools and development of design guidelines"* (El-Tawil, S., Li, H., Kunnath 2014). However, as noted earlier, most often research conducted in this area uses quasi-static tests or quasi-static modelling. This may inaccurately reflect phenomena such as explosions or impact which typically result in high loading rates and high strain rates.

Tyas et al. (2012) present the design and application of a novel testing rig together with a methodology for combined rotation-extension testing of simple steel beam to column joints at high rates of loading. The testing rig is shown in Figure 2.19. Loading time scales varied between a few milliseconds and several minutes. Results showed that simple flexible end plate connections exhibited a decrease in ductility when failed at high strain rates.

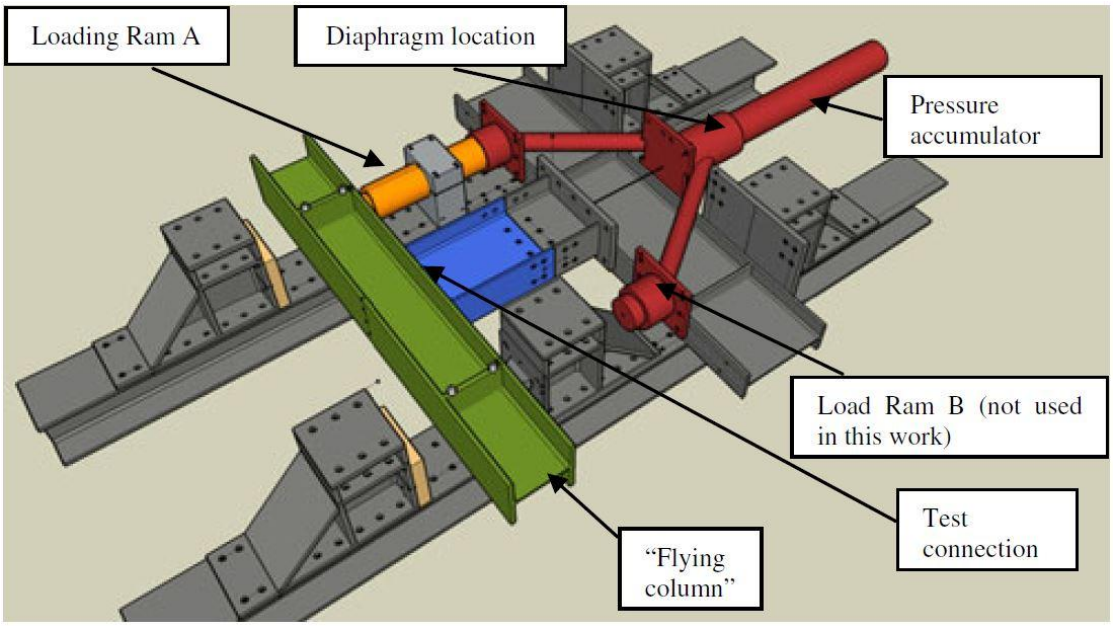

Figure 2.19: Testing rig used by Tyas et al. (2012)

Whole frame numerical models which incorporate perfectly pinned or perfectly-rigid connections have been shown to be inadequate when modelling progressive collapse (Stoddart 2012) or blast structure interaction (Stoddart et al. 2013). Equally, using full three-dimensional connection models with non-linear material models will create computational overload when used for modelling whole frames dynamically. Representing connections as non-linear springs has also been shown to present problems, because the horizontal forces which develop affect the joint stiffness, which cannot be accounted for with a single non-linear spring element (Stoddart et al. 2013). This problem also occurs during the modelling of frames subjected to fire, where thermal expansion followed by catenary action at higher

temperatures induces high horizontal forces. This problem was overcome by Yu et al. (2009), who incorporated temperature dependent component models into whole frame models. This avoids computational overload and was shown to accurately model the experimentally observed behaviour. This technique was subsequently shown to work for modelling progressive collapse (Stoddart et al. 2012) and blast structure interaction modelling (Stoddart et al. 2013), but using strain rate dependent material models based on the Malvar and Crawford constitutive model (Malvar 1998). Figure 2.20 illustrates a column loss scenario as modelled by Stoddart.

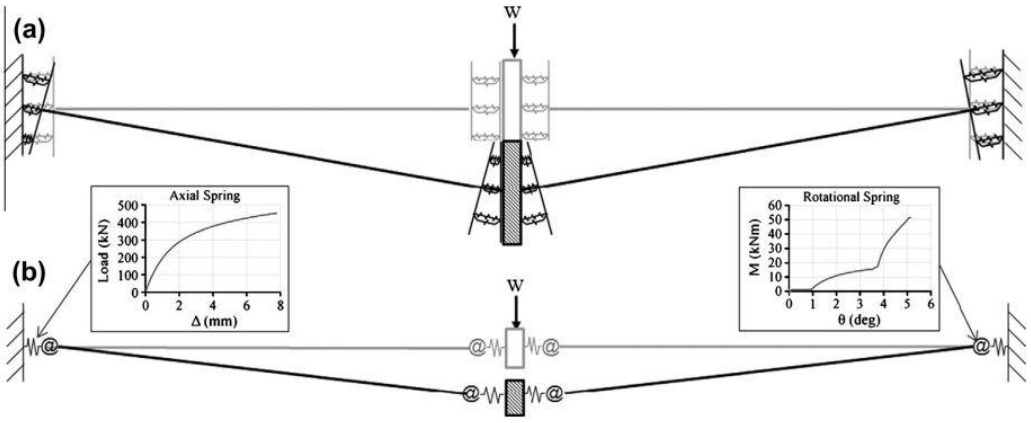

Figure 2.20: Column loss scenario using (a) component method and (b) rotational spring (Stoddart et al. 2013)

The equation proposed by Malvar and Crawford (1998) (Malvar 1998) was based on the study of reinforcement bars under different rates of loading:

$$\frac{\sigma_d}{\sigma_s} = \left(\frac{\dot{\varepsilon}}{10^{-1}}\right)^{\alpha} \tag{2.5}$$

$$\alpha_y = 0.074 - 0.040\,\frac{f_y}{414} \tag{2.6}$$

$$\alpha_u = 0.019 - 0.009\,\frac{f_u}{414} \tag{2.7}$$

where α_y is used to obtain the dynamic increase factor to be applied to the yield stress f_y of the material and α_u is used to obtain the dynamic increase factor to be applied to the ultimate stress f_u of the material.

These material models will be adopted later in the numerical modelling the connection under high loading rates, in order to account for the strain rate effects on the material properties.

2.6 Research carried out at the University of Coimbra

In the case of end-plate connections the Eurocode uses the T-stub model to describe the force-displacement response of the components in the tension zone of the joint. Experimental tests were carried out at the University of Coimbra on T-stub components with carbon steel bolts subjected to quasi-static and impact loading (Barata et al. 2014). Numerical FE models were created that accurately captured behaviour at both low and high strain rates (Ribeiro et al., 2015; 2016). The geometry of their T-stub model is presented in Figure 2.21.

Ribeiro et al. validated their numerical model using experimental tests carried out at the University of Coimbra and an analytical model developed by Yu et al. (2009). Good agreement was obtained with both the experimental tests and Yu's analytical model. Figure 2.22 shows the results from Ribeiro et al. (2015).

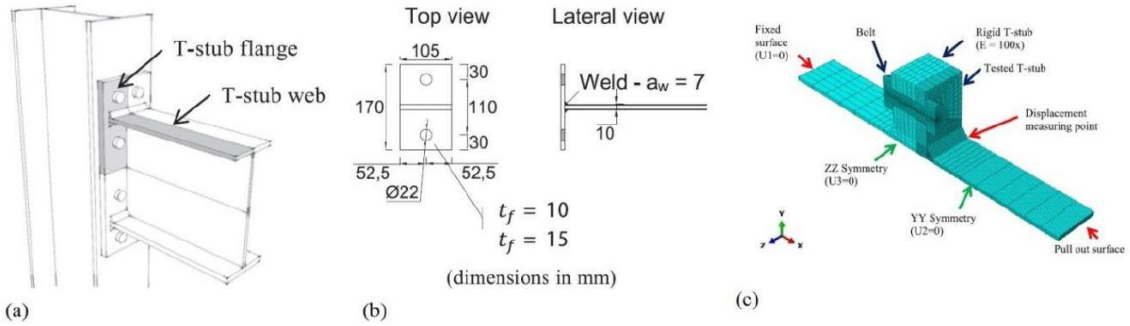

Figure 2.21: (a) T-stub fragment from joint (b) T-stub geometry (c) T-stub numerical model in ABAQUS (Ribeiro, Santiago, Rigueiro, et al. 2015)

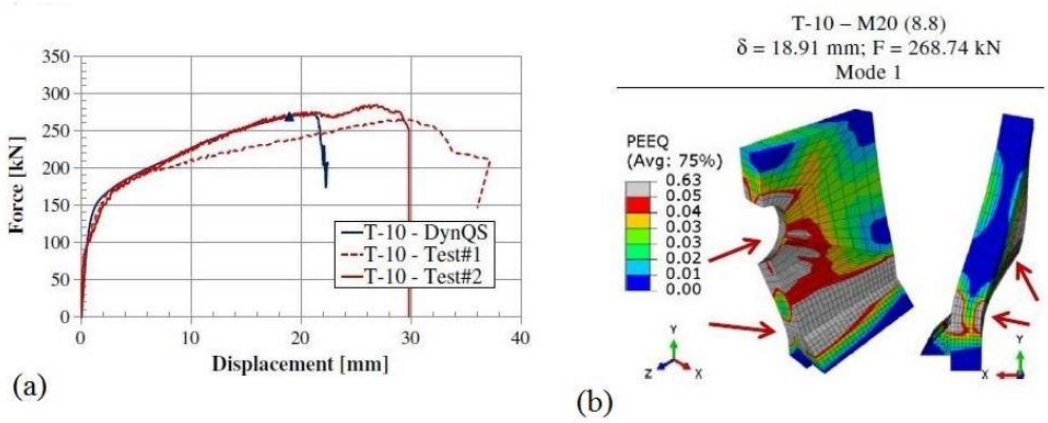

Figure 2.22: (a) Results for quasi-static case and (b) plastic strains and development of two plastic hinges (Ribeiro, Santiago, Rigueiro, et al. 2015)

Ribeiro et al. (2016) used the T-stub model shown above to perform various parametric studies on it. Two important parameters that were varied were loading time and plate

thickness. Figure 2.23 shows the results obtained by varying load application time and plate thickness. With a lower application time there is a dynamic increase in strength. As the plate thickness decreases there is an increase in the ductility of the T-stub but a decrease in its ultimate strength.

Experimental tests and numerical modelling were also carried out on moment connections at low and high strain rates. The experiments showed that the dynamic increase factor of the steel is reflected on the resistance of the connection as a whole, giving the connection a higher moment capacity (Ribeiro et al. 2015). Figure 2.24 illustrates the dynamic failure of the connections with a plate thickness of 10mm (a) and a plate thickness of 15mm (b).

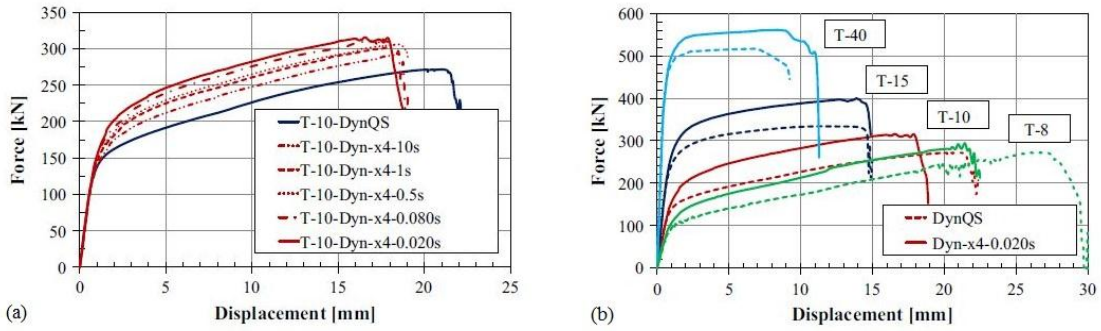

Figure 2.23: Force vs. displacement curves for (a) different applications times and (b) different end-plate thickness of T-stub

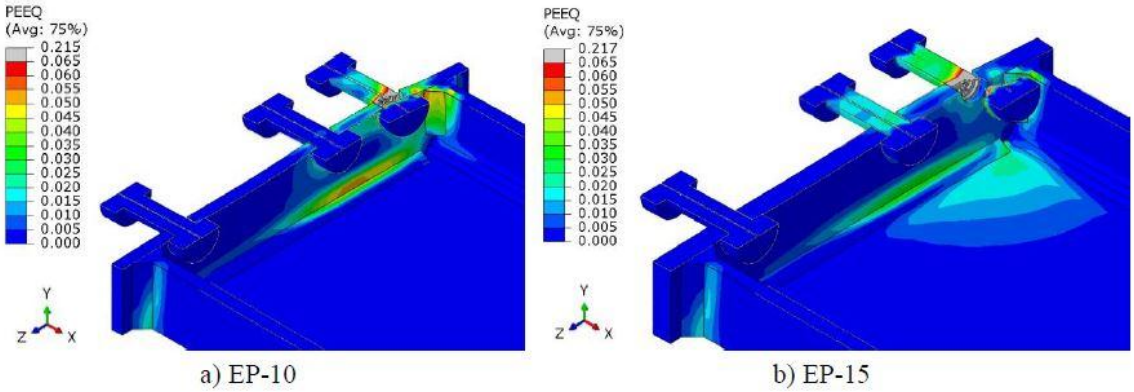

Figure 2.24: Dynamic numerical models failure – bolt rupture

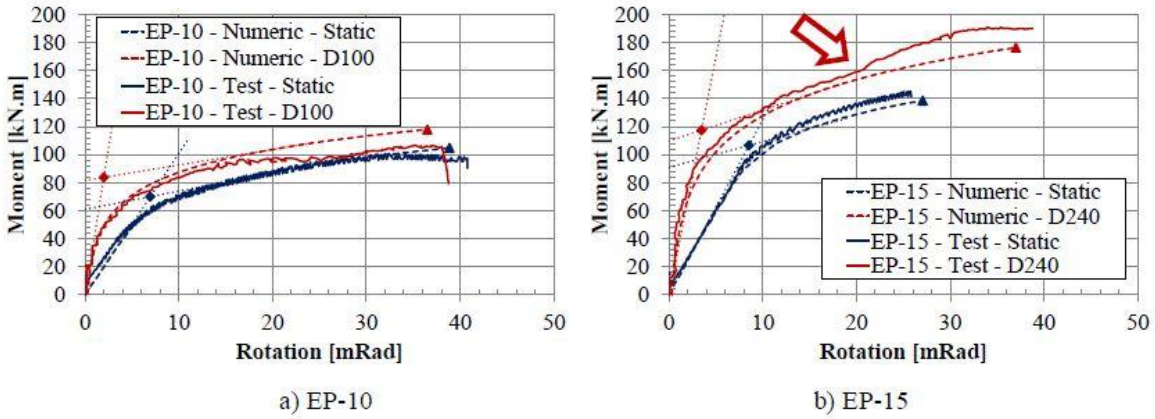

Figure 2.25: Comparison of the quasi-static and dynamic responses: a) EP-10; b) EP-15

Experimental work in the area of moment connections so far focused on testing connections with 2 or 3 bolt rows (Simões da Silva et al. 2001; 2002; Ribeiro et al. 2015; Kuhlmann et al. 2009; Grimsmo et al. 2015), see Fig. 1 (a). However, industry standard connections of high moment capacity often consist of end plates with five or more bolt rows (SCI, 1995), see Fig. 1 (b). Thus the tests carried out in this investigation included 5 and 7 bolt rows in order to investigate the performance of connections with more than 3 bolt rows.

2.7 Structure and composition of carbon and stainless steels

Carbon steel is steel in which the main interstitial alloying constituent is carbon in the range of 0.12-0.6%. It shows linear elastic behaviour up to the yield stress and a plateau before strain hardening. Stainless steel has a more rounded response with no well-defined yield stress; see Figure 2.26.

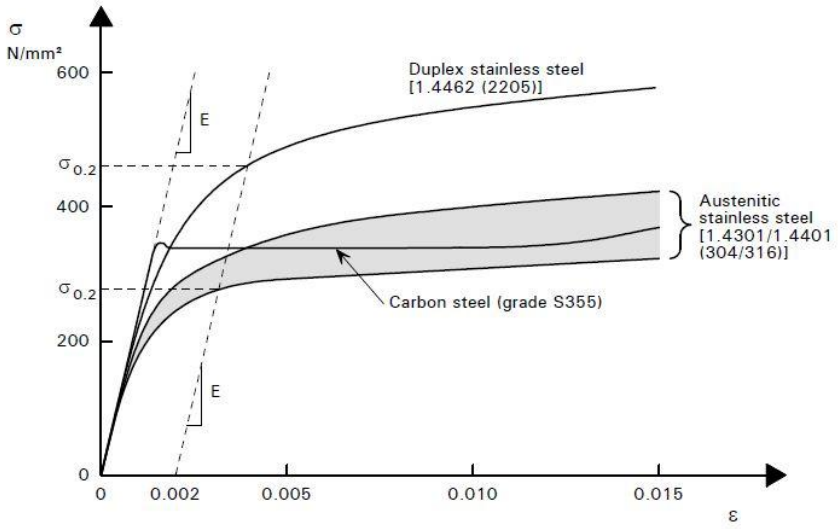

Figure 2.26: Example of difference in elastic-plastic transition for some carbon and stainless steels (Baddoo 2002)

Apart from the difference in the transition from the elastic to plastic response and the resistance to corrosion there are some important fundamental differences between carbon steel and stainless steel. These differences range from chemical composition and its effect on the crystal structure to their ductility and the way they experience plastic deformation. A brief explanation of the crystal structures and differences follows.

On cooling, carbon steel with carbon content below 0.77% transforms into a mixture of ferrite and pearlite grains (Totten 2006). Pearlite is a two-phased lamellar structure with 88% ferrite and 12% cementite. As the carbon content of the steel increases the amount of pearlite grains increases. This leads to an increase in strength and hardness and a reduction in ductility.

Ferrite, also known as alpha iron, is a solid solution of carbon in iron with a body centred cubic (BCC) crystal structure (Totten 2006). The BCC crystal structure is illustrated in Figure 2.27 (b). The BCC system has a net total of 2 lattice points (atoms) per unit cell. This system does not have any close-packed planes as is the case of the face centred cubic system (FCC).

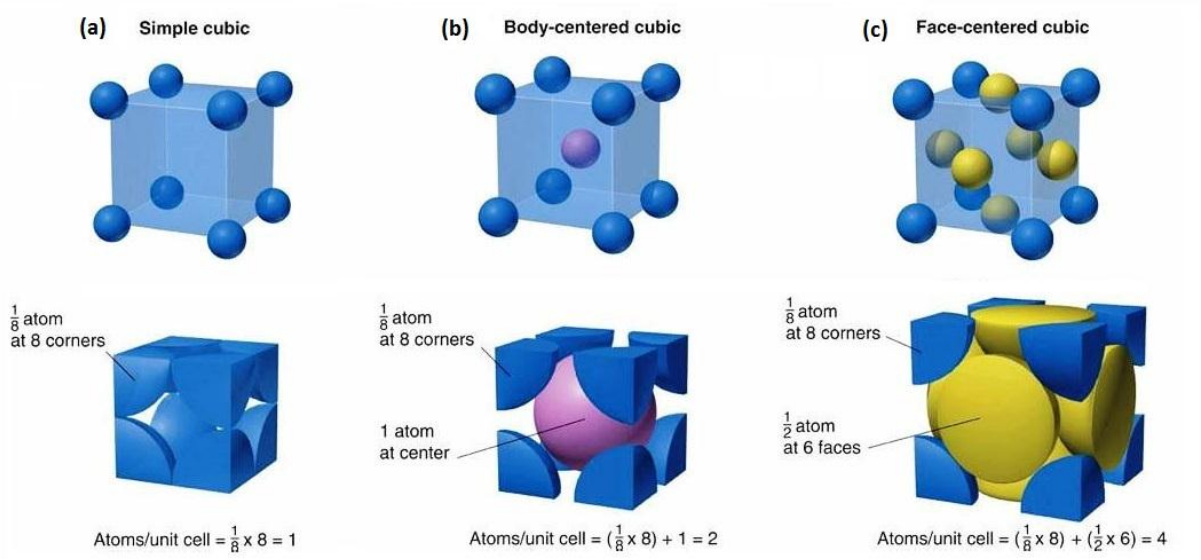

Figure 2.27: Comparison between BCC and FCC crystal structures (Kyawthetlatt 2013)

The most commonly used austenitic stainless steel is grade A2 also referred to as 304 or 18/8 for its composition of 18% Chromium and 8% Nickel. The second most common austenite steel is grade A4 also referred to as 316 or 18/10 for its composition of 18% Chromium and 10% Nickel.

Austenitic stainless steel of grades A2 and A4 contains a maximum carbon content of 0.07% and sufficient chromium, nickel and manganese to retain an austenitic crystal structure as its

primary phase at all temperatures from the cryogenic region to the melting point of the alloy (Dossett & Boyer 2006).

Austenite, also known as gamma iron, has a face centred cubic (FCC) crystal structure. The FCC crystal structure is illustrated in Figure 2.27 (c). The FCC system has a net total of 4 lattice points (atoms) per unit cell. In the FCC system the planes are more closely packed and slip occurs along the closely packed planes.

One type of bolts investigated in this research are grade 8.8 carbon steel bolts. Grade 8.8 is a type of medium-carbon steel and its chemical composition is detailed in Table 2.2.

The other type of bolts investigated in this research are grade A4 stainless steel bolts. Grade A4 is the second most common austenite steel and its chemical composition is detailed in Table 2.3.

Table 2.2: Chemical composition of grade 8.8 carbon steel (BS EN ISO 898-1:2013, 2013)

Property Class	Material and heat treatment	Chemical Composition limit (cast analysis, %)					Tempering temperature (°C)
		C		P	S	B	
		min	max	max	max	max	
8.8	Carbon steel with additives – quenched and tempered	0.15	0.40	0.025	0.025	0.003	425
	Carbon steel quenched and tempered	0.25	0.55	0.025	0.025		
	Alloy steel quenched and tempered	0.20	0.55	0.025	0.025		

Table 2.3: Chemical composition of grade A4 stainless steel (BS EN ISO 3506 - 1:2009, 2009)

Steel Group	Steel Grade	Chemical composition mass factor (%)								
		C	Si	Mn	P	S	Cr	Mo	Ni	Cu
Austenitic	A4	0.08	1	2	0.045	0.03	16 to 18.5	2 to 3	10 to 15	4

2.8 Plastic deformation at high strain-rates

When the stress in a ductile material exceeds the elastic limit, the material starts to deform plastically. This occurs both in quasi-static and dynamic deformation. High strain rate plastic deformation of materials is often described by constitutive equations that link stress with strain, strain rate, and often, temperature. The stress can be expressed schematically as:

$$\sigma = f(\varepsilon, \dot{\varepsilon}, T, deformation\ history) \tag{2.8}$$

According to Meyers (1994), two observations can be made about materials deforming at different rates and temperatures:

1. The yield stress increases with strain rates
2. The increase of yield stress with strain rates is more marked at lower temperatures

Equation (2.8) above can take a form so that it relates the dynamic stress in the material only to the strain rate, as is the case of the Cowper-Symonds and Malvar-Crawford versions which have been presented in the previous sections. It can also take a more general form as is the case of the Johnson-Cook equation, which relates the dynamic stress to the strain, strain rate and temperature.

In 1983, G. R. Johnson and W. H. Cook studied the behaviour of several metallic alloys at large strains, high strain rates and high temperatures including several types of steel, several types of aluminum alloys and other types of iron, copper, brass and nickel (Johnson & Cook 1983). The model for the von Mises flow stress σ was expressed as:

$$\sigma = [A + B\varepsilon^n][1 + C \ln \dot{\varepsilon}^*][1 - T^{*m}] \tag{2.9}$$

where ε is the equivalent plastic strain, $\dot{\varepsilon}^* = \dot{\varepsilon}/\dot{\varepsilon}_0$ is the dimensionless plastic strain rate for $\dot{\varepsilon}_0 = 1.0\ s^{-1}$ and T^* is the homologous temperature. The five material constants are A, B, n, C, m. The expression in the first set of brackets gives the stress as a function of strain for $\dot{\varepsilon}^* = 1.0$ and $T^* = 0$. The expressions in the second and third sets of brackets represent the effects of strain rate and temperature, respectively.

At the same time they also studied the fracture characteristics of three metals, namely OFHC copper, Armco iron and 4340 steel (Johnson & Cook 1985). A series of laboratory tests were performed to determine the effects of strain rate, temperature and pressure on the strain to fracture. A cumulative-damage fracture model was developed and evaluated with an

independent series of tests and computations. The strain at fracture, or fracture strain, is defined here as the strain value in the material at the moment when it fractures completely in such a way that it is unable to continue carrying the loads it is subjected to. The general expression of their proposed model for the strain at fracture ε^f was given by:

$$\varepsilon^f = [D_1 + D_2 exp D_3 \sigma^*][1 + D_4 \ln \dot{\varepsilon}^*][1 + D_5 T^*] \quad (2.10)$$

for constant values of the variables $(\sigma^*, \dot{\varepsilon}^*, T^*)$ and for $\sigma^* \leq 1.5$. The dimensionless pressure-stress is defined as $\sigma^* = \sigma_m/\bar{\sigma}$ where σ_m is the average of the three normal stresses and $\bar{\sigma}$ is the von Mises equivalent stress; this is also known as the stress triaxiality. The dimensionless strain rate $\dot{\varepsilon}^*$ and homologous temperature T^* are identical to those used in the model expressed in equation (2.9).

The austenitic grades are referred to as metastable because they have the ability to transform from the initial face-centred cubic austenite phase γ to body-centred cubic martensite α'. At a certain range of temperatures stress assisted martensite forms in response to an applied elastic stress. It occurs when the stress needed to start the transformation surpasses the flow stress of the γ phase, which should harden by plastic strain to extend the martensite formation process. This Strain Induced Martensitic Transformation (SIMT) acts as a new highly potent mechanism of α' germination associated with plastic deformation (Zaera et al. 2012). The transformation of austenite into martensite is comparable to a *dynamic composite effect* due to the progressive appearance of the martensite during straining. The yield strength of martensite is usually higher than that of the austenite, increasing yield stress and strain hardening of the two-phase steel. Additionally, the martensitic transformation causes the Transformation Induced Plasticity (TRIP) effect. Steels showing SIMT are usually known as TRIP steels.

Zaera et al. (2012) proposed a constitutive model for analysing martensite formation in austenitic steels deforming at high strain rates. They validate their model with experimental results of dynamic tests on AISI 304 (grade A2) sheet steel specimens. In agreement with the experimental observations, their simulations predict that austenite plays the role of the soft phase in the material deformation behaviour, Figure 2.28. It absorbs a major part of the energy supplied to the sample promoting the transformation. The strain as well as the strain rate of the austenite are quite close to the homogenized ones and much larger than those corresponding to the martensite. This behaviour triggers the transformation which, as mentioned above, increases flow stress and strain hardening of the material, as illustrated in

Figure 2.28. Zaera et al. show that the volume of martensite can increase to up to 20% in the tensile region of deformation when the strain is 0.1.

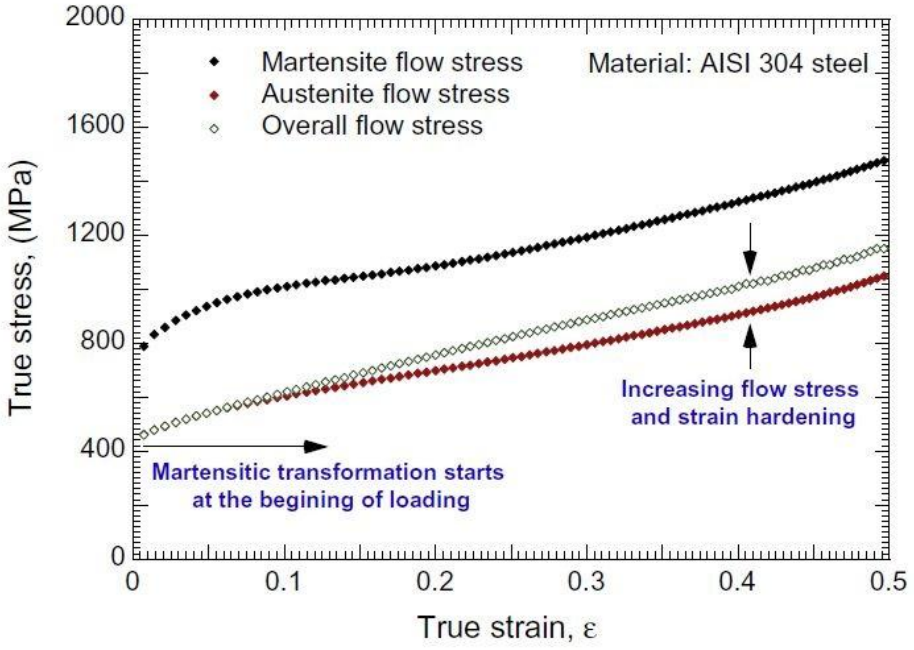

Figure 2.28: Evolution of martensite flow stress, austenite flow stress and homogenized flow stress as a function of strain for $\dot{\varepsilon} = 100s^{-1}$ (Zaera et al. 2012)

In another paper, the same authors carry out the experimental characterisation and modelling of the thermo-viscoplastic behaviour of steel AISI 304 for a wide range of strain rates at room temperature. Rusinek et al. (2015), with the extended Rusinek-Klepaczko (RK) model, provide a more accurate description of the material behaviour under a wide range of loading rates since it based on advanced physical constitutive descriptions unlike the traditionally used phenomenological hardening laws, i.e. the Cowper-Symonds and Johnson-Cook equations presented previously. The constitutive description is based on the additive decomposition of the equivalent stress:

$$\bar{\sigma}(\bar{\varepsilon}^p, \dot{\bar{\varepsilon}}^p, T) = \frac{E(T)}{E_0}\left[\sigma_\mu(\bar{\varepsilon}^p, \dot{\bar{\varepsilon}}^p, T) + \sigma^*(\dot{\bar{\varepsilon}}^p, T)\right] + \sigma_{vs}(\dot{\bar{\varepsilon}}^p) \qquad (2.11)$$

where $\bar{\sigma}$ is the equivalent stress, $\bar{\varepsilon}^p$ is equivalent plastic strain, $\dot{\bar{\varepsilon}}^p$ is the equivalent plastic strain rate, T is the temperature, $\frac{E(T)}{E_0}$ is Young's modulus evolution with temperature, σ_μ is the athermal stress, σ^* is the stress due to thermally activated barriers and σ_{vs} is the viscous drag stress. Rusinek et al. provide the detailed mathematical formulations of the components of stress in the equation above as well as references to the literature that was used in the

development of their model. They also provide the fourteen material constants needed for calibration of the extended RK model to viscous drag effect for steel AISI 304. By applying the material constants to the model, a three-dimensional surface of the effective stress can be obtained for a wide range of strains and strain rates. This is presented in Figure 2.29.

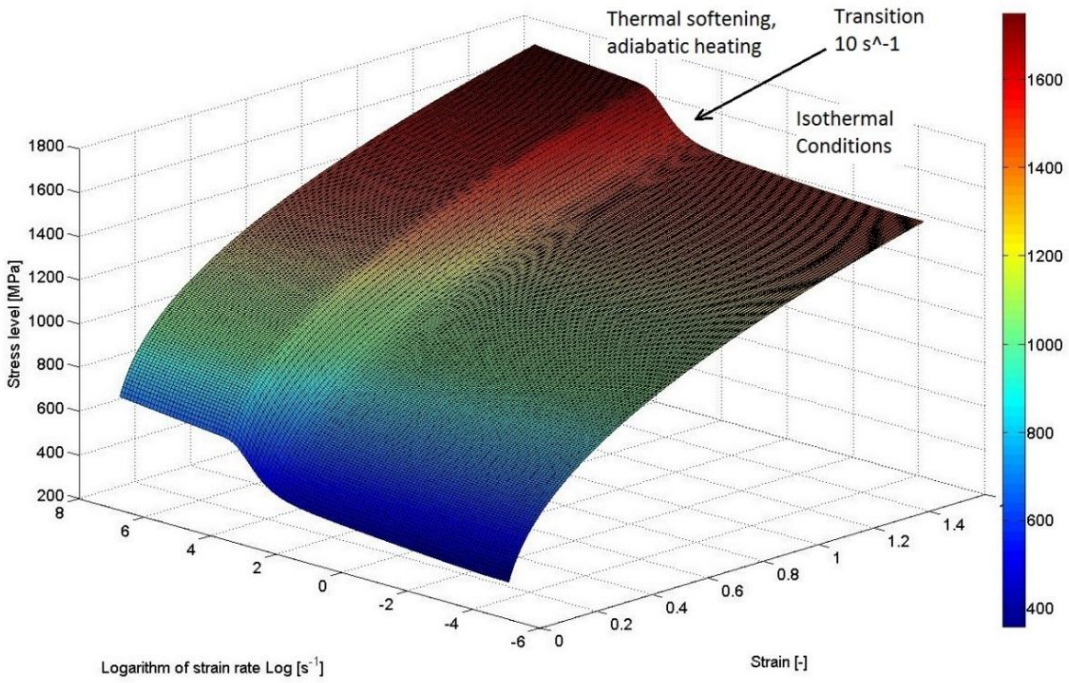

Figure 2.29: Analytical predictions of the constitutive description within wide ranges of strain rates for AISI 304 stainless steel using the extended Rusinek-Klepaczko model

2.9 Current status and simulation capabilities of common finite element analysis programs

As discussed in the previous sections, advanced material models were developed by Johnson and Cook, in the period 1983-1985, and more recently by Rusinek and Klepaczko, in 2015. These material models describe the relationship between stress, strain, strain rate and fracture strain for different steels. As part of their core capabilities, most finite element analysis programs are now able to include the option to define this material behaviour and to allow for nonlinear material and geometric effects in the 3D elements of the model.

Munoz-Garcia (2005), Sadek et al. (2013), Stoddart et al. (2013), Ribeiro et al. (2015) describe in their work the use of finite element analysis in combination with the aforementioned material models in order to study the behaviour of connections at different loading rates. Their work gives a picture of some of the current capabilities of two common commercial finite element packages, namely LS-DYNA and ABAQUS.

In this work, ABAQUS was used to perform the finite element analysis. The analysis capabilities of ABAQUS are thorough and comprehensive. The full capabilities are provided in the Abaqus Analysis User's Guide (Simulia 2015b) which comes with the program in electronic form. If printed this Analysis guide would likely be contained in several large volumes.

Of most concern here are the program's capabilities to deal with this type of nonlinear material behaviour, the basics of pre and post processing and the Abaqus modules and procedure. A more detailed account of these is given in Chapter 4.

2.10 Conclusions

Literature shows that stainless steel bolts are more ductile than carbon steel bolts under both static and dynamic loading. This increased ductility should intuitively lead to an increase in the ductility of connections, but there have been no reported investigations into connection tests where stainless steel bolts were used.

Most of the experimental testing carried out in this research area used quasi-static tests, achieved through testing methods where the strain rates are low with the material deforming plastically. Some tests have been carried out at high loading rates on simple or pinned connections, with some researchers suggesting that testing under high loading rates should more accurately represent scenarios such as column loss, impact or explosions.

Component models of connections where used should reflect more accurately the behaviour of connections in a whole frame model, compared to using simplifying assumptions of either nominally pinned or fully rigid connections.

Full detailed three dimensional finite element models should also better describe the non-linear force-displacement relationships of the critical active components at an individual level under both high and low loading rates.

Using the aforementioned findings, the decision was taken to test connections with stainless steel bolts under both low and high loading rates. These connections were then analysed both with full 3D finite element models and with finite element models which make use of connector elements that reduced computational time.

The following section presents the processed results from experimental testing of bolts and of the connections with both types of bolts under different loading rates. A brief overview of the reported material plastic deformation results and models has also been presented, as they will be shown to be used with the experimental data obtained in this study.

Chapter 3: Experimental testing

3.1 Introduction

A number of tests were conducted in order to establish the behaviour of moment resisting connections under static and dynamic loading conditions. Separate tests were also carried out on individual bolts and steel coupons at a range of strain rates to establish the strength, failure mechanism and the influence of strain rate.

The chapter begins with a description of the geometry and types of tested connections and the reasons behind their design. A bolt and connection design methodology is then concisely presented to give the reader an understanding of the most important steps involved in calculating the moment capacity of a connection.

3.2 Connection types designed and test programme overview

Experimental work carried out so far in the area of moment connections focused on testing connections with two or three bolt rows, such as the connections tested at the University of Liege (Kuhlmann et al. 2009), at the University of Coimbra (Ribeiro, Santiago & Rigueiro 2015) and at the Norwegian University of Science and Technology (Grimsmo et al. 2015). Figure 3.1 (a) shows the connection tested at the University of Liege as an example. However, industry standard connections of high moment capacity often consist of end plates with five or more bolt rows (SCI/BCSA 1995) such as the connection in Figure 3.1 (b). The test specimens in this investigation included five and seven bolt rows, in order to investigate the performance of connections with more than three bolt rows. Two types of moment resisting connections were tested: extended end-plate connections with seven bolt rows and flush end-plate connections with five bolt rows.

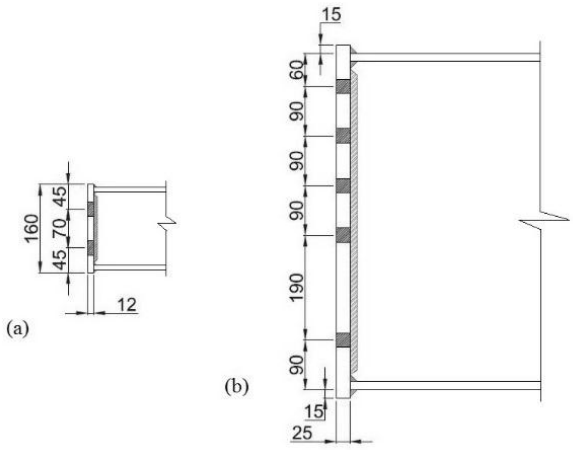

Figure 3.1: (a) Connection tested at University of Liege, (b) industry-standard connection

The extended end-plate connection was made of a beam stub of S355 steel welded with 8mm flange and web welds to a 12mm thick end plate, see Figure 3.2. It was tested with both M12 grade 8.8 carbon steel (CS) black bolts and M12 grade A4-70 stainless steel (SS) bolts.

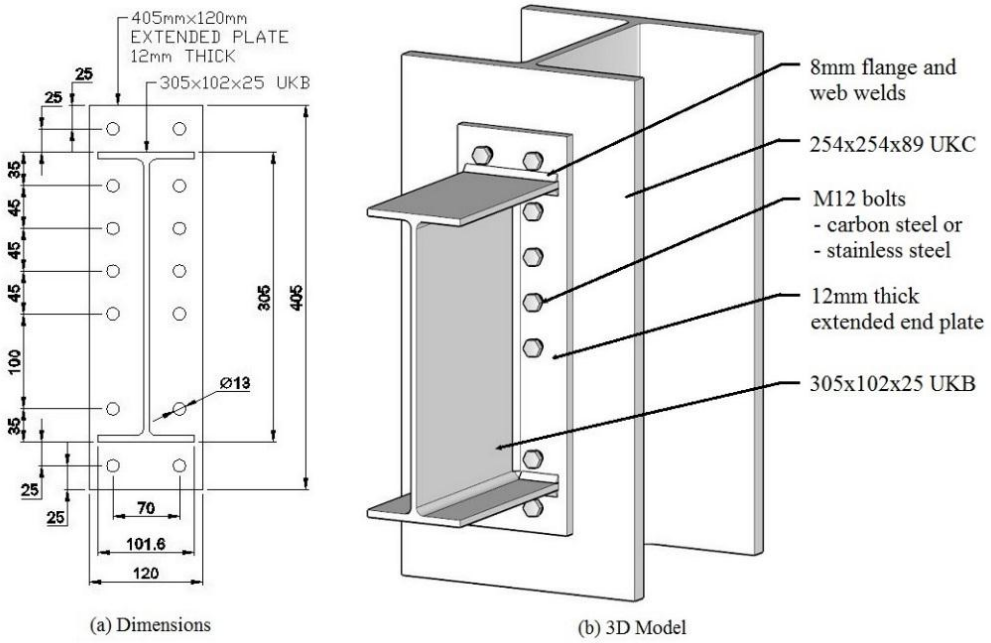

Figure 3.2: Extended end plate connection

The flush end-plate connection was made of a beam stub of S355 steel welded with 8mm welds to a 12mm thick flush end plate, see Figure 3.3. It was tested with both M12 grade 8.8 carbon steel (CS) black bolts and M12 grade A4-70 stainless steel (SS) bolts.

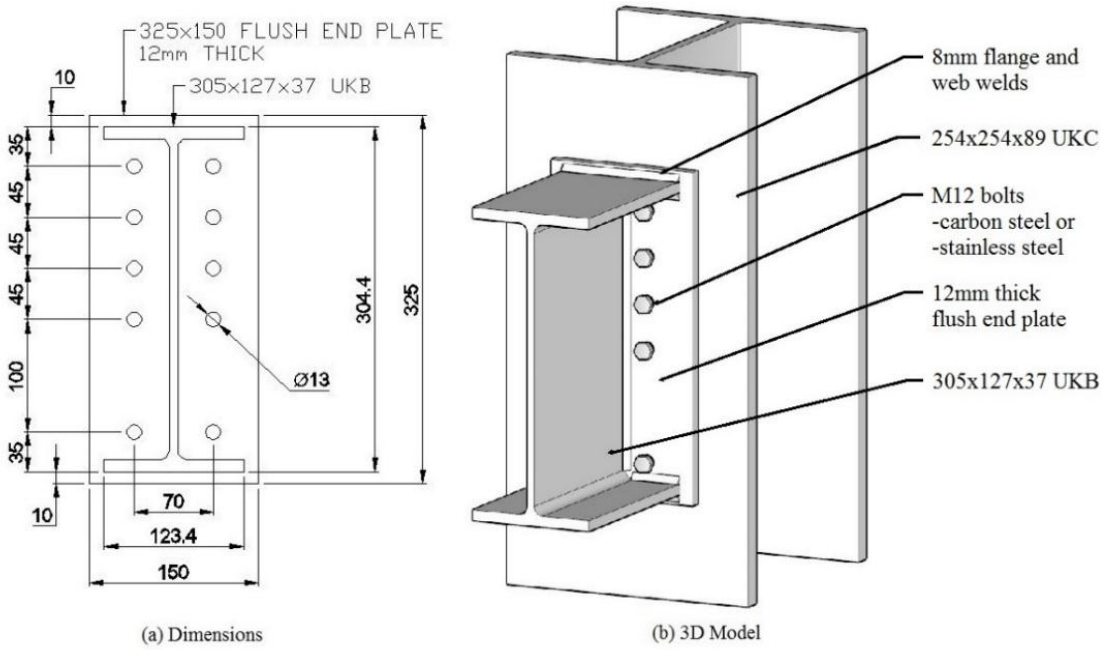

Figure 3.3: Flush end plate connection

Publication BCSA P398 (SCI/BCSA 1995) gives a table of standardised connections designed for different member sizes that lists the plate dimension, bolt size, number of bolt rows, whether the plate is flush or extended and the moment capacity of the connection. The connections in this work and shown in Figures 3.2 and 3.3 were designed to be half the scale of the standardised connections presented for section size 610x229x140 UB. In the case of the flush connection, the distance between the bolts is approximately half of the equivalent distance of the standard connection. In the case of the extended connection, the extension is approximately half the length of the extension of the standardized connections and the bolts are placed in the middle of the extension.

Every connection was tested both statically and dynamically leading to eight different testing configurations. The details of each test are listed in Table 3.1. Loading times and loading rates were recorded during the tests and used to estimate the strain rates involved in the testing, see Table 3.1.

Table 3.1: Experimental test programme (CS - Carbon Steel, SS - Stainless Steel)

Test No.	End plate type	Section size	Bolts type	Loading	Loading time	Loading rate	Approx. strain rates in the bolts	Video frames per second
T1	Extended	305x102x25	CS	Static	300 s	0.40 kN/s	0.002/s	10
T2A	Extended	305x102x25	SS	Static	300 s	0.40 kN/s	0.002/s	500
T7	Extended	305x102x25	CS	Dynamic	40 ms	20 kN/ms	20/s	500
T4	Extended	305x102x25	SS	Dynamic	40 ms	20 kN/ms	20/s	8000
T5	Flush	305x127x37	CS	Static	300 s	0.40 kN/s	0.002/s	500
T6	Flush	305x127x37	SS	Static	300 s	0.40 kN/s	0.002/s	500
T8	Flush	305x127x37	CS	Dynamic	40 ms	20 kN/ms	20/s	500
T11	Flush	305x127x37	SS	Dynamic	40 ms	20 kN/ms	20/s	8000

3.3 Bolt and connection design methodology

The moment connections tested in the experimental part of this research were designed using the philosophy and clauses in Eurocode 3 Part 1-8: Design of joints (CEN 2005). This section describes the approach and assumptions taken by the Eurocode to calculate the resistance of a moment connection. The calculations for the design were carried out with the aid of publications BCSA P398 (SCI/BCSA 1995) and BCSA P207/95 (SCI/BCSA 2013) on the design of moment resisting joints. These publications implement the Eurocode method. A description of the main steps is presented here.

The Eurocode assumes that, in bolted connections, an equivalent T-stub in tension may be used to model the design resistance of the end-plate in bending. Since in the connections studied the end-plate and the bolts are the critical components, there are only three possible failure modes that are of concern:

1. The end-plate deforms plastically and fractures close to the toe of the weld, with very little or no deformation in the bolts. In this case, the equivalent T-stub would deform and fail as illustrated in Mode 1 of Figure 3.4.
2. Both the end-plate and the bolts deform plastically and the bolts fail by fracture due to the prying action in the plate. In this case, the equivalent T-stub would deform and fail as illustrated in Mode 2 of Figure 3.4.
3. The connection fails through plastic elongation of the bolts in tension and their fracture, with very little deformation of the plate. In this case, the equivalent T-stub would deform and fail as illustrate in Mode 3 of Figure 3.4.

Three values can be calculated for the resistance of the equivalent T-stub, one for each of the modes described above. The connection will then fail through the mode represented by the lowest value. Before the expressions to determine these are presented, it is essential first to see what the resistance of a bolt in tension is. The resistance of a bolt $F_{t,Rd}$ in tension is given in the Eurocode as:

$$F_{t,Rd} = \frac{k_2 f_{ub} A_s}{\gamma_{M2}} \tag{3.1}$$

where F represents the "force", subscript t stands for "tension" and subscript Rd for "design resistance", $k_2 = 0.9$ unless it is a countersunk bolt, f_{ub} is the specified ultimate tensile strength of the bolt material, A_s is the tensile stress area of the bolt and $\gamma_{M2} = 1.25$ is a partial safety factor for the resistance of bolts. Note that in this case the ultimate strength of the bolt

is used, since bolt materials usually do not have an easily identifiable yield stress. The tensile area of the bolt is smaller than the area of the bolt body since it represent the area in the threaded region.

When designing a moment connection, the first step is to establish the resistance of the bolt rows in the tension zone. The resistance of a bolt row is given by the resistance of the equivalent T-stub. The resistance of the T-stub is calculated for three possible failure modes, shown in Figure 3.4. The lowest value obtained for each row is then used to calculate the final connection resistance.

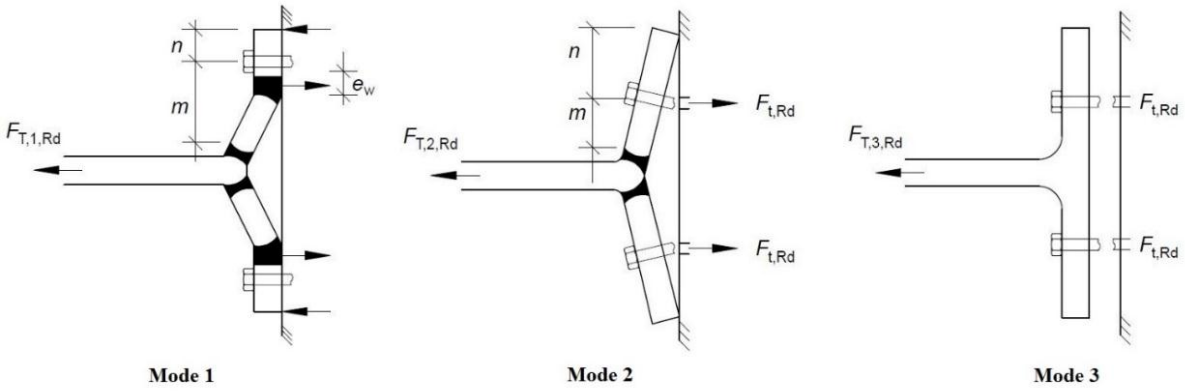

Figure 3.4: Possible T-stub failure modes, which are Mode 1, complete flange yielding, Mode 2, bolt failure with flange yielding, and Mode 3, bolt failure

In Mode 1, for complete flange yielding:

$$F_{T,1,Rd} = \frac{(8n - 2e_w)M_{pl,1,Rd}}{2mn - e_w(m+n)} \tag{3.2}$$

where $F_{T,1,Rd}$ stands for "design resistance of T-stub in tension if a mode 1 failure is assumed", e_w, m, n are dimensions as shown in Figure 3.4, $M_{pl,1/2,Rd}$ is the plastic resistance moment of the equivalent T-stubs for Mode 1 or 2 given by:

$$M_{pl,1/2,Rd} = \frac{{t_f}^2 f_y \sum l_{eff,1/2}}{4\,\gamma_{M0}} \tag{3.3}$$

where $l_{eff,1/2}$ is the effective length of the equivalent T-stub for Mode 1 or 2 and can be found using clause (6.2.6.5) of Eurocode 3 Part 1-8: Design of joints (CEN 2005), t_f is the thickness of the T-stub flange, f_y is the yield strength of the T-stub flange and γ_{M0} a factor equal to 1.

In Mode 2, for bolt failure with flange yielding:

$$F_{T,2,Rd} = \frac{2M_{pl,2,Rd} + n\left(\sum F_{t,Rd}\right)}{m+n} \quad (3.4)$$

where $M_{pl,1/2,Rd}$ is the plastic resistance moment of the equivalent T-stubs for Mode 1 or 2 given, $\Sigma F_{t,Rd}$ is the total tension resistance for the bolts in the T-stub and m, n are as shown in Figure 3.4.

In Mode 3, for bolt failure:

$$F_{T,3,Rd} = \sum F_{t,Rd} \quad (3.5)$$

where $\Sigma F_{t,Rd}$ is the total tension resistance for all the bolts in the T-stub

The compression resistance of the combined beam flange and web $F_{c,fb,Rd}$ in the compression zone is:

$$F_{c,fb,Rd} = \frac{M_{c,Rd}}{h_b - t_{fb}} \quad (3.6)$$

where $M_{c,Rd}$ is the design bending resistance of the beam cross section, h_b is the depth of the connected beam and t_{fb} is the flange thickness of the beam.

The Eurocode does not specify a bolt torque for calculating any of the resistances given above and does not mention how it might affect the resistance of a moment connection. It was therefore assumed that provided a bolt torque is not necessary and provided it exists it does not influence the expressions above or the resistance of the connection.

Generally, the tensile resistances of the bolt rows and of the compression flange are the most critical and have the greatest influence on the final value of the moment capacity of the connection. The connections were therefore dimensioned in order to obtain failure of the connection by either bolt failure, yielding of the end plate, buckling of the bottom flange of the beam stub, or a combination of all of these modes.

The method presented in the previous pages for calculating the resistance of equivalent T-stubs produces a plastic distribution of forces; see distribution labelled as “likely distribution” in Figure 3.5 (a). Publication BCSA P398 (SCI/BCSA 1995) states that some connections with smaller bolts and relatively thick end plates have little deformation capacity. In such cases there is a danger that the upper bolts may fail before resistance is generated in lower rows. If the

plate is not thin enough, the plastic distribution must be modified and the force assigned to any bolt restricted to the value resulting from a "triangular" limit, as shown in Figure 3.5 (a), indicated by the "assumed distribution" label.

Eurocode 3 Part 1-8: Design of joints (CEN 2005) omits the requirement that the forces assigned to bolts in such case must be restricted to a "triangular" limit. Instead it states that in such case, of the plate being too thick to allow redistribution of forces, the connection does not have sufficient rotation capacity for plastic analysis. It is unclear what the designer is supposed to do when it comes to assuming a force distribution or reducing the force distribution.

The issue of force distribution is presented again in the discussion section of this Chapter.

The predicted row resistance values for the tested connections together with the assumed distributions are shown in Figure 3.5. The design moment resistance of the connection is given by:

$$M_{j,Rd} = \sum_{r} h_r F_{tr,Rd} \tag{3.7}$$

where $F_{tr,Rd}$ is the effective design tension resistance of bolt row r, h_r is the distance from bolt row r to the centre of the compression and r is the bolt row number.

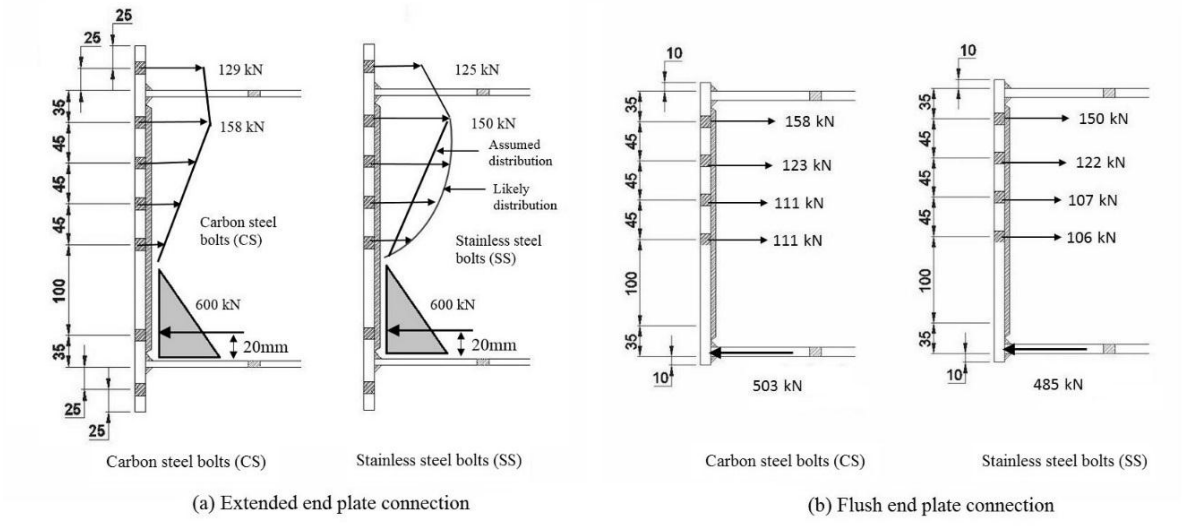

Figure 3.5: Force distributions for the calculated design moment capacity

In recently published literature, Stoddart et al. (Stoddart 2012) and Ribeiro et al. (Ribeiro, Santiago, Rigueiro, et al. 2015) suggest that in the case of high rate dynamic loading the strength of the end plate and bolt steels should be multiplied by the dynamic increase factor

(DIF) which can usually be observed in high rate material tests. The dynamic strength can be expressed simply as:

$$f_{y,dyn} = DIF_{steel} \cdot f_y \tag{3.8}$$

$$f_{ub,dyn} = DIF_{bolt} \cdot f_{ub} \tag{3.9}$$

where $f_{y,dyn}$ is the dynamic yield strength, $f_{ub,dyn}$ is the dynamic ultimate strength, and DIF is the Dynamic Increase Factor which can be calculated by carrying material tests and using an appropriate dynamic material model.

Two design moment capacities were calculated, one with safety factors and one without safety factors. The second allows a realistic comparison with experimental results. These are presented in Table 3.2 and were calculated using the material properties given in Table 3.3.

In the design stage of the dynamic case the material strengths were calculated using their corresponding dynamic increase factors. The DIFs can only be calculated for a fixed value of strain rate. As shown in Table 3.1, strain rates $\dot{\varepsilon}$ in the bolts and plates were estimated to be in the region of 20 s^{-1} so the DIFs were calculated for a more conservative value of 10 s^{-1}. The values of the DIFs and the material models used are listed in Table 3.3 and more details are presented in the next section.

Table 3.2: Design moment capacities of tested connection types

Test	Plate type	Bolts type	Design moment capacity with factors $M_{Rd}\ (kNm)$	Design moment capacity without factors $M^*_{Rd}\ (kNm)$	Beam stub capacity $M_{c,Rd}\ (kNm)$	Percentage of beam capacity
T1	Extended	CS	84	117	150 kNm	78%
T2A	Extended	SS	83	115	150 kNm	77%
T7	Extended	CS	93	130	190 kNm	68%
T4	Extended	SS	86	120	190 kNm	63%
T5	Flush	CS	76	105	215 kNm	48%
T6	Flush	SS	73	101	215 kNm	47%

T8	Flush	CS	83	115	300 kNm	38%
T11	Flush	SS	83	115	300 kNm	38%

Table 3.3: Material properties used

Connection element	Material designation	Average f_y (N/mm^2)	Average f_u (N/mm^2)	DIF_y	DIF_u	Material model used
305x102x25 UKB	S355	440	530	1.35	1.05	Malvar-Crawford (Malvar 1998)
305x127x37 UKB	S355	400	520	1.35	1.05	
End plate, 12mm thick	S355	407	560	1.35	1.05	
M12 carbon steel bolts	Grade 8.8	-	698	-	1.043	Johnson-Cook (Johnson & Cook 1983)
M12 stainless steel bolts	A4-70	-	665	-	1.063	

The Eurocode (CEN 2005) defines a partial-strength joint as one which has a design moment resistance lower than the plastic moment resistance of the connected beam or column. In all cases, the calculated moment capacity of the connections was less than the capacity of the beam. The extended end-plate connection achieves 77-78% of the beam capacity, whereas the flush-end-plate only 47-48%, see Table 3.2. Consequently all connection types are classified as partial strength according to the Eurocode (CEN 2005).

Lack of good manufacture and poor fit could lead to built-in stresses. Naturally, these will be dependent on the size and extent of any imperfections. The publications referenced in this section do not mention how these might affect the moment resistance of moment connections. The National Structural Steelwork Specification for Building Construction (BCSA 2010) specify tolerances for manufacturing and fit. As long as steelwork is built to these specifications any built-in stresses can probably be considered negligible.

3.4 Experimental testing of bolts and steel coupons

Bolts and steel coupon samples were tested in pure tension in order to find their material properties and failure mechanisms. The experiments were carried out in the controlled environment of the TSRL laboratory at the University of Southampton using the INSTRON 8032 testing machine. The machine is shown in Figure 3.6. This is a servo-hydraulic machine capable of delivering loads of up to 100kN with strain rates ranging from 0.0001/s to 1/s. The strain rate is a controlled parameter that is set before the test is started. The machine uses an electrically operated valve to control how the fluid is provided to the actuator, the motor controlling the movement of the system.

Figure 3.6: INSTRON 8032 testing apparatus

A testing rig was specifically designed for the testing of bolts in pure tension. The initial design of the rig is shown in Figure 3.7(a). Steel coupons were fabricated from the materials used for the subsequent connection endplates and beam stubs. The design for the coupons is shown in Figure 3.7 (b). These were tested under strain rates ranging from 0.001/s to 1/s in order to examine the effects of relatively low strain rates on the ultimate strength of the bolts. The data points returned by the machine included measurements of: time (s), displacement (mm) and force (N).

The improved testing rig for bolt testing comprised four separate steel components. Figure 3.8 (a) shows the four components separately. Figure 3.8 (b) shows how a bolt is placed between the two halves of the test rig. One nut was used to tighten the bolt being tested and hold the two halves of the test rig together. The four steel components were designed to fit within each other and held together by eight stainless steel bolts loaded in shear. Figure 3.8 (c) shows the assembled test rig. The two ends of this assembly are pulled apart in tension in the INSTRON machine presented previously.

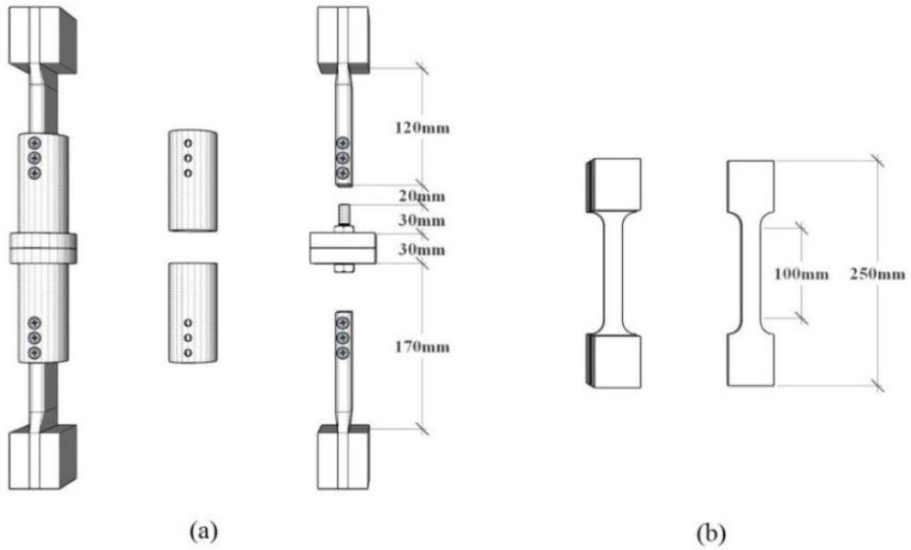

Figure 3.7: (a) Initial design of testing rig for bolts and (b) design of steel coupon

(a) Separate fabricated steel sections of testing rig

(b) Sample bolt placed between the two halves of the rig

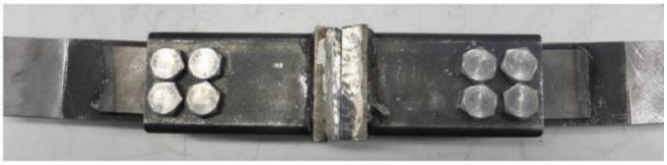

(c) Assembled test rig

Figure 3.8: Bolt testing rig used for testing bolts from low (0.001 s^{-1}) to medium strain rates (1 s^{-1})

The displacement of the actuator of the INSTRON test machine was recorded on a computer using 'StrainSmart 6200' software. The displacement of the actuator as well as the load being applied to the sample was recorded. These results were then imported into a Microsoft Excel spreadsheet, to allow the analysis of the recorded data to take place.

Tests were carried out by the author on A4-70 stainless steel bolts and grade 8.8 carbon steel bolts with one nut mainly at quasi-static strain rates of 0.001/s. More tests were carried out by Katharine Edwards (Edwards 2015) at different loading rates on A4-70 stainless steel bolts, grade 8.8 carbon steel bolts with one nut and grade 8.8 carbon steel bolts with two nuts. The bolts had an engage length, between the bolt head and the nut, of approximately 35mm. This engaged length corresponds to that used in the joints tests presented later in the chapter.

3.4.1 Failure mechanisms for bolts

All stainless steel bolts tested by the author were observed to fail through ductile body necking and fracture of the neck. This failure mode is counter-intuitive since the tensile area in the threaded region is smaller than the tensile area of the bolt body. This behaviour might be explained by the local increase in the strength levels for austenitic grades by cold working (SCI/EuroInox 2006). It is reported that the 0.2% proof strength is typically enhanced by a factor of 50% in the corners of cross sections by cold forming. It is possible that shank failure was obtained due to the high local strength in the threaded region of the austenitic stainless steel.

Figure 3.9 shows failure mechanisms for different types of bolts. All carbon steel bolts tested with one nut were observed to fail through thread stripping and all carbon steel bolts with two nuts were observed to fail through bolt body fracture.

Figures 3.10, 3.11 and 3.12 show the force versus displacement characteristics of a stainless steel bolt, a grade 8.8 bolt tested with one nut and a grade 8.8 bolt tested with two nuts. Each graph presents two tests, at a strain rate of 0.001 s^{-1} and of 1 s^{-1}.

These figures also show the fracture surface and illustrate the failure mechanism of each bolt. With increases in strain rates a dynamic increase in the ultimate strength of the bolt was observed. However, in all high rate cases the nut was observed to travel a shorter distance before fracture of the material occurred.

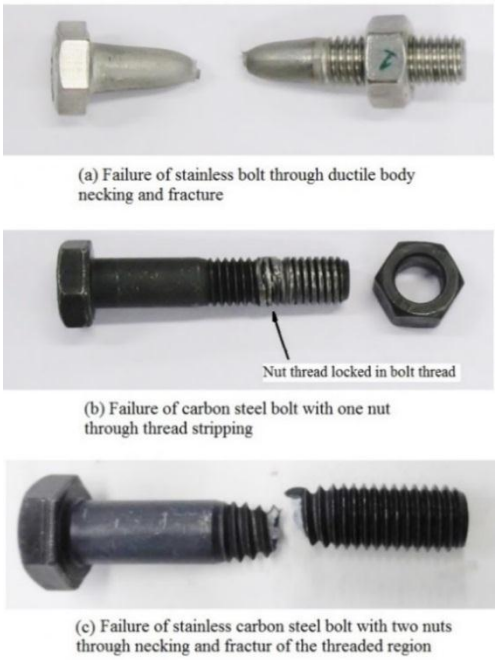

(a) Failure of stainless bolt through ductile body necking and fracture

(b) Failure of carbon steel bolt with one nut through thread stripping

(c) Failure of stainless carbon steel bolt with two nuts through necking and fractur of the threaded region

Figure 3.9: Failure mechanism for tested bolts

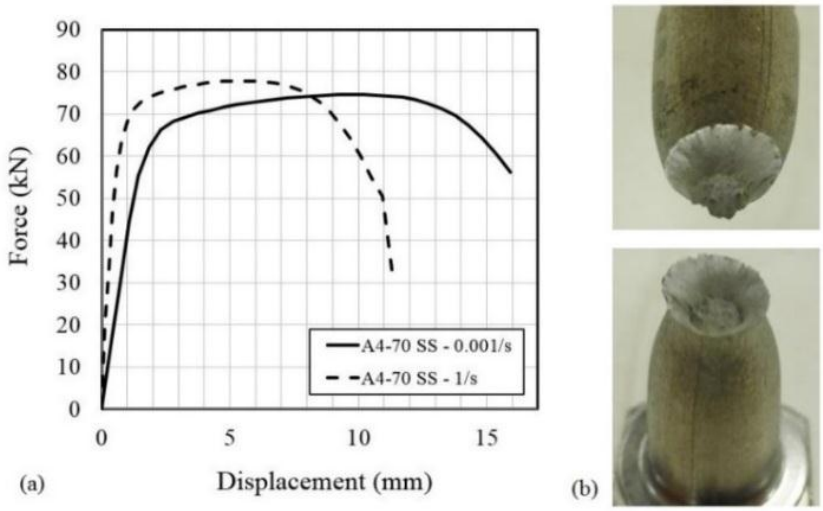

Figure 3.10: A4-70 stainless bolt, (a) force versus displacement and (b) fracture surface

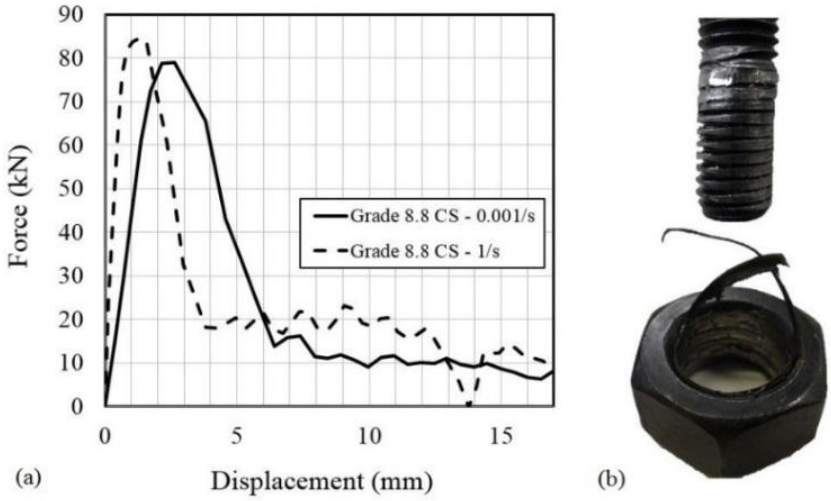

Figure 3.11: Grade 8.8 with one nut (a) force versus displacement and (b) thread stripping

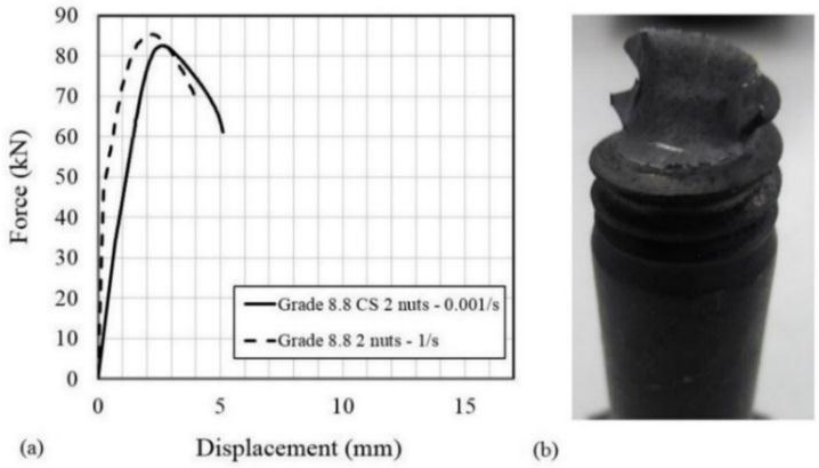

Figure 3.12: Grade 8.8 with two nuts (a) force versus displacement and (b) fracture surface

It was observed that the strength of both bolt types increases with increasing strain rates. In this case the Johnson-Cook (Johnson & Cook 1983) model was used to characterize this relationship:

$$\sigma = (\sigma_0 + K\varepsilon^n)\left(1 + C\ ln\frac{\dot{\varepsilon}}{\dot{\varepsilon}_0}\right)\left[1 - \left(\frac{T - T_r}{T_m - T_r}\right)^m\right] \tag{3.10}$$

where σ is the stress, σ_0 is the yield stress under static conditions, the constants K, n and m are material parameters, T_r is the reference temperature, T_m the melting point, $\dot{\varepsilon}_0$ the reference strain rate, and importantly here the C parameter characterises the strain-rate dependence. Considering only the strain rate dependence above, the DIF can be expressed as:

$$DIF_{bolt} = \frac{\sigma_{dynamic}}{\sigma_{static}} = 1 + C\ ln\frac{\dot{\varepsilon}}{\dot{\varepsilon}_0} \tag{3.11}$$

The dynamic increase factor is plotted for corresponding strain rates in Figure 3.13 for both bolt types. Logarithmic trend lines and their equations are shown on the graph together with the equivalent Johnson-Cook C parameters. The C parameters are 0.0047 and 0.0069 for carbon steel and stainless steel respectively.

The fracture strain is defined here as the strain value in the material at the moment when it fractures completely in such a way that it is unable to continue carrying the loads it is subjected to. With increasing strain rates, a decrease in ductility was observed in both bolt types. In the case of the stainless steel bolts the fracture strain can be estimated using measurements of the initial radius and the radius of the neck at fracture (Bao & Wierzbicki 2004):

$$\varepsilon_f = \ln\frac{A_0}{A_f} = \ln\frac{r_0^2}{r_f^2} \tag{3.12}$$

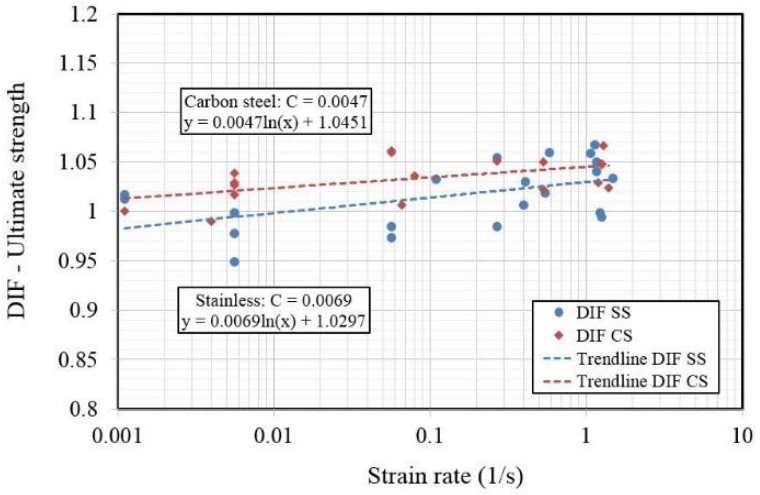

Figure 3.13: Dynamic increase factor (DIF) versus strain rate from bolt tests

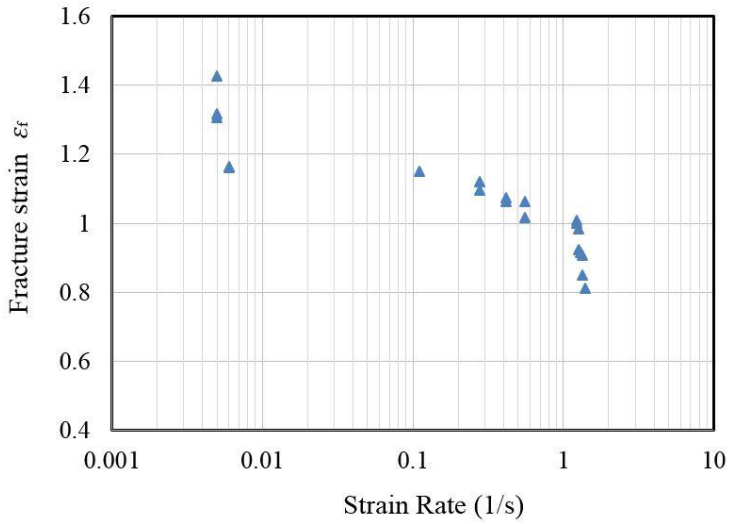

Figure 3.14: Fracture strain versus strain rate for stainless steel bolts

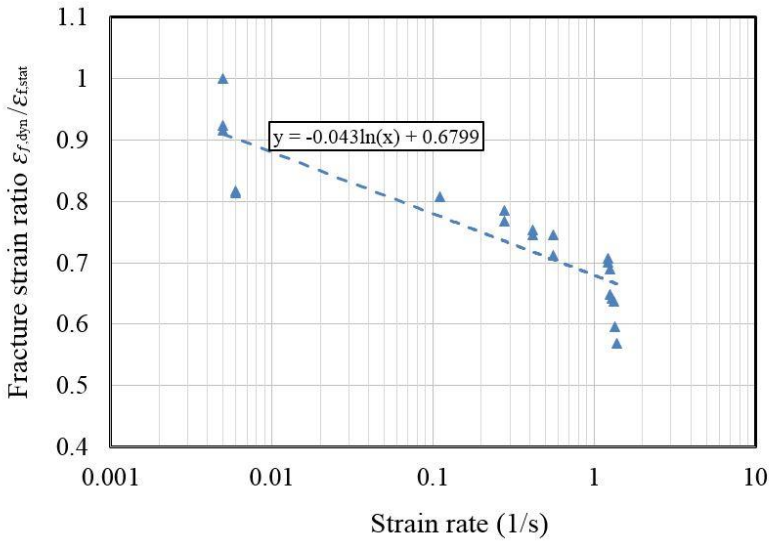

Figure 3.15: Fracture strain ratio $\frac{\varepsilon_{f,dyn}}{\varepsilon_{f,stat}}$ versus strain rate for stainless steel bolt

The relationship between the fracture strain and strain rate is shown in Figure 3.14 and the one between fracture strain ratio and strain rate in Figure 3.15. Fitting a trend line to the latter is more consistent with the material model as is discussed below.

In damage mechanics, the Johnson-Cook damage model is commonly used to describe the fracture strain (Johnson & Cook 1985). Using this model in a simplified form, considering only the strain-rate sensitivity, an expression for the Dynamic Reduction Factor (DRF) can be found for the fracture strain:

$$DRF = \frac{\varepsilon_{f,dyn}}{\varepsilon_{f,stat}} = 1 - D\ ln\frac{\dot{\varepsilon}}{\dot{\varepsilon}_0} \tag{3.13}$$

Where $\varepsilon_{f,dyn}$ is the dynamic fracture strain, $\varepsilon_{f,stat}$ is the static fracture strain corresponding to the reference strain rate $\dot{\varepsilon}_0$, $\dot{\varepsilon}$ is the dynamic strain rate, and the D parameter characterises the strain-rate dependence. In the case of stainless steel the value for the D parameter for strain rates ranging from 0.001/s to 1/s was found to be 0.043.

Tensile tests were also carried out for steel coupons cut from the beam stubs and end plates for the same range of strain rates. The stress strain relationship for the S355 end plate steel is shown in Figure 3.16 for two selected strain rates. In the case of the S355 steel it was observed that the dynamic effect is greater on the yield stress than on the ultimate stress. These observations are consistent with those made by Malvar and Crawford (Malvar 1998) when conducting tests on steel reinforcing bars for strain rates ranging from 0.001/s to 10/s.

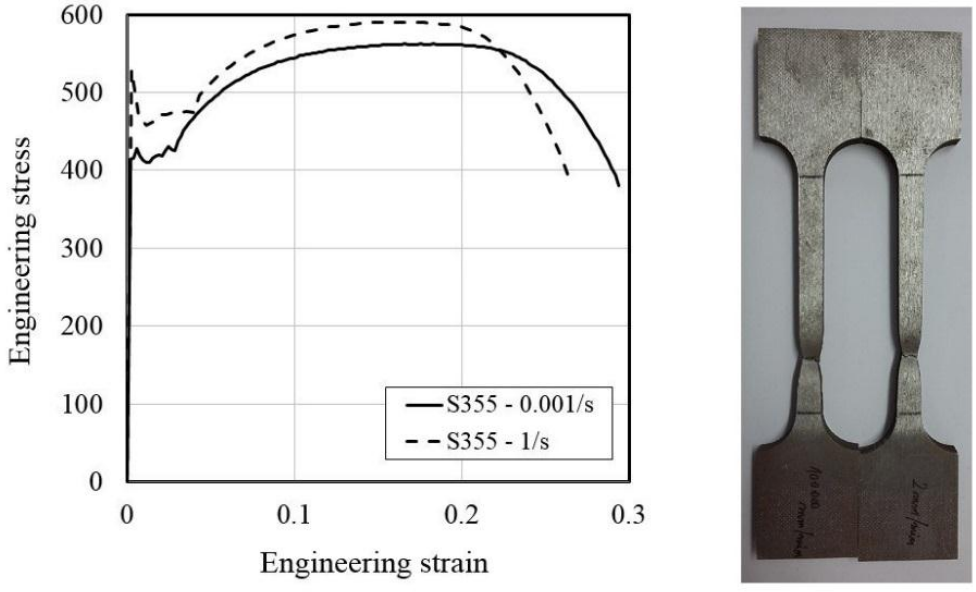

Figure 3.16: Engineering stress strain curves for S355 steel taken from end plate for selected strain rates

The Malvar and Crawford model appears to accurately predict the DIF in the case of the S355 steel. The equations to calculate the DIF from the strain rate and static yield strength were proposed as:

$$DIF = \left[\frac{\dot{\varepsilon}}{10^{-4}}\right]^{\alpha} \tag{3.14}$$

where, for the dynamic yield stress:

$$\alpha_y = 0.074 - 0.040\frac{f_y}{414} \tag{3.15}$$

and for the dynamic ultimate stress:

$$\alpha_u = 0.019 - 0.009\frac{f_y}{414} \tag{3.16}$$

Figure 3.17 shows the true stress strain curves for three materials. Ribeiro et al. (2015) provided the true stress strain data for grade 8.8 carbon steel bolts and that data is used in this figure. Using the experimental data in this work it was possible to calculate true stress strain curves for the S355 steel and the A4-70 stainless steel bolts. More details about how these were derived can be found in Chapter 4 and Appendix C.

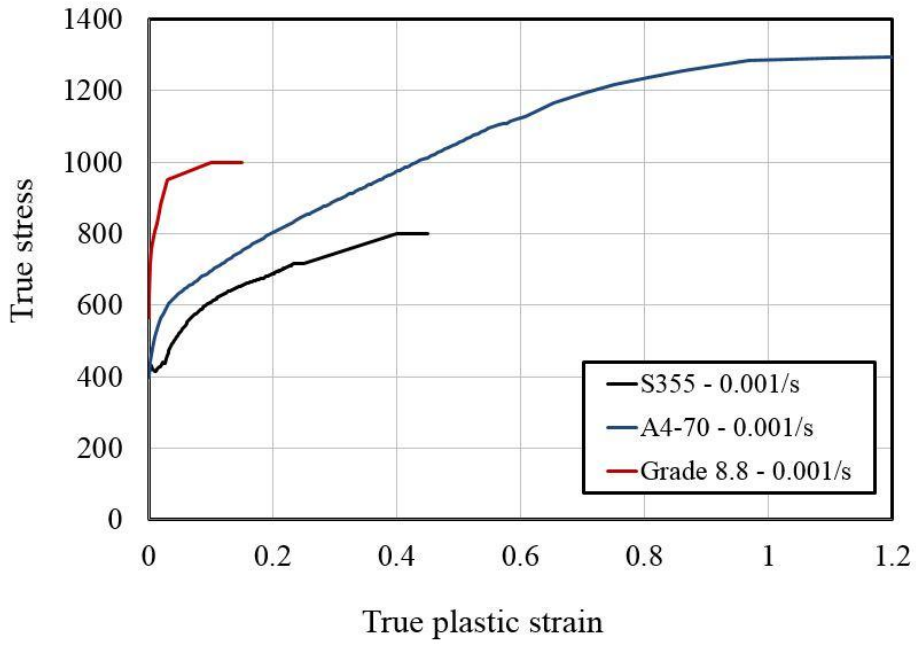

Figure 3.17: True stress versus true plastic strain for different materials

The length of each curve in Figure 3.17 is a direct reflection of the ductility of the materials. Grade 8.8 steel is the least ductile material, grade S355 is somewhat ductile and grade A4-70

stainless steel is the most ductile. This figure contains the most essential data necessary for finite element modelling of the plastic behaviour of these materials.

To summarise, it was found that the dynamic effects on the steels in this work were typical behaviours exhibited by steels at high strain rates in general (Meyers 1994):

- There is a dynamic increase in the yield and ultimate stresses with increasing strain rates;
- There is often a reduction in ductility or fracture strain with increasing rates;
- In the case of S355 steel there is a greater dynamic increase effect on the yield stress than on the ultimate stress.

3.5 Test rig design and set-up

As part of the research carried out by Tyas et al. (2012) an experimental testing rig was developed at the Civil Engineering Department of University of Sheffield (CEDUS) laboratory in Buxton; see Figure 2.19 in Chapter 2. The same rig was modified to carry out the experimental tests presented in this work. New items had to be designed for the rig only for the purpose of these experimental tests. The items are shown in Figure 3.18 in white and are as follows:

- the beam stub with the connection to be tested
- an extension piece, i.e. a column stub bolted to the "flying column"
- two angle supports that are bolted to a base beam and hold the beam stub to be tested

Apart from the above, the only other major modification to the rig was removal of the other loading ram, since the rig can function with two loading rams at the same time. Only one loading ram because the load had to be applied at a distance from the connection, creating the lever arm needed to give a moment large enough to break the connection. The load cell, the laser displacement gauges (LDGs) and the data capturing system were all provided by the laboratory at Buxton.

The tests are unusual from the perspective that most tests of this kind are carried out under controlled displacement for safety reasons, allowing the load to reduce slowly and failure to occur in a controlled manner. Here the load was maintained during failure. Arguably this more closely matches the loading experienced in a real structure. From a test point of view this presents hazards because the energy in the system is released rapidly at failure, so personnel triggered the testing apparatus while located behind a protective wall.

A 3D model of the testing rig used to carry out the experimental tests is shown in Figure 3.18. In the *quasi-static* tests the pressure is released through a cylinder and slowly increased to push the piston or loading ram. Load is applied through the loading ram only at one end of "the flying column" and is measured at the point of application using a load cell. The load increases to 120 kN in 300 seconds, giving loading rates of 0.40 kN/s.

In the *dynamic* tests the pressure accumulator labelled in Figure 3.18 was pressurised up to approximately 100 atmospheres until a brass diaphragm failed. This released the compressed air into the piston and caused the loading ram to extend completely in 40 ms, which in turn loaded the flying column. The load thus suddenly increases to 120 kN in under 10 ms after the brass diaphragm bursts, giving loading rates of up to 20 kN/ms.

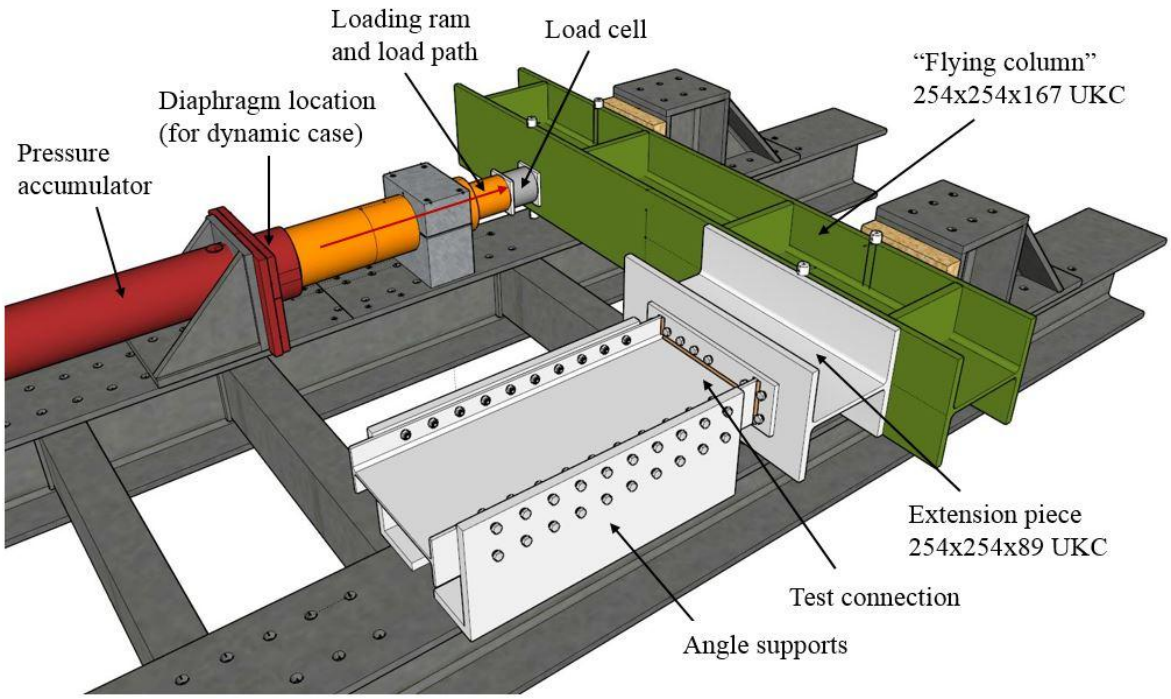

Figure 3.18: 3D model of testing rig used for testing of designed moment connections from low (0.001 s^{-1}) to high strain rates (up to 100 s^{-1})

The load is applied through the loading ram at one end of "the flying column" and is measured at the point of application using a load cell, see Figure 3.19. The tested connection is located at the other end of the "column" and is held in place by two robust angle supports.

Calibrated compression load cells were used to measure the loads applied to the column section throughout the tests. The load cells were mounted at a fixed distance from the end of the column section and a hemispherical steel bearing ensured they measured the applied load perpendicular to the column flange, Figure 3.19.

Displacements were measured at five points using laser displacement gauges (LDGs). LDG1 and LDG2 measured the displacement of the "flying column" in the direction of the loading ram. These measurements enabled calculation of the rotation α of the column. LDG3 measured the axial displacement of the "column". It was found in preliminary set-up tests that the supporting angles were susceptible to rotation, so LDG4 and LDG5 were located to measure displacements of the angles and were used to calculate the rotation β of the angles. The location of the LDGs is shown schematically in Figure 3.20.

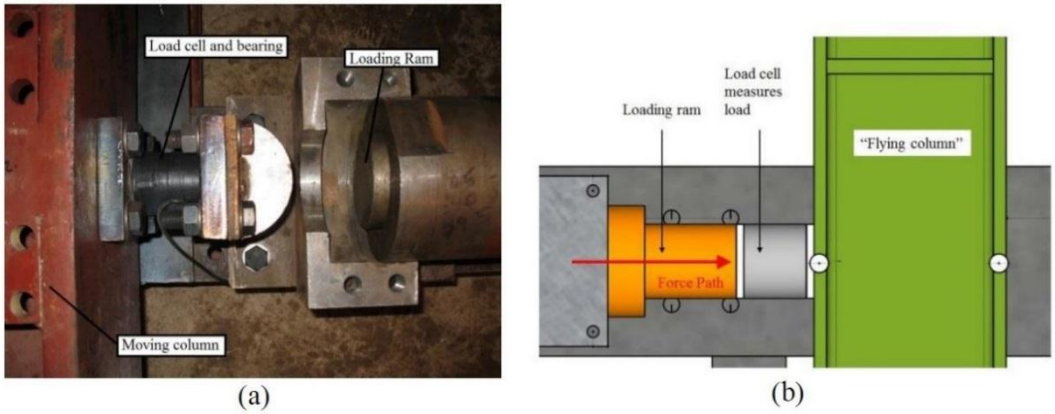

Figure 3.19: (a) Photo of load cell and loading ram and (b) illustration of force path through ram

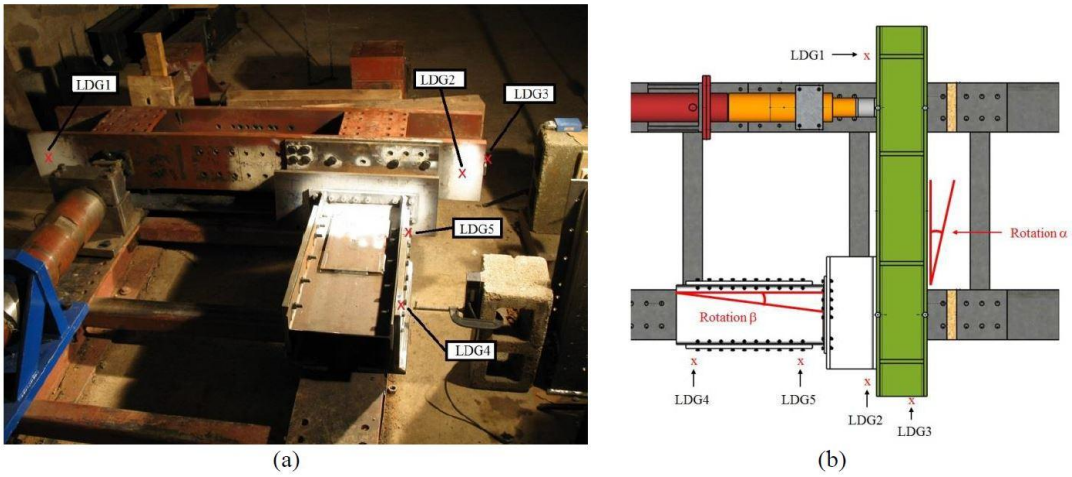

Figure 3.20: Displacement measurement locations illustrated on (a) photo of rig and (b) 3D model

A high speed camera Phantom V4.2 was used to film the failure of the connections in order to allow a video analysis of the failure process after the experimental tests. High intensity lights were also set up to give a clear video picture. This set-up is illustrated in Figure 3.21. The video was recorded 6918 frames at a resolution of 160x232 with a frame rate of 500fps for quasi-static tests and 8000fps for dynamic tests. Table 3.4 presents the camera settings and data sampling frequency for each tests.

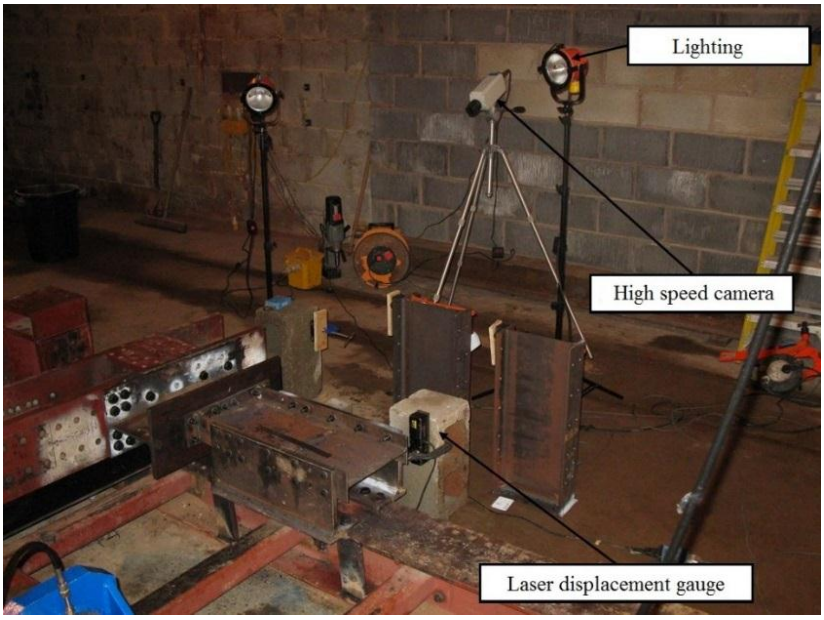

Figure 3.21: High speed camera and lighting set-up

Table 3.4: Video settings and data sampling frequency

Test	Loading	Video camera			Load cell and LDGs data sampling		Video save trigger point
		Image resolution	No. of frames	Frames per second	No. samples	Frequency	
T1	Static	160x232	6918	10fps	100k	99.995 Hz	At start
T2A	Static	160x232	6918	500fps	100k	99.995 Hz	Manually at break
T7	Dynamic	160x232	6918	500fps	100k	195.313 kHz	
T4	Dynamic	160x232	6918	8000fps	100k	195.313 kHz	
T5	Static	160x232	6918	500fps	100k	99.995 Hz	
T6	Static	160x232	6918	500fps	100k	99.995 Hz	
T8	Dynamic	160x232	6918	500fps	100k	195.313 kHz	
T11	Dynamic	160x232	6918	8000fps	100k	195.313 kHz	

The loads were applied by the pneumatic ram using a variety of loading conditions dictated by the diaphragm installed in the pressure receiver. A series of bursting trials were carried out previously by Tyas et al. (2012) in order to predict the load-time history for a variety of diaphragm arrangements. The diaphragms were made from either 0.51mm (thin) or 0.9mm (thick) brass and bolted into a specially constructed cassette with a 27mm aperture, Figure 3.22. Figure 3.23 shows the results from these trials, which all demonstrate a rise time of

approximately 40ms showing that this is governed mainly by the aperture size and not by the forcing pressure.

The target moment was achieved by setting a lever arm of approximately 1.1 meters. This lever arm multiplied by an estimate load of approximately 121kN, which would be obtained with a relatively thick diaphragm, would give a moment of approximately 133kN. This moment was large enough to make all connections fail.

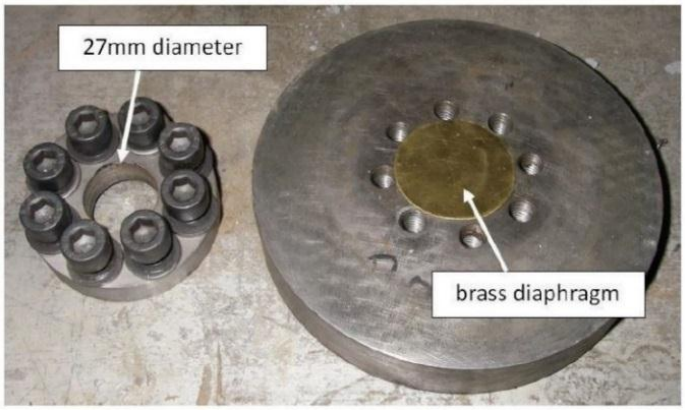

Figure 3.22: Diaphragm and cassette system (Stoddart 2012)

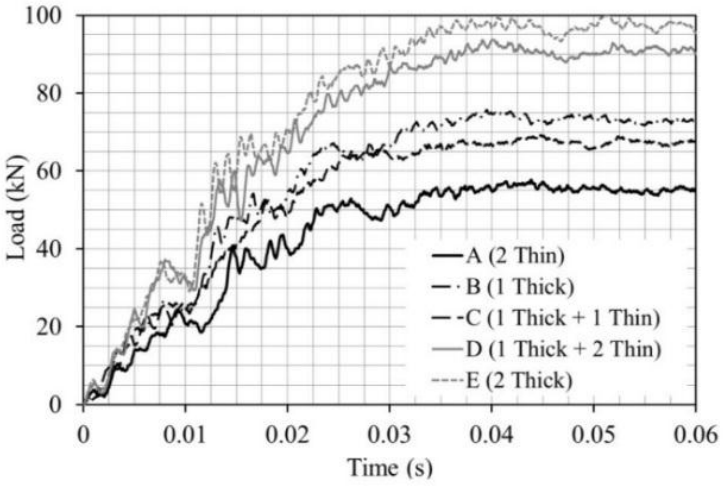

Figure 3.23: Diaphragm bursting trials (Stoddart 2012)

The analysis of the experimental data was first carried out for the *quasi-static* loading case. In this case the inertia effects are ignored. From force and moment equilibrium, Figure 3.24 (a), the connection force and moment are given by:

$$F_C = F_A \tag{3.17}$$

$$M_C = d \cdot F_A \tag{3.18}$$

where F_C and M_C are the connection force and moment, F_A is the load applied, and d is the distance between the loading ram and the centre of the moment connection. Distance d is equal to $1105mm$ in all tests. Figure 3.24 (b) presents the load applied F_A versus time for test T2A to exemplify the general character of loading in quasi-static cases.

When load is applied to the "flying column", the column, connection and beam stub all move together as a rigid body. This rigid body has a tendency to rotate about a point which is called here the instantaneous centre of rotation (ICR). Initially, rotation takes place around the centre of mass of the rigid body which is close to the centre of the connection, approximately half way between the top and bottom flange. So the ICR is in the position of the centre of mass of the rigid body. When the connection fails, however, the bodies separate and the ICR moves from the centre of mass to the bottom flange. The ICR is important because its movement changes the value of the lever arm in the test, albeit by a small amount of 150mm. This has a direct effect on the difference between the experimental and numerical values presented and will be discussed in more detail in the following sections.

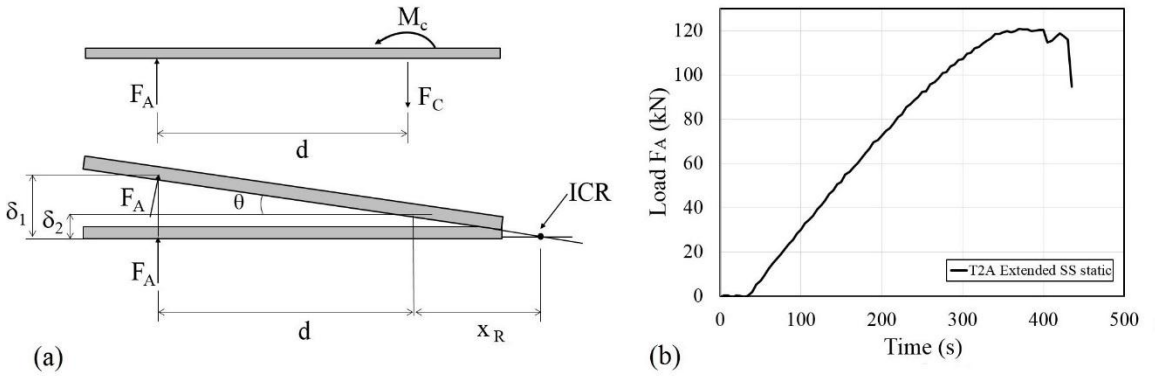

Figure 3.24: Quasi-static loading scenario: (a) free body diagram and (b) test T2A load versus time

In the case of *dynamic* loading of the connection, inertia effects are no longer negligible. From force and moment equilibrium, Figure 3.25 (a), the connection force is given by:

$$F_C(t) = F_A(t) \cdot cos[\theta(t)] - F_I(t) = F_A(t) \cdot cos[\theta(t)] - m_c\ddot{\delta}_c \tag{3.19}$$

where F_C is the connection force, F_A is the applied load, F_I is the inertia force, m_c is the mass of the flying column and extension piece and $\ddot{\delta}_c$ is acceleration of the centre of mass. Figure 3.25 (b) presents the load applied F_A versus time for test T4 to exemplify of the general character of loading in dynamic cases.

The “flying column” is much heavier than the beam stub and angles, so it was modelled as a rigid beam for simplicity. Evidence of vibration is observed in experimental data but appears small.

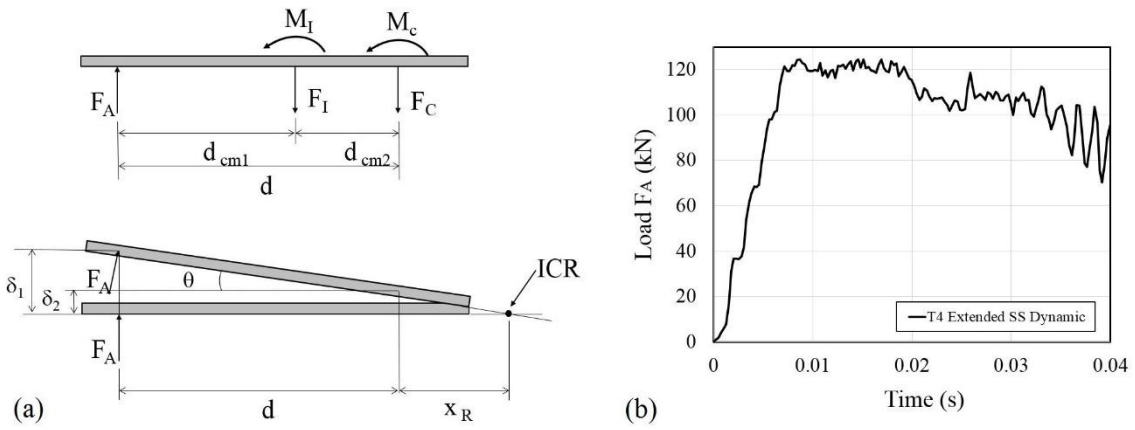

Figure 3.25: Dynamic loading scenario: (a) free body diagram and (b) test T4 load versus time

In order to calculate the connection moment the equilibrium equation for moments is written so that inertia effects are taken into account resulting in the following equation:

$$M_C(t) = d_{cm1} \cdot F_A(t) \cdot cos[\theta(t)] + d_{cm2} \cdot F_C(t) - I_{mc} \cdot \ddot{\theta}(t) \qquad (3.20)$$

where M_C is the connection moment, d is the distance between the loading ram and the centre of the connection, d_{cm1} is the distance between the loading ram and centre of mass, d_{cm2} is the distance between the centre of mass and the centre of the connection, I_{mc} is the mass moment of inertia about the centre of mass and was calculated as 339kgm^2. It was observed in the experiments that both the column and the angle supports rotated; see Figure 3.26. This was considered and displacements were recorded at the ends of both.

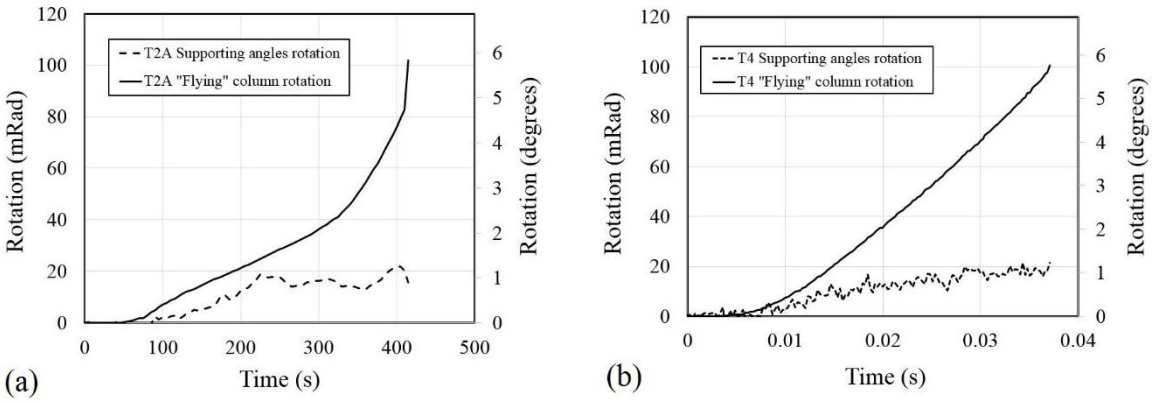

Figure 3.26: Rotation versus time for dynamic test T2A and T4

The rotations of the column α and the supports β, and the relative rotation θ are given by:

$$\alpha = \tan^{-1}\left(\frac{\delta_1 - \delta_2}{d_{12}}\right) \tag{3.21}$$

$$\beta = \tan^{-1}\left(\frac{\delta_4 - \delta_5}{d_{45}}\right) \tag{3.22}$$

$$\theta = \alpha - \beta \tag{3.23}$$

where δ_1 and δ_2 are the displacements at the ends of the column, d_{12} is the distance between the two laser gauges pointed at the column, δ_4 and δ_5 are the displacements at the ends of the angles, and d_{45} is the distance between the two laser gauges pointed at the angles. Figure 3.26 shows the rotation of the "flying column" α and of the supporting angles β in dynamic test T4. All graphs are plotted versus the relative rotation θ.

In order to establish the strength, ductility and energy absorption capacity of connections, graphs of moment versus rotation were plotted for the experimental tests. The ultimate moment $M_{ult,exp}$ is the maximum moment value, the ductility $\varphi_{max,exp}$ is given by the amount of rotation to the point of complete failure and the energy absorption E_{exp} is given by the area under the moment versus rotation graph. These can be expressed by the following equations:

$$M_{ult,exp} = \max(\{M(\varphi)\}) \tag{3.24}$$

$$\varphi_{max,exp} = \max(\{\varphi\}) \tag{3.25}$$

$$E_{exp} = \int_0^{\varphi_{max,exp}} M(\varphi)d\varphi \tag{3.26}$$

Graphs of moment versus rotation and tabulated values for the above are presented in the following section.

3.6 Results

The strength, ductility and energy absorbed for each connection test is summarised in Table 3.5. The design moment capacities do not include factors of safety, which were removed in order to more clearly reveal the accuracy of the Eurocode 3 design expressions. There was a good agreement between the predicted and experimental test results under quasi-static loading. Under dynamic loading the stainless steel bolted flush end-plate connection strengthened, as would be expected from the dynamic increase in material properties discussed earlier. The stainless steel bolted extended end-plate connection weakened under dynamic loading, but still achieved the design strength. This connection failed by flange buckling and this may have prevented a dynamic strength increase developing, although this is discussed in more detail later. The experimental testing of carbon-steel bolts under high strain rates would suggest an increase in strength of the connections under high strain-rate loading, although this was not observed. In fact these connections were significantly understrength and this highlights the known reliability problems when using dynamic increase factors for material properties for calculating design strengths (Smith et al. 2010). Important from a robustness point of view, stainless steel bolted connections can be seen to have absorbed approximately 4 times the energy of the carbon steel connections.

Table 3.5: Connection test results (* calculated without safety factors)

Test	Connection type	Bolt type	Loading type	Design capacity* $M_{Rd}\ (kNm)$	Experimental capacity $M_{RExp}\ (kNm)$	Rotation capacity $\varphi_{exp}\ (°)$	Absorbed energy $E\ (kJ)$
T1	Extended	Carbon steel	Static	117	127	1.20	2.0
T2A	Extended	Stainless steel	Static	115	133	4.22	8.3
T7	Extended	Carbon steel	Dynamic	117	90	0.70	2.5
T4	Extended	Stainless steel	Dynamic	115	115	4.40	8.3
T5	Flush	Carbon steel	Static	105	98	1.20	1.6
T6	Flush	Stainless steel	Static	101	105	3.42	6.9
T8	Flush	Carbon steel	Dynamic	105	87	0.80	1.8
T11	Flush	Stainless steel	Dynamic	101	115	3.50	6.9

3.6.1 Quasi-static connection tests

Figure 3.27 shows the moment rotation behaviour for the static tests with values of strength labelled at selected points. The tests loaded the connections over a period of approximately 300 seconds, after which failure occurred in less than 100 milliseconds. The carbon steel bolts reached their ultimate strength with no significant plastic deformation of the end plate, after which they failed in a brittle manner. This is evident both in the moment versus rotation relationships, where the maximum rotation is found to be just over 1 degree, as well as from the photographs of the connections taken after failure.

The stainless steel bolts deformed plastically and this caused significantly more deformation in the plate than for the carbon steel bolted connections, see Figure 3.28. It is important to note that bottom flange buckling was observed in the case of the extended end-plate connection with stainless bolts. The compression flange buckles and plastic deformation spreads through the web in compression. Referring to the possible failure modes of a T-stub in Figure 3.4, the carbon steel bolts led to a mode 3 failure. Although the stainless steel bolts have a lower ultimate strength than carbon steel bolts, they changed the T-stub failure to a mode 2 failure due to their superior ductility. Thus, the ductility of stainless bolts is reflected in an increase in the ductility of the connections.

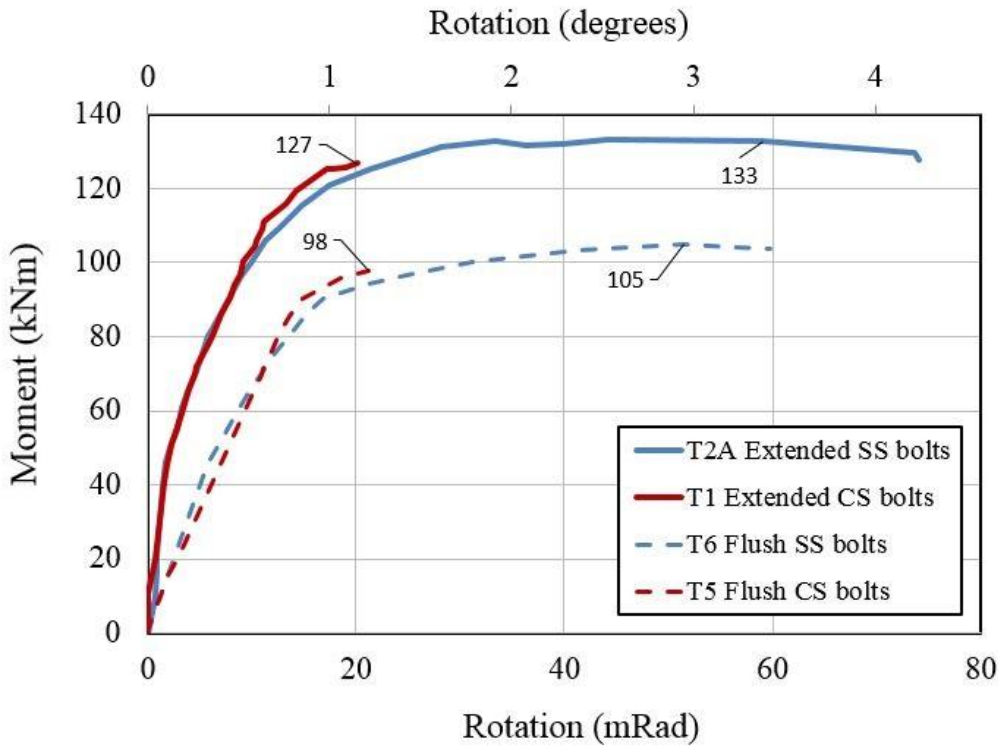

Figure 3.27: Moment versus rotation for quasi-static tests

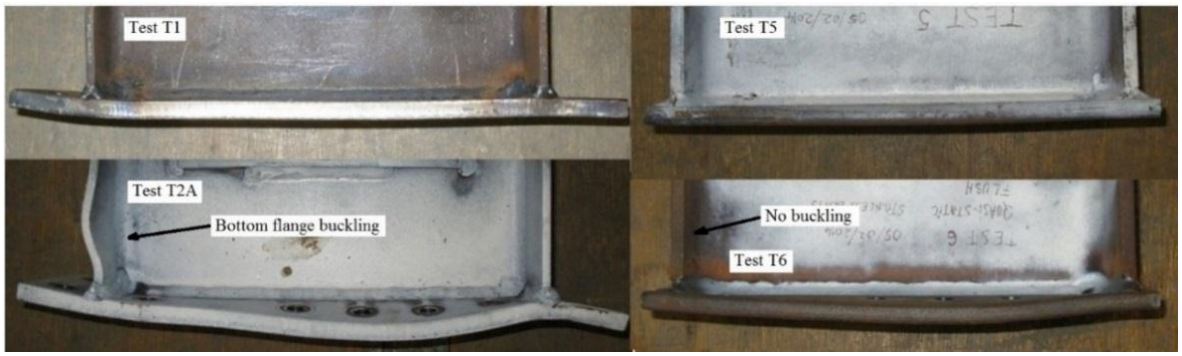

Figure 3.28: Plate deformation with carbon steel (top) and stainless steel bolts (bottom) for quasi-static tests

3.6.2 Dynamic connection tests

When the connections were loaded dynamically the moment increases to a first initial peak value in a time period of 4 milliseconds. In test T7, after the first peak, the resistance of the carbon steel bolted connection plateaus for 6 milliseconds as the threads of the nut deform plastically, Figure 3.29. Once the deformation commenced the resistance of the connection decreased linearly to zero in less than 20ms. As the high-speed digital camera frame rate was 500fps, the entire loading and failure was captured with sufficient detail to understand the failure process. Figure 3.29 shows three frames at the commencement of thread stripping, during the process, and after most threads are completely stripped. The end plate remains flat during this process.

In test T4, the stainless steel bolted connection shown in Figure 3.29, the extended end plate and bolts are seen to deform plastically, resulting in a gradual increase in moment capacity. The frame captured at 22ms shows significant plastic deformation of the end plate, the bolts, and the asymmetrical buckling of the compression flange. Moment versus rotation relationships are presented in Figure 3.30 for the extended end plate connection together with the static loading cases.

This asymmetric buckling is most likely the cause of the reduction in the dynamic strength of the extended end-plate connection. It leads to out-of-plane motion that causes the bolt diagonally opposite the buckle fail first and likely at a different time then the bolt next to it in the same row, i.e. 1-2ms difference. The buckle can be seen most clearly at the 31ms Frame in Figure 3.29. By comparison, flange buckling did not occur in the flush end-plate connection. The absence of this failure mode may have allowed the stainless steel flush end-plate connection to develop a dynamic strength increase, as was expected from the bolt material property tests.

A similar sequence of events was observed for the dynamic tests of the flush end plate connections. Several important differences must be noted in test T11 on the stainless steel bolted flush connection, Figure 3.31. Here there was no buckling of the bottom flange and this is the only test where a dynamic increase in the moment capacity of the whole connection was observed, as Figure 3.31 illustrates.

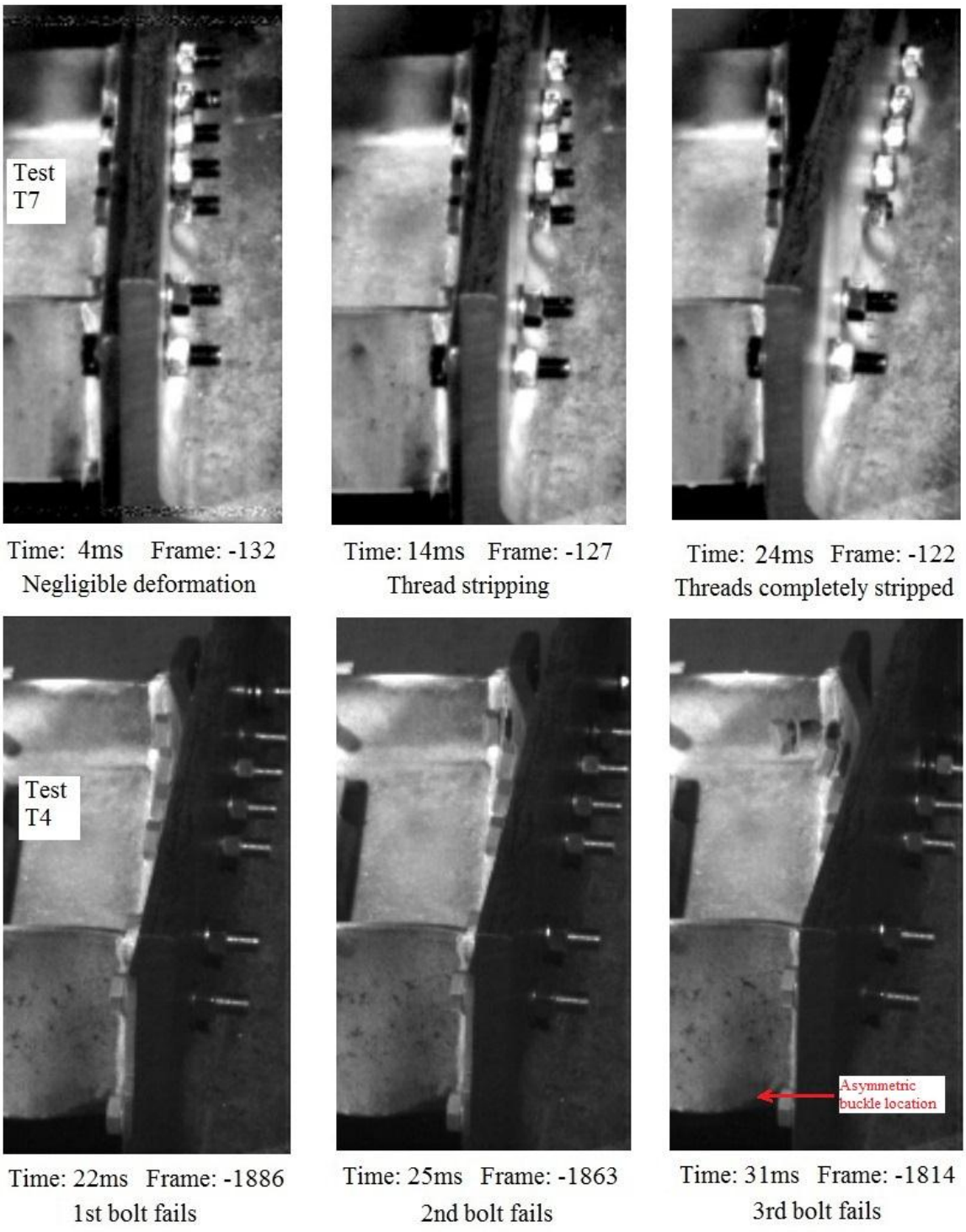

Figure 3.29: Frames captured after commencement of dynamic loading for carbon steel bolted connection (top row) and stainless steel bolted connection (bottom row)

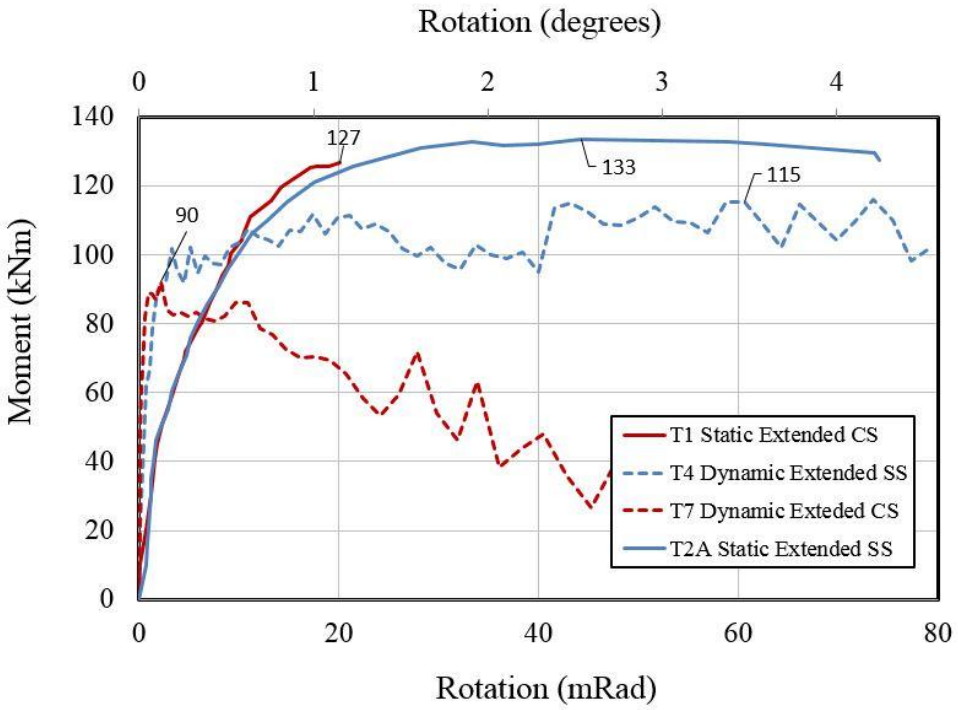

Figure 3.30: Moment versus rotation for static and dynamic extended plate tests

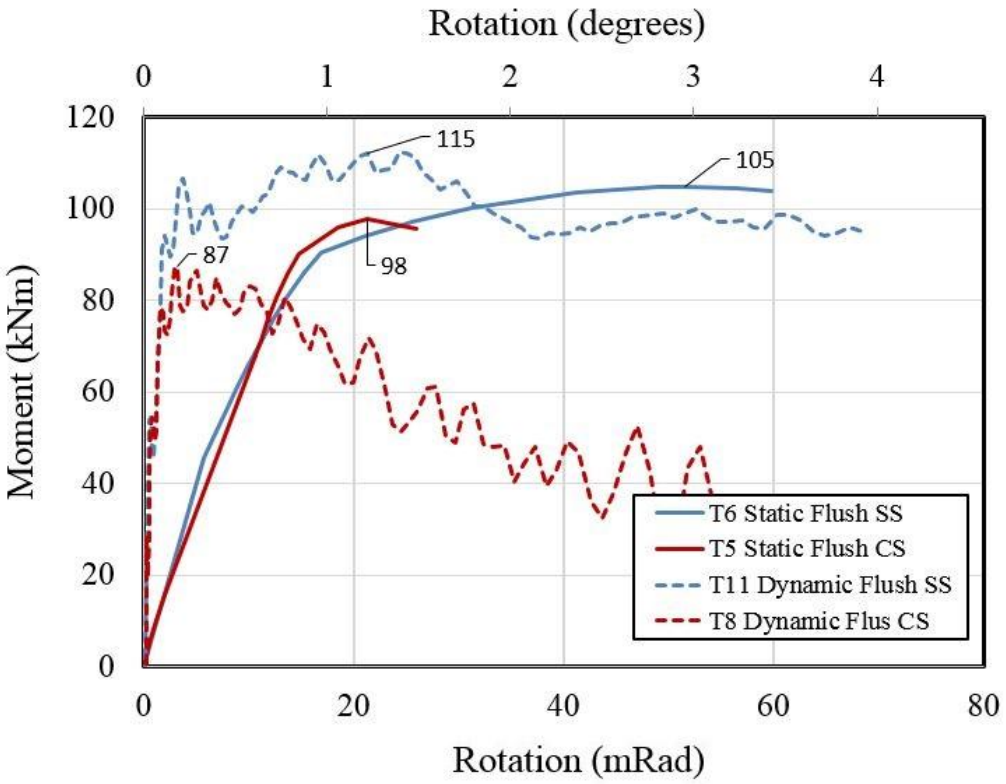

Figure 3.31: Moment versus rotation for static and dynamic flush plate tests

In the carbon steel bolted connections thread stripping leads to a rapid loss of connection strength. In the case of the stainless steel bolted end-plate connections, the bolt ductility provides time for end-plate deformation before final failure, allowing for greater overall connection ductility, as illustrated by the difference between the top and bottom rows of images in Figure 3.29.

In the dynamic cases, the movement of the instantaneous centre of rotation (ICR) from the centre of the connection, a value of 0.150m, to the bottom flange, a value of 0m, is more evident. This change is illustrated in Figure 3.32 for tests T7, T8, and T11. Test T4 is the only test where the instantaneous centre of rotation moves to a position which is 100mm from the bottom flange, 50mm lower than the centre of the connection. This can be attributed to the asymmetrical buckling of the bottom flange as it is the only test that shows such asymmetry. Using this data, the position of the centre of compression can be estimated at approximately 50mm. This is only an approximation as there is no clear correlation between the centre of rotation and centre of compression, apart from the fact that the compression centre should be lower than the rotation centre.

It is important to note in Figure 3.32 that the changes in ICR, of approximately 0.15m, are relatively small compared to the length of the lever arm, 1.1m, so they have a small effect on the experimental results.

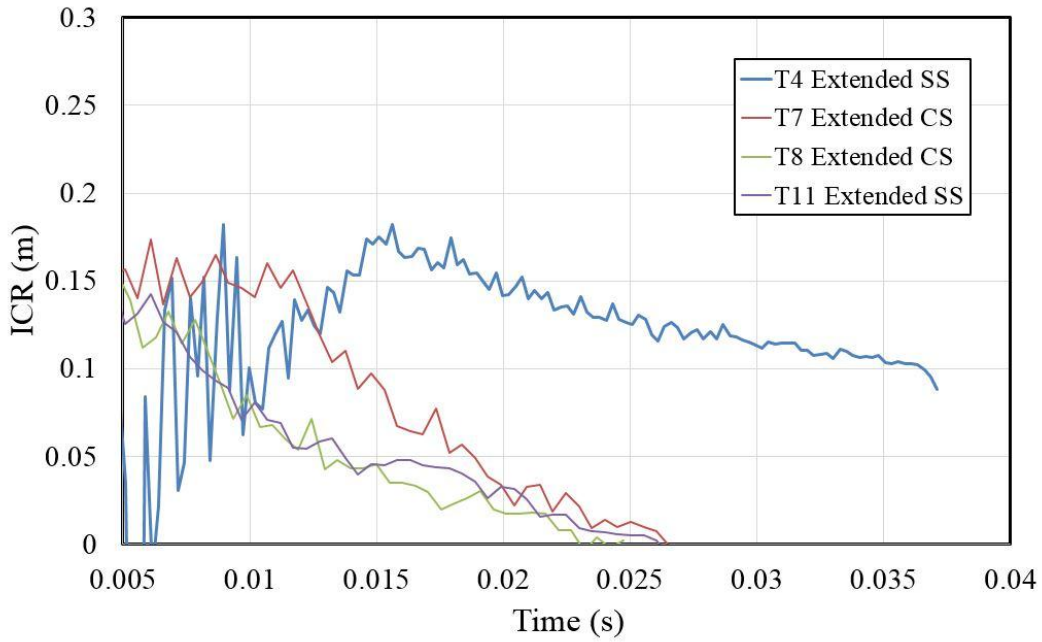

Figure 3.32: ICR vs time for dynamic tests, note changes are small in comparison to lever arm

3.6.3 Discussion

In this section it is discussed how the assumed force distribution affects the capacity of the connection, how a different distribution might have to be assumed for the dynamic case and how the Eurocode should give better guidance on what distribution the designer should assume.

In the case of the extended end plate connection the sum of the bolt row resistances in tension exceeds the resistance of the beam flange in compression. The Eurocode (CEN 2005) requires the designer to reduce the tensile forces below the resistance of the beam flange and web in compression, so bolt forces were reduced accordingly. Publications BCSA P398 [2] gives further guidance on the distribution to be assumed for the bolt row forces. The suggested distribution is shown in black in Figure 3.33 (a) and (b) and indicates that a linear distribution should be taken for the internal bolt rows with the force in the plate extension treated separately. This distribution predicts a moment capacity which is lower than the experimental capacity, with or without safety factors. The values for the design capacity that uses the standard methodology are presented in the first two columns of Table 3.6. These values are lower than the experimental capacity because, as experimental evidence suggests in the static cases, nonlinear distributions may fully develop before failure. A more likely distribution is shown by the blue curve in Figure 3.33 (b).

Table 3.6: Proposed design values using conservative distributions for the dynamic cases

Test	Plate type	Bolts	Load type	Design capacity without factors M^*_{Rd} (kNm)	Design capacity with factors M_{Rd} (kNm)	Test capacity M_{RExp} (kNm)	Proposed capacity M^*_{Rd} (kNm)	Proposed capacity with factors M^*_{Rd} (kNm)	Proposed distribution Figure 3.33
T1	Ext.	CS	Static	117	84	127	117	84	(a)
T2 A	Ext.	SS	Static	115	83	133	115	83	(b)
T7	Ext.	CS	Dyn.	130	93	90	90	65	(c)
T4	Ext.	SS	Dyn.	120	86	115	115	83	(d)
T5	Flush	CS	Static	105	76	98	98	71	(a)
T6	Flush	SS	Static	101	73	105	101	73	(b)
T8	Flush	CS	Dyn.	115	83	87	87	63	(c)
T11	Flush	SS	Dyn.	115	83	115	110	79	(d)

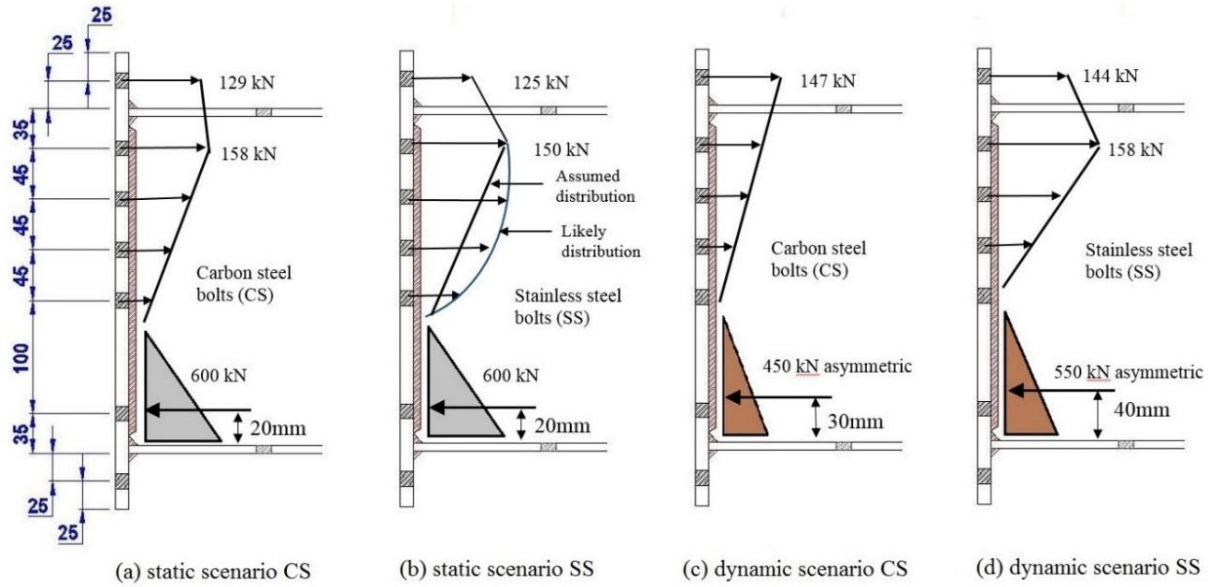

Figure 3.33: Force distribution in static and dynamic loading scenarios

The Eurocode and aforementioned publications do not give indications on the treatment of the dynamic loading cases where high loading rates may be expected. In the case of carbon steel bolted connections, using the standard distribution in the dynamic case may give a higher capacity than that observed experimentally even if safety factors are used, as seen in test T7. Although dynamic increase factors were observed from material tests on the bolts and plates steel, these only result in a dynamic increase in the moment capacity of the whole connection in the case of the flush end plate connection with stainless bolts.

In order to understand this phenomenon we must consider the reduced ductility in the dynamic case coupled with the increased likelihood of asymmetrical loading. The asymmetrical buckling in test T4 led to upward movement of the compression centre and therefore a reduction in the lever arms for each row in tension. This coupled with a reduced ductility did not allow the plastic distribution to fully develop by the time the first row of bolts failed, causing a progressive failure of the bolts.

Although no asymmetry can be observed through visual inspection in the case of carbon steel bolted connection because of negligible plate deformation, due to the low ductility of the carbon steel bolts it is possible that even the slightest asymmetry had an effect on the moment capacity in that case. Similarly, a higher centre of compression and failure for a fully nonlinear distribution to be developed can be assumed. In the dynamic case, the negligible plate deformation indicates that a linear distribution starting from the row in the plate extension may be more appropriate.

Based on experimental evidence, observations and experimental data in the dynamic loading cases, more conservative force distributions are proposed. Such distributions will consider:

- The possibility of asymmetric loading in the compression region leading to a higher centre of compression than in a symmetrically loaded static case and to reduced lever arms for bolt rows
- The reduced ductility at high strain rates leading to failure of a full force distribution to be realised

In the dynamic case of the carbon steel bolted connection a more appropriate distribution is proposed in Figure 3.33 (c). In the case of the stainless steel bolted connection the proposed distribution considers only the additional possibility of asymmetric loading in the compression region; see Figure 3.33 (d).

These propositions are made based on limited experimental evidence so they must not be taken as a rule without further experimental investigation and study. For every entry Table 3.6, only one test was carried out for each configuration, with no repeat tests.

3.6.4 Comparison with experiments at the University of Coimbra

Experimental tests on moment connections were also recently carried out at the University of Coimbra (Ribeiro, Santiago & Rigueiro 2015). Figure 3.34 shows a schematic comparison between connections tested in this work and connections tested at the University of Coimbra. Both had beam stubs of similar depths, approximately 300mm deep sections. The main difference between connections tested in this work and the connections tested at Coimbra consists in the size of the bolts and the thickness of the end plate. While connections tested in this work used five to seven rows with M12 bolts, connections tested at Coimbra used three rows with M20 bolts. All connections tested in this work had 12mm thick end plates whereas connections at the University of Coimbra had 10mm and 15mm thick plates. Figure 3.35 shows a comparison between moment rotation graphs of connections tested at Buxton and connections tested at Coimbra.

Of all the curves in Figure 3.35 the green ones represent the tests on stainless steel bolted connections. These are also the ones that achieve the highest rotation capacity of all the curves, i.e. up to 73 mrad (4.2 degrees) in the case of the stainless bolted extended plate.

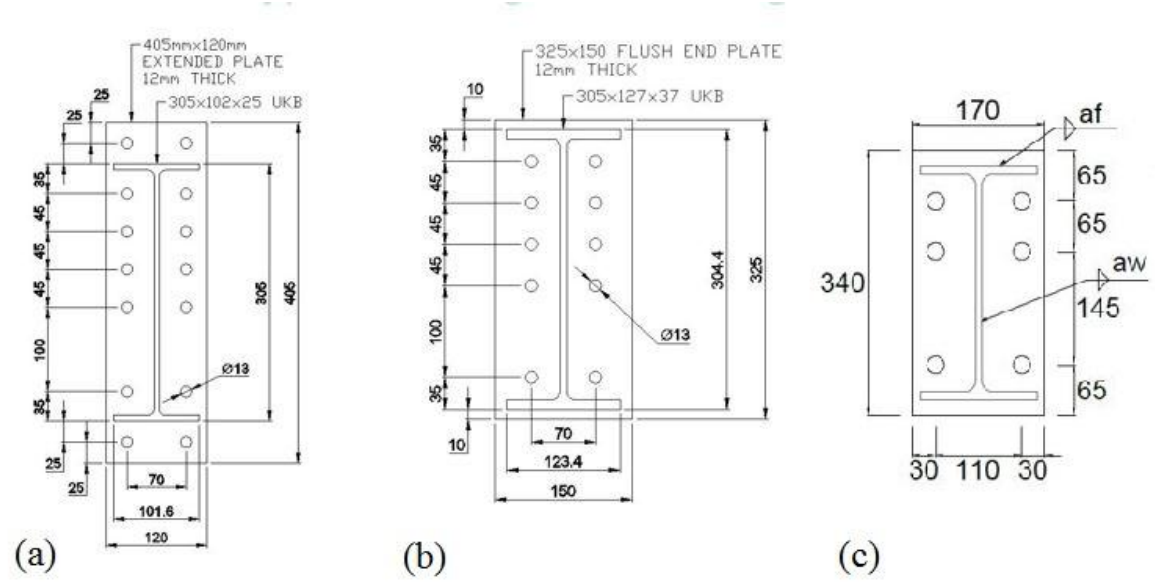

Figure 3.34: Comparison between connections tested in this work and at the University of Coimbra

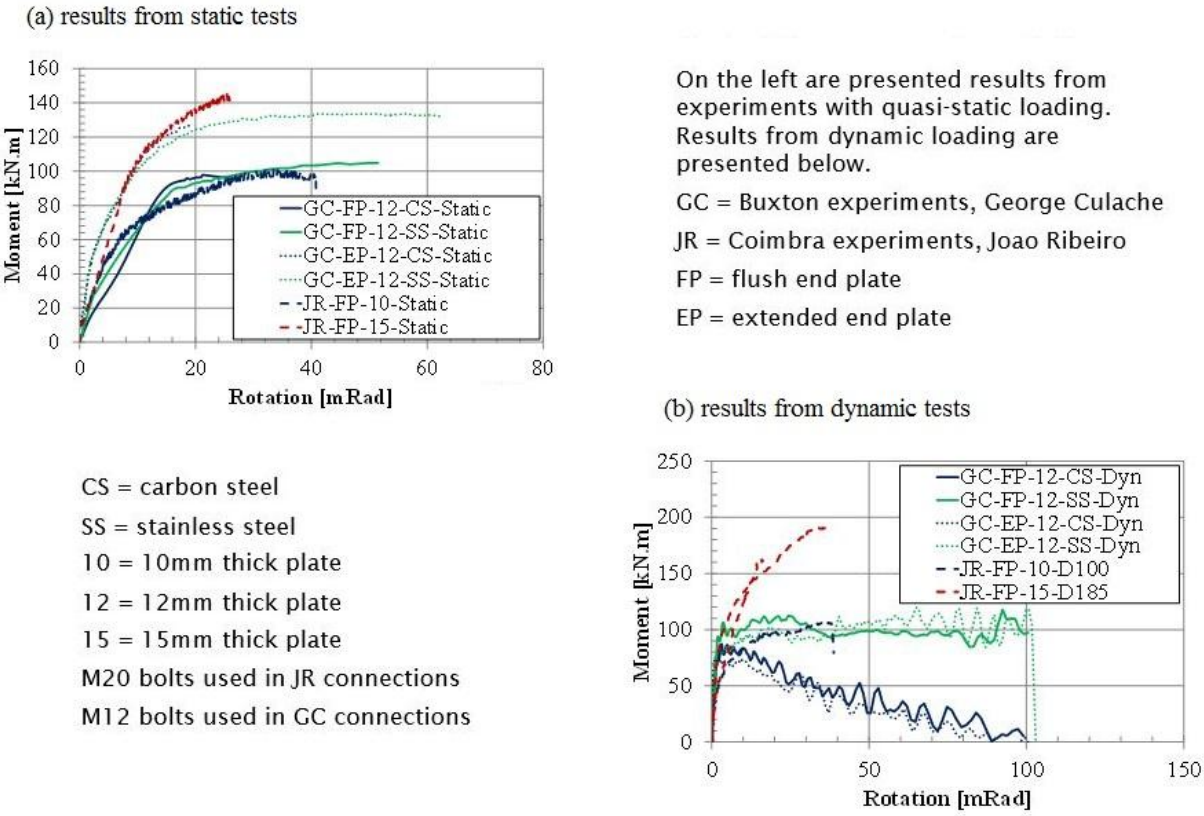

Figure 3.35: Comparison of moment versus rotation graphs

3.7 Conclusions

Experimental tests on bolts have been presented. These were carried out under quasi-static and elevated strain rates. Carbon steel bolts are shown to fail through thread stripping, whereas ductile necking was observed in stainless steel bolts. Both bolt types showed a strength enhancement under elevated strain rates, in a manner consistent with the literature. However, these strength enhancements at the component level did not always translate into increased connection strength. The stainless steel bolted connections were found to absorb the same amount of energy before failure under static and high strain-rate loading. They were also shown to be able to achieve their design values of strength under high-strain rate loading. In comparison, the carbon steel connections were found to be under-strength under high strain-rate loading; i.e. the dynamic increase in material properties demonstrated in the bolt tests did not translate into increased connection strength under high-strain rate loading.

The quasi-static experimental connection strengths showed good agreement with the Eurocode 3 design strengths for carbon steel and stainless steel connections. During the quasi-static tests loading occurred over a period of 300 seconds, after which failure occurred in an explosive manner in less than a $1/10^{th}$ of a second. The carbon steel bolted connections reached their ultimate strengths with no observable plastic deformation, whereas failure was preceded by extensive plastic deformation in both the bolts and the end-plates in the stainless steel bolted connections.

In the dynamic tests the load reached a peak in under 10ms and the connections failed in under 30ms. The movement of both the "flying column" and the supporting angles as a rigid body followed by their separation caused the centre of rotation to change in time as the two bodies separated. This had implications on the rotation, acceleration and inertia that cannot be fully corrected for. In addition, the asymmetrical nature of the boundary conditions further adds to the difficulties of processing the data in a meaningful way so as to arrive at useful conclusions and allow comparison with modelling results presented in subsequent chapters.

This chapter demonstrates that the simple replacement of carbon-steel bolts with their stainless steel equivalent will improve strength, ductility and the ability to resist dynamic loading for the end-plate beam-column connections investigated. Since experiments are difficult and expensive to carry out the ability to carry out modelling that reflects the behaviour observed experimentally is important. Therefore, finite elements models were created and are presented in the following chapters and calibrated against experimental data. In the final chapter models were created of a connection too large to have been tested to failure in the current testing rig, thus highlighting the usefulness of the finite element method.

Chapter 4: Finite element analysis, material behaviour and component modelling

4.1 Introduction

This chapter presents a general overview of the finite element analysis process and the practical implementation of this process with Abaqus (Simulia 2015a). The material properties and behaviour concepts that were used in the analysis are presented. Material properties, as determined from experimental tests, were used in the model for the main components of the connections. Models are developed for the steel coupon cut from the plate and the two types of bolts.

4.2 Overview of finite element modelling

4.2.1 Pre-processing phase

A finite element analysis requires a pre-processing phase in which the structural component or assembly of components is modelled by taking the following steps:

1. One or more components are created in 2D or 3D modelling space.
2. Materials are defined with the relevant material behaviours such as: density, elastic properties, plastic properties which can be rate or temperature dependant, ductile damage and damage evolution.
3. Materials are assigned to section properties which are then assigned to the relevant components.
4. Each component of the assembly is meshed with one element type of a particular size. An example of an element type is the linear 8-node brick element with reduced integration, also called simply C3D8R in Abaqus. Each component can have a different global element size so the number of elements can vary significantly from one component to the other.
5. An assembly of the required parts is defined and an analysis step is created. An analysis step implies the use of only one analysis procedure. The most important general procedures here are the Dynamic-Implicit and the Dynamic-Explicit procedures. These will be described in more detail within this chapter.
6. The analysis is then configured by defining boundary conditions, loading conditions, and requesting field or history outputs. With this step the pre-processing phase is complete.

Abaqus has two main modules. Abaqus/Standard is the module that includes the elements and procedures for the Dynamic Implicit analysis. Abaqus/Explicit includes the elements and procedures for Dynamic Explicit analysis.

4.2.2 Processing phase

Once the pre-processing is complete, the analysis can be run by defining and submitting a job in Abaqus. During the job definition Abaqus allows the use of multiple processors in one analysis, an option also known as parallelization. An Intel Core i7 processor was used for the analysis. It is made of 8 cores, so 8 central processing units (CPUs) can be used simultaneously for the analysis with Abaqus Standard or Explicit. Abaqus/Standard also allows for the use of general-purpose graphics processing units (GPGPUs) that are located on the graphics card. These represent processing power which is additional to the parallelisation obtained through the use of multiple CPUs.

If different models are compared which may have different types of elements, it is important to mention the concept of parallelisation, CPUs and GPGPUs. It is only once these initial conditions have been established that models can be compared in terms of computational efficiency or run time.

The run time for a bolt or connection model can vary from less than 1 minute to over 24 hours depending on: modelling space, element types and sizes, procedure types and their application, the use of parallelisation, number of CPUs used, number of GPGPUs used and potential simplifying assumptions.

4.2.3 Post-processing phase

Once the analysis is completed, Abaqus returns an output database. The output database contains the data requested by the user as field and history output requests. The most important data to be requested is related to the relevant nodes or elements and includes: displacements, resultant forces, stresses, strains, strain rates, the damage variable and element status.

The data in the output database is further processed in order to obtain the moment applied and the rotation of the connection. Once these relationships are established they can be reported by Abaqus and compared with the equivalent relationship obtained from experimental testing.

4.3 Material behaviour

4.3.1 Elastic and plastic behaviour

The density of both carbon steel and stainless steel was taken as $7800\ \mathrm{kg/m^3}$. The elastic modulus, or Young's modulus for steel was taken as 200 GPa and Poisson's ratio as 0.3.

When a steel specimen is tested in a tensile-strength testing machine the length l of the specimen increases with the applied force F. Once the yield stress is reached the steel begins to deform plastically and experiences extension and thinning of the material. This process is called necking and is important to numerical modelling. The engineering stress σ_e is defined as the force F divided by the initial cross-sectional area A_0:

$$\sigma_e = \frac{F}{A_0} \tag{4.1}$$

The engineering or nominal strain ε_e is defined as:

$$\varepsilon_e = \frac{\Delta l}{l_0} = \frac{l_1}{l_0} - 1 \tag{4.2}$$

where Δl is the change in length, l_0 is the initial length and l_1 is the final length of the tested specimen.

Necking, the localisation of plastic deformation, represents the localized reduction in cross-sectional area. During this process the force applied to the specimen and therefore the engineering stress reach a maximum. The behaviour of the material within the neck can no longer be described using the engineering stress. The *true stress* is the force applied over the neck area. The true stress σ_t continues to rise because the cross-sectional area A decreases and the material work-hardens in the neck region. The *true normal stress* σ_t is defined as the resistance per unit area:

$$\sigma_t = \frac{F}{A} \tag{4.3}$$

The incremental true strain ε_t is defined as:

$$d\varepsilon_t = \frac{dl}{l} \tag{4.4}$$

where dl is the change in length at one time step and l is the length at the beginning of the time step.

Integrating the expression above gives the longitudinal true strain ε_t of the material:

$$\varepsilon_t = \int_{l_0}^{l_1} \frac{dl}{l} = ln\frac{l_1}{l_0} \tag{4.5}$$

When strains are reasonably small, such as when the metal deforms elastically the change in cross-sectional area is less than 1% for most steels so the engineering and true strains and stress are approximately the same. However, during plastic deformation the difference between the true and engineering values become significantly larger as is the case for the tensile failure of bolts. The importance of the true stress and strain is underlined by Meyers and Chawla (Meyers & Chawla 2008). In Abaqus, true stress and true plastic strain must be used to define the plastic behaviour (Simulia 2015b).

Using the equations presented above and the fact that the volume of the specimen remains constant Meyers and Chawla (Meyers & Chawla 2008) express the true stress in terms of engineering stress and strain:

$$\sigma_t = (1 + \varepsilon_e)\sigma_e \tag{4.6}$$

Similarly, the true strain can be expressed in terms of engineering strain:

$$\varepsilon_t = \ln(1 + \varepsilon_e) \tag{4.7}$$

The total strains are decomposed into elastic and plastic components and the plastic strain ε_{pl} is calculated:

$$\varepsilon_{pl} = \varepsilon_t - \frac{\sigma_t}{E} \tag{4.8}$$

Plasticity is both rate and temperature dependant. One of the most common plasticity models is the Johnson-Cook model (Johnson & Cook 1983). The stress is described by a constitutive equation which incorporates both strain rate and thermal effects. Abaqus uses Johnson-Cook plasticity:

$$\sigma = (A + B\varepsilon^n)\left(1 + C\ ln\frac{\dot{\varepsilon}}{\dot{\varepsilon}_0}\right)\left[1 - \left(\frac{T - T_r}{T_m - T_r}\right)^m\right] \tag{4.9}$$

where σ is the stress, A is the yield stress under static conditions, the constants B, n and m are material parameters, T_r is the reference temperature, T_m the melting point, $\dot{\varepsilon}_0$ the reference strain rate, and importantly here the C parameter characterises the strain-rate dependence. Considering only the strain rate dependence above, the dynamic increase factor (DIF) can be expressed as before, in equation (3.11) as:

$$DIF = \frac{\sigma_{dynamic}}{\sigma_{static}} = 1 + C\ ln\frac{\dot{\varepsilon}}{\dot{\varepsilon}_0} \tag{4.10}$$

In the case of the S355 steel it was observed that the dynamic effect is greater on the yield stress than on the ultimate stress. These observations are consistent with those made by Malvar and Crawford (Malvar 1998) when conducting tests on steel reinforcing bars for strain rates ranging from 0.001/s to 10/s.

The Malvar and Crawford model appears to accurately predict the DIF in the case of the S355 steel. The equations to calculate the DIF from the strain rate and static yield strength were proposed as:

$$DIF = \left[\frac{\dot{\varepsilon}}{10^{-4}}\right]^{\alpha} \tag{4.11}$$

where, for the dynamic yield stress:

$$\alpha_y = 0.074 - 0.040\frac{f_y}{414} \tag{4.12}$$

and for the dynamic ultimate stress:

$$\alpha_u = 0.019 - 0.009\frac{f_y}{414} \tag{4.13}$$

Abaqus gives the user several options to define the material data:

- Specifying all the parameters of the Johnson-Cook equation: A, B, C, n, m, $\dot{\varepsilon}_0$
- Inserting columns of data in tabular form with stress, strain, strain rate, temperature
- Inserting columns of data only for stress and strain and defining the Johnson-Cook parameters for rate dependence, the C and $\dot{\varepsilon}_0$ parameters

The definition of hydrostatic stress, the von Mises equivalent stress and stress triaxiality are necessary when discussing the concept of damage in the material and the fracture strain since the fracture strain of a material varies with triaxiality. These were briefly defined in the following section through their relationships to the stress invariants.

4.3.2 Stress invariants

In continuum mechanics, the Cauchy stress tensor $\boldsymbol{\sigma}$ is a second order tensor with six independent components that completely define the state of stress at a point inside a material in the deformed state, placement or configuration:

$$\boldsymbol{\sigma} = \begin{bmatrix} \sigma_{11} & \sigma_{12} & \sigma_{13} \\ \sigma_{12} & \sigma_{22} & \sigma_{23} \\ \sigma_{13} & \sigma_{23} & \sigma_{33} \end{bmatrix} \tag{4.14}$$

where σ_{ij} is a stress component in this three dimensional state as illustrated in Figure 4.1.

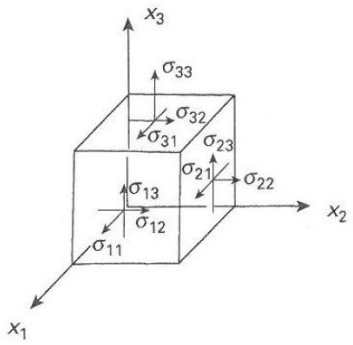

Figure 4.1: Unit cube in body subjected to tri-dimensional stress (Meyers & Chawla 2008)

The frame invariant part of the stress is described by the first invariant of the Cauchy stress tensor $\boldsymbol{\sigma}$ and the second and third invariants of the corresponding deviatoric stress tensor $\boldsymbol{s} = \boldsymbol{\sigma} - (tr\boldsymbol{\sigma}/3)\boldsymbol{I}$:

$$I_1 = tr(\boldsymbol{\sigma}) \tag{4.15}$$

$$J_2 = \frac{1}{2}\, tr(\,\boldsymbol{s^2}) = \frac{1}{6}[(\sigma_1 - \sigma_2)^2 + (\sigma_2 - \sigma_3)^2 + (\sigma_3 - \sigma_1)^2] \tag{4.16}$$

$$J_3 = \det(\boldsymbol{s}) \tag{4.17}$$

The hydrostatic stress σ_m and the von Mises equivalent stress σ_{VM} are respectively proportional to the first and second invariants:

$$\sigma_m = \frac{1}{3} I_1 \tag{4.18}$$

$$\sigma_{VM} = \sqrt{3J_2} \tag{4.19}$$

The stress triaxiality is defined as the ratio of the mean stress and equivalent von Mises stress:

$$\eta = \frac{\sigma_m}{\sigma_{VM}} = \frac{I_1}{3\sqrt{3J_2}} \tag{4.20}$$

4.3.3 Progressive damage and failure

The failure of steel when loaded in tension quasi-statically is characterised by a ductile fracture mechanism. Ductile plastic damage is the phenomenon of initiation and growth of cavities and micro cracks induced by large deformations in metals. This phenomenon has been studied by means of micro-mechanics analysis. According to Lemaitre (Lemaitre 1985), although a good representation of physical mechanisms can be introduced at the microscale level, difficulties arise when these analyses have to be included in large structures to predict ductile failure because of a lack of accuracy in stress calculations at microscale level. Between the microscale level ($10^{-3} - 10^{-2}$mm) and the structure scale level ($10^{2} - 10^{3}$mm) there exists a macroscale level of constitutive equations for the strain behaviour (Lemaitre 1985).

The continuous damage mechanics approach deals within the macroscale level defining a damage variable as an effective surface density of cracks or cavity intersections with a plane. A damaged body is considered where a macroscale volume element has been isolated, Figure 4.2. Within the overall section area S of that element defined by its normal $\boldsymbol{n}$ there is an area S_D that includes all the micro cracks and cavities intersected with that section. The effective resisting area $\tilde{S}$ takes into account the area S_D, the microstress concentrations in the vicinity of discontinuities and the interactions between closed defects so that:

$$\tilde{S} < S - S_D \tag{4.21}$$

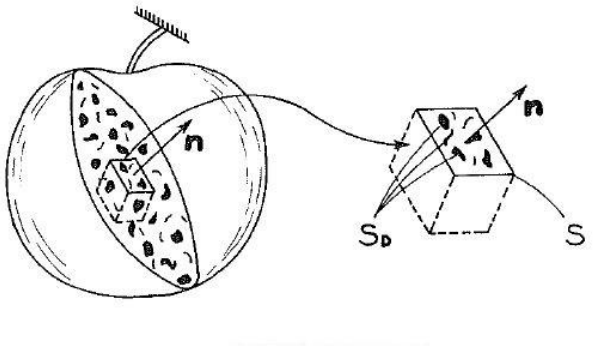

Figure 4.2: Damaged element (Lemaitre 1985)

The damage variable D associated with the normal $\boldsymbol{n}$ is:

$$D_n = \frac{S - \tilde{S}}{S} \tag{4.22}$$

From a physical point of view the variable D_n is the corrected area of cracks and cavities per unite surface cut by a plane perpendicular to $\boldsymbol{n}$. The damage variable D_n is a scalar variable that can be interpreted in the following way:

- $D_n = 0$ corresponds to the undamaged state;
- $D_n = 1$ corresponds to rupture of the element into two parts;
- $0 < D_n < 1$ characterizes the damaged state.

This work is restricted to the isotropic case, so cracks and voids are equally distributed in all directions. As D_n does not depend upon $\boldsymbol{n}$, the intrinsic damage variable is the scalar D. Since D is a scalar, once damage is initiated, the Cauchy stress tensor $\boldsymbol{\sigma}$ is then given by the scalar damage equation:

$$\boldsymbol{\sigma} = (1 - D)\bar{\boldsymbol{\sigma}} \tag{4.23}$$

where $\boldsymbol{\sigma}$ stress tensor of the damaged element, D is the overall damage variable and $\bar{\boldsymbol{\sigma}}$ is the effective (undamaged) stress tensor.

The characteristic stress-strain behaviour of a material undergoing damage is illustrated in Figure 4.3. In the case of an elastic-plastic material with isotropic hardening, the damage manifests in: softening of the yield stress and degradation of the elasticity. The solid curve in the figure represents the damaged stress-strain response and the dashed curve represents the response in the absence of damage.

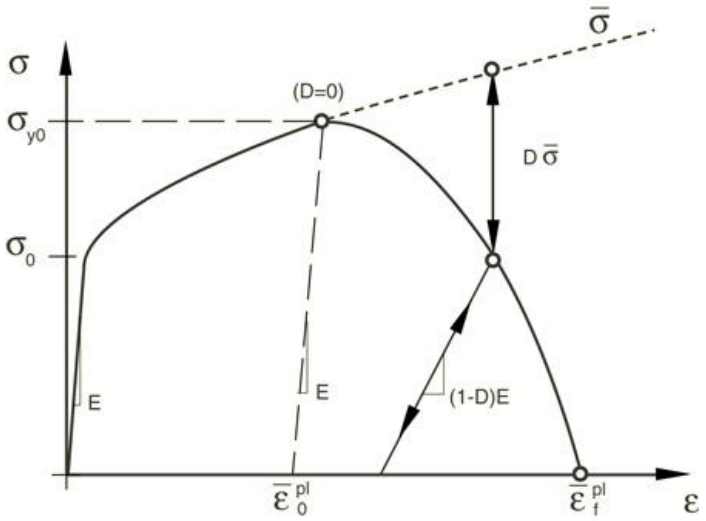

Figure 4.3: Stress-strain curve with progressive damage (Simulia 2015b)

In the figure σ_{y0} and $\bar{\varepsilon}_0^{pl}$ are the yield stress and equivalent plastic strain at the onset of damage and $\bar{\varepsilon}_f^{pl}$ is the equivalent plastic strain at failure, when the overall damage variable reaches the value $= D_c$.

The critical damage D_c value can be defined as the damage value at which fracture occurs, i.e. the plastic strain reaches the fracture strain $\bar{\varepsilon}_f^{pl}$.

Strictly speaking, as discussed by Lemaitre (Lemaitre 1985), the figure above is an idealisation since the critical value for damage D_c has been shown by many experiments to be in the following interval:

$$0.2 < D_c < 0.8 \tag{4.24}$$

In Abaqus, the overall damage variable D captures the combined effect of all active damage mechanisms. The value of the equivalent plastic strain at failure, $\bar{\varepsilon}_f^{pl}$, depends on the characteristic length of the element and cannot be used as a material parameter for the specification of the damage evolution law (Simulia 2015b). Instead, the damage evolution law is specified in terms of equivalent plastic displacement, $\bar{u}^{pl}$, or in terms of fracture energy dissipation, G_f.

When material damage occurs, the true stress-strain relationship no longer accurately represents the material's behaviour. Continuing to use the stress-strain relation induces a strong mesh dependency based on strain localization, such that the energy dissipated decreases as the mesh is refined. A different approach is required to follow the strain-softening branch of the stress-strain response curve. Abaqus uses Hillerborg's (Hillerborg et al. 1976) fracture energy proposal to reduce mesh dependency by creating a stress-displacement response after damage is initiated. Hillerborg defines the energy required to open a unit area of crack G_f as a material parameter. The implementation of this stress-displacement concept in a finite element model requires the definition of a characteristic length L associated with an integration point. The fracture energy is then:

$$G_f = \int_{\bar{\varepsilon}_0^{pl}}^{\bar{\varepsilon}_f^{pl}} L\sigma_y \, d\bar{\varepsilon}^{pl} = \int_0^{\bar{u}_f^{pl}} \sigma_y \, d\bar{u}^{pl} \tag{4.25}$$

This expression introduces the definition of the equivalent plastic displacement $\bar{u}^{pl}$ as the fracture work conjugate of the yield stress after the onset of damage. Before damage initiation:

$$\dot{\bar{u}}^{pl} = 0 \tag{4.26}$$

where $\dot{\bar{u}}^{pl}$ is the effective plastic displacement rate, which is non-zero after damage initiation.

Once the damage initiation criterion has been reached, the effective plastic displacement is defined with the evolution equation:

$$\dot{\bar{u}}^{pl} = L\dot{\bar{\varepsilon}}^{pl} \tag{4.27}$$

where L is the characteristic length of the element and $\dot{\bar{\varepsilon}}^{pl}$ is the equivalent plastic strain rate.

In Abaqus, the evolution of the damage variable with the relative plastic displacement can be specified in tabular, linear or exponential form. For simplicity, a linear evolution of damage has been assumed in this work. If a linear evolution of damage is assumed with effective plastic displacement, only the effective plastic displacement at the point of failure $\bar{u}_f^{pl}$ needs to be specified. In this case the damage variable increases according to:

$$\dot{d} = \frac{L\dot{\bar{\varepsilon}}^{pl}}{\bar{u}_f^{pl}} = \frac{\dot{\bar{u}}^{pl}}{\bar{u}_f^{pl}} \tag{4.28}$$

where $\dot{d}$ is the damage rate, L is the characteristic length of the element, $\dot{\bar{\varepsilon}}^{pl}$ is the equivalent plastic strain rate, $\dot{\bar{u}}^{pl}$ is the effective plastic displacement rate and $\bar{u}_f^{pl}$ is the effective displacement at fracture of an element.

This definition ensures that when the effective plastic displacement reaches the value $\bar{u}_f^{pl}$, the damage reaches the critical damage value, $D = D_c$.

When $D = D_c$ the stiffness of the damaged element is fully degraded and its status variable changes from 1 to 0, i.e. the element is no longer visible in the model.

4.3.4 Fracture strain and dynamic fracture model

If a steel specimen is tested in a tensile-strength testing machine the steel will elongate and fracture at a particular critical value of strain. A good estimate of the true fracture strain ε_f can be obtained after testing using the following relationship:

$$\varepsilon_f = \ln\left(\frac{A_0}{A_f}\right) \tag{4.29}$$

where the area A_0 represents the initial cross-sectional area which can be measured before the experiment and the area A_f represents the cross-sectional area of the specimen at the point of fracture which can be measured after the experiment. If the cross-section is circular, the fracture strain ε_f can be expressed as:

$$\varepsilon_f = \ln\left(\frac{r_0^2}{r_f^2}\right) \tag{4.30}$$

where r_0 is the initial radius of the cross-section and r_f is the final radius of the cross-sectional area which. Similarly, r_0 and r_f can be measured before and after the experiment respectively.

In the 1980s Johnson and Cook carried out tests on three different metals subjected to various strains, strain rates and temperatures. They proposed a model for von Mises stress flow which now bears their name and is represented by the constitutive equation presented previously.

In a different paper on the fracture characteristics of the three metals Johnson and Cook (Johnson & Cook 1985) also proposed a simple fracture model that relates the fracture strain to triaxiality, strain rate and temperature.

Abaqus (Simulia 2015b) enables the use of the Johnson-Cook model for dynamic fracture. In Abaqus, the Johnson-Cook criterion is a special case of the ductile criterion in which the equivalent plastic strain at the onset of damage $\bar{\varepsilon}_D^{pl}$ is assumed to be of the form:

$$\bar{\varepsilon}_D^{pl} = [d_1 + d_2 exp(-d_3\eta)]\left[1 + d_4 \ln\frac{\dot{\bar{\varepsilon}}^{pl}}{\dot{\varepsilon}_0}\right]\left[1 + d_5\hat{\theta}\right] \tag{4.31}$$

where $d_1 - d_5$ are failure parameters, η is the stress triaxiality, $\dot{\bar{\varepsilon}}^{pl}$ is the plastic strain rate, $\dot{\varepsilon}_0$ is the reference strain rate and $\hat{\theta}$ is the non-dimensional temperature.

In pure tension the triaxiality η is 0.33 on average and considering only the strain rate effect for simplicity the above equation can be changed to:

$$\frac{\bar{\varepsilon}_{D,dynamic}^{pl}}{\bar{\varepsilon}_{D,static}^{pl}} = 1 + d_4 \ln\frac{\dot{\bar{\varepsilon}}^{pl}}{\dot{\varepsilon}_0} \tag{4.32}$$

Due to the way in which the relationship between plastic strain at the onset of damage $\bar{\varepsilon}_D^{pl}$, critical damage value D_c and displacement at fracture $\bar{u}_f^{pl}$ is defined, several sets $\left(\varepsilon_{D,0}^{pl}, \bar{u}^{pl}, D_{max}\right)$ can be found that give acceptable results.

4.4 Element types

4.4.1 The continuum brick element

General properties

Continuum or solid elements can be used to model a wide variety of components. Conceptually, continuum elements model small blocks of material in a component. The continuum element used predominantly in this work is the brick element C3D8R. The name of the element can be explained as follows:

- "C" means the element belongs to the continuum stress/displacement family. The degrees of freedom (dof) for stress/displacement simulations are the translations at each node.
- "3D" means the element is three dimensional. Other elements may be a link (1D) or two dimensional (2D).
- "8" represents the number of nodes. Linear brick elements have 8 nodes and quadratic elements have 20 nodes.
- "R" represents reduced integration. Reduced integration elements use one fewer integration point in each direction than the fully integrated elements. Reduced integration reduces running time, especially in three dimensions.

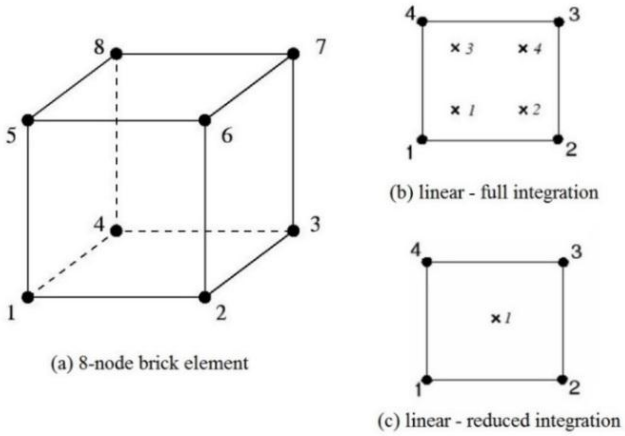

Figure 4.4: The continuum brick element (Simulia 2015b)

Hourglassing can be a problem with first-order, reduced-integration elements (C3D8R and others) in stress/displacement analyses. Since the elements have only one integration point, it is possible for them to distort in such a way that the strains calculated at the integration point are all zero, which, in turn, leads to uncontrolled distortion of the mesh. First-order, reduced-integration elements in Abaqus include hourglass control.

The user has control over how Abaqus treats elements with severe damage. An upper bound D_{max} can be specified to the overall damage variable D. No further damage is accumulated at an integration point once D reaches D_{max}.

Output variables for element C3D8R

In Abaqus the x, y and z directions are represented by numbers 1, 2 and 3. The important output variables for this element are as follows:

- Uij is the displacement in the direction ij and U, Magnitude is the resultant displacement

- S, Mises and Sij are Von Mises stresses σ_{VM} and stresses in the direction ij
- TRIAX represents the stress triaxiality η
- PEEQ represents the equivalent plastic strain $\bar{\varepsilon}^{pl}$ which is defined as:

$$\bar{\varepsilon}^{pl} = \int_0^t \dot{\bar{\varepsilon}}^{pl} dt \tag{4.33}$$

where

$$\dot{\bar{\varepsilon}}^{pl} = \sqrt{\frac{2}{3}\dot{\varepsilon}^{pl} : \dot{\varepsilon}^{pl}} \tag{4.34}$$

- ER represents all mechanical strain rate components.
- SDEG represents the overall scalar stiffness degradation D.
- STATUS represents the status of the element. It has a value of 1 if the element is active and once D reaches D_{max} the element is deleted and the status has a value of 0. Elements with null status are removed from the viewport.

4.4.2 The connector element

The analyst is often faced with modelling problems in which two different parts are connected in some way. Connector modelling consists of:

- choosing and defining the appropriate connector elements;
- defining the connector behaviour;
- defining any connector actuations;
- monitoring connector output.

General properties

Connector elements are available for two-dimensional or three-dimensional analyses and can define a connection between two nodes. Figure 4.5 shows the conceptual representation of the connector as presented by the Abaqus Analysis User (Simulia 2015b). Two connector elements are provided depending on the dimensionality of the analysis CONN2D2 and CONN3D2:

- CONN represents the connector element type
- 2D or 3D represents the dimension
- 2 represents the number of nodes it connects

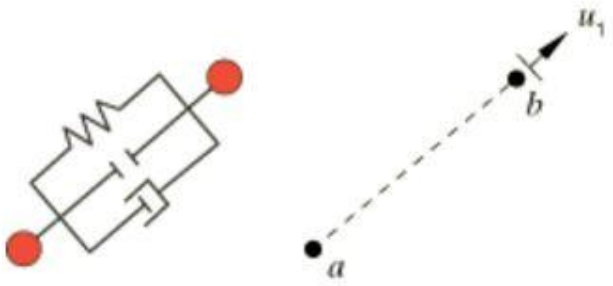

Figure 4.5: Conceptual representation of connector element (Simulia 2015b)

The connection attributes define the connector element's function. In the most general case, the following attributes are specified:

- The connector type is specified as basic Axial + Rotation. Connection type basic Axial + Rotation provides a connection between two nodes where the relative displacement is along the line separating the two nodes. It models discrete physical connections such as axial springs.
- The local directions associated with the connector's nodes. The available components are displacement in the 1 direction U1 and rotations in three directions UR1, UR2, UR3. Other components are not constrained.
- The connector behaviour includes in this case elastic, plastic and damage definitions.

Connector behaviour

Spring-like elastic connector behaviour can be defined in any connector with available components of relative motion. It can be specified for each available component of relative motion independently, in which case the behaviour can be linear or nonlinear. In the simplest case of linear uncoupled elasticity the spring stiffnesses is defined for the selected components (i.e., D_{11} for component 1, D_{22} for component 2, etc.), which are used in the equation:

$$F_i = D_{ii} u_i \ \ (no\ sum\ on\ i) \tag{4.35}$$

where F_i is the force or moment in the i^{th} component of relative motion and u_i is the connector displacement or rotation in the i^{th} direction. Note that here D_{ii} represents the stiffness of the element in the i^{th} direction.

The plasticity formulation in connectors is similar to the plasticity formulation in metal plasticity. In connectors the stress (σ) corresponds to the force (f), the strain (ε) corresponds to the constitutive motion (u), the plastic strain (ε^{pl}) corresponds to the plastic relative motion (u^{pl}) and the equivalent plastic strain ($\bar{\varepsilon}^{pl}$) corresponds to the equivalent plastic relative motion ($\bar{u}^{pl}$). The yield function φ is defined as:

$$\varphi\left(\mathbf{f}, \overline{\mathbf{u}}^{\mathbf{pl}}\right) = P(\mathbf{f}) - F^0 \leq 0 \tag{4.36}$$

where $\mathbf{f}$ is the collection of forces and moments in the available components of relative motion that ultimately contribute to the yield function; the connector potential, $P(\mathbf{f})$, defines a magnitude of connector tractions similar to defining an equivalent state of stress in Mises plasticity and is either automatically defined by Abaqus or user-defined; and F^0 is the yield force/moment. The connector relative motions, $\mathbf{u}$, remain elastic as long as $\varphi < 0$; and when plastic flow occurs, $\varphi = 0$.

If yielding occurs, the plastic flow rule is assumed to be associated; thus, the plastic relative motions are defined by

$$\dot{\mathbf{u}}^{pl} = \dot{\bar{u}}^{pl} \frac{\partial \varphi}{\partial \mathbf{f}} \tag{4.37}$$

where $\dot{\mathbf{u}}^{pl}$ is the rate of plastic relative motion and $\dot{\bar{u}}^{pl}$ is the equivalent plastic relative motion rate.

If relative forces or motions in a connection exceed critical values, the connector starts undergoing irreversible damage (degradation). Upon additional loading there is further evolution of damage leading to eventual failure. If damage has occurred, the force response in the connector component *i* will change according to the following general form:

$$F_i = (1 - d_i) F_{eff,i}\,, \qquad 0 \leq d_i \leq 1 \quad no\ sum\ on\ i \tag{4.38}$$

where d_i is a scalar damage variable and $F_{eff,i}$ is the response in the available connector component of relative motion i if damage were not present (effective response).

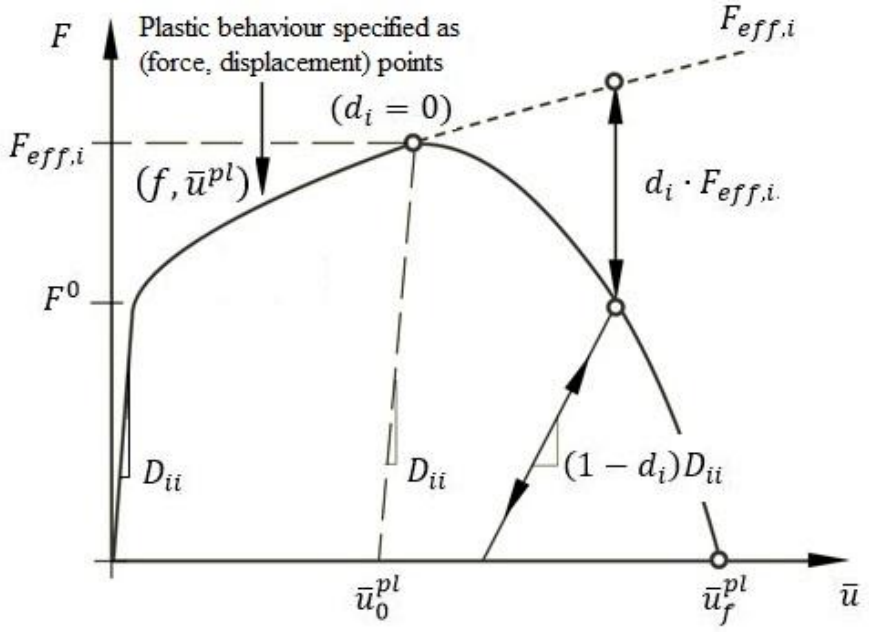

Figure 4.6: Force-displacement curve with progressive damage necessary for the definition of the behaviour of the connector element (Simulia 2015b)

To define a connector damage mechanism, you specify the following:

- a criterion for damage initiation; and
- a damage evolution law that specifies how the damage variable *d* evolves (optional).

Prior to damage initiation, *d* has a value of 0.0; thus, the force response in the connector does not change. Once damage has been initiated, the damage variable will monotonically evolve up to the maximum value of 1.0 if damage evolution is specified. Complete failure occurs when *d* = 1.0.

Abaqus allows you to specify a maximum degradation value (the default value is 1.0); damage evolution will stop when the damage variable reaches this value, and the element will be deleted from the mesh by default. Alternatively, you can specify that the damaged connector elements remain in the analysis with no further damage evolution. The maximum degradation value is used to evaluate the damaged stiffness in the remaining part of the analysis.

Output variables for element CONN3D2

The important output variables for this element are as follows:

- CTF represent connector total forces and moments
- CU represents connector relative displacements and rotations
- SDEG represents the overall scalar stiffness degradation D.

- STATUS represents the status of the element. It has a value of 1 if the element is active and once D reaches D_{max} the element is deleted and the status has a value of 0. Elements with null status are removed from the viewport.

4.5 Abaqus modules and general procedures

Abaqus/Standard is a general-purpose analysis module that can solve linear and nonlinear problems involving the static, dynamic and thermal response of components (Simulia 2015c). Implicit direct integration is provided in Abaqus/Standard.

Abaqus/Explicit is a special-purpose analysis module that uses an explicit dynamic finite element formulation. It is suitable for short, transient dynamic events, such as impact or blast problems, and is also efficient for highly nonlinear problems involving changing contact conditions (Simulia 2015c). Explicit direct integration is provided in Abaqus/Explicit.

For both the implicit and the explicit time integration procedures, equilibrium is defined in terms of the external applied forces, **P**, the internal element forces, **I**, and the nodal accelerations **ü**:

$$\mathbf{M\ddot{u}} = \mathbf{P} - \mathbf{I} \tag{4.39}$$

where **M** is the mass matrix. Both procedures solve for nodal accelerations and use the same element calculations to determine the internal element forces. The biggest difference between the two procedures lies in the manner in which the nodal accelerations are computed. In the implicit procedure a set of linear equations is solved by a direct solution method. The computational cost of solving this set of equations is high when compared to the relatively low cost of the nodal calculations with the explicit method (Simulia 2015c).

The *dynamic, implicit* procedure uses automatic incrementation based on the full Newton iterative solution method. Newton's method seeks to satisfy dynamic equilibrium at the end of the time increment $t + \Delta t$ and to compute displacements at the same time. The time increment Δt is large compared to that used in the explicit method because the implicit scheme is unconditionally stable (Simulia 2015c). Each Newton iteration solves for a correction $\boldsymbol{c_j}$ to the incremental displacements $\Delta \boldsymbol{u_j}$. Each iteration requires the solution of a set of simultaneous equations:

$$\widehat{\mathbf{K}}_j \boldsymbol{c_j} = \mathbf{P}_j - \mathbf{I}_j - \mathbf{M}_j \ddot{\mathbf{u}}_j \tag{4.40}$$

which is an expensive procedure for large models. The effective stiffness matrix $\widehat{\mathbf{K}}_j$ is a linear combination of the tangent stiffness matrix and the mass matrix for the iteration. The iterations continue until several quantities are within prescribed tolerances.

The *dynamic, explicit* procedure uses a central difference rule to integrate the equations of motion explicitly through time, using the kinematic conditions at one increment to calculate the kinematic conditions at the next increment. At the beginning of the increment the program solves for dynamic equilibrium, which states that the nodal mass matrix **M** times the nodal accelerations **ü** equals the net nodal forces (the difference between the external applied forces **P** and internal element forces **I**) as described by Equation 4.1. The accelerations at the beginning of the current increment (time) are calculated as:

$$\ddot{\mathbf{u}}|_{(t)} = (\mathbf{M})^{-1} \cdot (\mathbf{P} - \mathbf{I})\big|_{(t)} \tag{4.41}$$

Since the explicit procedure always uses a diagonal, or lumped, mass matrix, solving for the accelerations is trivial; there are no simultaneous equations to solve. The acceleration of any node is determined completely by its mass and the net force acting on it, making the nodal calculations very inexpensive.

The accelerations are integrated through time using the central difference rule, which calculates the change in velocity assuming that the acceleration is constant. This change in velocity is added to the velocity from the middle of the previous increment to determine the velocities at the middle of the current increment:

$$\dot{\mathbf{u}}|_{\left(t+\frac{\Delta t}{2}\right)} = \dot{\mathbf{u}}|_{\left(t-\frac{\Delta t}{2}\right)} + \frac{\left(\Delta t|_{(t+\Delta t)} + \Delta t|_{(t)}\right)}{2} \ddot{\mathbf{u}}|_{(t)} \tag{4.42}$$

The velocities are integrated through time and added to the displacements at the beginning of the increment to determine the displacements at the end of the increment:

$$\mathbf{u}|_{(t+\Delta t)} = \mathbf{u}|_{(t)} + \Delta t|_{(t+\Delta t)} \dot{\mathbf{u}}|_{\left(t+\frac{\Delta t}{2}\right)} \tag{4.43}$$

Thus, satisfying dynamic equilibrium at the beginning of the increment provides the accelerations. Knowing the accelerations, the velocities and displacements are advanced "explicitly" through time. The term "explicit" refers to the fact that the state at the end of the increment is based solely on the displacements, velocities, and accelerations at the beginning of the increment. This method integrates constant accelerations exactly. For the method to

produce accurate results, the time increments must be quite small so that the accelerations are nearly constant during an increment. Since the time increments must be small, analyses typically require many thousands of increments.

The time step or time incrementation scheme in Abaqus/Explicit is fully automatic and requires no user intervention. Abaqus/Explicit uses an adaptive algorithm to determine conservative bounds for the highest element frequency. This is to ensure that the waves through the smallest elements are captured.

A trial stable increment is computed for each element in the mesh using the following expression:

$$\Delta t = \frac{2}{\omega_{max}^{element}} \tag{4.44}$$

where $\omega_{max}^{element}$ is the element maximum eigenvalue. A conservative estimate of the stable time increment is given by the minimum taken over all the elements. The above stability limit can be rewritten as:

$$\Delta t = \min\left(\frac{L_e}{c_d}\right) \tag{4.45}$$

where L_e is the characteristic element dimension and c_d is the current effective, dilatational wave speed of the material. The characteristic element dimension is derived from an analytic upper bound expression for the maximum element eigenvalue.

Fortunately, each increment is inexpensive because there are no simultaneous equations to solve. Most of the computational expense lies in the element calculations to determine the internal forces in the elements acting on the nodes. The element calculations include determining element strains and applying material constitutive relationships (the element stiffness) to determine element stresses and, consequently, internal forces (Simulia 2015c).

4.6 Steel coupon model

4.6.1 Material characterisation

Steel coupon specimens were cut from end plates tested. The main body of a steel coupon was 70mm long with a 10mm x 10mm square cross section. From pure tension tests on coupons the engineering stress strain relationships were obtained, Figure 4.7. Using these, the true stress versus true plastic strain curves were calculated, Figure 4.8. The dashed line represents the response in the absence of damage, i.e. the continuation of the stress strain relationship with constant slope. For details on defining the behaviour in Abaqus see Appendix C.1.

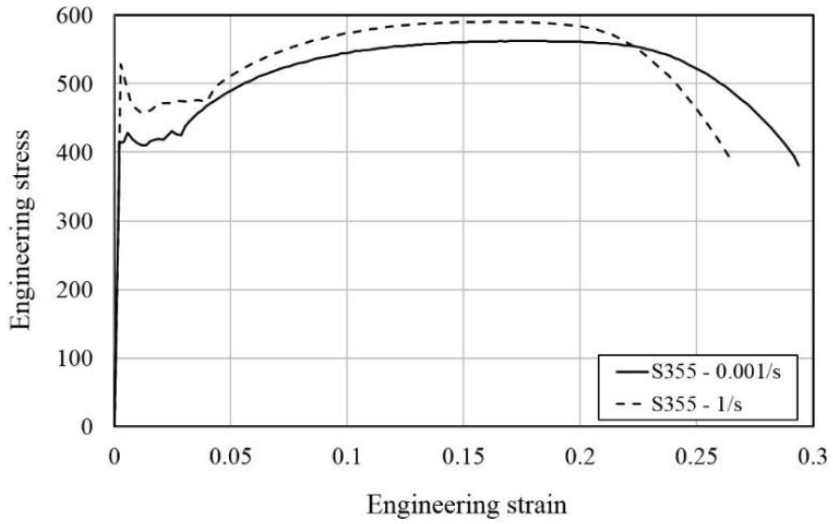

Figure 4.7: Engineering stress versus engineering strain

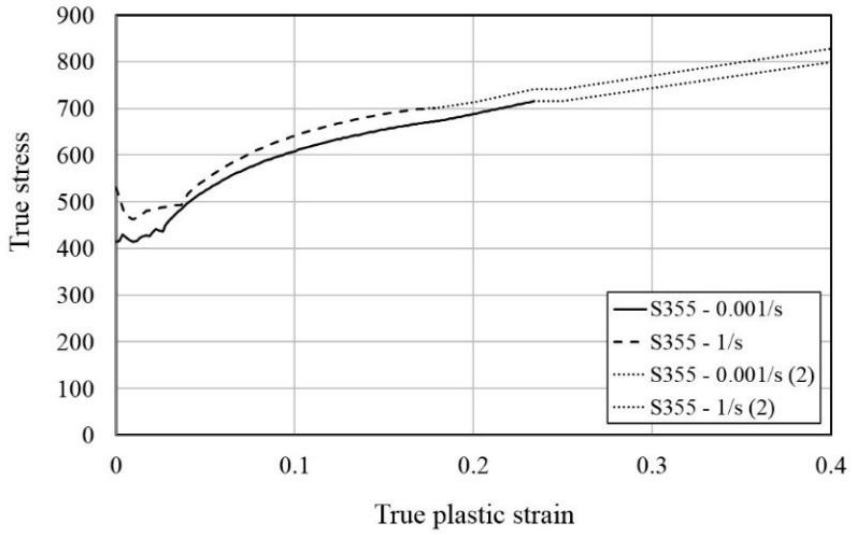

Figure 4.8: True stress versus true plastic strain

4.6.2 Finite element model of a coupon

Using symmetry, only a quarter of the main body of the steel coupon (70mm x 5mm x 5mm) was modelled to reduce model size and computational time. The model and boundary conditions are shown in Figure 4.9. Linear 8-node brick elements with reduced integration C3D8R and hourglass control was applied. The global size of the elements was 1mm generating a uniform mesh of 1800 elements. Abaqus/Standard element library and the Dynamic, Implicit solver with quasi-static application were used in the static case. Abaqus/Explicit element library and the Dynamic Explicit solver were used in the dynamic case.

4.6.3 Static analysis results

In the static case, the displacement was applied by increasing it linearly from 0m to 22mm in 600s in a single analysis step. The initial increment size was 1s with minimum and maximum increments defined as 0.0005s and 12s. The nodes of the surface being pulled were tied as a rigid body and a reference point was defined. Field output requests for the whole model included stresses, strains, displacements, forces, the damage variable and the status variable. Contour plots for stress, plastic strain and the damage variable for an applied displacement of 19.66mm are presented in Figure 4.10. Note the development of extensive plastic deformation and damage in the neck region.

4.6.4 Dynamic analysis results

In the dynamic case, the coupon deforms less before fracture. The displacement was increased linearly from 0mm to 19mm in a time period of 360ms and in a single analysis step. The plasticity was defined as rate-dependent using the Malvar-Crawford model and input in tabular form. The incrementation is automatic. Contour plots for equivalent plastic strains, strain rates before fracture and scalar stiffness degradation after fracture are shown in Figure 4.11.

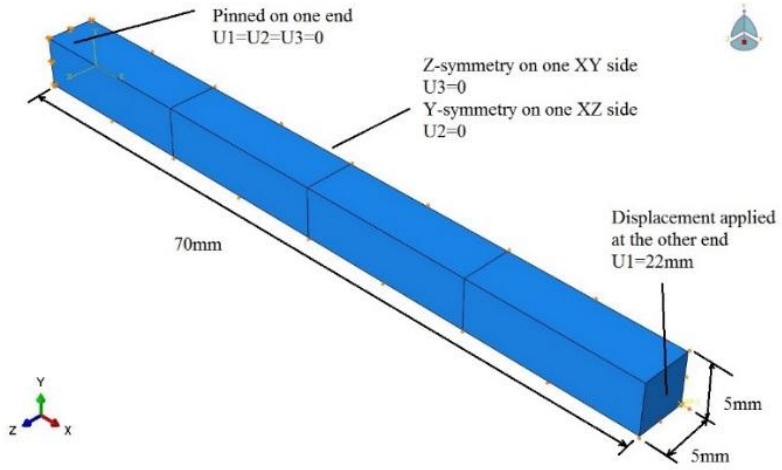

Figure 4.9: Model, dimensions and boundary conditions

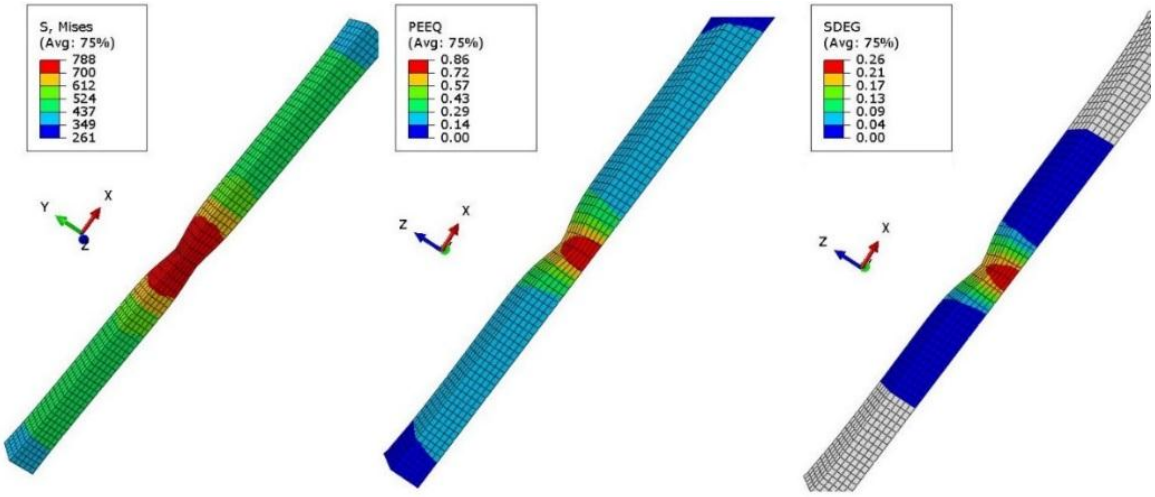

Figure 4.10: Contour plots of Von Mises stresses (S, Mises), equivalent plastic strain (PEEQ) and scalar stiffness degradation (SDEG) at a total displacement of 19.66mm, step time 536s, just before fracture

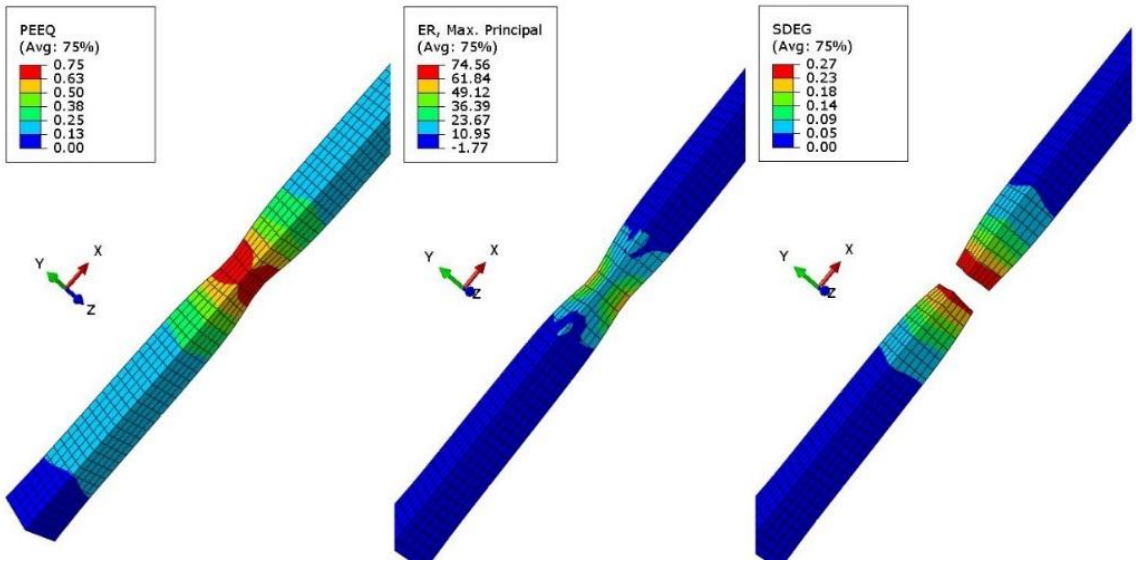

Figure 4.11: Contour plots of equivalent plastic strain (PEEQ) and strain rate (ER) at displacement of 18.12mm before fracture and scalar stiffness degradation (SDEG) after fracture

4.6.5 Final results and comparison of computational requirements

The final model results show good agreement with experimental results, in both the static and dynamic cases. The force versus displacement curves obtained from steel coupon tests and from their corresponding finite element models are shown in Figure 4.12. A summary of each analysis type and a comparison between different types of analysis in terms of computational demands is presented in Table 4.1 below.

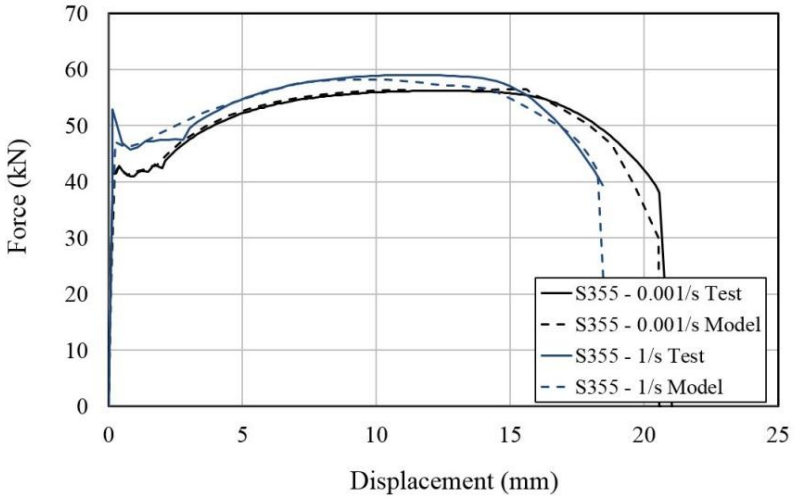

Figure 4.12: Force versus displacement result for tests and models at selected strain rates

Table 4.1: Comparison of analysis type and computational demands for steel coupon models

Analysis type	Static	Dynamic
Density	True	True
Behaviour	Plasticity	Rate dependent plasticity
Material model	True stress strain	Malvar-Crawford
Damage and element deletion	Yes	Yes
Elements	1800 C3D8R Standard	1800 C3D8R Explicit
Procedure	Implicit	Explicit
Application	Quasi-Static	Dynamic
Parallelization	4 CPUs & 40 GPGPUs	4 CPUs
Increments	141	2676562
Incrementation	User-defined step sizes	Automatic
Analysis time	1min 10 sec	18min

4.7 Stainless steel bolt model

4.7.1 Material characterisation

Stainless steel bolts of grade A4-70 were tested in an Instron machine at different strain rates. From material tests, true stress true strain curves were obtained up to the initiation of material damage, as shown in Figure 4.13. After tensile damage begins in the form of void coalescence the true stress true strain relationship is assumed to continue with a constant slope. These values together with the damage definition are used in the Abaqus model to define the effective stress values right before fracture. The dependence of fracture strain ratio on strain rate is used in the Johnson-Cook dynamic fracture model and is shown in Figure 4.14. For details on defining the behaviour in Abaqus see Appendix C.2.

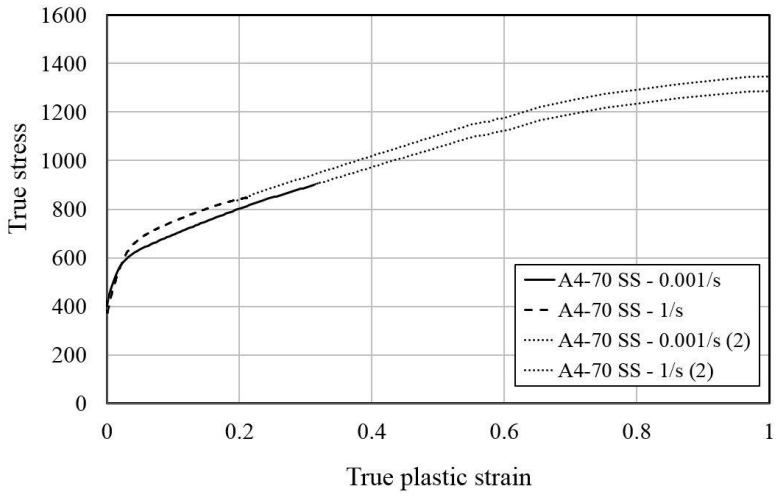

Figure 4.13: True stress versus true plastic strain curves at selected strain rates

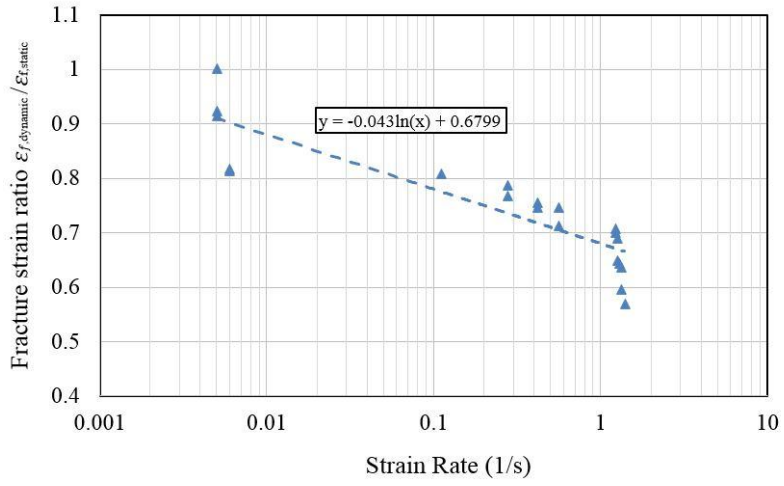

Figure 4.14: Fracture strain ratio $\frac{\varepsilon_{f,dyn}}{\varepsilon_{f,stat}}$ versus strain rate for stainless steel bolts

4.7.2 Finite element model of a bolt

Using symmetry in the vertical plane, only half of the bolt body was modelled to reduce the model size and computational time. The model represents a 30mm length of the bolt body with a 12mm diameter. The model and boundary conditions are shown in Figure 4.15 below. The nodes of the surface being displaced were tied together as a rigid body and a reference point was defined. Relevant field and history output requests were defined at the reference point.

Linear 8-node brick elements with reduced integration and hourglass control were used (C3D8R). The global size of the elements was 1mm generating a uniform mesh of 2280 elements. Element deletion with a maximum element degradation of 0.4 was used. The model mesh is shown in Figure 4.16.

4.7.3 Static analysis

In the static case, the displacement was increased linearly from 0 to 16mm in 600s in a single analysis step. The initial increment size was 0.01s, with minimum and maximum increments defined as 0.0006s and 12s. Contour plots for stress, plastic strain and the damage variable for an applied displacement of 14.10mm are presented in Figure 4.17. Note the development of extensive plastic deformation and damage in the neck region.

4.7.4 Dynamic analysis

In the dynamic case, the bolt deforms less before fracture. The displacement was increased linearly from 0 to 13mm in a time period of 337ms. This loading time is identical to the loading time for bolt tests carried out at the highest loading rates. The plastic behaviour was defined as rate-dependent using the Johnson-Cook model and input in tabular form. The incrementation was automatic. Contour plots for equivalent plastic strains, strain rates before fracture and scalar stiffness degradation after fracture are shown in Figure 4.18.

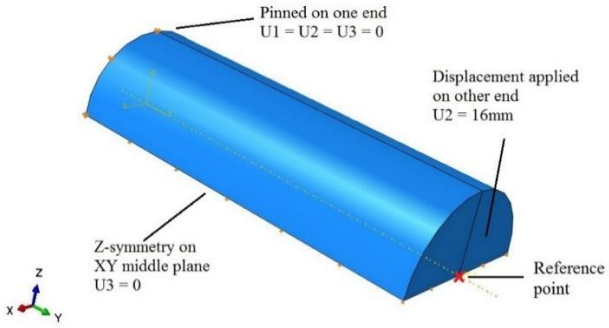

Figure 4.15: Model and boundary conditions

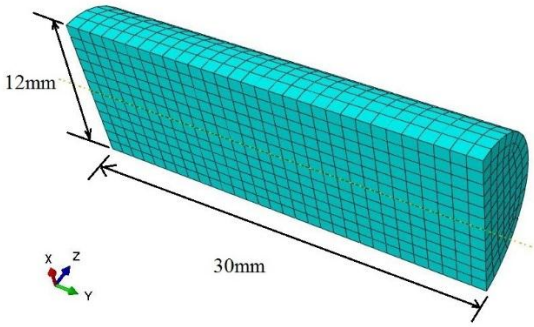

Figure 4.16: Model mesh

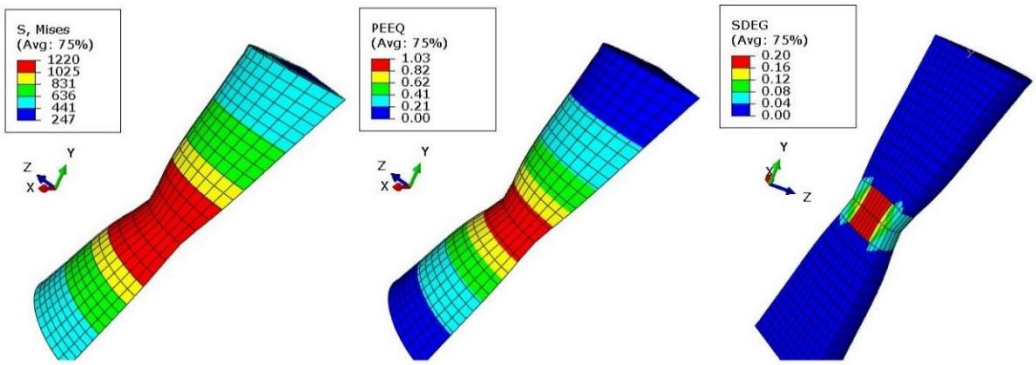

Figure 4.17: Contour plots of Von Mises stresses (S, Mises), equivalent plastic strain (PEEQ) and stiffness degradation (SDEG) at a total displacement of 14.10mm, step time 497.5s, before fracture

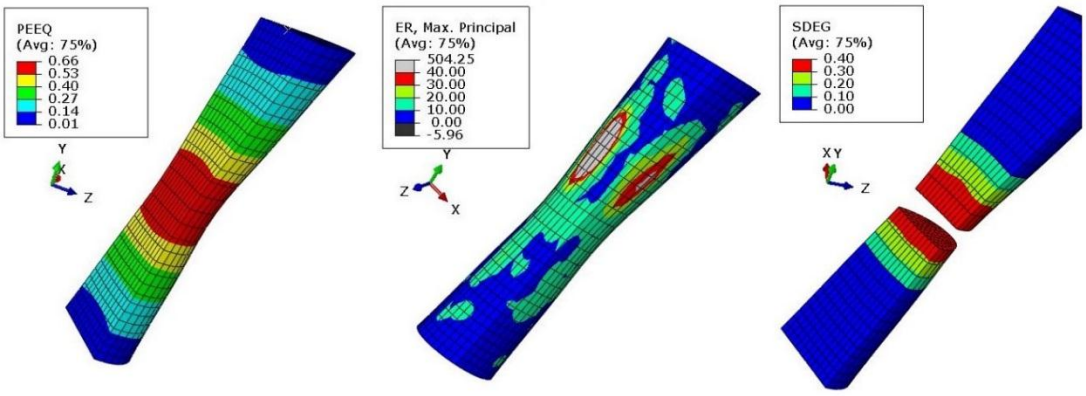

Figure 4.18: Contour plots of equivalent plastic strain (PEEQ) and strain rate (ER) at displacement of 11.05mm before fracture and scalar stiffness degradation (SDEG) after fracture

4.7.5 Connector modelling

In order to model the stainless steel bolt behaviour and represent its behaviour with a connector element, two rigid rods are placed at a distance equal to the length of a bolt. Figure 4.19 shows two rods and two reference points, each representing a rod. A reference point (RP) is a point that has to be designated to a rigid body of any kind. The reference point can translate in the X, Y and Z directions together with the rigid body it represents.

Once the two reference points have been defined, a connector can be defined between these two. The connector is a blue dotted line between the two reference points and a wire feature represented by a yellow line and the label for the connector type, i.e. Axial + Rotation. The connector essentially represents the shank of the bolt in the model. However, due to minor plastic deformation in the washers, the connector is a spring representing the elastic, plastic and damage behaviour of the bolt-nut-washer system. Visually inspecting the experimental data presented in Figure 4.20 it can be assumed that the spring yields at a force of approximately 55kN when the total elongation between the washers is 1.44mm.

In this case the elastic modulus can be defined as:

$$D_{11} = \frac{F_1}{u_1} = \frac{55.3kN}{1.44mm} = 38.2kN/mm \tag{4.44}$$

Since the bolt system yields at approximately 55kN then the plastic motion at that point is $\bar{u}^{pl} = 0.0\text{mm}$. The plastic behaviour is defined by a set of force and plastic motion points $\{(\mathbf{f}, \bar{\mathbf{u}}^{\mathbf{pl}})\}$ where the last point is the one of maximum force 74.5kN where the plastic motion is 7.86mm:

$$\{(\mathbf{f}, \bar{\mathbf{u}}^{\mathbf{pl}})\} = \begin{Bmatrix} (55.3\text{kN}, 0.0\text{mm}) \\ \dots \\ (59.8\text{kN}, 0.13\text{mm}), \\ (64.0\text{kN}, 0.37\text{mm}) \\ \dots \\ (74.5\text{kN}, 7.86\text{mm}) \end{Bmatrix} \tag{4.45}$$

For more details about defining this connector behaviour in Abaqus see Appendix C.3.

After the point of maximum force the damage d_i is defined by:

$$d_1 = 1 - \frac{F_1}{F_{eff,1}} \tag{4.46}$$

Taking $F_{eff,i}$ as the maximum force, when the force in the bolt decreases to $64.3kN$ a damage value of 0.137 is obtained as described by the following:

$$d_1 = 1 - \frac{64.3kN}{74.5kN} = 0.137 \tag{4.47}$$

The damage evolution in direction 1 can be described by a set of points $\{(d_1, \bar{\mathbf{u}}^{\mathbf{d}})\}$ that define the behaviour from the point of maximum force to the point of bolt fracture:

$$\{(d_1, \bar{\mathbf{u}}^{\mathbf{d}})\} = \begin{Bmatrix} (0,0.0\text{mm}) \\ \dots \\ (0.137,5.01\text{mm}) \\ \dots \\ (0.453,7.49\text{mm}) \end{Bmatrix} \tag{4.48}$$

In the connector model of the stainless steel bolt the critical damage value derived from test data appears to be $d_c = 0.453$ and the damage motion is 7.49mm. At this critical value the connector can no longer carry any force and the total motion is obtained by adding the elastic motion 1.44mm, the plastic motion 7.86mm and the damage motion 7.49mm. This gives a total of 16.79mm. Since the sets of values above are derived directly from experimental testing it follows that the output of the connector model will naturally be identical with the test data. Therefore a figure comparing the two results is not necessary. Since the bolts are mainly in tension, the connector is assumed and defined to carry only axial load. For more details about defining this connector behaviour in Abaqus see Appendix C.3.

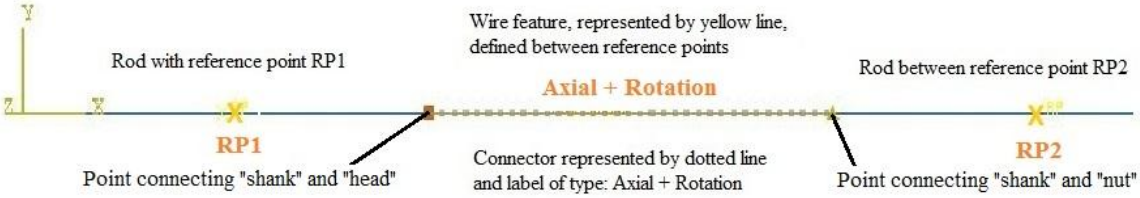

Figure 4.19: Connector geometry

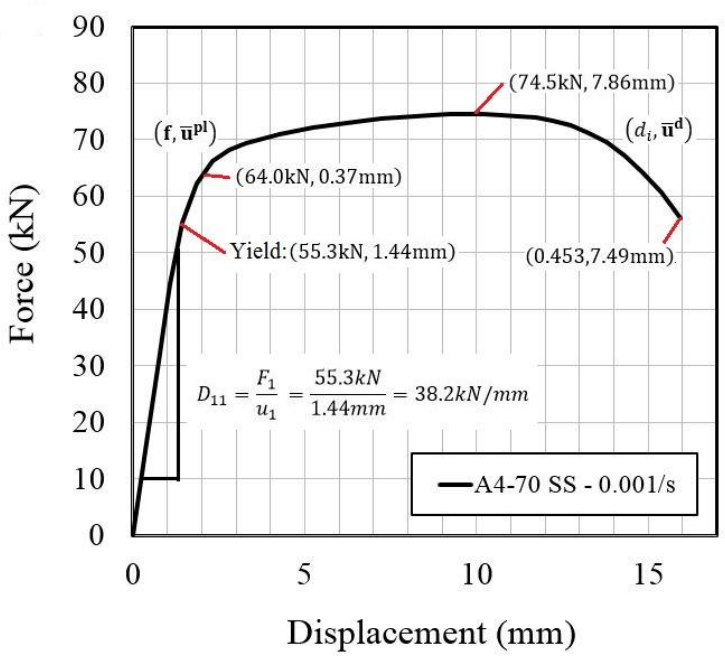

Figure 4.20: Graph and data defining connector behaviour

Figure 4.21 illustrates how one connector, in the top bolt row, is represented in the 3D model. Figure 4.21 (a) shows the connector in the assembly module of Abaqus. The connector, represented by a dotted line and the label "Axial+Rotation", connects reference point "RP-2" to reference point "RP-9", where the reference points are represented by two "X" symbols. The surface representing the area where the bolt body meets the bolt head is shown in red. Figure 4.21 (b) shows the mesh. The red area or "t_Set-56" ties all the nodes within as a rigid body. This tie constraint is defined as "Constraint-27" and its definition is illustrated in Figure 4.21 (c). The reference point associated with this rigid body is "RP-2", the same as used in the connector definition, and this effectively ties the 2D one element connector to the set of 3D brick elements within the bolt head.

a)

Representation of connector in the assembly module

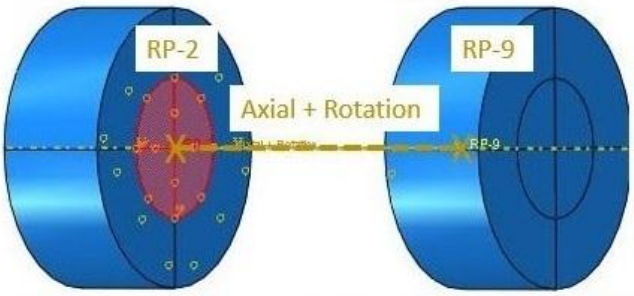

b)

Representation of connector in the mesh module

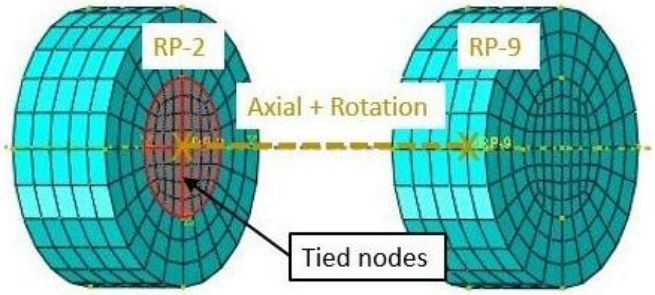

c)

Tie constraint used to connect the connector to the bolt head

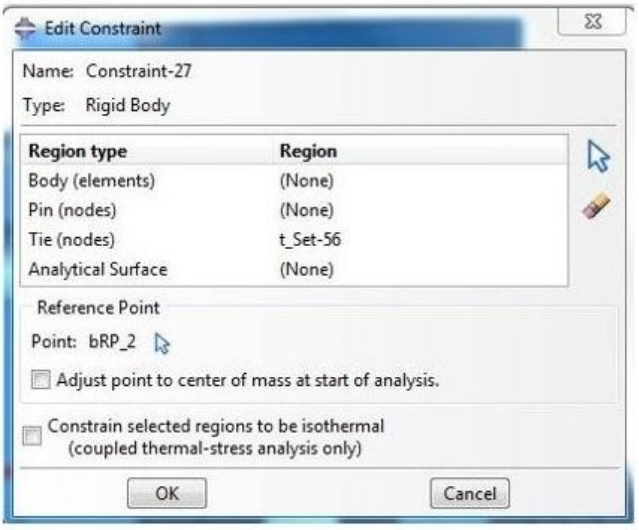

Figure 4.21: Representation of connector in the model and constraint needed to tie the connector to nodes of the bolt head and nut

4.7.6 Final results and comparison of computational requirements

The final model results show good agreement with experimental results, for both the static and dynamic cases. The force versus displacement curves obtained from stainless steel bolt tests and from their corresponding finite element models are shown in Figure 4.22. A summary of each analysis type and a comparison between different types of analysis in terms of computational demands is presented in Table 4.2 below.

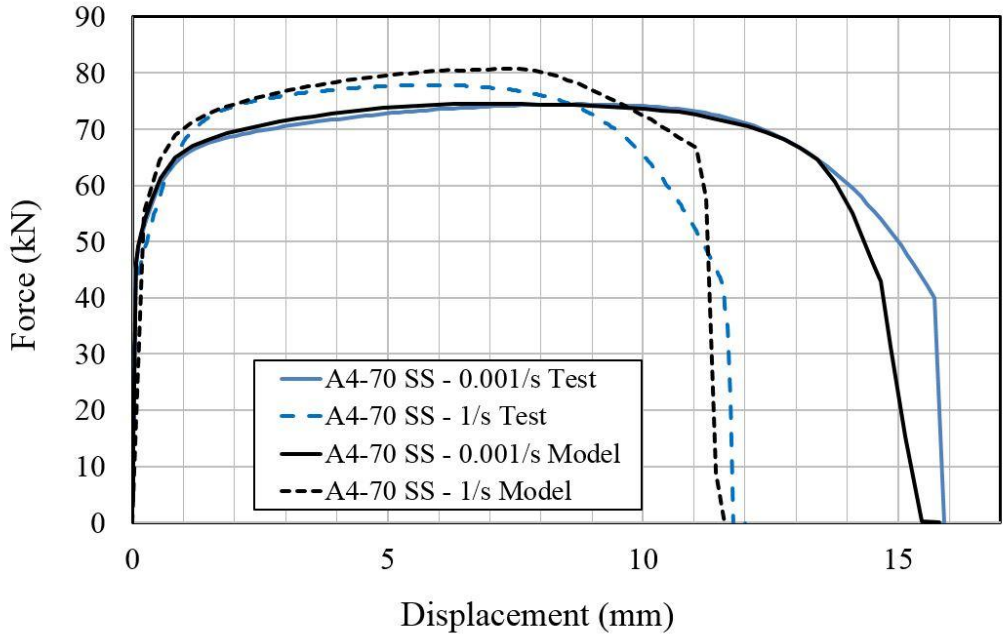

Figure 4.22: Comparison of force-displacement graphs from stainless steel bolt tests and finite element models at two selected stain rates (0.001 strain/s and 1 strain/s)

Connector elements (CONN2D2) are simple elements that can model nonlinear springs and can be used in two dimensional or three dimensional space. The force-displacement characteristic of the bolts can be input directly as the connector behaviour. The static model runs in 1 or 2 seconds, faster than the three dimensional model which on the same computational system took 46 seconds for static analysis with the Implicit procedure, since 1 element replaces 2280 elements. If the connector model response were included in Figure 4.22 it would overlap the test results exactly, since the two are identical.

Table 4.2: Comparison of analysis type and computational requirements for full 3D models that use different procedures

No.	1	2
Analysis type	Static, full 3D model	Dynamic, full 3D model
Density	True	True
Behaviour	Plasticity	Rate dependent plasticity
Material model	True stress strain	Johnson-Cook
Damage and element deletion	Yes	Yes
Damage model	Johnson-Cook	Johnson-Cook
Elements	2280 C3D8R Standard	2280 C3D8R Explicit
Procedure	Implicit	Explicit
Application	Quasi-Static	Dynamic
Increments	69	3660046
Analysis time	46 sec	32min
Parallelization	4 processors 40 GPGPU	4 processors
Agreement	Good	Good

4.8 Carbon steel bolt model

Ribeiro et al. (2016) present a numerical assessment of a T-stub component subjected to impact loading. They also provided true stress versus true plastic strain data that was used to model the Grade 8.8 bolt. Using this data and a dynamic increase factor as was determined experimentally in our case, the carbon steel bolts were modelled in an identical manner to how the stainless steel bolt was modelled, i.e. with no detail of the threaded region incorporated.

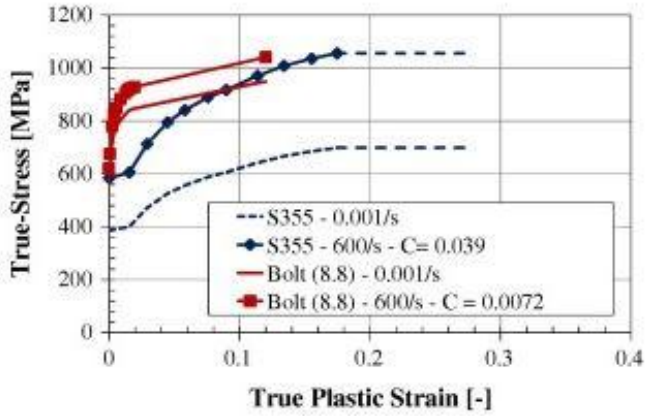

Figure 4.23: True stress true plastic strain curve (Ribeiro et al. 2016)

Figure 4.24 presents the force versus displacement graphs comparing test results and FE model results for Grade 8.8 carbon steel bolts. There is good agreement between the test and the model in terms dynamic increase factor and in terms of displacement at failure.

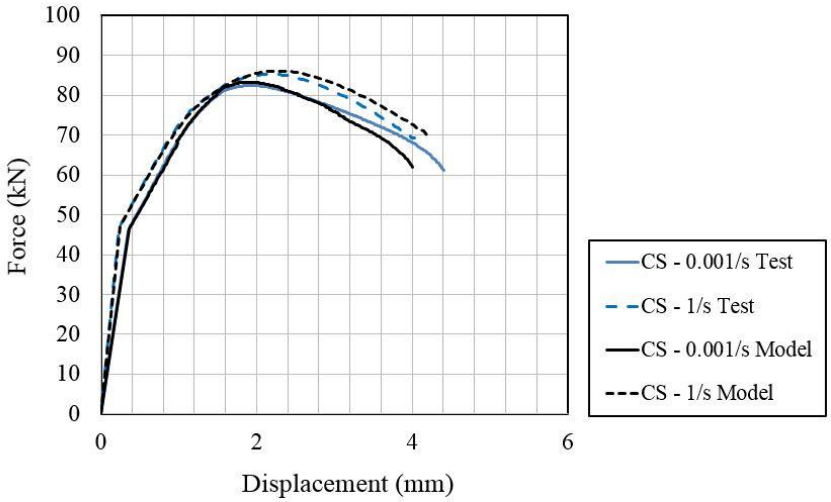

Figure 4.24: Comparison of force-displacement graphs for carbon steel bolts (test and FE predictions) for different strain rates (0.001 strain/s and 1 strain/s)

4.9 Conclusions

This chapter presented a general overview of the steps required to produce and solve a finite element model for simulations of both static and dynamic loading scenarios. Two types of elements were described in more detail, since they were the main elements used in modelling the connection components: the continuum brick element and the connector element. The material behaviour of the components had to include definitions of rate-dependent plasticity and damage behaviour, especially for the modelling of components subjected to high loading rates.

High-rate material tests on steel show that there usually is an increase in strength with higher strain rates and a decrease in fracture strain. The Johnson-Cook and Malvar-Crawford material models were used to model the increase in strength for the bolts and the end-plate steels respectively. Reasonably good agreement with test results was obtained when using these material models.

For both the steel coupon and the stainless steel bolt models the analysis types were described in detail including the procedures used, the number of increments, the analysis time and parallelization. The static and dynamic models were compared in terms of computational requirements in order to illustrate the difference in the resources required.

These analysis steps and procedures, models for material behaviour and element types will now be used in the following chapters to develop the larger FE modelled assemblies required to model the full behaviour of the connections.

Chapter 5: Numerical assessment of moment resisting connections under different loading rates

5.1 Introduction

This chapter presents the detailed process of modelling the moment connections in 3D space in Abaqus. The finite element model was developed using the material models presented in the previous chapter. Quasi-static analysis was carried out with the Abaqus/Standard module and dynamic, high rate, analysis was carried out using the Abaqus/Explicit module. The model results are compared to test results and these will be discussed. A parametric study is also carried out where the connections tested are replaced by models with different plate thicknesses. Conclusions are drawn about the behaviour of the connections from the results of the simulations.

5.2 Finite element model

Using symmetry in the horizontal plane, only half of the assembly tested experimentally was modelled in order to reduce computational demands. The assembly included half of each of the following components: the beam stub, the end plate, the bolts, the extension piece and the flying column. The geometry, model and boundary conditions are illustrated in Figure 5.1. In this figure only the flush endplate connection is presented. The same assembly was used in the extended endplate connection model.

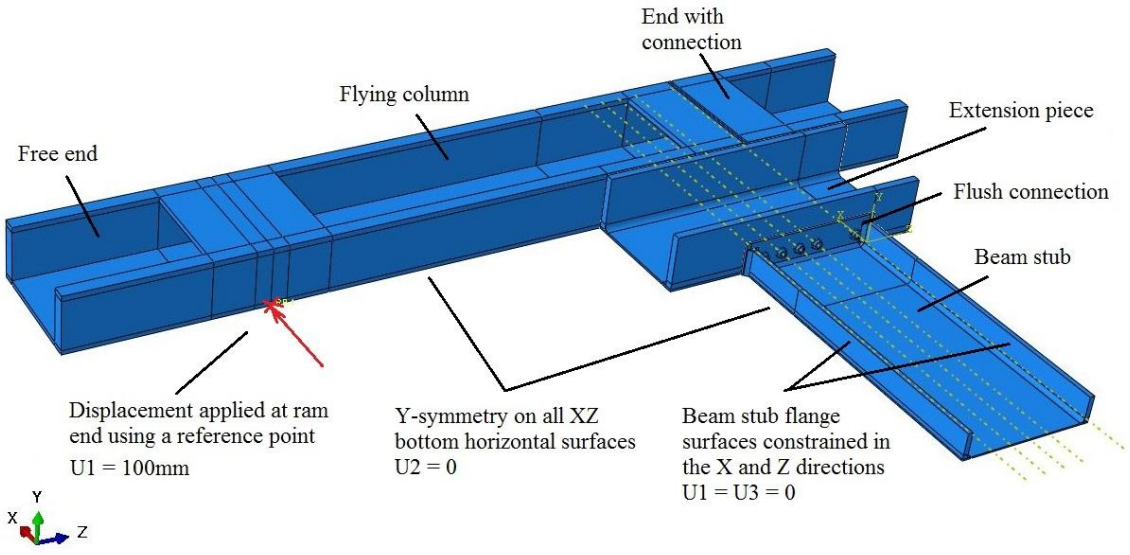

Figure 5.1: Geometry, model and boundary conditions of column-beam assembly

The bottom horizontal surfaces of the assembly are not visible in the figure. These represent the horizontal plane of symmetry where boundary conditions where applied by constraining the nodes from movement in the Y direction, i.e. U2 = 0. The surfaces of the beam stub flanges were constrained against movement in the X and Z directions, i.e. U1 = U3 = 0. A strip on the face of the flying column in the region of the loading ram was tied as a rigid body and a reference point was assigned to it. In the analysis, the displacement was applied at this reference point increasing in the X-direction.

The material behaviour for the bolts, end plate and beam stub included plasticity and ductile damage. Since no plastic deformation was observed in the flying column and the extension piece in the experimental testing only elastic behaviour was defined for these components.

The whole model consisted of a total of 45,000 elements of which approximately 35% of the elements were those used for modelling the bolts. For the full model of the flush end plate connection, each bolt consists of 3,200 solid brick elements of a global size of 2mm. The end plate consisted of 15,500 solid brick elements of size 2mm. For the welds, a total of 2,400 solid wedge elements of size 2mm were used. For the beam stub, 20mm size elements were used generating 2,500 elements. The extension piece and the flying column consisted of a total of 8,500 elements of size 20mm and 50mm respectively.

All solid brick elements used were C3D8R elements. Element deletion was defined for the end plate, the welds and the bolts. The model mesh is shown in Figure 5.2. The flying column and the extension piece have a generally uniform mesh. The mesh is more refined in the vicinity of the bolt holes in the case of the end plate and in the body of the bolts as illustrated by Figure 5.2 (b) and (c).

The same modelling approach was used to create the extended endplate connection model. The model consisted of 100,900 elements of which approximately 75% were those used for modelling the bolts. The main difference is that the plate is extended at the top and bottom of the connection; there are two additional bolt rows and two additional holes in the extension piece. In this case, each bolt consisted of 10,500 elements of a global size of 1mm. The end plate consisted of 13,500 elements of size 4mm; these were 2mm in depth through the plate thickness.

Figure 5.3 shows the meshes for the two types of connections to illustrate the main differences. Another significant difference is that the extended end-plate is attached to a 305x102x25 UKB section and the flush endplate is attached to a 305x127x37 UKB.

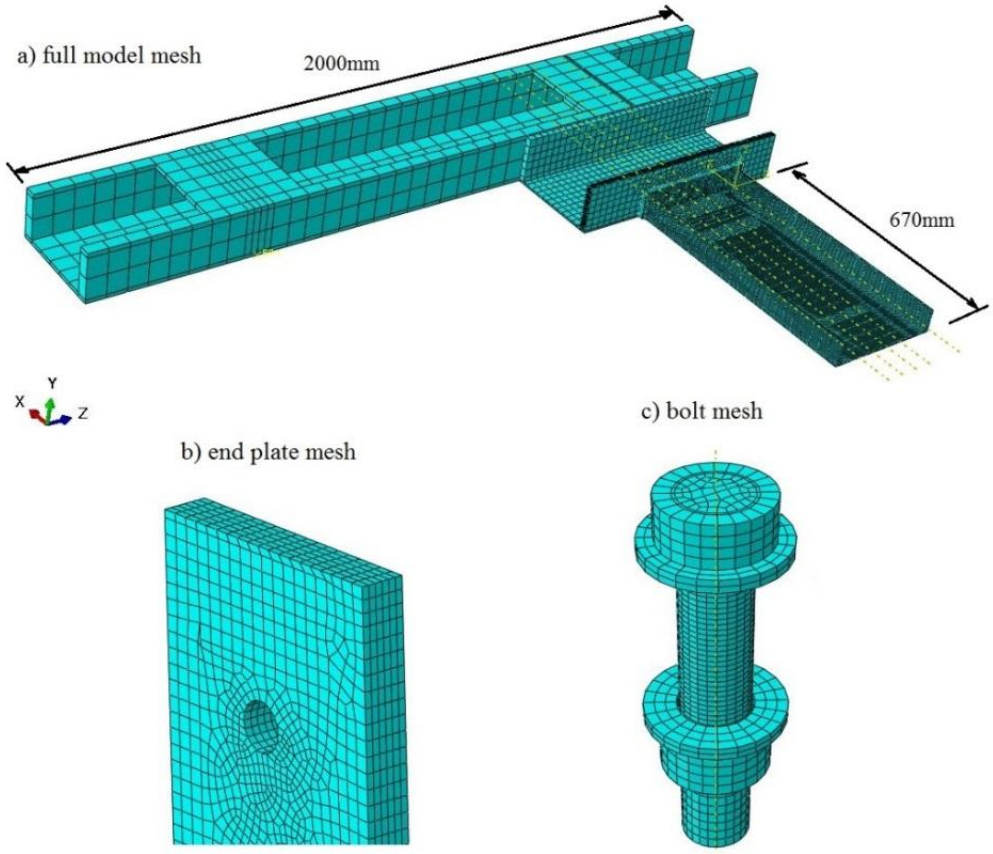

Figure 5.2: Finite element model mesh

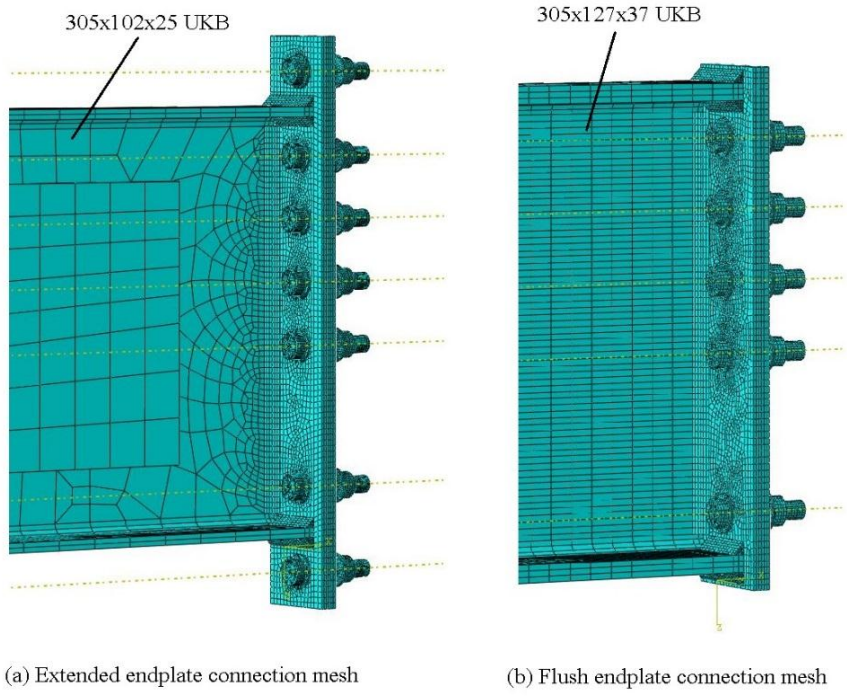

Figure 5.3: The two different types of model connections

5.3 Static analysis of connections

In the static case, the displacement at the position of the loading ram was increased linearly from 0 to 100mm in the X-direction in a time period of 300 seconds at the reference point, which corresponds to the location of the loading ram. The analysis used a general dynamic implicit procedure with quasi-static application. The initial increment size was 0.3s with minimum and maximum increments defined as 10^{-6}s and 10s respectively.

Field output requests for the whole model included stresses, strains, displacements, forces, the damage variable and the status variable. History outputs of the force were requested at the reference point and for displacement were requested at either end of the flying column. The analysis used parallelization with 4 CPUs and 40 GPGPUs. With the described settings, the analysis was complete in approximately 1.4 hours in the case of the flush endplate connection and in approximately 1.8 hours in the case of the extended end plate connection.

Examples of contour plots of von Mises stresses and equivalent plastic strain are plotted for the flush endplate connection in Figure 5.4 at increment 47 after 282 seconds. At this step the model connection rotates 3.06 degrees, developing the highest moment value of 106kNm which was close to failure. The fact that the connection is close to failure is indicated by the high value of equivalent plastic strain, 1.07 in the neck of the top bolt and damage variables close to the value of 0.4 in the neck of the bolt. Damage was initiated in the bolt and the first bolt fails completely soon after damage initiation.

As it rotates, the displacement of the "flying column" is mainly in the X direction. Figure 5.5 shows the contour of total displacement for at a step time of 282 seconds when the connection is close to failure. The red region indicates displacement between 14mm and 17mm. At the centre of the concentric circles representing bands of different displacement is located the centre of rotation. This is the centre about which the "flying" column rotates and it lies slightly above the bottom flange.

By taking the inverse tangent of the ratio between the displacement of the nut, approximately 17mm, and the distance between the centre of rotation and the top bolt, approximately 262mm, an estimate of the connection rotation of 3.71 degrees can be obtained.

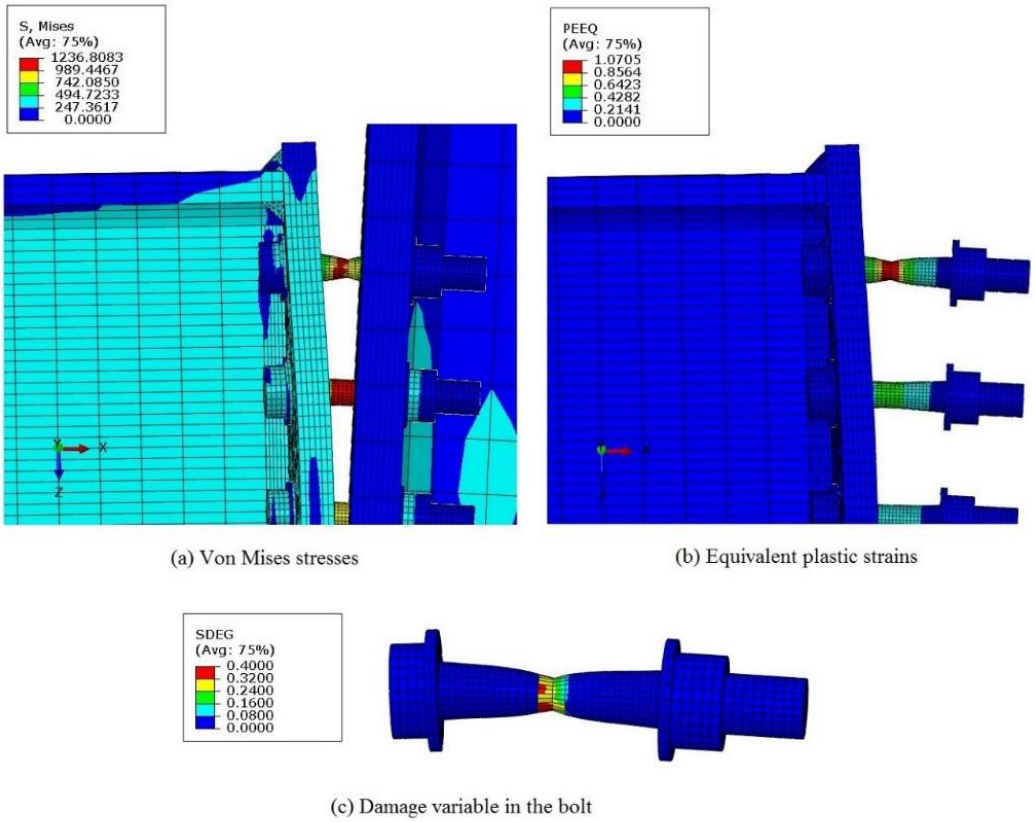

Figure 5.4: Contour plots of (a) Von Mises stresses, (b) plastic strains and (c) damage variable in the bolt for a connection rotation of 3.06 degrees when the applied moment reaches the maximum value of 108.5kNm

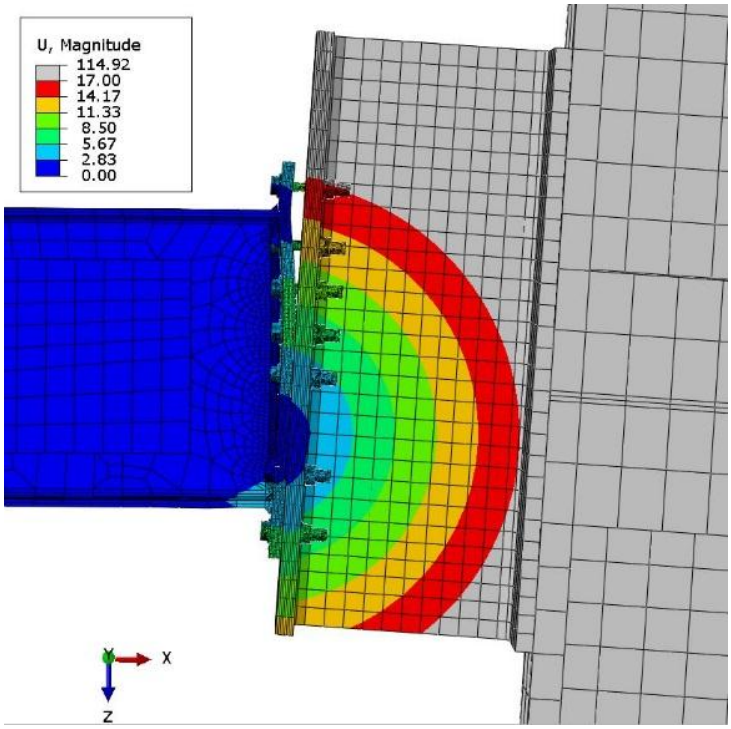

Figure 5.5: Contour plot for total displacements, mainly X direction, for the connection close to failure

Examples of contour plots of von Mises stresses and equivalent plastic strain are plotted for the extended endplate connection in Figure 5.6 at increment 60 after 294 seconds. At this step the model connection rotates 4.12 degrees, developing a moment value of 133kNm which was close to failure.

Finite element models showed good agreement with experimental testing in terms of rotation at failure and ultimate moment over predicting these by negligible amounts. Figure 5.7 presents graphs of the moment versus rotation for flush connection tests and models.

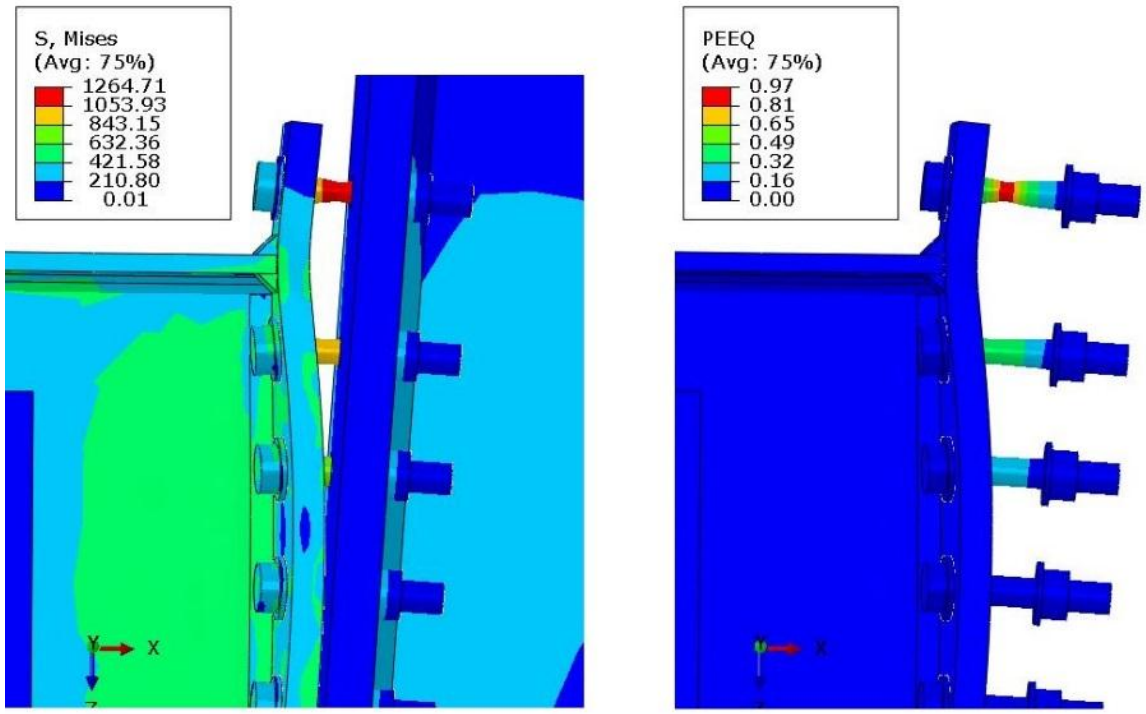

(a) Von Mises Stresses

(b) Equivalent plastic strains

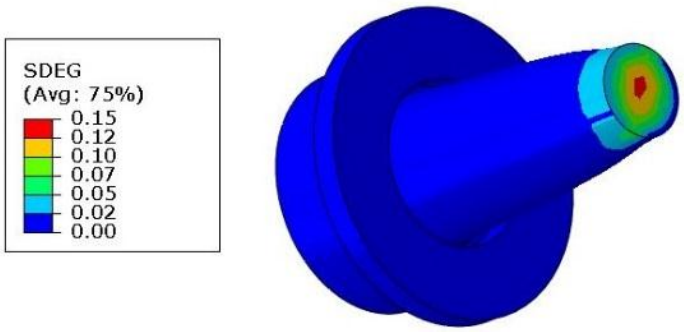

(c) Damage variable in the bolt

Figure 5.6: Contour plots of (a) Von Mises stresses, (b) plastic strains and (c) damage variable in the bolt for a connection rotation of 4.12 degrees when the moment reaches the value of 133kNm

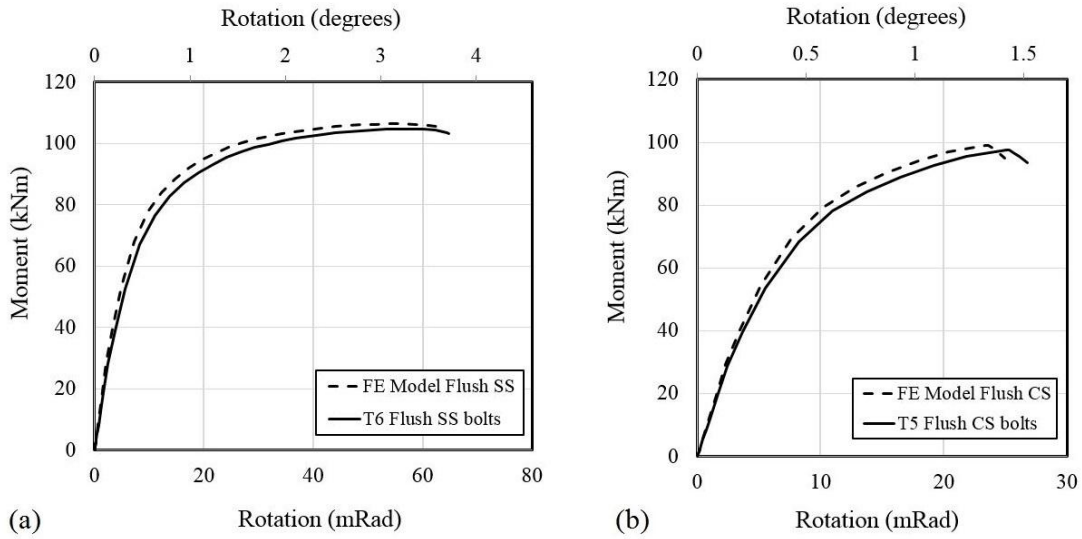

Figure 5.7: Moment versus rotation graphs for flush connections tests and models

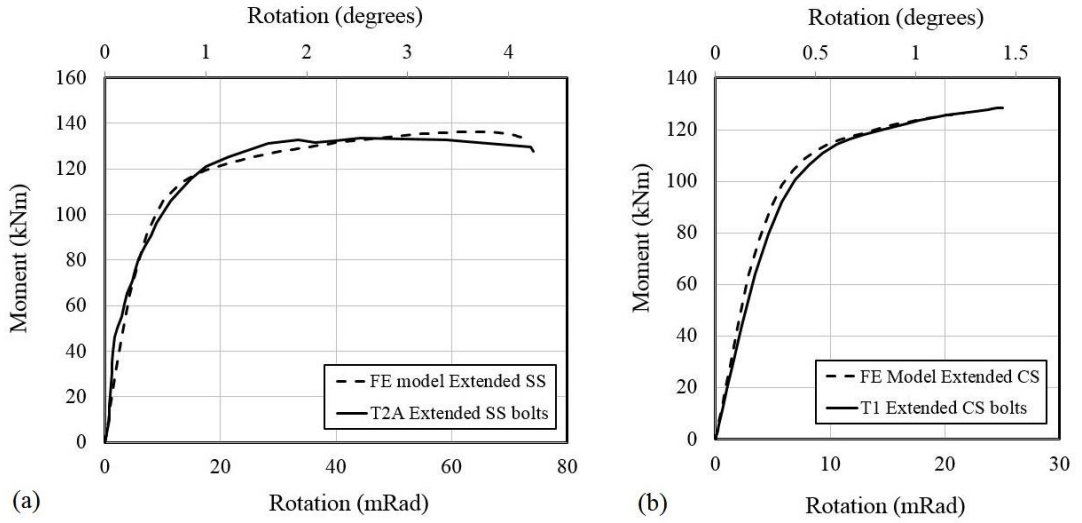

Figure 5.8: Moment versus rotation graphs for extended endplate connections tests and models

Both models had a large number of finite elements. In the case of the flush end-plate connection 35% of the elements were used in modelling the bolts and in the extended end-plate connections 75% of the elements were used for modelling the bolts. The difference comes from the size of the elements: elements of size 2 mm were used in the former case and size 1 mm elements were used in the later. The reason different element sizes were used was to enable comparison of the different models in terms of computational time. The time required to run the models on 4 CPUs was 1.4 hours and 1.8 hours respectively. This time can be reduced by 35% to 0.91 hours and by 75% to 0.45 hours respectively by using connector elements. Connector elements are simple 2D elements that may replace the whole body of the bolt.

5.4 High rate analysis of flush endplate connection with stainless bolts

In the dynamic test on the flush connection with stainless bolts the measured load increases to a peak value in approximately 6 milliseconds, maintains a plateau for 10 milliseconds and then decreases in the last 10 milliseconds. Figure 5.9 shows the applied load versus time. Abaqus/Explicit was used to carry out the dynamic analysis. The data in the figure was input in tabular form as amplitude of the defined maximum load against each time step. Modelling data was processed in the same way as experimental data as was discussed in the previous chapters, using the moment equilibrium equation and subtracting inertia effects.

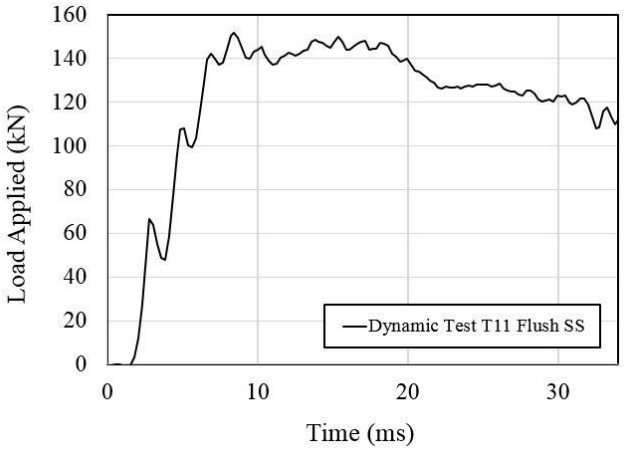

Figure 5.9: Applied load measured in the test and defined for the model

Figure 5.10 (a) shows the comparison, FE model versus test results, of the relative rotation of the "flying column" versus time. Figure 5.10 (b) shows the location of the instantaneous centre of rotation versus time, where this distance is measured from the bottom flange. In the experimental tests there is additional movement from slip of the bolts within the holes of the supporting angles, flexibility or movement of the angles and minor twisting from the asymmetric boundary conditions since the beam stub is only held on one side.

This movement causes the whole assembly including the beam stub and the angles to move as a single rigid body in the first 16ms. This can be observed in Figure 5.10 (b) between 6ms and 16ms as the difference between the experimental and numerical centres of rotation increases to approximately 0.10m.

In the experiment, since the centre of mass of the assembly is close to the centre of the connection, the centre of rotation for the "flying column" with the additional beam stub and angles is initially in the middle of the connection; this results in a centre of rotation that located 0.14m from the bottom flange between 11ms and 16ms.

In the model, this is not the case. The beam flanges do not move as they have fixed boundary conditions defined; this results in a centre of rotation located 0.04m from the bottom flange throughout the deformation of the connection.

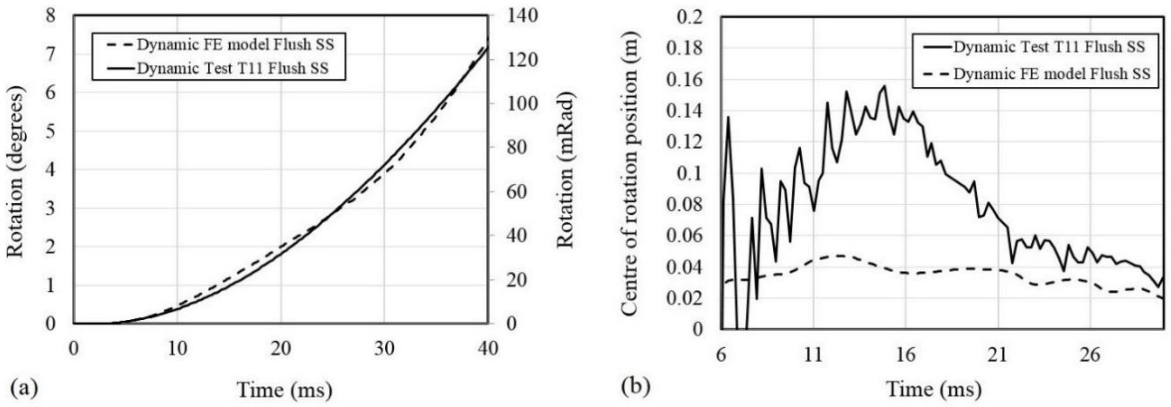

Figure 5.10: (a) Rotation versus time and (b) ICR versus time, note changes are small in comparison to lever arm

In the experiment, once movement of the beam stub flanges ceases because the flanges stop moving, the bolts start deforming plastically and as they fail the centre of rotation moves closer to the bottom of the flange. After 26ms both experimental and numerical results predict an almost identical centre of rotation. The location of the centre of rotation has a great influence on many variables including the change in rotation and rotational acceleration versus time. Figure 5.11 shows the moment versus time and rotation respectively. The greatest difference between the experimentally and numerically predicted values lies in the time period where the difference in the centres of rotation is the greatest.

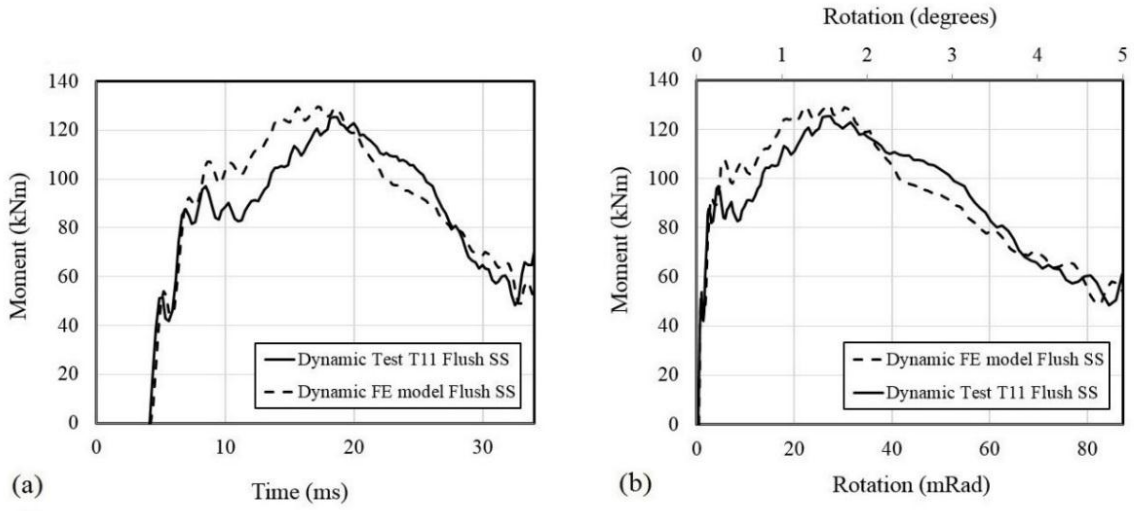

Figure 5.11: Moment versus rotation for extended end-plate model with stainless bolts

Figure 5.12 shows the failure of the first two bolt rows in the model and in the test. The first bolt fails after 21ms from the start of the force application when the connection rotated approximately 3 degrees. The second bolt fails after 25ms when the connection rotated approximately 3.8 degrees. Figure 5.13 shows the failure of the third and fourth bolt rows after 28ms and 31ms after the connection rotated 4.5 and 5 degrees respectively.

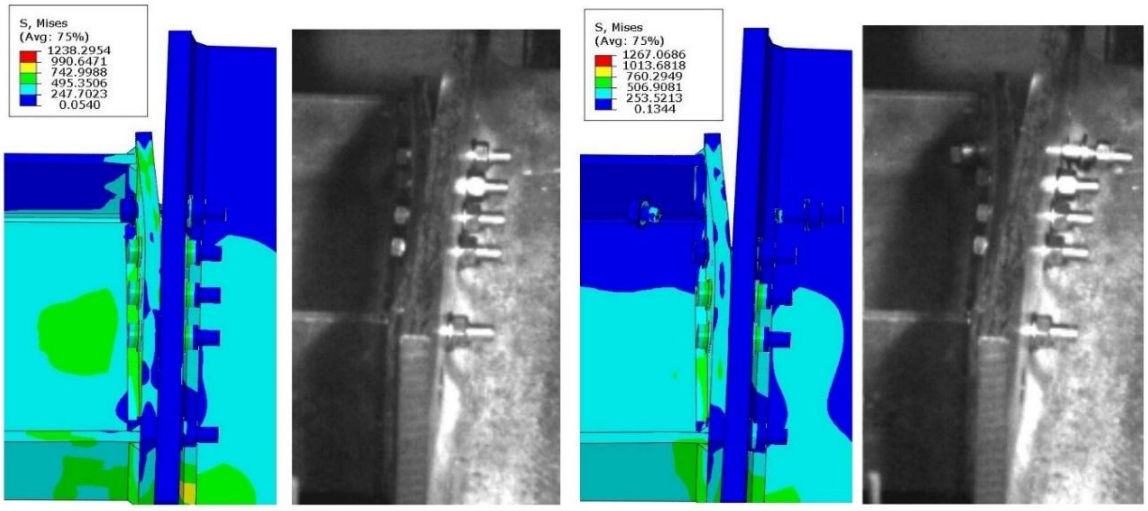

(a) 21ms, 3 degree rotation (b) 25ms, 3.8 degrees rotation

Figure 5.12: 1st and 2nd bolts fails at 21ms and 25ms, predicted and experimental results

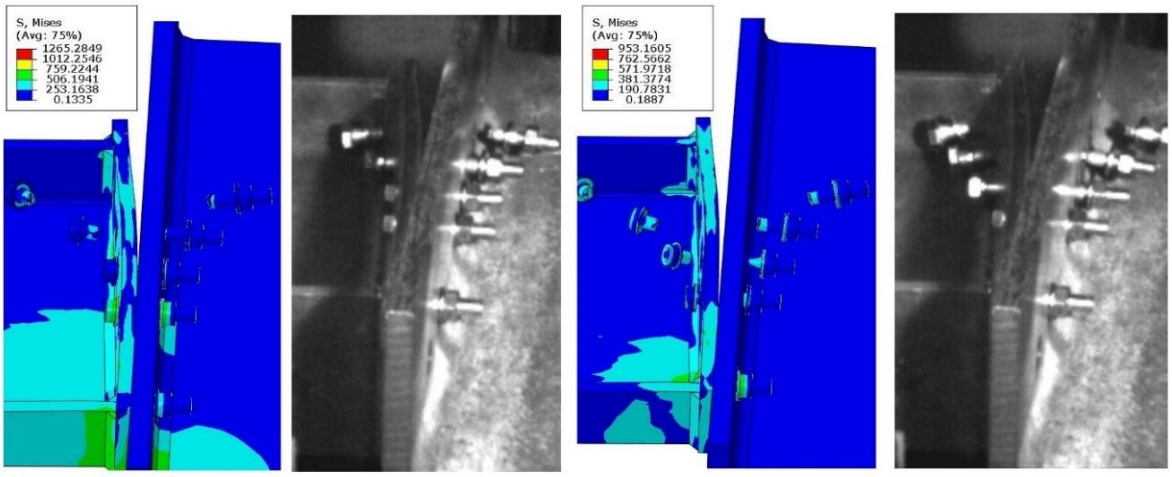

(a) 28ms, 4.5 degrees rotation (b) 31ms, 5 degrees rotation

Figure 5.13: 3rd and 4th bolts fail at 28ms and 31ms, predicted and experimental results

Once the elements within the plastic neck of the bolt reach the fracture strain characteristic for the strain rate the Damage variable value has the maximum value of 0.4. The element stiffness is degraded to 0 and its Status variable is changed from 1 to 0. The elements are therefore automatically deleted and excluded from the viewport so they are no longer present in the model. A fraction of the strain energy is released instantaneously and the bolts fly off in the same manner as observed in the experiments. (See accompanying submitted videos.)

5.5 High rate analysis of extended endplate connection with stainless bolts

In the dynamic test on the extended end-plate with stainless steel bolts the load also rises sharply to a peak value after which it maintains a plateau. This is shown in Figure 5.14. Data is input in tabular form and the model is solved with the Abaqus/Explicit module.

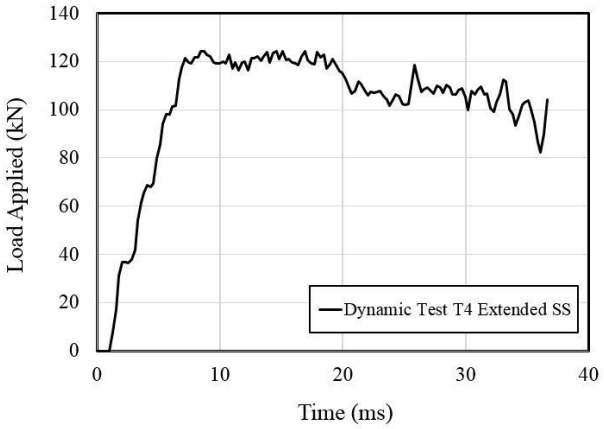

Figure 5.14: Applied load measured in the test and defined for the model

Test T4 was unique when compared to all other dynamic tests because the column hit a wooden stop before the connection failed completely, i.e. after the first two bolts fracture. This leads to an even greater disagreement between experimental results and numerical predictions of rotation versus time and centre of rotation as is demonstrated by Figure 5.15. Additionally, the bottom flange buckles asymmetrically in a way which cannot be captured by the model. The asymmetric buckle causes a reduction in the ultimate moment capacity, since the centre of compression moves higher reducing the lever arms of the bolt rows. It also causes the plate to deform more than predicted by the model.

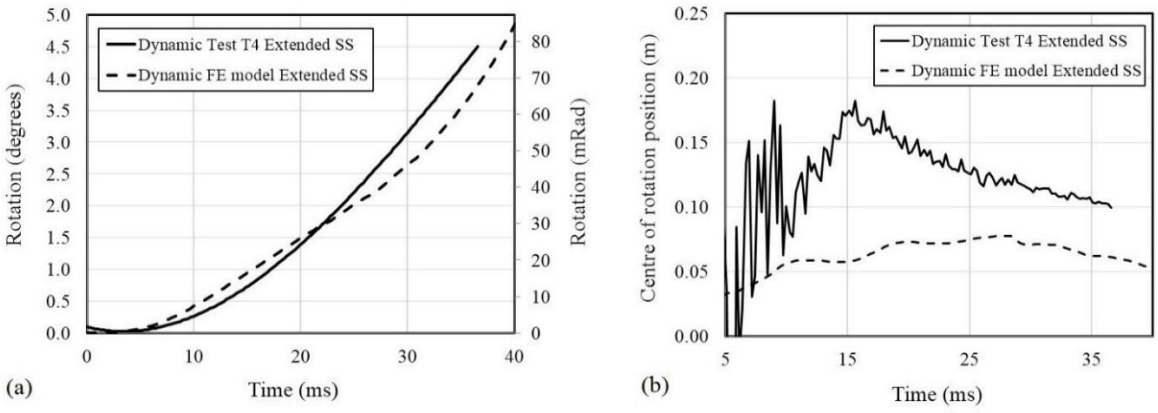

Figure 5.15: (a) Rotation versus time and (b) ICR versus time, note changes are small in comparison to lever arm

Figure 5.16 shows the experimental and numerically predicted moment versus time and rotation respectively. Once again, the greatest difference between these two is where the difference between the centres of rotation is the greatest. This greatest difference is approximately 20kNm in the first 20ms.

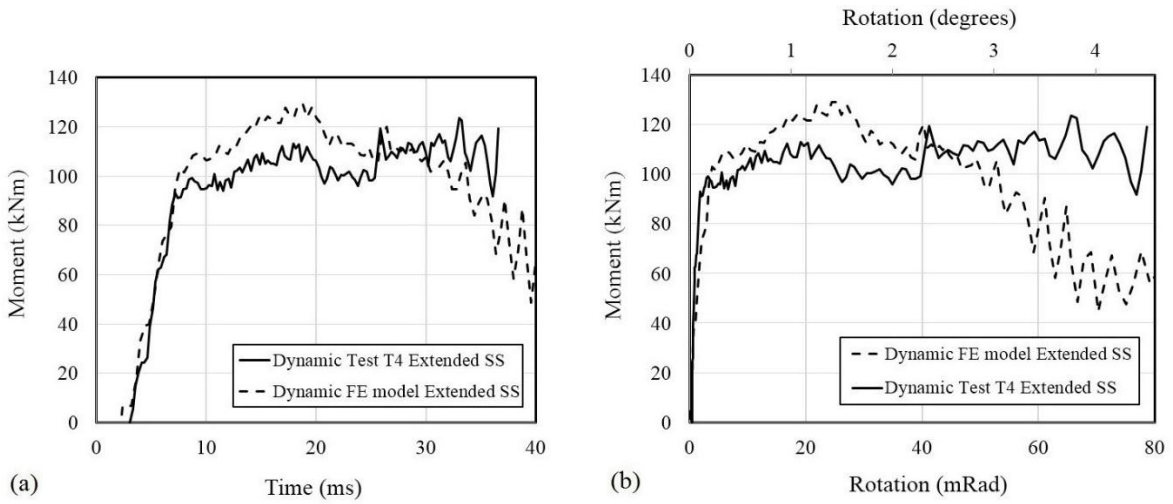

Figure 5.16: Moment versus rotation for extended end-plate model with stainless steel bolts

Figure 5.17 shows the 1st bolt failing after approximately 21ms and the 2nd bolt failing after 25ms. After approximately 28ms the "flying column" hits a wooden stop thus slowing down. The wooden stop is removed but absorbs some of the energy from the "flying column", thus apparently increasing the moment capacity and delaying the bolt failure by over 5ms. In the model this delay is not present, so the remaining bolts continue to fail shortly after.

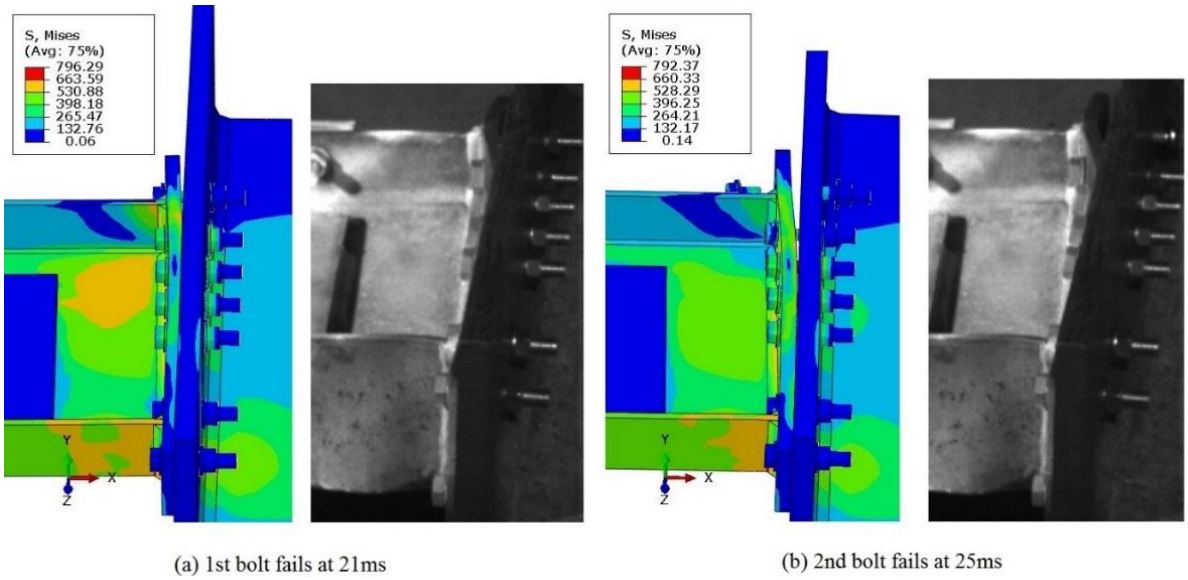

Figure 5.17: 1st bolt fails at 21ms and 2nd bolt fails at 25ms

Both the experimental circumstances of the asymmetric buckle and the wooden stop and the fact that the finite element model only models half of the connection leads to the endplate in the model deforming less plastically than the one in the experiments. This discrepancy can be observed in Figure 5.17. It is also observable in Figure 5.16 since the model predicts that the peak moment capacity and the reduction of the capacity as the connection fails happen sooner in the model than it happens in the test.

Despite the major difference between experimental and numerical results in the case of test T4, reasonable agreement is obtained between the two results for practical purposes. The difference is not greater than 16% in terms of moment capacity and the superior ductility of the connection is still captured by the model.

5.6 Conclusions

This chapter described the steps taken to model the complete moment connections under both quasi-static and dynamic loading. Meshing the model required careful consideration, since the mesh has to be more refined at the connection and less refined away from the connection to reduce computational requirements.

Both models had a large number of finite elements. In the case of the flush end-plate connection 35% of the elements were used in modelling the bolts and in the extended end-plate connections 75% of the elements were used for modelling the bolts. The difference comes from the size of the elements: size 2 elements were used in the former case and size 1 elements were used in the later. The time required to run the models on 4 CPUs was 1.4 hours and 1.8 hours respectively. This time can be reduced by 35% to 0.91 hours and by 75% to 0.45 hours respectively by using connector elements. Connector elements are simple 2D elements that may replace the whole body of the bolt.

The moment versus rotation characteristic of the connections with both types of bolts can be predicted with good accuracy by the numerical models in the quasi-static case. However, the dynamic case involves a series of phenomena and events that is difficult to replicate exactly in the model. First of all, the whole assembly, including the supporting angles, moves as a rigid body, in the first 10 milliseconds of loading causing the centre of rotation to be located close to the middle of the connection and move toward the bottom flange as the connection fails. This cannot be fully replicated in the model, since the beam stub is fixed as if the supporting angles were not able to move at all. This causes the centre of rotation to be located closer to the bottom flange from the very beginning of the connection loading. The difference in the value for moment capacity comes from the slightly different centres of rotation.

In conclusion, good agreement was obtained in the quasi-static case and reasonable agreement was obtained for the dynamic case for practical purposes. Computational requirements can be reduced significantly by paying particular attention to the meshing process and by using connector elements. The latter reproduces good results of the bolt and full connection behaviour, but at significantly reduced computational time.

Chapter 6: Models of full scale moment connections

6.1 Introduction

Industry standard moment connections of high moment capacity that are likely to be found in large scale structures are used in conjunction with beams of greater depth, such as 600mm deep beams or more.

The previous chapters present experimental tests and numerical models of connections for 300mm deep beams. These connections were chosen for testing as a scaled-down version of industry standard moment connections. Their moment capacity was low enough to allow their testing to failure in the available experimental rig.

This chapter presents numerical models of industry standard moment connections, which may be of greater interest to the practicing structural engineer. End-plate thickness was varied from 10mm to 30mm in a parametric study that informs the engineering community on the variation of ultimate moment and rotation capacity with plate thickness.

6.2 Connection geometry

The 1995 edition of the Joints in Steel Construction publication by the BCSA presents capacity tables and dimensions for detailing connections for beams that vary in depth from 762mm to 254mm. The dimensions of a standard connection for a beam of serial size 610x229x125 UKB are given in Figure 6.1 (a).

The position of the bolts for the standard connection is labelled as P1. The centre of the top row of bolts is located 60mm below the top of the flange which makes the distance between the toe of the weld and the edge of the bolt approximately 6mm. Since this distance is so small compared to the other dimensions it limits the rotation of the end-plate when the connection is deformed plastically. In order to increase the ductility of the connection the bolt holes were relocated further away from the web and the top flange, in a new position labelled P2 shown in Figure 6.1 (b).

The extended version of the connection described above involves a plate extension where the bolts are located 40mm above the top flange, see Figure 6.2. Similarly, bolts are located in two different positions, the original position P1 and the new position P2.

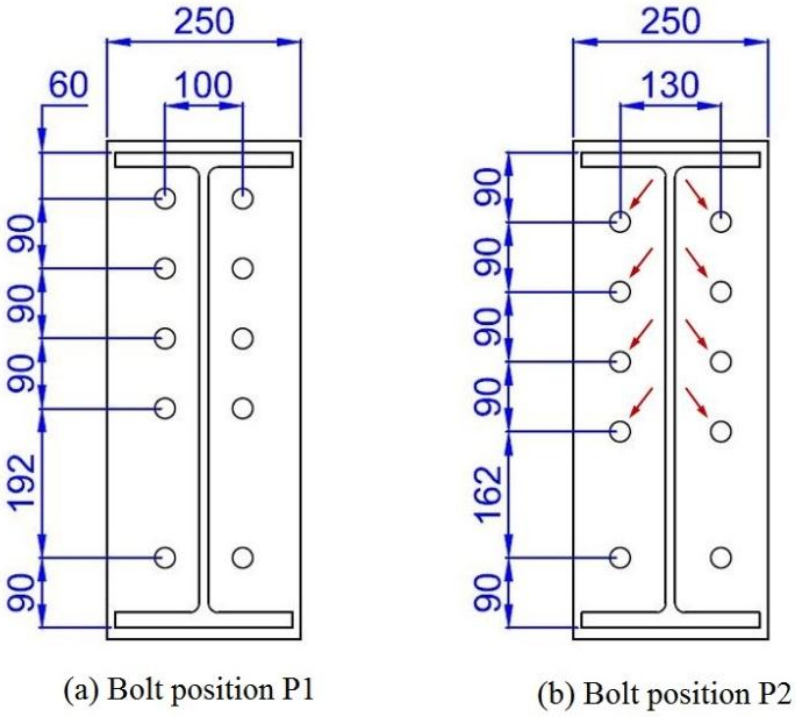

(a) Bolt position P1 (b) Bolt position P2

Figure 6.1: Position of bolt holes for the flush end-plate connection

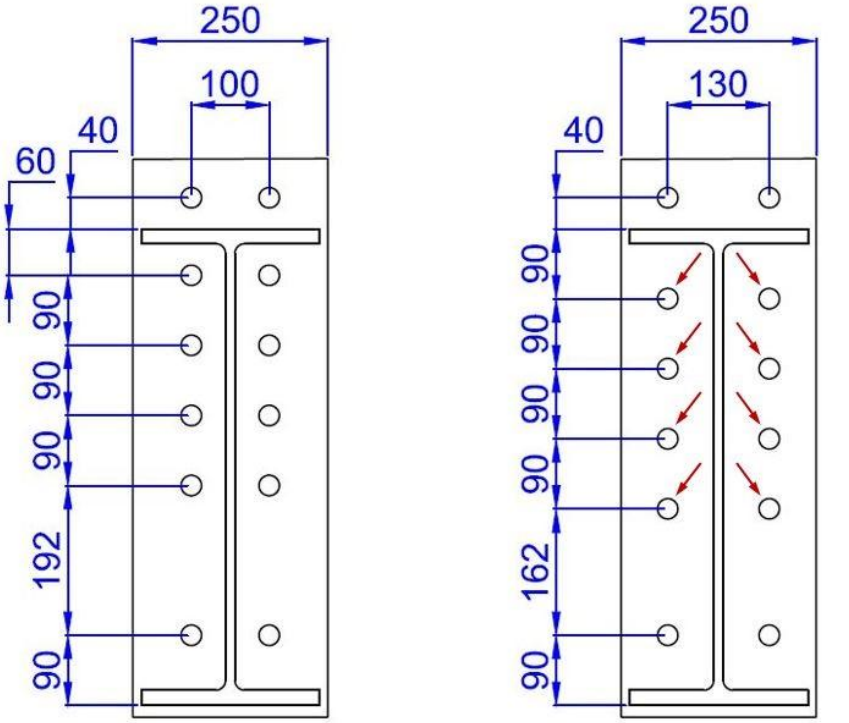

(a) Bolt position P1 (b) Bolt position P2

Figure 6.2: Position of bolt holes for the extended plate connection

6.3 Finite element model

The assembly was meshed with solid linear brick elements that make use of reduced integration, i.e. Abaqus element type C3D8R. The column was meshed with elements having edges approximately 50mm long apart from the region in contact with the end plate. Here the mesh was more refined with elements having edge sizes ranging from 4mm to 10mm. For the end plate elements ranged in size from 4mm around the bolt holes to 8mm in the rest of the end-plate. The bolts had elements of 3mm size. It was important that the regions where the column contacts the end-plate were more refined and with similar element sizes in order to prevent contact errors or element penetration errors. Figure 6.3 shows the mesh of the model and Figure 6.4 is a close-up illustrating the refined mesh used in the contact region.

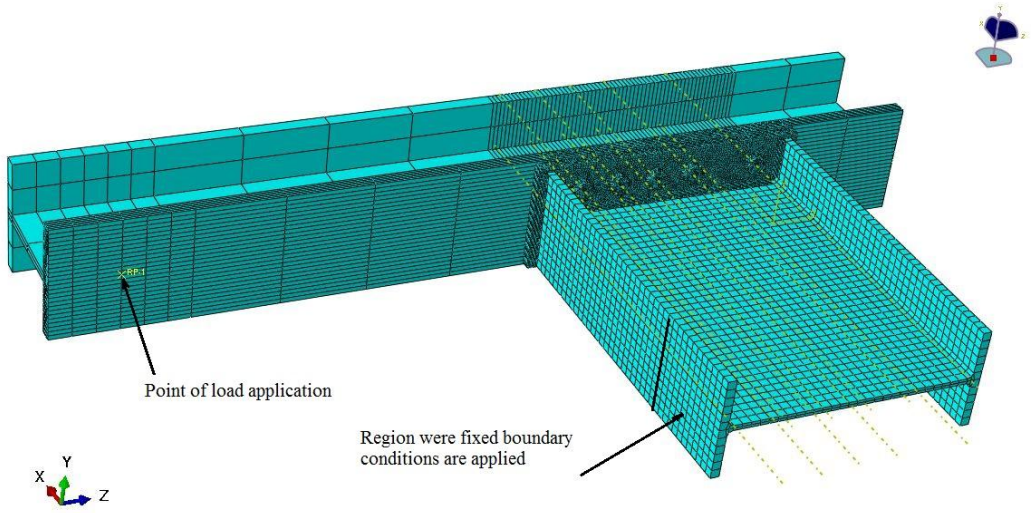

Figure 6.3: Finite element model mesh

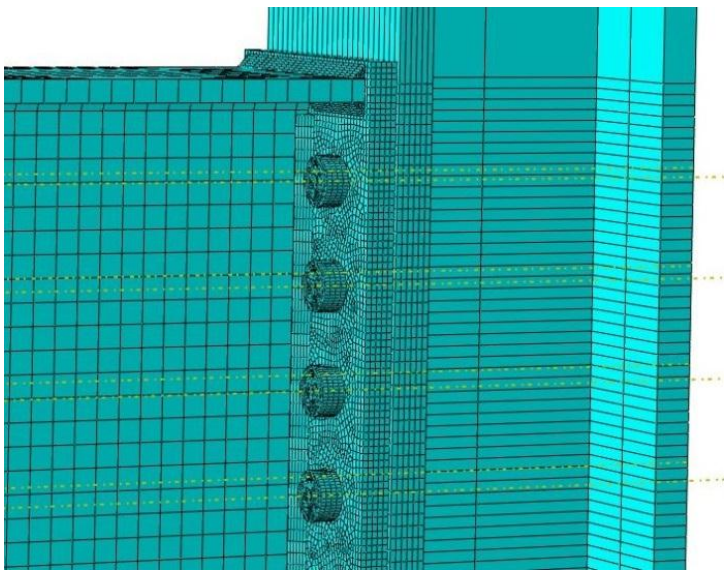

Figure 6.4: Detail illustrating mesh refinement at contact region

The 600mm deep modelled beam stub had a total length of 800mm and the ends were constrained for a length of 200mm against displacement in the three directions. This allows the rest of the beam stub to be free and increases the likelihood of flange buckling in compression. The displacement was applied at one end of the column at a distance of 1.228m from the centre of the connection. This was assumed to represent the lever arm of the resulting force and was used to calculate the moment capacity of the connection.

As opposed to previous models, the full scale connection models do not make use of connection symmetry. The full connection is modelled thus allowing bottom flange buckling to develop more naturally. Figure 6.5 shows Mises contour plots and illustrates how the bottom flange buckling is more pronounced in the case of the extended plate connection than in the case of the flush connection. The highest stresses and strain are found in the bolts and at the toe of the welds to the end-plate.

Figure 6.6 illustrates the difference in plate deformation for an extended end-plate connection with 10mm and 25mm thick plates respectively. Both connections in Figure 6.6 use stainless steel bolts. The 10mm thick plate deforms much more and the top row T-stub fails through a mode 2 failure mode, so the plate deforms more (see Figure 3.4 on page 51). By contrast, the 25mm plate undergoes negligible deformation and the top row T-stub fails through a mode 3 failure mode (see Figure 3.4 on page 51). Although the plate deforms more if it is thinner, the bolt bends more and fracture is initiated at a slightly smaller bolt average strain. The surprising result is that these two particular connections rotate the same amount before fracture, namely 2.92 degrees (51 milliradians), despite the different failure modes. In connections with plates thicker than 15mm fracture occurs in the bolts, no matter the T-stub failure mode. In connections with plates less than 15mm thick, it is equally likely that fracture occurs in the extension of the end-plate, at the toe of the weld.

Please refer to Figure 3.4 on page 51 for an illustration of T-stub failure modes.

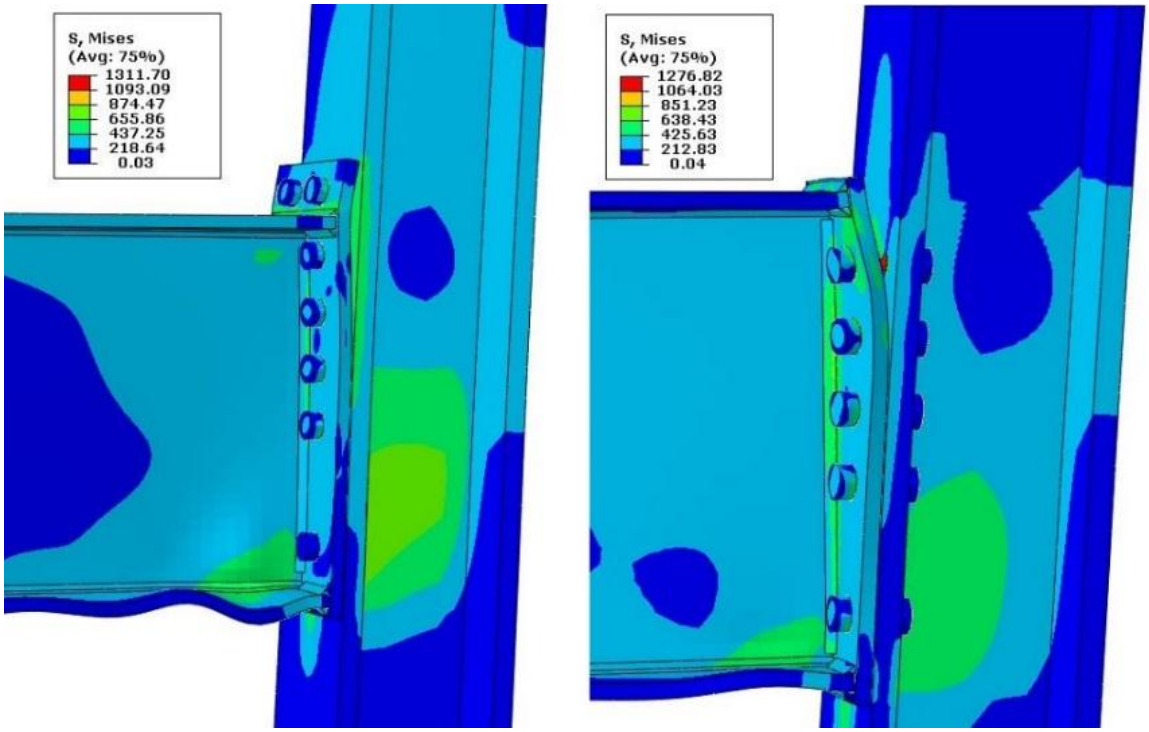

Figure 6.5: Von Mises contour plots for the two types of connections with 20mm thick plates and stainless steel bolts

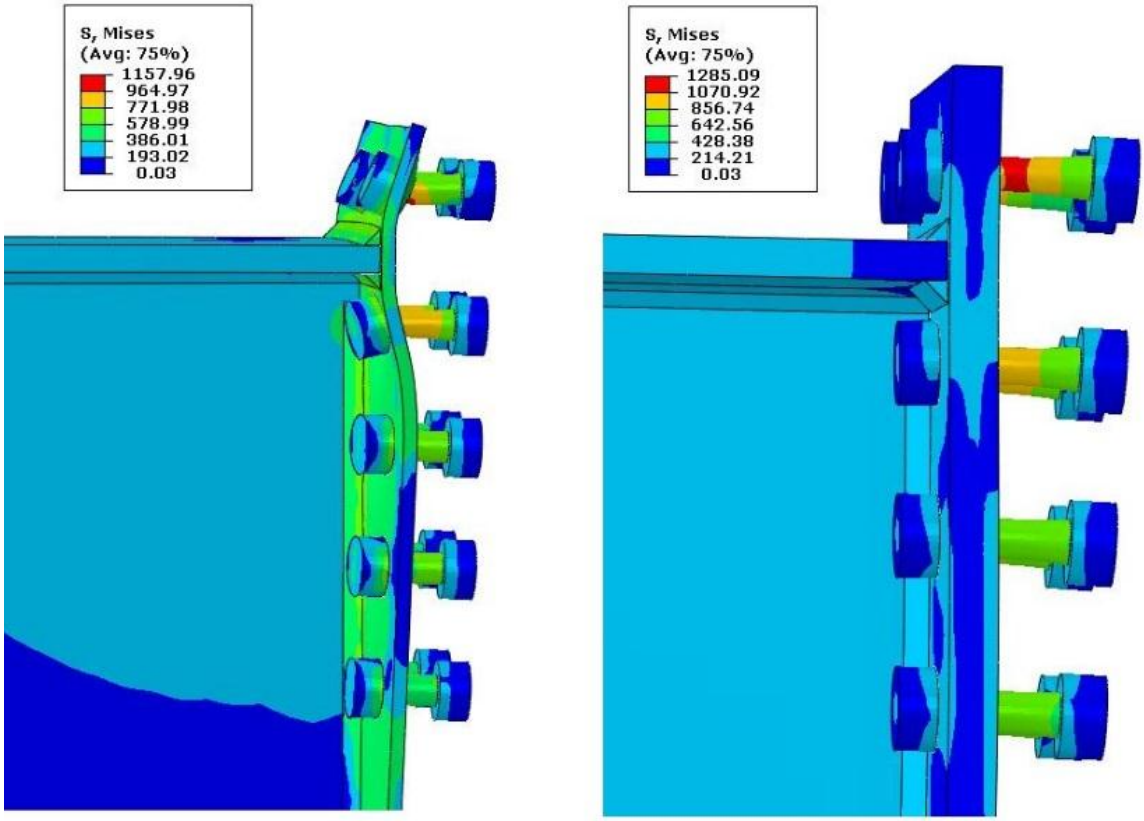

(a) 10 mm thick end-plate

(b) 25mm thick end-plate

Figure 6.6: Close-up of extended end-plate connection stress plots

6.4 Results

Figure 6.7 shows the variation in the rotation capacity for different plate thicknesses for extended end-plate connections with both types of bolts (stainless and carbon) and with different positioning of bolts (P1 and P2). By changing the bolts from position P1 to P2 the rotation capacity decreases by 0.3 degrees in the case of the stainless steel bolted connections. In the case of carbon steel bolts rotation capacity increases by 0.2 degrees for plates 25mm thick or thicker, stays the same for plates 15mm and 20mm thick and increases by 0.5 degrees for 10mm thick plates. Compared to the average rotation capacity of 3.15 degrees for stainless bolts and 1.05 degrees for black carbon bolts, the changes in rotation capacity achieved by changing bolt positions are small: 6% to 9% change.

Figure 6.8 shows that the moment capacity decreases with decreasing plate thickness. For example, if the plate is changed from a 25mm plate to a 10mm plate, the moment capacity drops by 23% from 1085kNm to 838kNm in the case of the connection with stainless steel bolts.

Figure 6.9 illustrates the difference in plate deformation for flush end-plate connections with plate thicknesses of 10mm and 25mm respectively. Most of the plastic deformation in the case of the connection with a 10mm plate occurs in the top row bolts and at the toe of the weld in the proximity of the second row of bolts. Note that there is little plastic deformation in the bolts from the middle rows since displacement is allowed by mid-plate rotation. In this case the first row T-stub heads towards a mode 2 failure and the second row T-stub heads towards a mode 1 failure. The strain reaches critical values at the toe of the weld, indicating that the plate would fracture first. In practice, it is likely that the bolts in the first row fracture soon after fracture is initiated in the plate and before the fracture has the chance to propagate throughout the whole plate. In the case of the connection with a 25mm plate, all plastic deformation as well as fracture occurs in the bolts. For both 10mm and 25mm thick plates the rotation capacity is 3.9 degrees (68 milliradians).

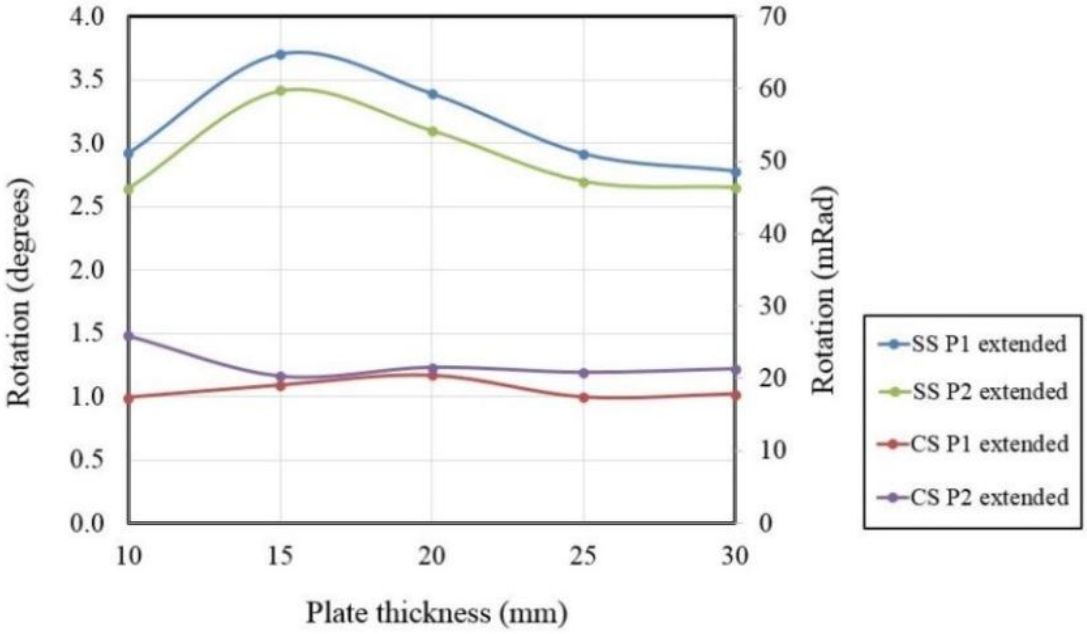

Figure 6.7: Rotation versus plate thickness for extended end-plate connection models

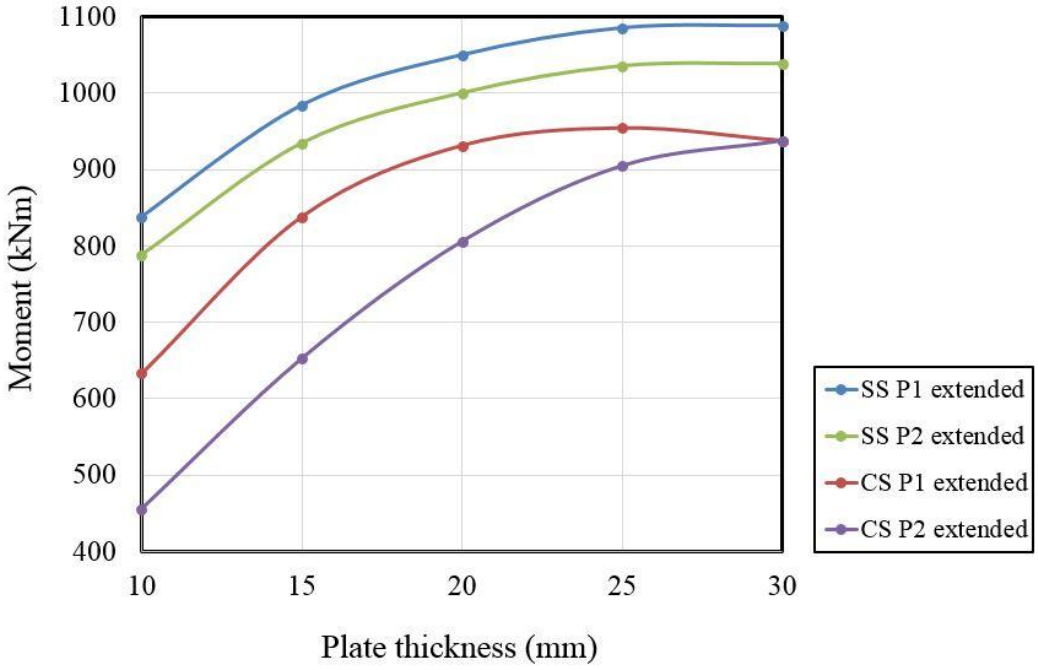

Figure 6.8: Moment versus plate thickness for extended end-plate connection models with stainless (SS) and carbon steel (CS) bolts

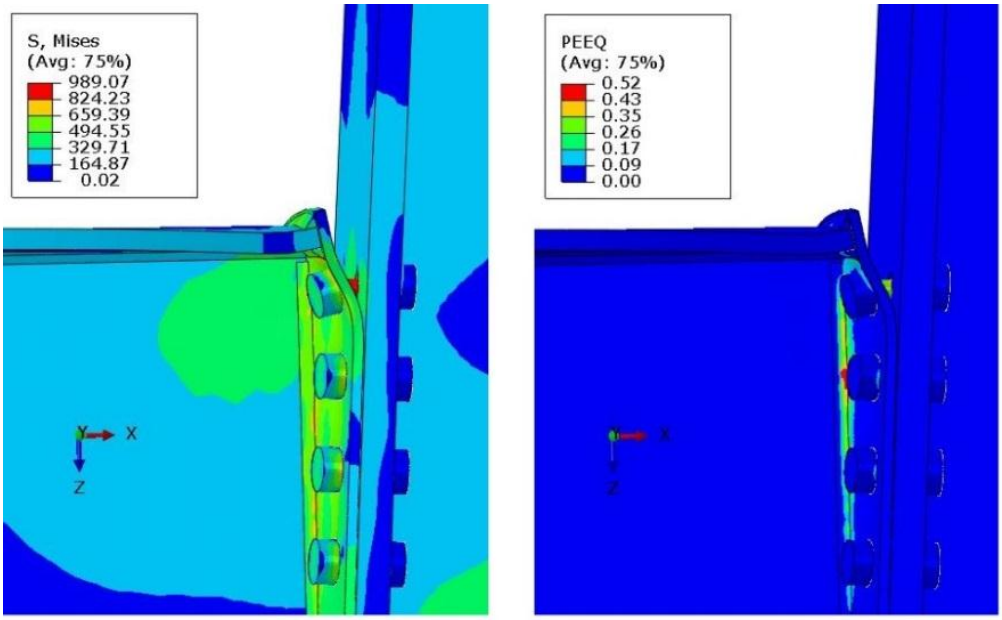

(a) equivalent stresses and plastic strains for 10mm thick flush end-plate

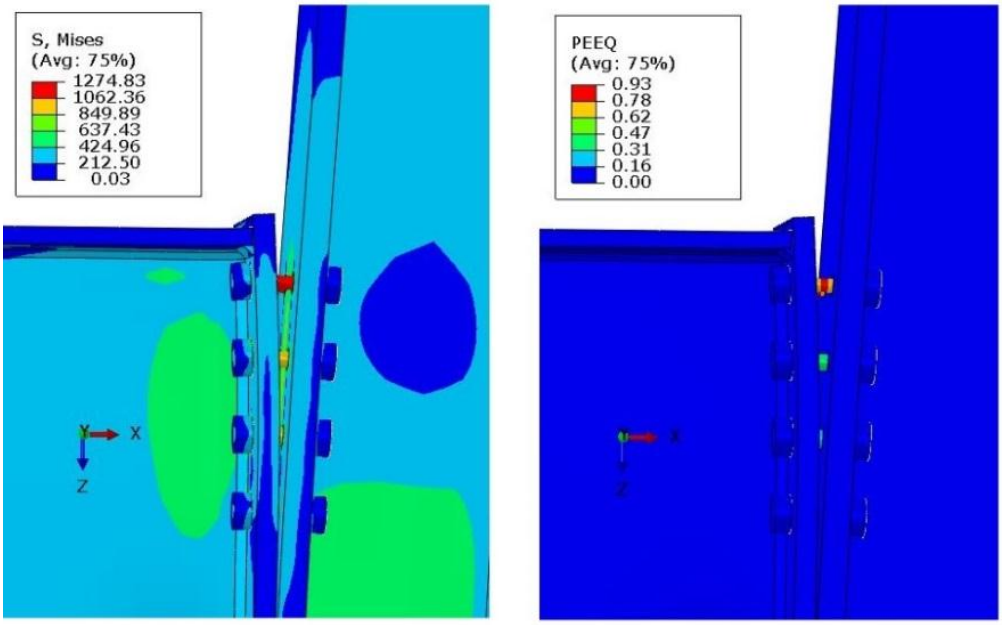

(b) equivalent stresses and plastic strains for 25mm thick flush end-plate

Figure 6.9: Comparison of flush end-plate connections of different thicknesses

Figure 6.10 shows the variation in rotation capacity versus plate thickness for flush end plate connections with both types of bolts (stainless and carbon). In the case of the connection where the stainless bolts are located in position P1 the plate thickness has little effect on the ultimate rotation of the connection. However, when the bolts are moved to position P2, the rotation capacity decreases by 0.5 degrees in the case of the 10mm plate and increases by 0.5 degrees for plates that are at least 15mm thick. The variation in plate thickness therefore has a greater effect on rotation capacity when the bolts are placed in position P2 rather than

in position P1. For connections with carbon steel bolts the rotation capacity lies between 1.0 and 1.5 degrees with higher capacity achieved for thinner plates, 1.3 degrees, or when the bolts are placed in position P2, 1.8 degrees.

Figure 6.11 shows that the moment capacity of connections always reduces with decreasing plate thickness. For example, if the plate thickness is changed from 25mm to 10mm there is a decrease in capacity that ranges from 28% to 31% depending on bolt type and bolt position.

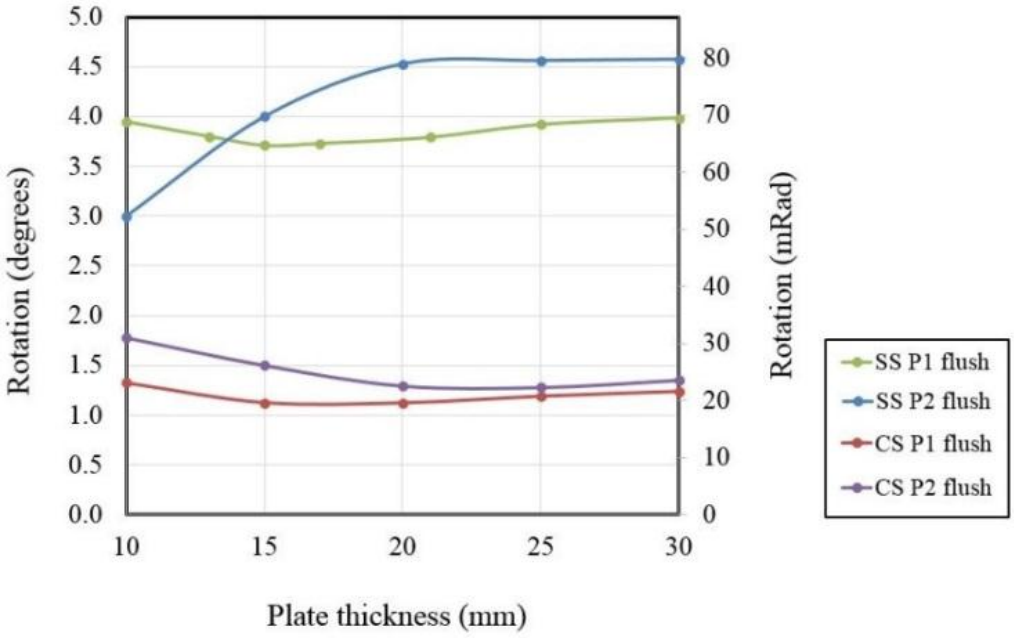

Figure 6.10: Rotation versus plate thickness for flush end-plate connection models

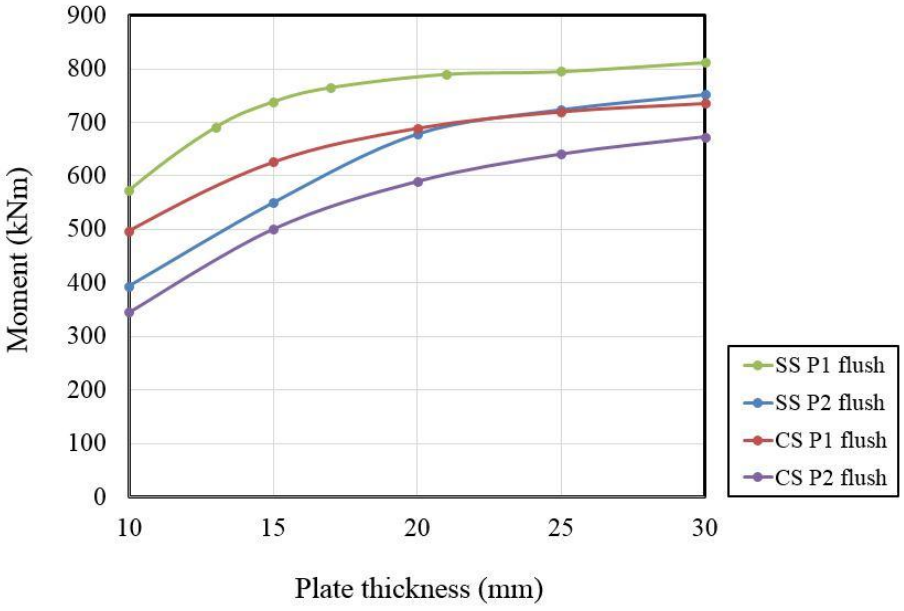

Figure 6.11: Moment versus plate thickness for flush end-plate connection models

6.5 Conclusions

In this chapter numerical models of industry standard moment connections were presented, which may be of greater interest for the practicing structural engineer. End-plate thickness was varied from 10mm to 30mm in a parametric study that can inform the engineering community on the variation of ultimate moment and rotation capacity with plate thickness.

Firstly, this chapter demonstrates that the plate thickness has a significant influence on the moment capacity of the connection. The moment capacity can decrease by up to 30% when the thickness of the end plate is decreased from 25mm to 10mm. The moment capacity always decreases with decreasing plate thickness, no matter the bolt types or the position of the bolts.

Secondly, it was shown that plate thickness has a greater effect on the rotation capacity when the bolts are placed in a position that allows the plate to deform more (P2) in case of connection failure. There was not always a direct or clear relationship between plate thickness and rotation capacity. The rotation capacity may increase with thinner plates if the bolts are carbon steel, or it may decrease with thinner plates if the bolts are stainless steel. One possible reason why there is not a clear trend is because bolt bending and bolt-plate interaction may influence the location where fracture is initiated in the bolt.

Finally, no matter the plate thickness or the bolt position in the plate, connections with stainless steel bolts have a rotation capacity which is usually at least three times higher than connections with carbon steel bolts. This puts an end to the possibility of speculation by the engineering community when the choice of bolt type is weighed against other possible measures to improve capacity such as plate thickness or bolt position.

A simple straightforward solution in the opinion of the author is for the engineer to choose a plate thickness of 25mm which corresponds to the thickness of standard connections provided in the BCSA Green Book and to use stainless steel bolts if an increase in capacity and energy absorption is required.

Chapter 7: Discussion

In an extreme event that would result in high rate loading of a structure it is most likely that failure occurs in the connections first because the strength or moment resistance of the connection is generally lower than that of the connecting members.

For this reason these connections are called partial strength connections and are usually bolted, i.e. plates of members are bolted together. Fully welded connections represent a realistic alternative to providing bolted connections in a building. However, fully welding a connection requires the presence of specialist welding labour on site, welding equipment and takes longer than bolting the connection. Furthermore, their brittleness is likely comparable to that of connections with carbon steel bolts. For this reason, bolted connections are the most common connections. They are preferred by the construction industry, particularly by steelwork contractors, because of the ease of erection and assembly of the frame.

Catenary action supposedly occurs in double joints where two beams are connected to a damaged column. If the column is damaged at lower levels it should theoretically be supported by the tensile action in the beams provided the connections are ductile enough. The importance of providing adequate tying was known to World War 2 investigators.

Previous research showed that common connection types can resist the tying forces as specified by the codes at that time although plastic deformation was required. The tie force regulation did not, however, stipulate rotation requirements and it was subsequently demonstrated that the industry standard connections used in most UK steel framed buildings lack the rotation capacity to support columns through catenary action. Despite this shortcoming the tie force method remains popular with regulators and has been incorporated into Eurocode 1.

As part of the research carried out by Tyas et al. (2012) an experimental testing rig was developed at the Civil Engineering Department of University of Sheffield (CEDUS) laboratory in Buxton (see Figure 2.19 in Chapter 2). The same rig was modified to carry out the experimental tests presented in this work. New items had to be designed for the rig only for the purpose of these experimental tests. The new items were: the beam stub with the connection to be tested; an extension piece; two angle supports that are bolted to a base beam and hold the beam stub to be tested.

Apart from the above, the only other major modification to the rig was removal of the other loading ram, since the rig can function with two loading rams at the same time. Only one loading ram was used because the load had to be applied at a distance from the connection, creating the lever arm needed to give a moment large enough to break the connection. The load cell, the laser displacement gauges (LDGs) and the data capturing system were all provided by the laboratory at Buxton.

The target moment was achieved by setting a lever arm of approximately 1.1 meters. This lever arm multiplied by an estimate load of approximately 121kN, which would be obtained with a relatively thick diaphragm, would give a moment of approximately 133kN. This moment was large enough to make all connections fail.

When load is applied to the "flying column", the column, connection and beam stub all move together as a rigid body. This rigid body has a tendency to rotate about a point which is called here the instantaneous centre of rotation (ICR). Initially, rotation takes place around the centre of mass of the rigid body which is close to the centre of the connection, approximately half way between the top and bottom flange. So the ICR is in the position of the centre of mass of the rigid body. When the connection fails, however, the bodies separate and the ICR moves from the centre of mass to the bottom flange. The ICR is important because its movement changes the value of the lever arm in the test, albeit by a small amount of up to 150mm. This has a direct effect on the difference between the experimental and numerical values presented previously.

Video recordings of the tests and the experimental data showed there was vibration and movement in the angle supports that hold the beam stub. This lead to further discrepancies between experimental data and the connection models data and makes the experimental data difficult to process. A more robust support would be desirable if such tests are carried in the future. Some ways of making the angle supports more robust may be:

- Making the angles larger and heavier;
- Bolting the angles to the base beam with Tension Control Bolts (TCB) bolts should provide a stronger friction grip between the bolts and plates of the angles and base beam;

Evidence of column out of plane movement and flange buckling was also found from the experimental data and video recordings. This resulted in an asymmetrical failure of the connection thus leading to a lower moment capacity than predicted.

When a connection is designed, the engineer has to assume a certain distribution for bolt forces depending on whether the plate is predicted to deform plastically or not. BCSA publications make it clear that a certain distribution has to be assumed by the design engineer. The Eurocode, however, is unclear if such a distribution should be assumed and does not give any indication of its form. As was observed in the experimental tests, the connection may deform with flange buckling and fail in an asymmetrical way. In the dynamic case bolts deform less plastically so it is less likely that forces are plastically redistributed. Both these scenarios could lead to a more unfavourable distribution and result in the reduction of the capacity of the connection. The aforementioned publications do not give any method for the treatment of these scenarios.

Advanced material models were developed by Johnson and Cook, in the period 1983-1985, and more recently by Rusinek and Klepaczko, in 2015. These material models describe the relationship between stress, strain, strain rate and fracture strain for different steels. As part of their core capabilities, most finite element analysis programs are now able to include the option to define this material behaviour and to allow for nonlinear material and geometric effects in the 3D elements of the model.

Others describe in their work the use of finite element analysis in combination with the aforementioned material models in order to study the behaviour of connections at different loading rates. Their work gives a picture of some of the current capabilities of two common commercial finite element packages, namely LS-DYNA and ABAQUS.

In this work, ABAQUS was used to perform the finite element analysis. The analysis capabilities of ABAQUS are thorough and comprehensive. The full capabilities are provided in the Abaqus Analysis User's Guide (Simulia 2015b) which comes with the program in electronic form. The complete Abaqus Guide is contained in several large volumes.

One serious issue is defining the material model in the finite element package. The software packages do not usually have the material data points pre-defined, i.e. tables of strain, stress and strain rate. The user has to manually input the data points that were determined experimentally for the plastic behaviour. Also, the parameters of the material models cannot be determined without the same experimentally determined data points. For many materials, papers have been published with data points, material models and their parameters. However, they are very rarely the exact same type of material in terms of strength, structure or chemical composition. So data from other papers is not easily transferable and applicable to the materials tested in this research.

Material tests were carried out on bolts and steel coupons in order to obtain the data points required by ABAQUS for material definition. These data points were used to model the bolts statically and dynamically with 3D brick elements. Another serious modelling issue is that for one single bolt, the dynamic analysis time is much longer (32 minutes) compared to the static analysis time (46 seconds). Some literature suggests that modifying the value of the material density significantly reduces the computational time. Although this is true it also affects the inertia effects in the damage region therefore changing the relationship between stress, fracture strain and damage. This can occasionally lead to a bolt that does not fracture, but deforms plastically indefinitely and would require an altered damage definition. Since this complicates the modelling and data processing immensely especially at the connection modelling level the idea of factored density was abandoned completely and removed from this work altogether.

Bolts can be modelled with 3D brick elements but they can also be modelled with single 2D connector elements. Modelling with connector elements will result in computational time saving. For example, in the case of the flush end-plate connection models, the number of bolt elements represented 35% of the total number of brick elements in the whole connection model. When bolt elements were replaced with 2D connector elements, the computational time was reduced by 35%. See page 117 for details.

In the case of extended end plate connections the bolts in the top row come in contact with the plate at the edge of the hole. The 3D model has a contact definition applied to elements known as “hard contact”. This means that when gaps close a pressure develops between elements and they do not go through each other. If contact is not defined properly elements may overlap with no pressure between them and errors may occur or the results may exclude the effect of the contact. When the bolt interacts with the plate it leads to some bolt bending and shear potentially causing the bolt to fail at a lower strain than if it were in pure tension.

It is important to note that when connectors are used, no “hard contact” occurs between the single spring connector element and the surrounding wall even if the plate deforms significantly. The connector may even overlap with 3D elements without errors occurring. This will lead to a less realistic model which may result in the prediction of rotations larger than predicted by the full 3D model. In this work the bolts were mainly in tension and very little shear. More complex loading scenarios can be considered, where the bolts had been subjected to tension, bending and shear. However, modelling the bolts with connectors that take into account all these behaviours may be more challenging.

Chapter 8: Conclusions and future recommendations

8.1 Introduction

This chapter presents the general conclusions of this research project, a summary of findings and future work that could be carried out in order to further advance knowledge in this field.

8.2 General conclusions

Field investigations into recent structural collapses caused by terrorist attacks showed that buildings are particularly vulnerable to progressive or disproportionate collapse.

What investigators found was that in the event of a high-explosive blast or airplane impact failure occurred initially in the connections of structural members resulting in loss of carrying capacity of some of these members. This failure propagated and eventually caused partial or total collapse of the structures. These events usually led to loading and failure of the connections in time periods of less than 100 milliseconds.

A review of recent literature indicated that there was an intensification of research papers in this field in the past decade. The primary tools in this research area are computational modelling and simulation since there is significant risk, cost and effort associated with high-quality experimental testing. For this reason particular attention was given to research papers that also contained experimental testing of bolts or threaded assemblies, connections, beam-column assemblies or column removal scenarios. Most importantly, the focus was on literature that also presented high-rate testing, with strain rates in the region of 1/s to 100/s, in addition to the usual low-rate tests, with strain rates in the region of 0.001/s. Although the literature showed that stainless steel bolts deform more plastically, no attempts were made to study the effect these bolts had on the behaviour and ductility of the connection.

In this research high and low rate tests were carried out on two types of bolts. Carbon steel bolts of grade 8.8 were shown to fail through nut thread stripping when one nut was used no matter the loading rate. When two nuts were used the bolts failed through fracture of the threaded region which was consistent to findings from literature. Stainless steel bolts of grade A4-70 consistently failed through ductile body necking and fracture. These deformed plastically three to four times the amount that carbon steel bolts deformed and absorbed more strain energy. Both types of bolts showed a dynamic increase in strength and a reduction in

fracture strain when tested at high strain rates, which is consistent with findings reported in the literature.

High and low rate tests were also carried out on end-plate moment connections. Both in the dynamic case and in the static case, connections with stainless steel bolts were found to rotate before failure at least threefold the amount that the connections with carbon steel bolts rotated. They also absorbed three to four times more strain energy. Stainless steel is a type of steel that shows the transformation induced plasticity (TRIP) effect. Some of the austenite in its structure changes to martensite consequently showing an increase in yield stress and plastic strain. No matter the loading rates, the reason why connections with stainless steel bolts perform better lies in the superior properties of stainless steel.

8.3 Summary of findings

The following conclusions were drawn as a result of this work; these conclusions should always apply no matter the size or scale of the bolts and connections considered:

- Stainless steel bolts deform plastically about three to four times as much as the total deformation in carbon steel bolts, absorbing more energy in the process no matter the loading rates. (see Figures 3.10 to 3.12 in Chapter 3)
- When bolts or steel coupons are tested individually there is a dynamic increase in yield and ultimate strength with high strain rates and a decrease in fracture strain. (see Figures 3.13 to 3.15 in Chapter 3)
- Depending on connection type and testing circumstances, the dynamic increase in strength at individual component level does not always translate into increased connection strength when tested under high loading rates. (see tests T4 and T7 in Figure 3.30 in Chapter 3)
- No matter the loading rates, connections with stainless bolts have at least triple the rotation capacity and energy absorption of connections which use carbon steel bolts. (see Table 3.5 in Chapter 3)
- Both the low rate and high rate behaviour of the connections can be modelled numerically in FE with good or reasonable accuracy with solvers using implicit and explicit methods respectively. (see Figures 5.8, 5.11, 5.16 in Chapter 5)
- When connectors are used in the FE models, the computational time can be reduced by an amount approximately equal to the percentage that the number of elements in the bolt body represents out of the total number of elements in the full model. (see Section 5.3 in Chapter 5)

- The practical way of implementing the component-based method found in this work was through the use of connectors. (see Section 5.3 in Chapter 5)
- There is a decrease in moment capacity with decreasing end-plate thickness. (see Figures 6.8 and 6.11 in Chapter 6)
- The end-plate thickness has an effect on the ultimate rotation capacity, but it is usually of minor significance compared to the effect that the type of bolts produces. (see Figures 6.7 and 6.11 in Chapter 6)
- The end-plate thickness combined with a change in bolt position has a greater influence on rotation capacity. (see Figures 6.7 and 6.11 in Chapter 6)
- In the case of full scale connections, the rotation capacity of connections with carbon steel bolts is generally between 1 and 2 degrees and that of connections with stainless steel bolts is generally between 3 and 4 degrees. (see Figures 6.7 and 6.11 in Chapter 6)

8.4 Future work

Advanced material testing methods and material models are available that allow the characterization of material behaviour under a high range of strain rates and temperatures. However, this type of testing is expensive and the calibration of the material constants requires significant time and experience. In existing literature material constants characterizing the plastic behaviour of grade A2 (AISI 304) steel can be found. However, these properties vary with nickel content and material constants characterizing the plastic behaviour of grade A4 are not available in the literature to the author's knowledge. It is therefore recommended that an advanced material characterization is carried out for grade A4 steels. These steels are important since they have higher proof and ultimate stresses than A2 steels.

Material constants in simple mathematical models characterizing the damage and fracture behaviour obtained through specialized testing techniques are not available in the literature. Most literature in the area of calibrating damage and fracture models is found for different materials and usually involves complex material models. These could not be transferred to the study of stainless and carbon steels studied in this work in a straightforward manner. A specialist characterization of damage and fracture properties of carbon steel and stainless steel is therefore recommended. This kind of material study is difficult, since these properties may vary significantly with strain rates and temperature and even advanced tests cannot always provide numerical values for a very wide range of strain rates.

As the connections failed, the "flying column" rotated about an instantaneous centre of rotation. In the process both the angles and the "flying column" moved significantly. In particular, the movement of the supporting angles caused the centre of rotation to change location. This had implication on the true values of the lever arm of the moment, the velocity and acceleration of the column and the estimates of inertia effects from experimental data. This movement leads to an influence in the experimental data that cannot be accounted for in the model. The model assumes the supporting angles as rigid. There is no way to modify data from the modelling or from the tests so as to "correct" completely the effect of the changing centre of rotation. This is the main reason for differences between the test and the predicted results especially in the case of the dynamic tests. Another issue was that boundary conditions in the test were slightly asymmetrical, so that bolts at the top row didn't really fail at exactly the same time. The numerical model is perfectly symmetrical at least as long as symmetry is assumed.

The quality of the tests is of paramount importance if more meaningful data is to be obtained and models should resemble the testing conditions as closely as possible. If future testing work is carried out, it is a recommendation of the author that at least one part of the failing connection or component is to be fixed so as to prevent any kind movement. In addition, efforts should be made to ensure the components deform symmetrically as far as it is practically possible. This should allow better agreement between predicted and experimental results.

It is obvious that an improvement of ductility and strength of the connections through the use of stainless steel bolts would lead to a more ductile and stronger frame. For example, if a column removal scenario were considered then the column moving downwards would displace at least three times as much before complete loss of load carrying capacity if stainless steel bolts were used. Both the strength and ductility would be higher. However, if a plane impact scenario is considered then it is not easy to establish the extent of damage caused to a steel frame without carrying out an analysis of a large scale model.

As an example, the WTC Impact Analysis could be reconsidered where some key changes are made to the model. Connections could be redesigned, so they have a moment capacity above 90% of the connecting member capacity as opposed to a mere 20% or 30% and the bolt material model is replaced with a stainless steel grade model. The extent of the damage to the columns in the inner core should be recalculated under these conditions to investigate if significant damage reduction would be possible.

Appendices

Appendix A

A.1 The Building Regulations 2000 – Approved Document A: 2004 Edition

The 2004 edition of Approved Document A was initially published by The Stationery Office (ISBN 0-11-753909-0). It was republished later in 2004 with amendments by NBS (ISBN 1-859462-00-6). The former is marked '2004 edition' in a green flash on the front cover; the latter, which is the still-current edition and discussed in section 2.3.5, is marked '2004 edition incorporating 2004 amendments'. There are key differences between the two versions, which are noted in the following discussion.

With the publication of Approved Document A: 2004, some key changes were introduced from earlier editions, notably:

- the extension of the robustness requirements to all buildings, except single-occupancy houses not exceeding four storeys, agricultural buildings and buildings into which people rarely go whose collapse would not impact on other occupied buildings or areas where people do go.
- the introduction of building risk classes, briefly:

  Class 1 buildings: typically single-occupancy houses not exceeding four storeys, agricultural and unoccupied buildings

  Class 2A buildings: buildings typically with four or fewer storeys, industrial and retailing premises with three or fewer storeys, five-storey single-occupancy houses, single-storey schools and educational buildings

  Class 2B buildings: buildings typically with between five and fifteen storeys, schools and educational buildings exceeding one storey, hospitals with fewer than three storeys, car parks with fewer than six storeys, and buildings with floor areas exceeding 2000m² per storey, and

  Class 3 buildings: all buildings exceeding 15 storeys, with floor areas exceeding 5000m² per storey, grandstands accommodating more than 5000 spectators and buildings containing hazardous substances and/or processes.

- the requirement for the provision of effective horizontal ties for Class 2A buildings: such buildings were previously exempt from any requirements for robustness
- the exclusion of basements from the definition of the number of storeys of the building, provided the basement construction fulfils the robustness requirements for Class 2B buildings (broadly buildings of five or more storeys); and
- the introduction of a requirement for buildings above 15 storeys to be designed through a systematic risk assessment, which was required to take into account all the normal hazards that may reasonably be foreseen, together with any abnormal hazards.

The building classes are described in full in Table 11 of Approved Document A, reproduced below as Table A.1. The building classes, together with the requirements for robustness, imply the Government's assessment of the tolerable risk of structural collapse.

Table A.1. Approved Document A Table 11: Building classes

Table 11 Building Classes

Class	Building Type and Occupancy
1	Houses not exceeding 4 storeys.
	Agricultural buildings
	Buildings into which people rarely go, provided no part of the building is closer to another building, or area where people do go, than a distance of 1.5 times the building height
2A	5 storey single occupancy houses
	Hotels not exceeding 4 storeys
	Flats, apartments and other residential buildings not exceeding 4 storeys
	Offices not exceeding 4 storeys
	Industrial buildings not exceeding 3 storeys
	Retailing premises not exceeding 3 storeys of less than 2000m² floor area in each storey
	Single storey educational buildings
	All buildings not exceeding 2 storeys to which members of the public are admitted and which contain floor areas not exceeding 2000m² at each storey
2B	Hotels, flats, apartments and other residential buildings greater than 4 storeys but not exceeding 15 storeys
	Educational buildings greater than 1 storey but not exceeding 15 storeys
	Retailing premises greater than 3 storeys but not exceeding 15 storeys
	Hospitals not exceeding 3 storeys
	Offices greater than 4 storeys but not exceeding 15 storeys
	All buildings to which members of the public are admitted which contain floor areas exceeding 2000m² but less than 5000m² at each storey
	Car parking not exceeding 6 storeys
3	All buildings defined above as Class 2A and 2B that exceed the limits on area and/or number of storeys
	Grandstands accommodating more than 5000 spectators
	Buildings containing hazardous substances and/or processes

NOTE 1: For buildings intended for more than one type of use the Class should be that pertaining to the most onerous type.

NOTE 2: In determining the number of storeys in a building, basement storeys may be excluded provided such basement storeys fulfil the robustness requirements of Class 2B buildings.

The requirements for robustness are stated as follows:

‘5.1. The requirement will be met by adopting the following approach for ensuring the building is sufficiently robust to sustain a limited extent of damage or failure, depending on the class of the building, without collapse:

a) Determine the Building Class from Table 11.
b) For Class 1 buildings – Provided the building has been designed and constructed in accordance with the rules given in this Approved Document, or other guidance referenced under Section 1, for meeting compliance with requirement A1 and A2 in normal use, no additional measures are likely to be necessary.
c) For Class 2A buildings – Provide effective horizontal ties, or effective anchorage of suspended floors to walls, as described in the Codes and Standards listed under paragraph 5.2 for framed and load-bearing wall construction; the latter being defined in paragraph 5.3 below.
d) For Class 2B buildings – Provide effective horizontal ties, as described in the Codes and Standards listed under paragraph 5.2 for framed and load-bearing wall construction; (the latter being defined in paragraph 5.3 below), together with:

   - effective vertical ties, as defined in the Codes and Standards listed under paragraph 5.2, in all supporting columns and walls, or alternatively,

   - check that upon the notional removal of each supporting column and each beam supporting one or more columns, or any nominal length of load-bearing wall (one at a time in each storey of the building) that the building remains stable and that the area of floor at any storey at risk of collapse does not exceed 15% of the floor area of that storey or 70m², whichever is smaller, and does not extend further than the immediate adjacent storeys (see Diagram 25).

   Where the notional removal of such columns and lengths of walls would result in an extent of damage in excess of the above limit, then such elements should be designed as a “key element” as defined in paragraph 5.3 below.

e) For Class 3 buildings – A systematic risk assessment of the building should be undertaken taking into account all the normal hazards that may reasonably be foreseen, together with any abnormal hazards.

   Critical situations for design should be selected that reflect the conditions that can reasonably be foreseen as possible during the life of the building. The structural form

and concept and any protective measures should then be chosen and the detailed design of the structure and its elements undertaken in accordance with the Codes and Standards given in paragraph 5.2.

5.2. Details of the effective horizontal and vertical ties, together with the design approaches for checking the integrity of the building following the notional removal of vertical members and the design of key elements, are available in the following Codes and Standards […].

5.3. Definitions

Nominal length of load-bearing wall

The nominal length of load-bearing wall construction referred to in 5.1d should be taken as follows:

- in the case of a reinforced concrete wall, the distance between lateral supports subject to a maximum length not exceeding 2.25H.

- in the case of an external masonry wall, or timber or steel stud wall, the length measured between vertical lateral supports.

- in the case of an internal masonry wall, or timber or steel stud wall, a length not exceeding 2.25H.

- where H is the storey height in metres.

Key Elements

A "key element", as referred to in paragraph 5.1d, should be capable of sustaining an accidental design loading of 34 kN/m² applied in the horizontal and vertical directions (in one direction at a time) to the member and any attached components (e.g. cladding etc.) having regard to the ultimate strength of such components and their connections. Such accidental design loading should be assumed to act simultaneously with 1/3 of the normal characteristic loading (i.e. wind and imposed loading.

Load-bearing construction

For the purposes of this Guidance the term "load-bearing wall construction" includes masonry cross-wall construction and walls comprising close centred timber or lightweight steel section studs.'

A.2 Comparison of high-rise buildings and aircraft sizes

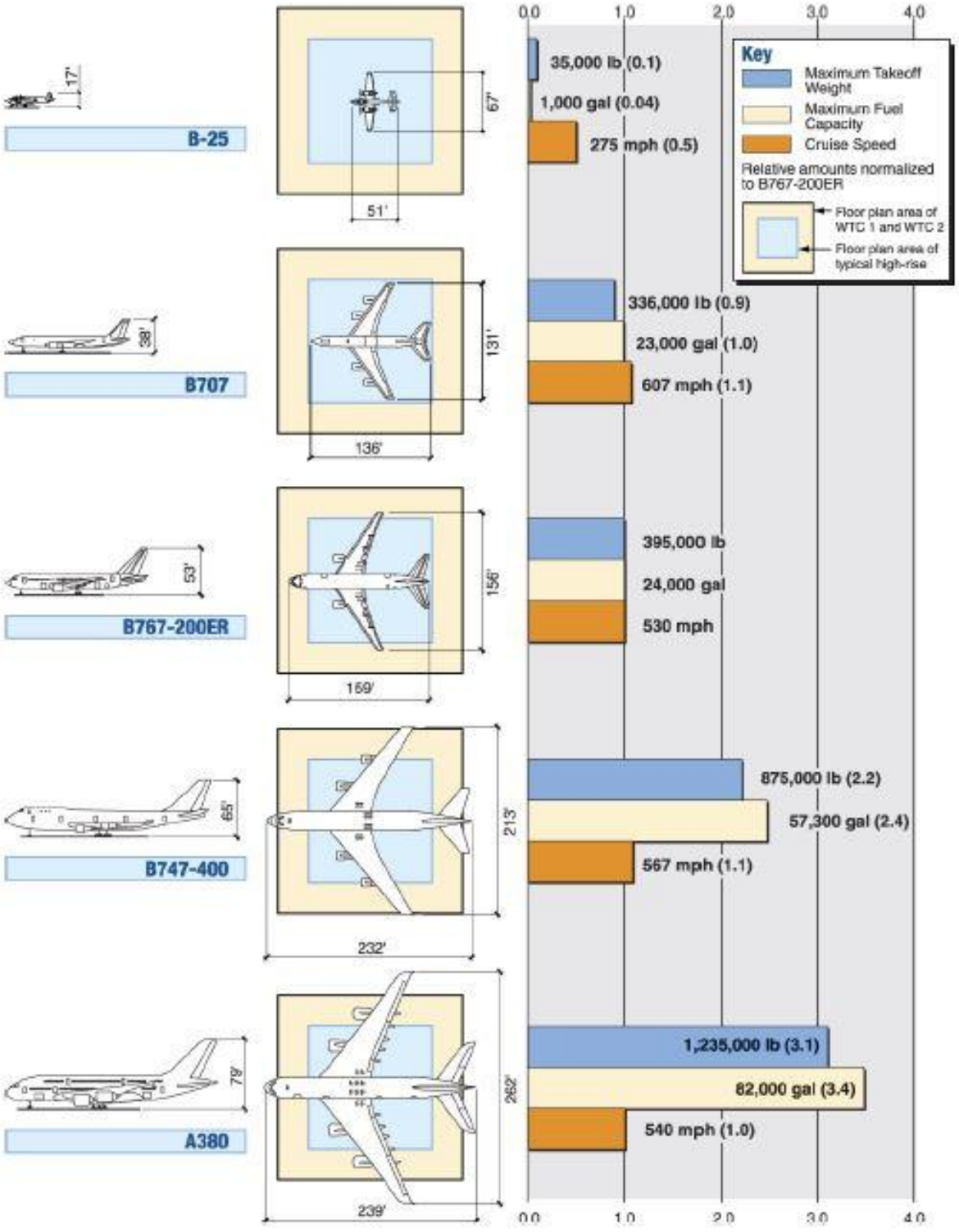

Appendix B

B.1 Arrangement and fabrication drawings for tested connections

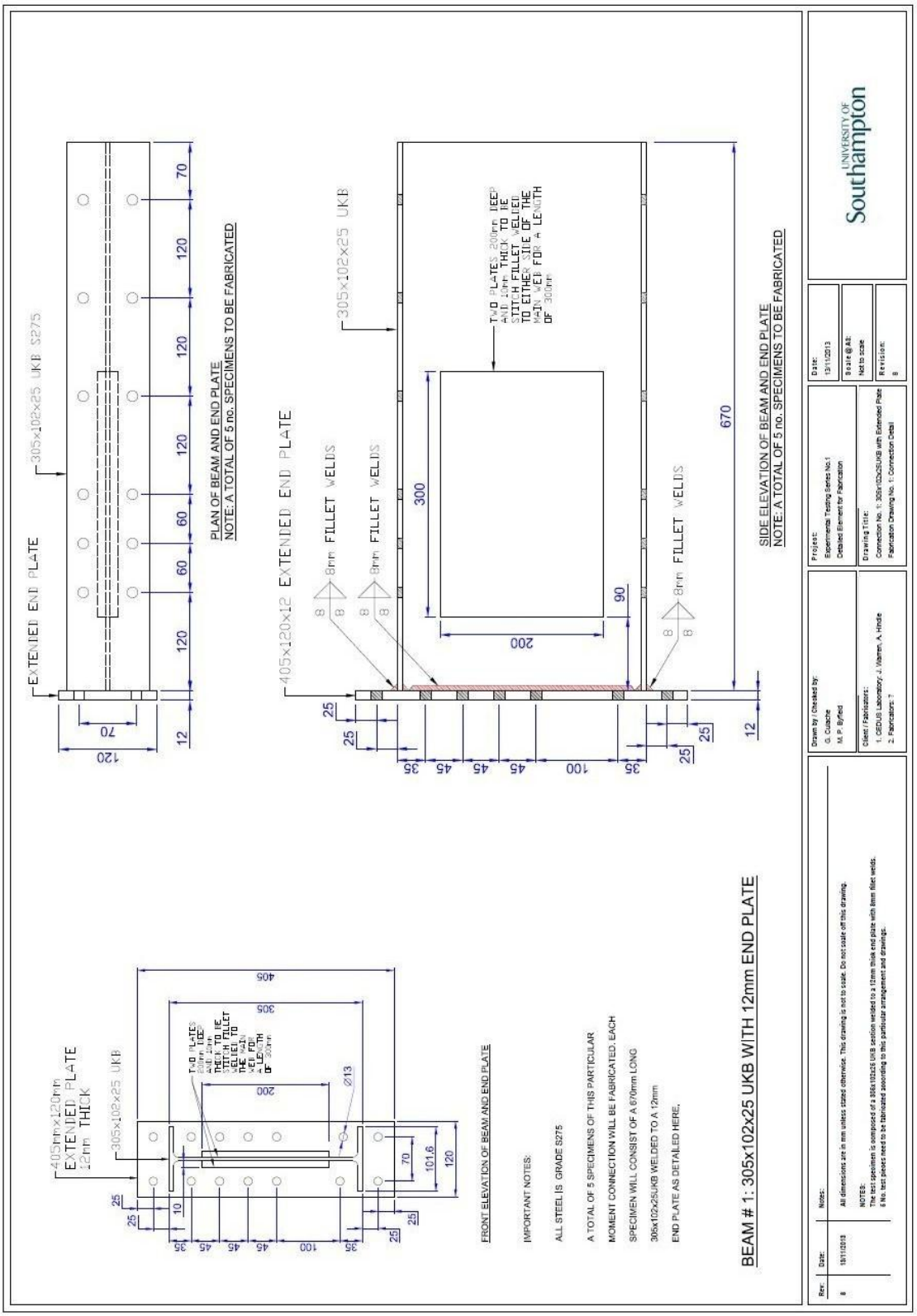

Drawing B 1: Fabrication drawing of extended end plate connection

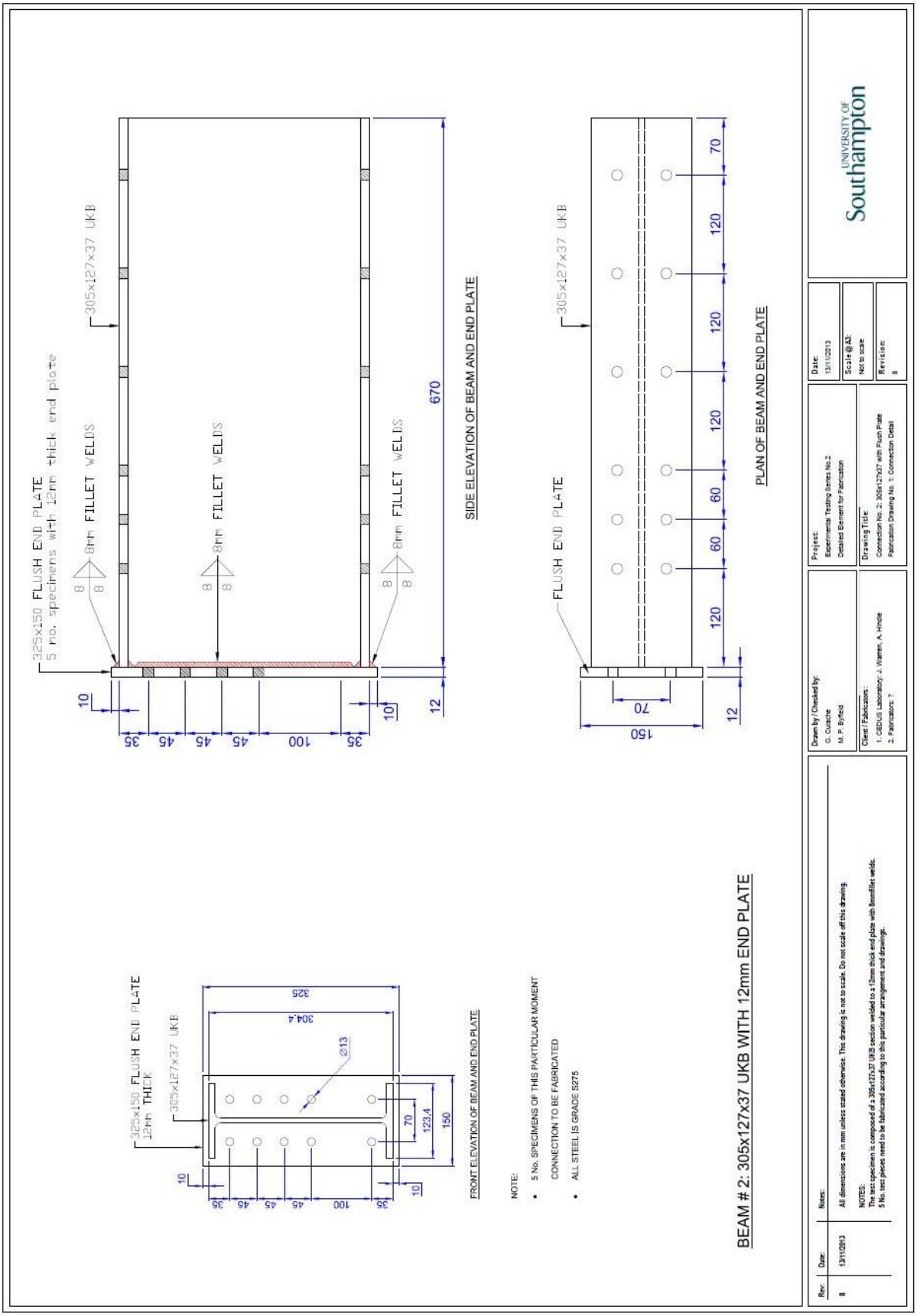

Drawing B 2: Fabrication drawing of flush end plate connection

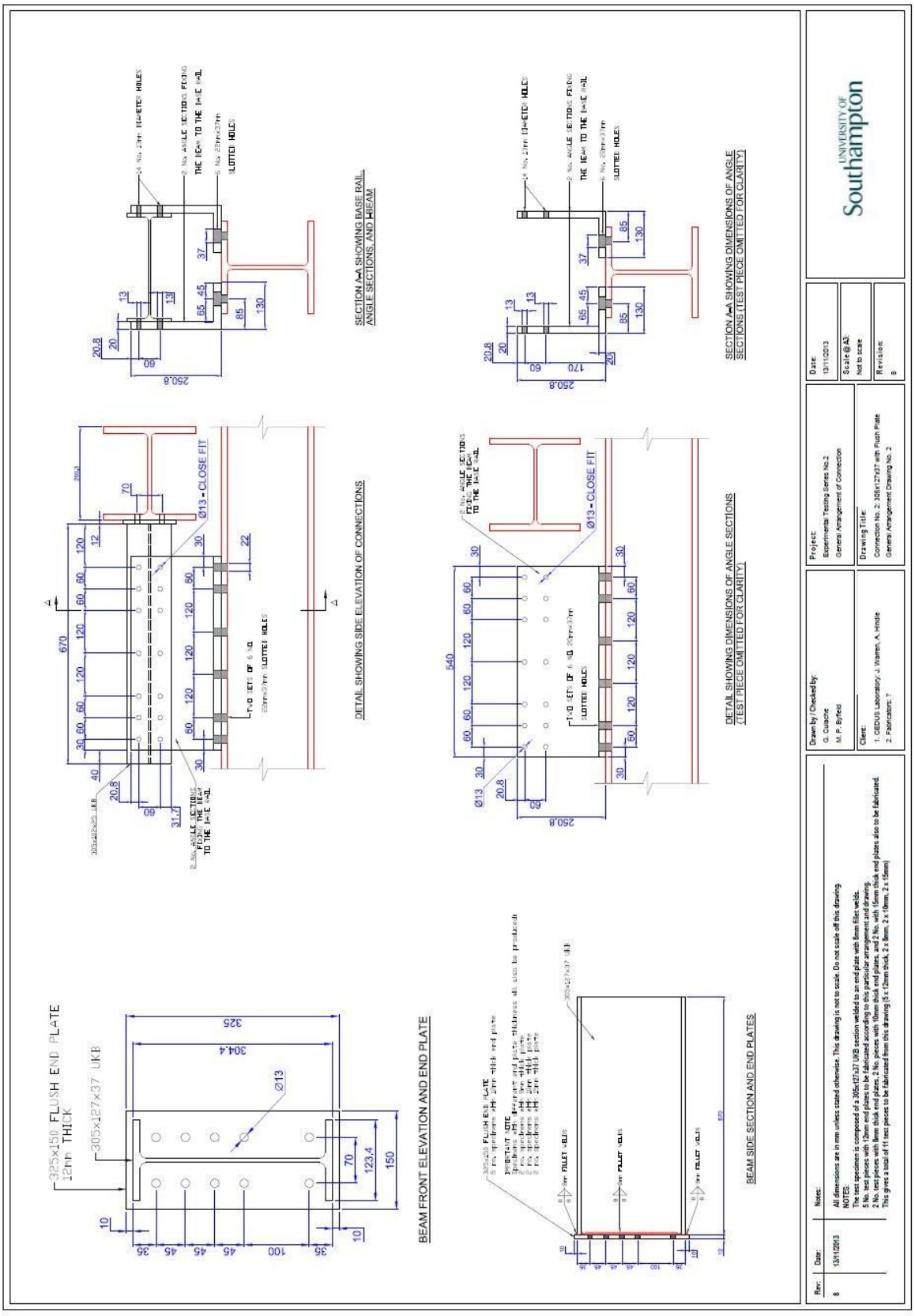

Drawing B 3: Drawing showing angle sections used to support the tested beam stub

B.2 Figures with unprocessed experimental data from connection tests

Please see section 3.2 for the connection descriptions.

B.2.1 Extended end plate connections under static loading

Test 1, Loading no. 5, M12 Black bolts, Grade 8.8

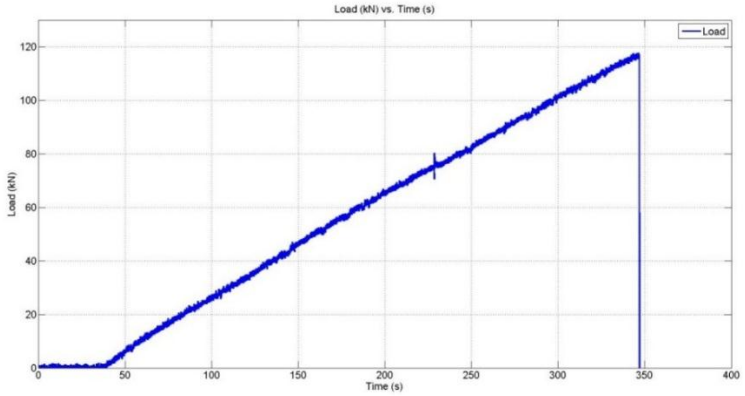

Figure B 1: T1 - Load (kN) vs. time (s)

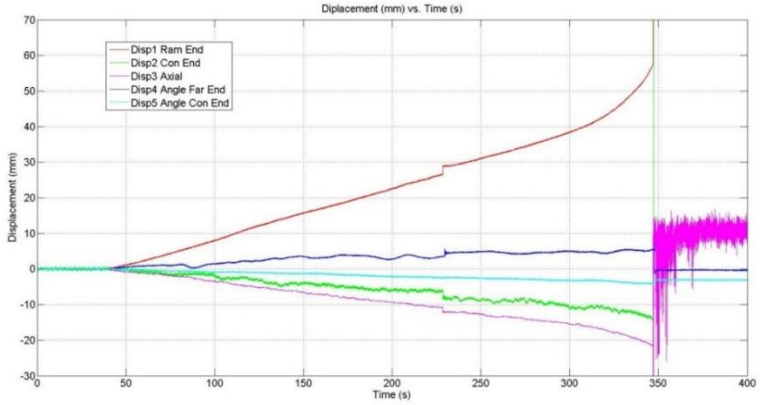

Figure B 2: T1 - Displacement (mm) vs. time (s)

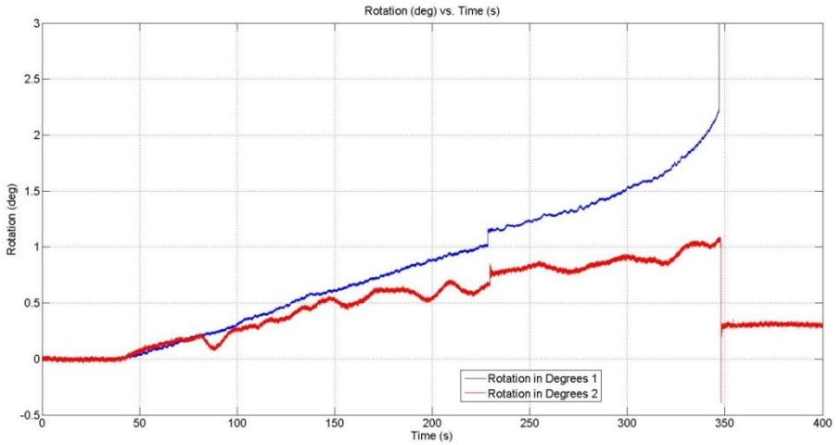

Figure B 3: T1 - Rotation (deg) vs. time (s) of "flying column" (blue) and angle supports (red)

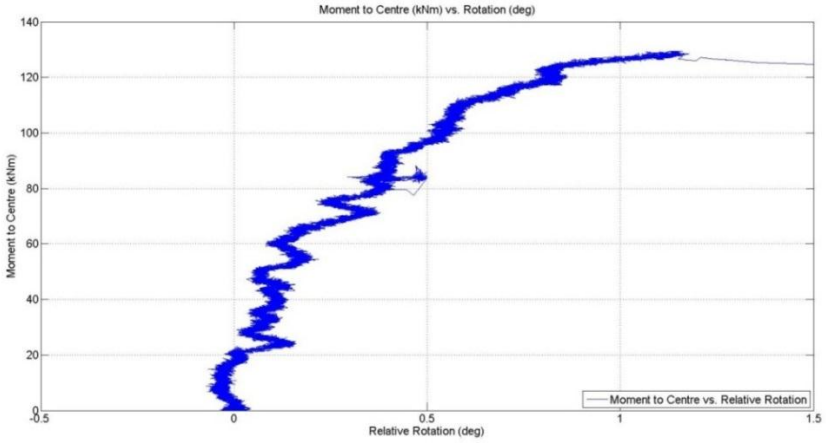

Figure B 4: T1 - Moment to Centre (kNm) vs. Net Rotation (degrees)

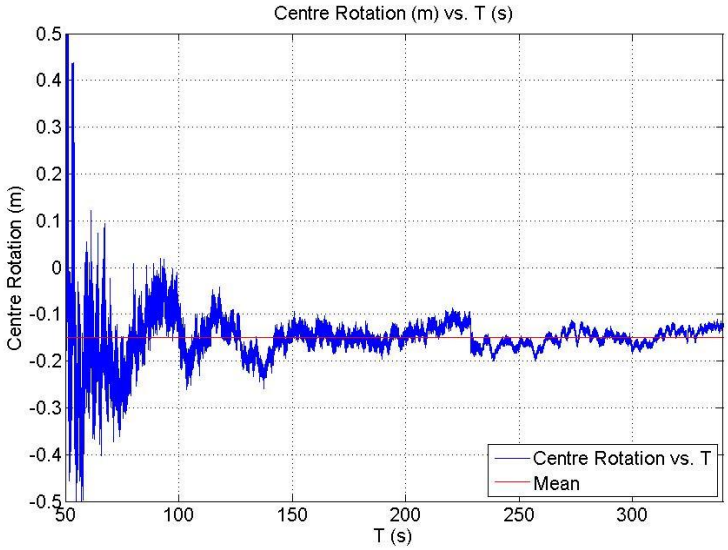

Figure B 5: T1 - Centre of Rotation and its mean of -0.150m from the bottom flange

Test 2, Loading no. 1, M12 Stainless Steel bolts, Grade A4-70

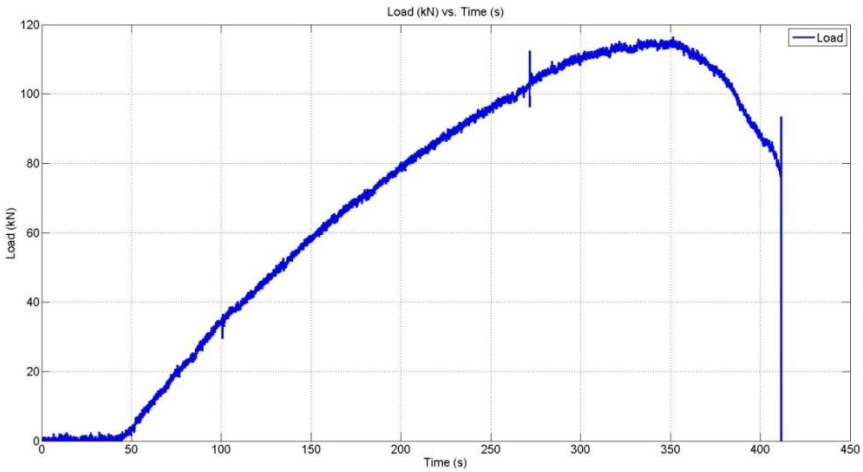

Figure B 6: T2 - Load (kN) vs. time (s)

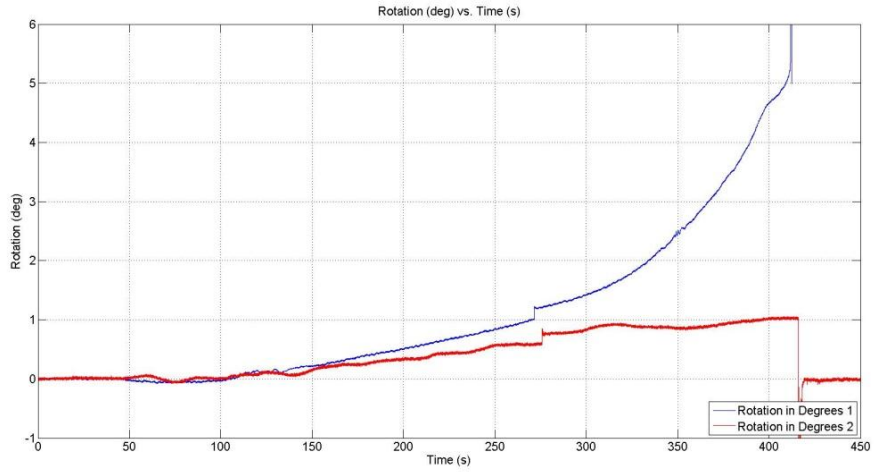

Figure B 7:T2 - Rotation (deg) vs. time (s) of "flying column" (blue) and angle supports (red)

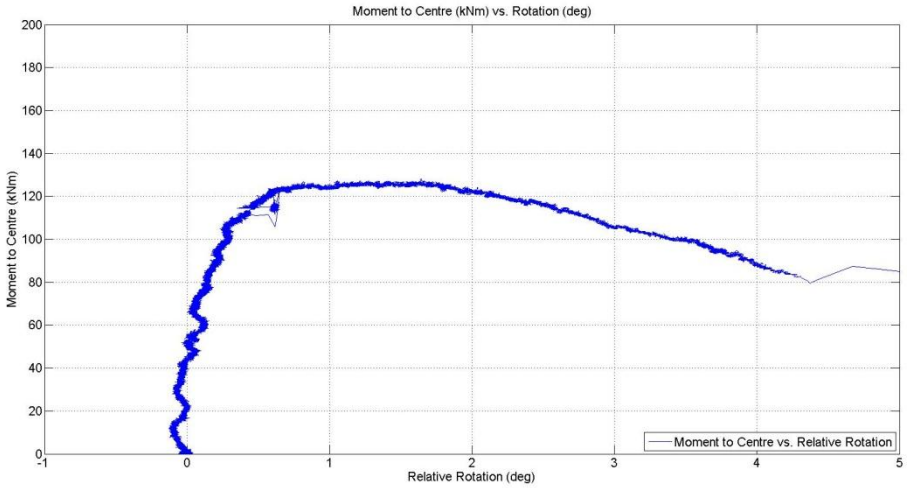

Figure B 8: T2 - Moment to Centre (kNm) vs. Net Rotation (degrees)

Comparison of Test 1 Loading 5 to Test 2 Loading 1

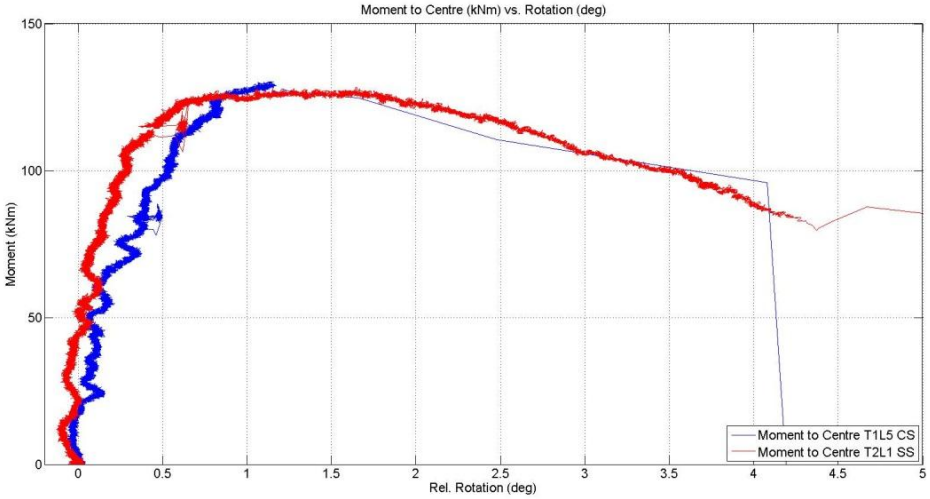

Figure B 9:T1, T2 - Moment to Centre (kNm) vs. Rotation (degrees)

B.2.2 Flush end plate connections under static loading

Test 5, Loading no. 1, M12 Black bolts, Grade 8.8

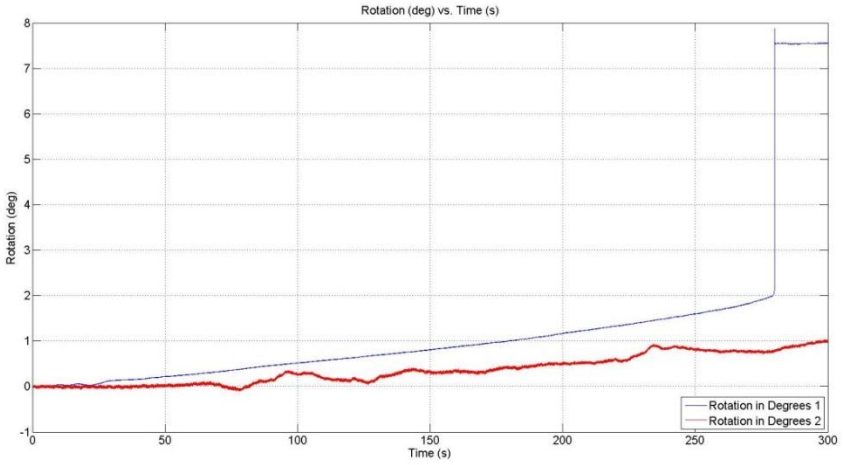

Figure B 10: T5 - Rotation (deg) vs. time (s) of "flying column" (blue) and angle supports (red)

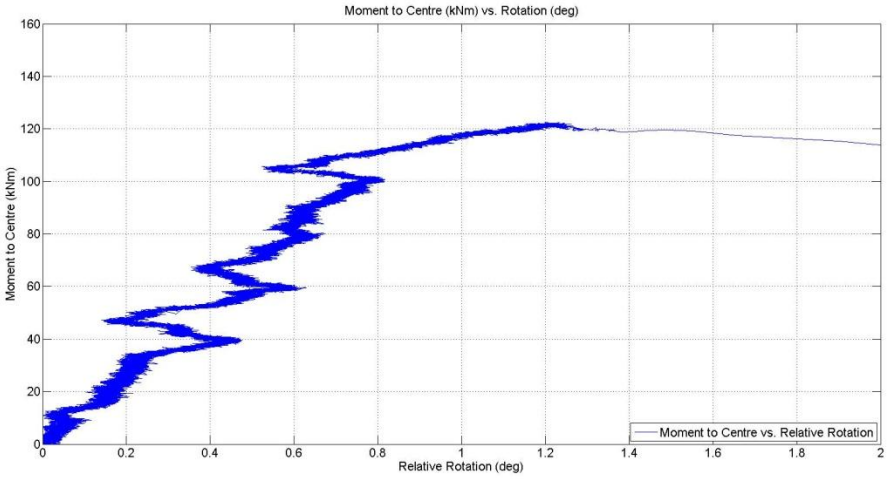

Figure B 11: T5 - Moment to Centre (kNm) vs. Net Rotation (degrees)

Test 6, Loading no. 1, M12 Stainless Steel Bolts, Grade A4-70

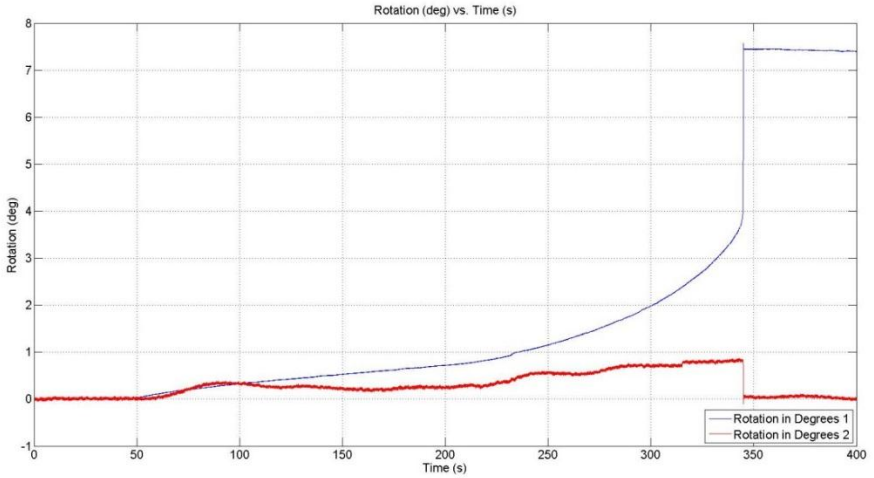

Figure B 12: T6 - Rotation (deg) vs. time (s) of "flying column" (blue) and angle supports (red)

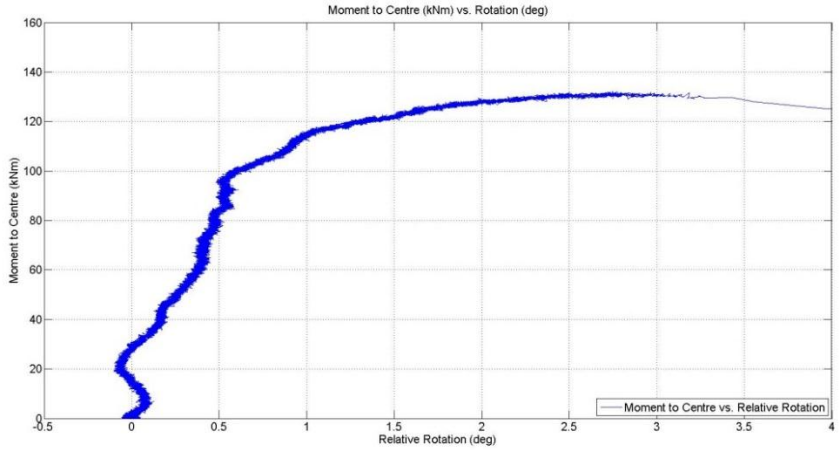

Figure B 13: T6 - Moment to Centre (kNm) vs. Net Rotation (degrees)

Comparison of Test 5 to Test 6; Moment versus Rotation

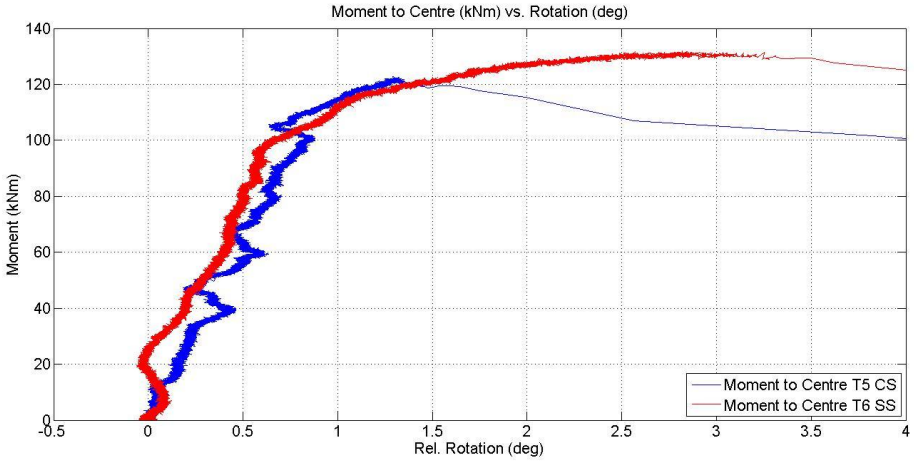

Figure B 14:T5, T6 - Moment to Centre (kNm) vs. Rotation (degrees)

Comparison of T1, T2, T5, T6

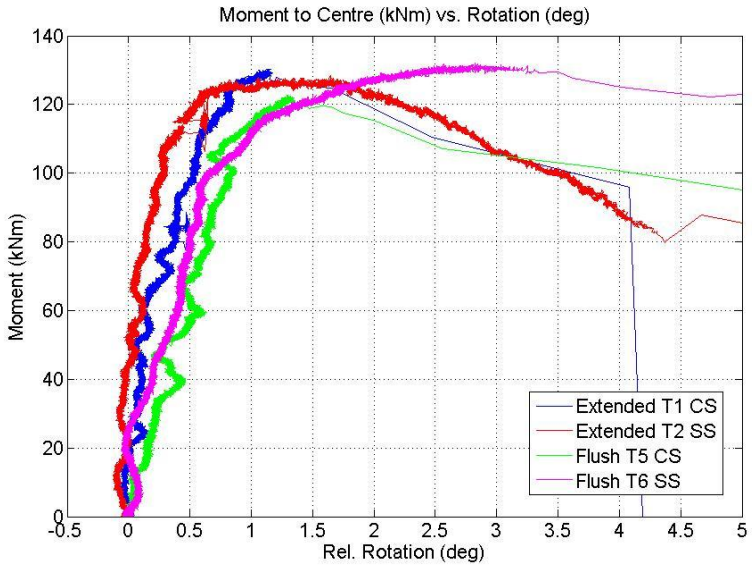

Figure B 15: Moment rotation graphs for tests T1, T2, T5, T6

B.2.3 Extended end plate connections under dynamic loading

Test 4, Loading no. 1, M12 Stainless Steel bolts, Grade A4-70

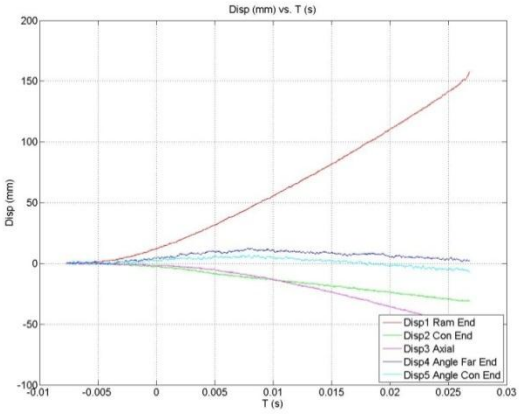

Figure B 16:T4 - Displacement (mm) vs. time (s)

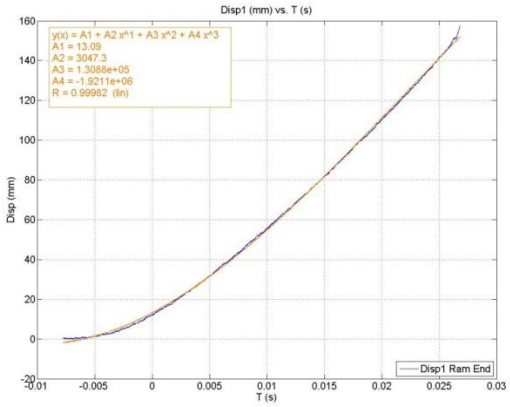

Figure B 17: T4 - Disp1 (mm) vs. time (s)

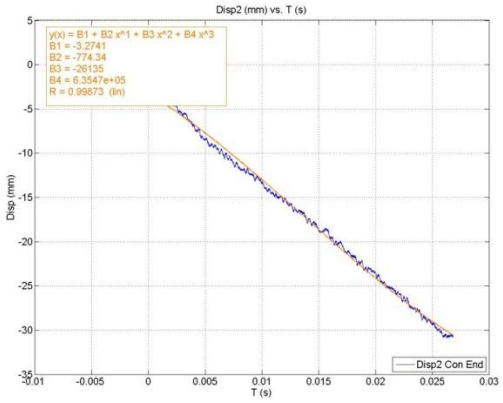

Figure B 18: T4 - Disp2 (mm) vs. time (s)

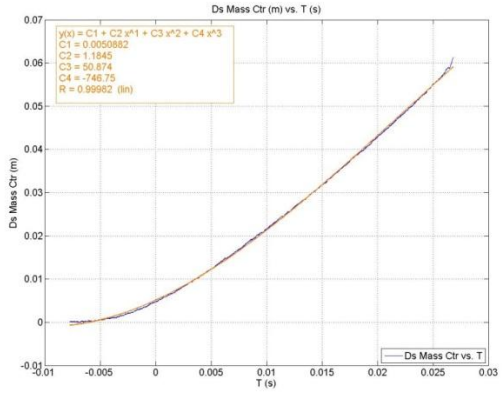

Figure B 19: T4 - Displacement of mass centre (m) vs. time (s)

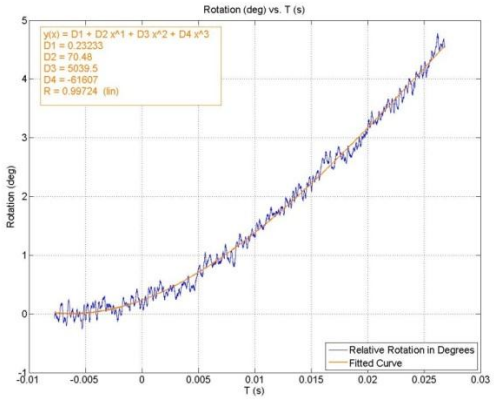

Figure B 20: T4 - Rotation (degrees) vs. time (s)

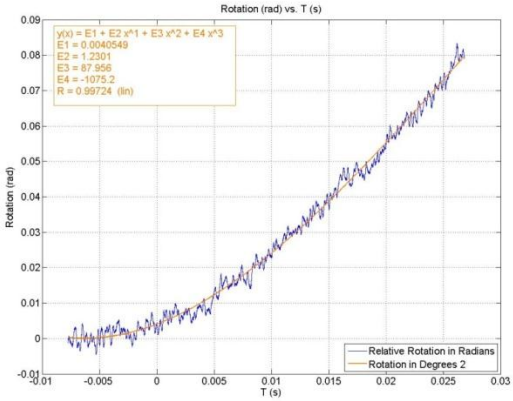

Figure B 21: T4 - Rotation (radians) vs. time (s)

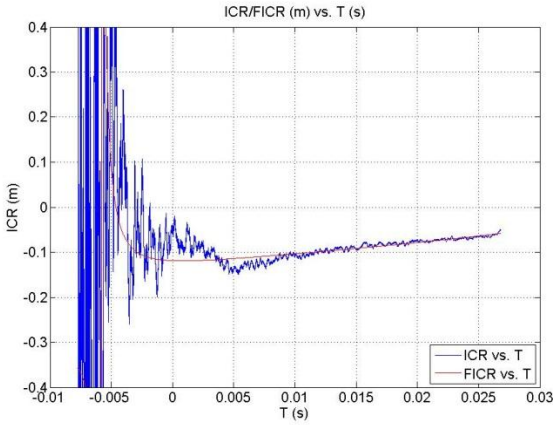

Figure B 22: T4 - Instantaneous centre of rotation (m) vs. time (s)

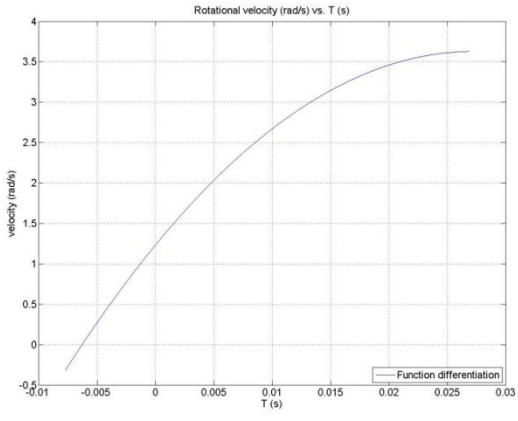

Figure B 23: T4 - Rotational velocity (rad/s) vs. time (s)

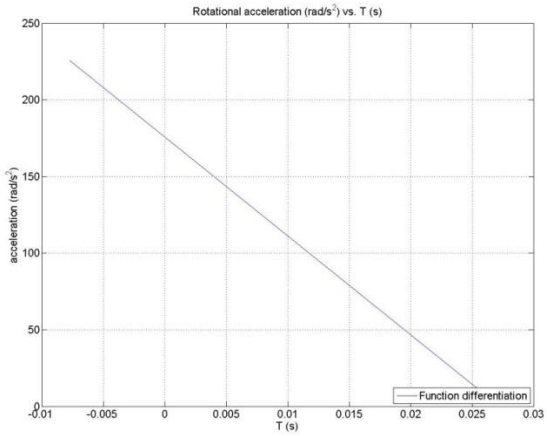

Figure B 24: T4 - Rotational acceleration (rad/s^2) vs. time (s)

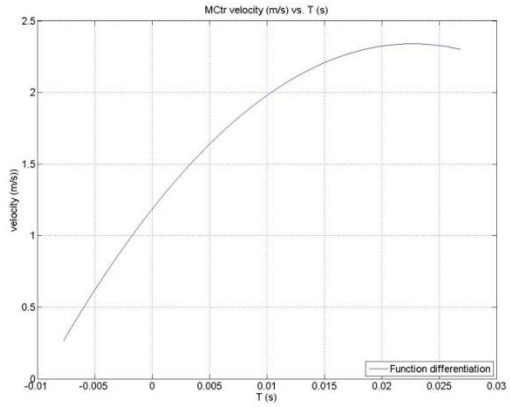

Figure B 25: T4 - Mass centre velocity (m/s) vs. time (s)

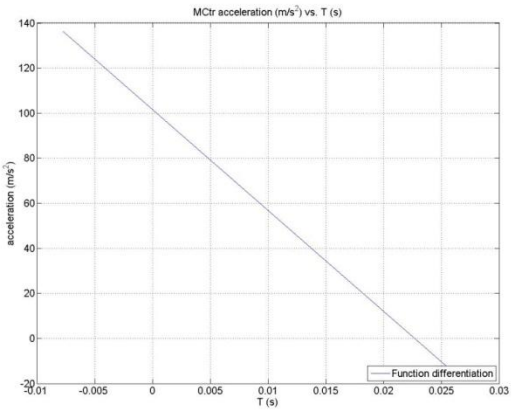

Figure B 26: T4 - Mass centre acceleration (m/s^2) vs. time (s)

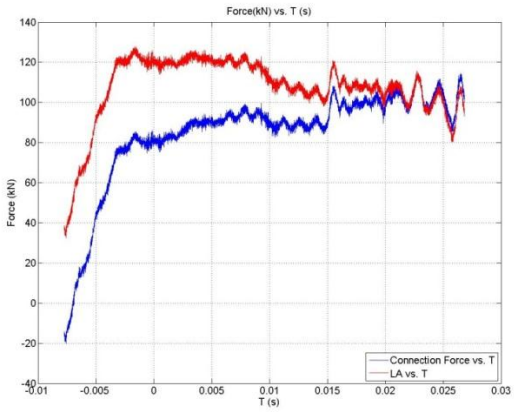

Figure B 27: T4 - Applied load (red) and connection force (blue) vs. time (s)

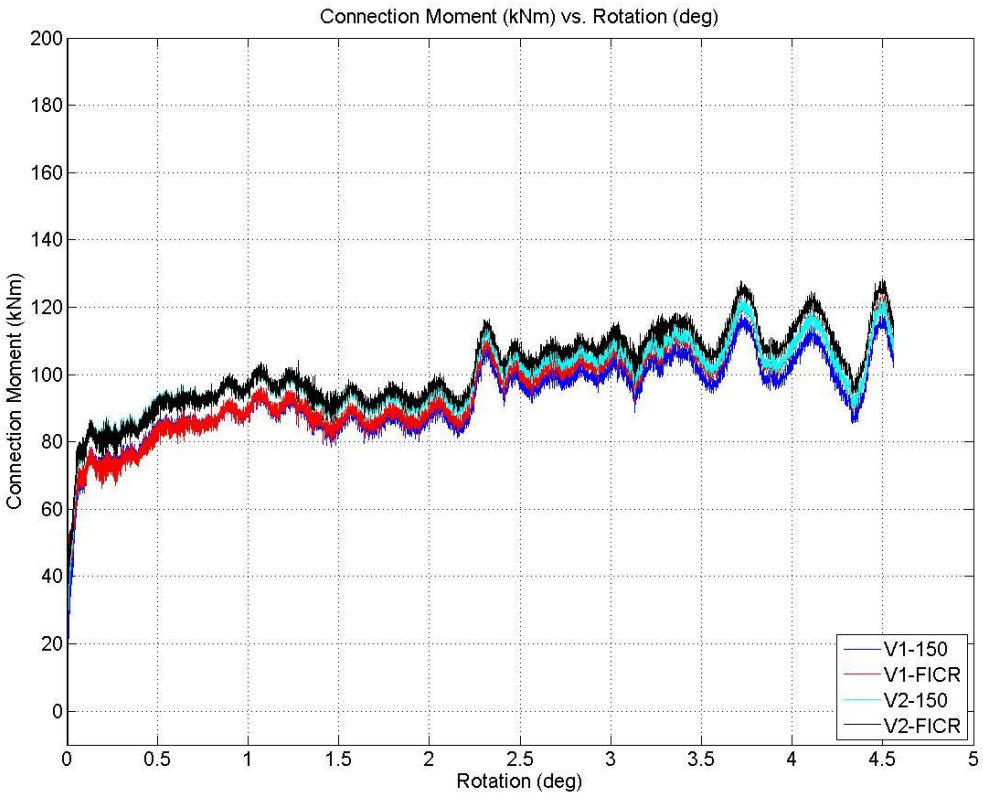

Figure B 28: T4 - Connection moment (kNm) vs. Net rotation (degrees); The four curves represent four versions of the same equation; They give similar values; Only one version of the equation was chosen to be compared with modelling results.

Test 7, Loading no. 1, M12 Black bolts, Grade 8.8

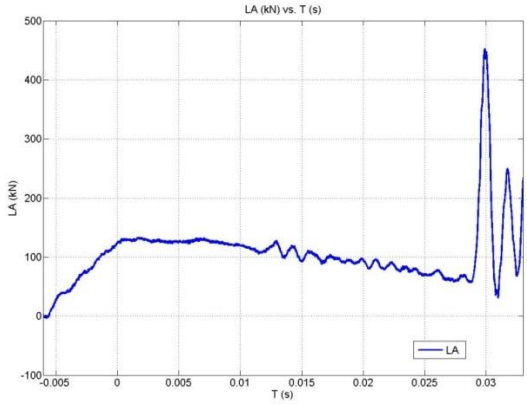

Figure B 29: T7 - Load (kN) vs. time (s)

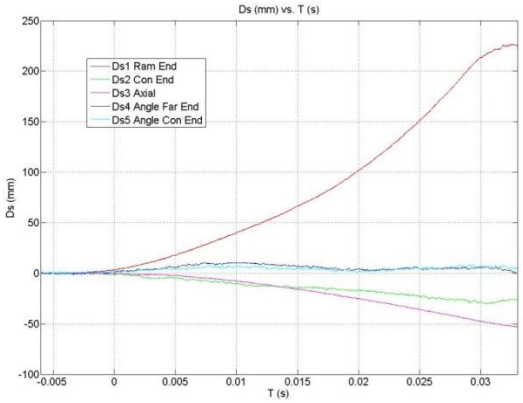

Figure B 30: T7 - Displacement (mm) vs. time (s)

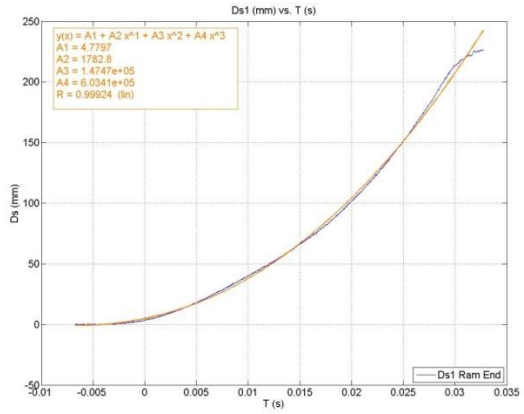

Figure B 31: T7 - Disp1 (mm) vs. time (s)

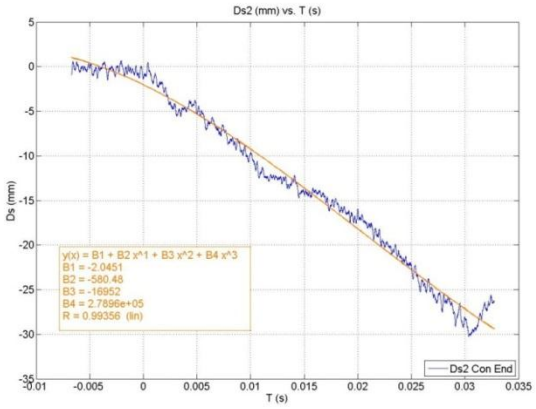

Figure B 32: T7 - Disp2 (mm) vs. time (s)

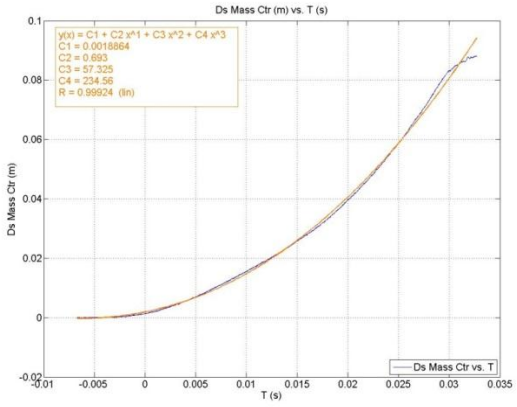

Figure B 33: T7 - Displacement of mass centre (m) vs. time (s)

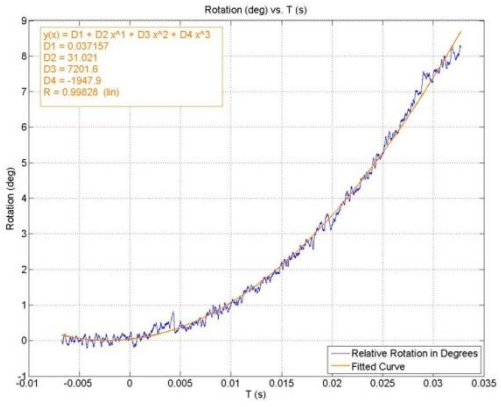

Figure B 34: T7 - Rotation (degrees) vs. time (s)

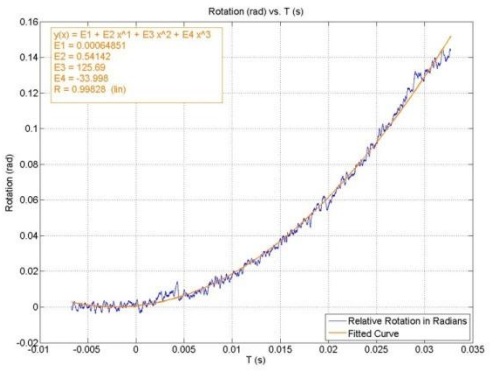

Figure B 35: T7 - Rotation (radians) vs. time (s)

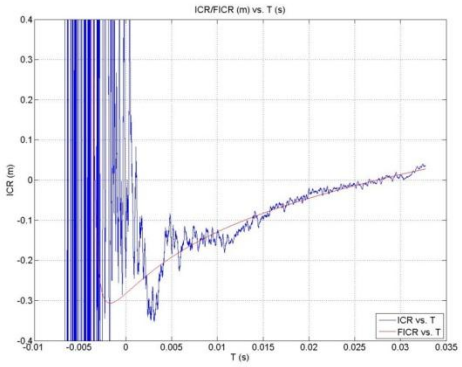

Figure B 36: T7 - Instantaneous centre of rotation (m) vs. time (s)

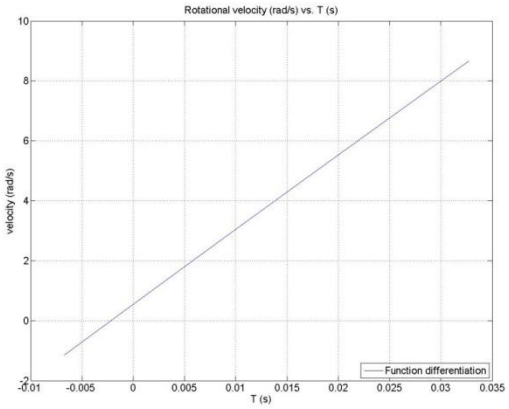

Figure B 37: T7 - Rotational velocity (rad/s) vs. time (s)

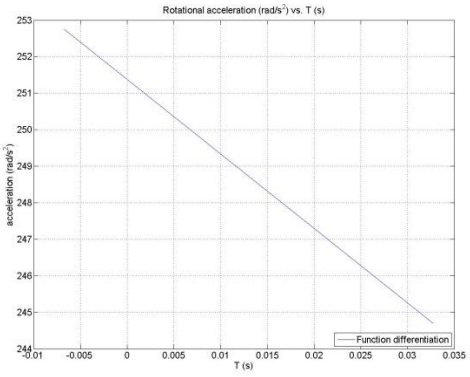

Figure B 38: T7 - Rotational acceleration (rad/s^2) vs. time (s)

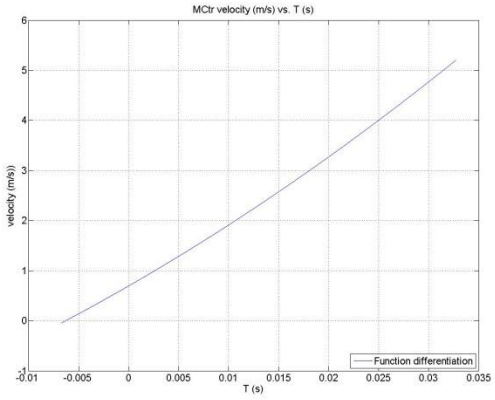

Figure B 39: T7 - Mass centre velocity (m/s) vs. time (s)

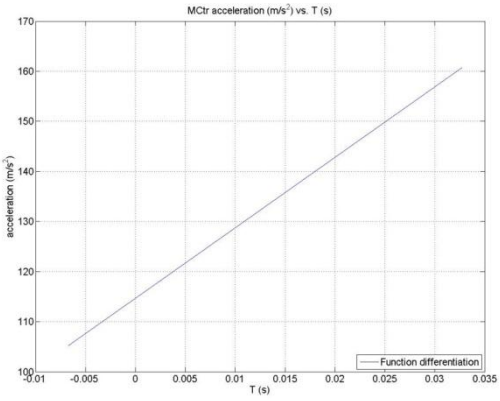

Figure B 40: T7 - Mass centre acceleration (m/s^2) vs. time (s)

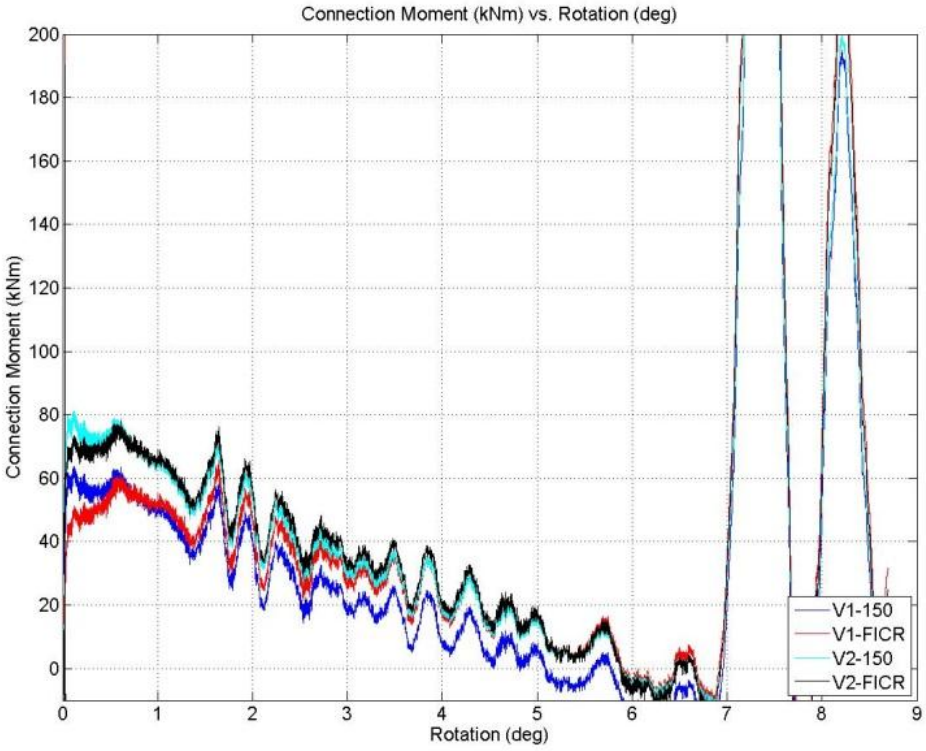

Figure B 41: T7 - Connection moment (kNm) vs. rotation (degrees)

B.2.4 Flush end plate connections under dynamic loading

Test 8, Loading no. 1, M12 Stainless Steel bolts, Grade A4-70

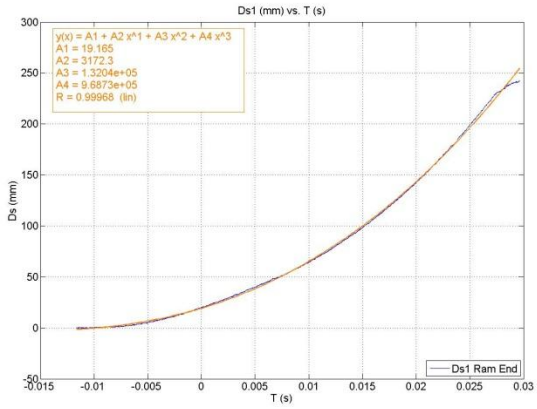

Figure B 42: T8 - Disp1 (mm) vs. time (s)

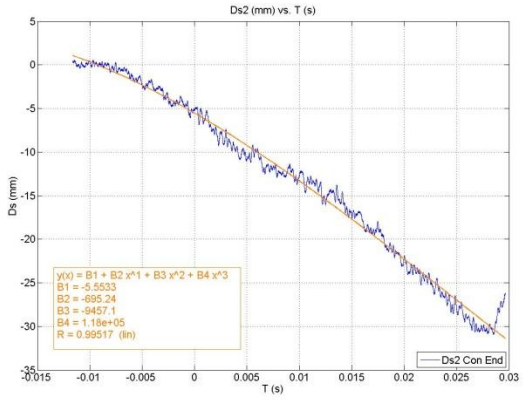

Figure B 43: T8 - Disp2 (mm) vs. time (s)

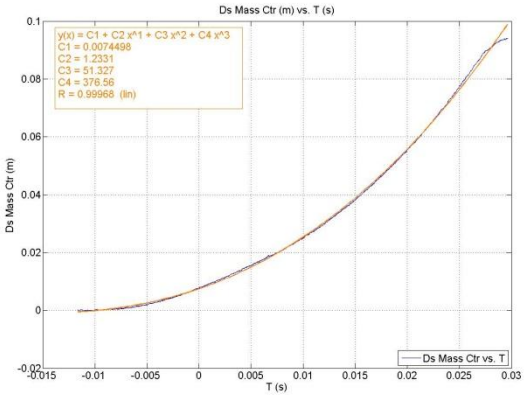

Figure B 44: T8 - Displacement of mass centre (m) vs. time (s)

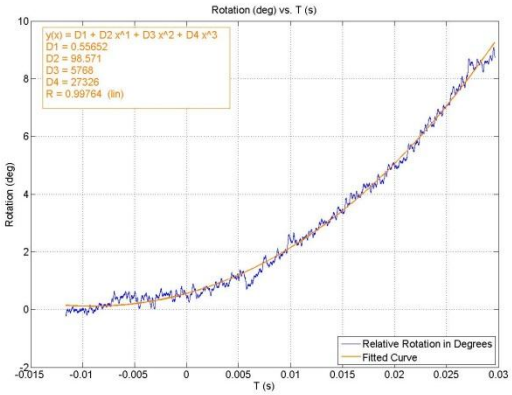

Figure B 45: T8 - Rotation (degrees) vs. time (s)

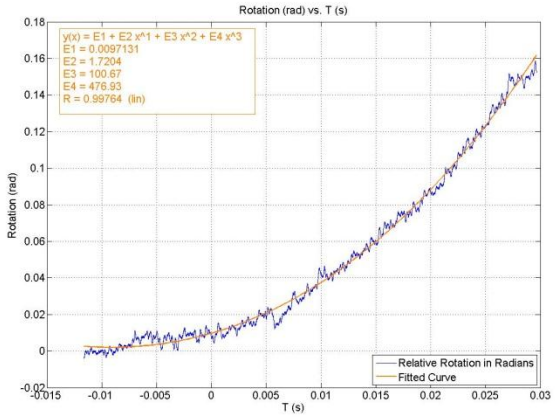

Figure B 46: T8 - Rotation (radians) vs. time (s)

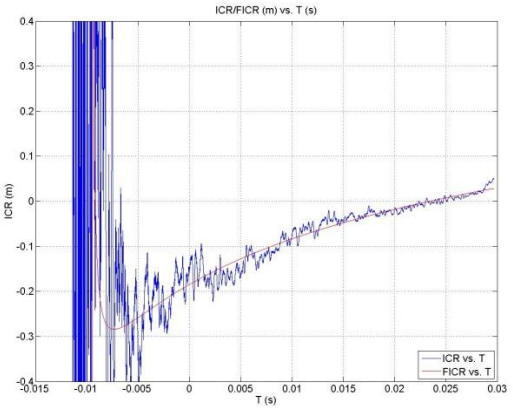

Figure B 47: T8 - Instantaneous centre of rotation (m) vs. time (s)

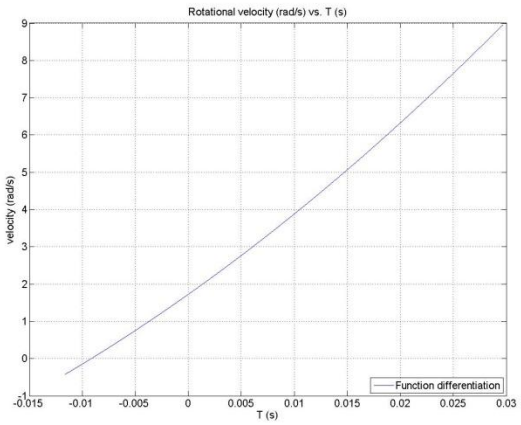

Figure B 48: T8 - Rotational velocity (rad/s) vs. time (s)

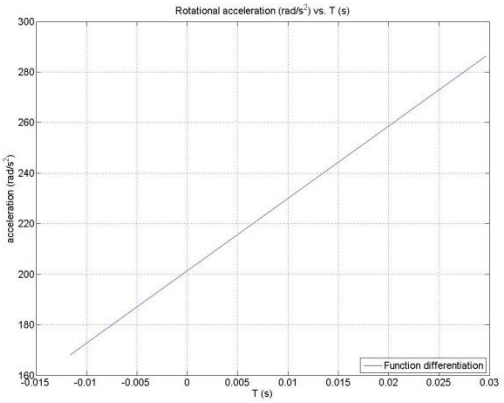

Figure B 49: T8 - Rotational acceleration (rad/s^2) vs. time (s)

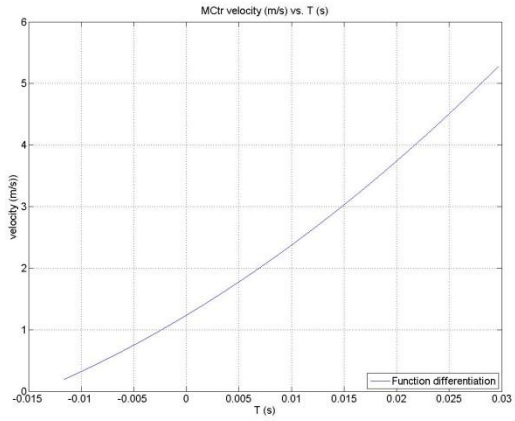

Figure B 50: T8 - Mass centre velocity (m/s) vs. time (s)

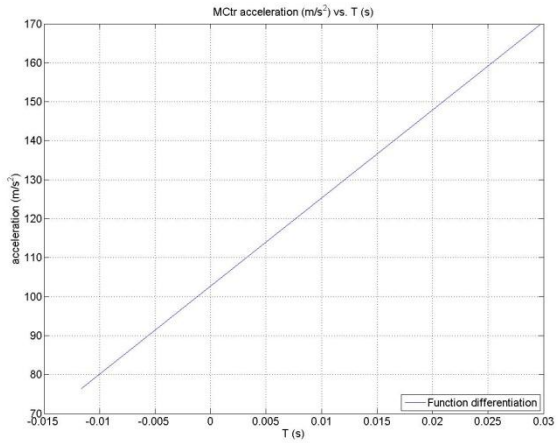

Figure B 51: T8 - Mass centre acceleration (m/s^2) vs. time (s)

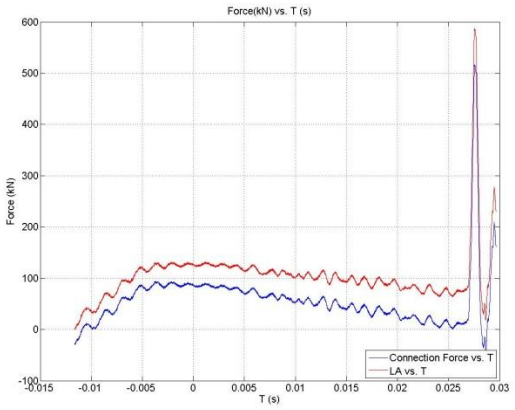

Figure B 52: T8 - Applied load (red) and connection force (blue) vs. time (s)

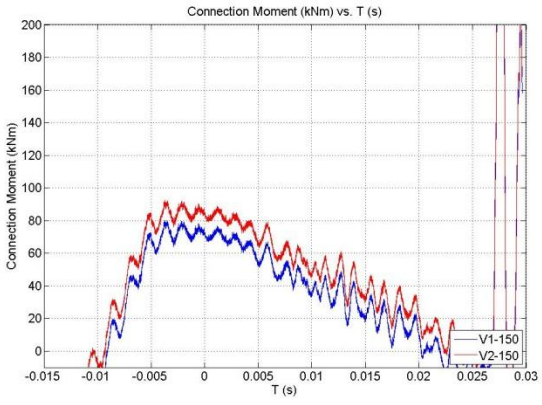

Figure B 53: T8 - Connection moment V1-150, V2-150 (kNm) vs. time(s)

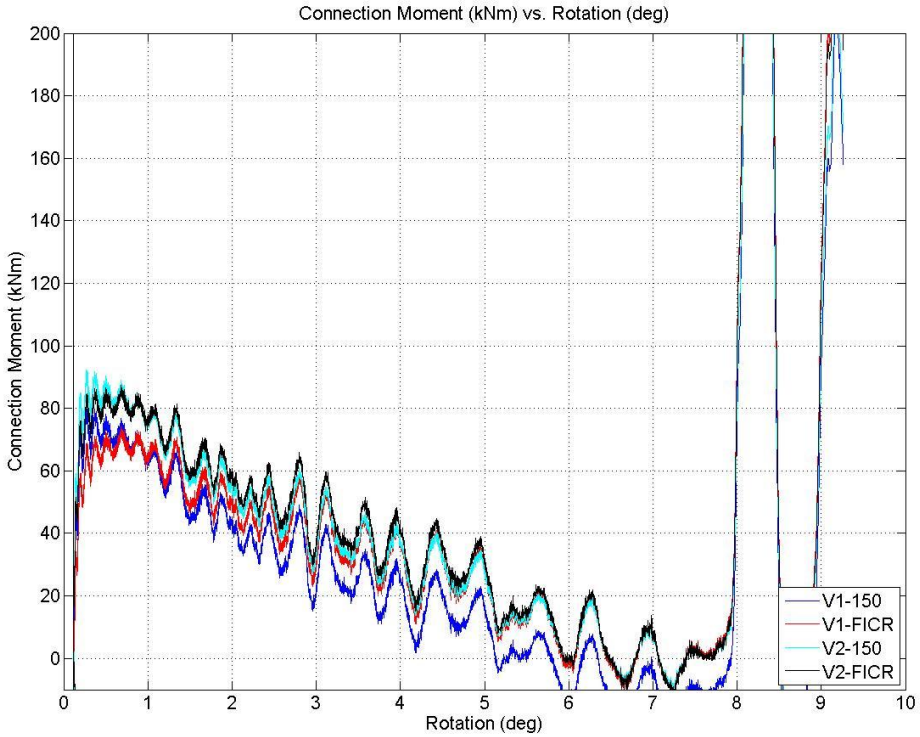

Figure B 54: T8 - Connection moment (kNm) vs. rotation (degrees)

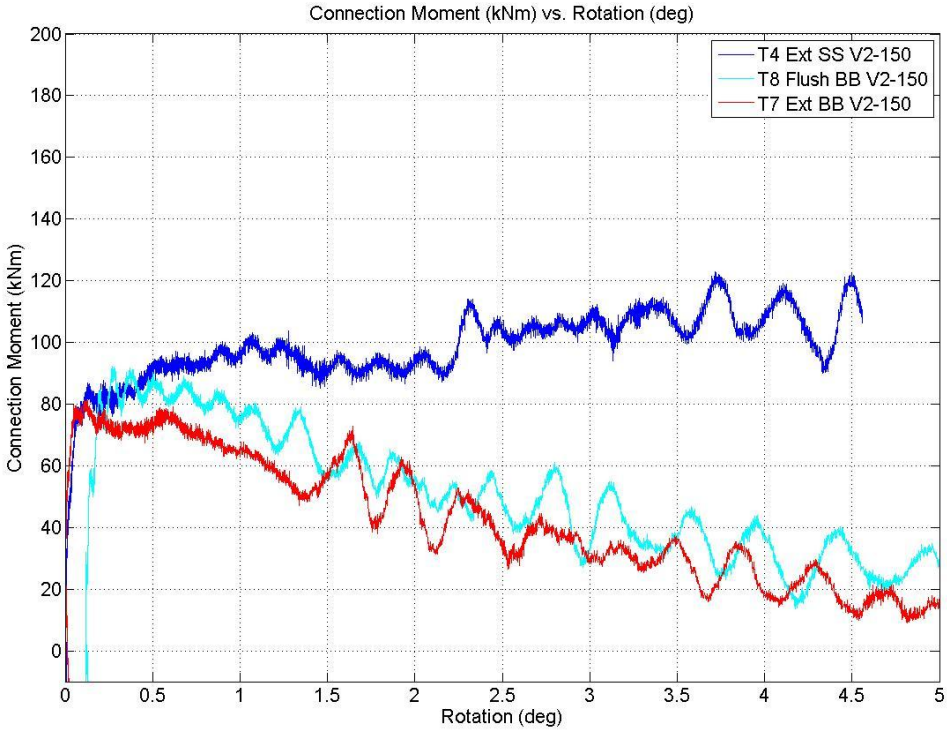

Figure B 55: T4, T7, T8 - Comparison of moment-rotation graphs from dynamic tests

B.3 Experimental data from connection tests

EXTENDED end plate connections: measurements of deformation after failure

The following tests are presented in the planned logical order, not the numerical order in which they took place.

BB = Black bolts. SS = Stainless steel bolts, $\Delta L = 30mm$

No.	Test type	Location	Plate def. **(mm)**	Bolt deformation			
				Top Row		Bottom Row	
				ΔL **(mm)**	$\varepsilon = \frac{\Delta L}{L_0}$ **(%)**	ΔL **(mm)**	$\varepsilon = \frac{\Delta L}{L_0}$ **(%)**
T1	**Static; BB; Extended end plate**	Top end	4.0	Avg = 1.8 Stdev = 2.5	Avg = 5.9 Stdev = 7.9	Avg = 1.3 Stdev = 2.3	Avg = 4.4 Stdev = 7.8
		Row 1	2.5	1 (st)	3.3	1 (st)	3.3
		Row 2	0	0 (st)	0	1 (st)	3.3
		Row 3	0	0 (st)	0	0 (st)	0
		Row 4	1.5	5 (fr)	16	0 (st)	0
		Row 5	1.5	0 (st)	0	6 (fr)	20
		Row 6	0	5 (fr)	16	0 (st)	0
		Row 7	4.0	0 (ok)	0	0 (ok)	0
		Bottom end	8.0	Note: ▪ Bolts generally failed through thread stripping with very little or no elongation. Three bolts fractured, elongating approximately 5 to 6 mm in the process. ▪ The averages and standard deviations above are calculated for the first six rows.			
	Bottom flange buckling		1.5	Note: The bottom flange of the beam stub buckled so that the deformation was similar on both sides of the web.			
T2	**Static; SS; Extended end plate**	Top end	9.0	Avg = 11.6 Stdev = 5.0	Avg = 38.7 Stdev = 16.9	Avg = 11.8 Stdev = 5.2	Avg = 39.2 Stdev = 17.3
		Row 1	5.0	15 (fr)	50	16 (fr)	53
		Row 2	2.5	14 (fr)	47	14 (fr)	47
		Row 3	9.0	14 (fr)	47	14 (fr)	47
		Row 4	9.0	13 (fr)	43	13 (fr)	43
		Row 5	7.5	12 (fr)	40	12 (fr)	40
		Row 6	4.0	1.5 (bent)	5	1.5 (bent)	5
		Row 7	6.5	0 (ok)	0	0 (ok)	0
		Bottom end	13.0	Note: ▪ The first 5 rows of bolts all failed through bolt body breaking. The bolts from the bottom two rows did not fail. ▪ The averages and standard deviations above are calculated for the first six rows.			
	Bottom flange buckling		4.0	Note: The bottom flange of the beam stub buckled so that the deformation is similar on both sides of the web.			

T7	**Dynamic; BB; Extended end plate**	Top end	2.5	Avg = 0.8 Stdev = 0.3	Avg = 2.5 Stdev = 0.9	Avg = 0.7 Stdev = 0.4	Avg = 2.2 Stdev = 1.3
		Row 1	1.5	1 (st)	3.3	0 (st)	0
		Row 2	0	1 (st)	3.3	0.5 (st)	1.7
		Row 3	1.5	0.5 (st)	1.7	1 (st)	3.3
		Row 4	1.5	1 (st)	3.3	1 (st)	3.3
		Row 5	1.5	0.5 (st)	1.7	0.5 (st)	1.7
		Row 6	0	0.5 (st)	1.7	1 (st)	3.3
		Row 7	4.0	0 (ok)	0	0 (ok)	0
		Bottom end	5.0	Note: ▪ All bolts from the first six rows failed through thread stripping. The bolts from the last row were undeformed. ▪ The averages and standard deviations above are calculated for the first six rows.			
	Bottom flange buckling		0	Note: No buckling of bottom flange			
T4	**Dynamic; SS; Extended end plate**	Top end	7.5	Avg = 11.8 Stdev = 3.4	Avg = 39.5 Stdev = 11.3	Avg = 11.7 Stdev = 3.8	Avg = 38.8 Stdev = 12.9
		Row 1	4.0	14 (fr)	47	14 (fr)	47
		Row 2	4.0	14 (fr)	47	14 (fr)	47
		Row 3	9.0	13 (fr)	43	13 (fr)	43
		Row 4	10.0	13 (fr)	43	12 (fr)	40
		Row 5	9.5	12 (fr)	40	13 (fr)	43
		Row 6	5.0	5 (bent)	17	4 (bent)	13
		Row 7	7.5	0 (ok)	0	0.5 (ok)	0.8
		Bottom end	11.5	Note: ▪ The first 5 rows of bolts all failed through bolt body breaking. The bolts from the bottom two rows did not fail. ▪ The averages and standard deviations above are calculated for the first six rows.			
	Bottom flange buckling		6.5	Note: Buckling of the bottom flange is significant only on one side of the web giving a maximum deformation of approximately 6.5mm.			

BB = M12 Black Bolts of Grade 8.8
SS = M12 Stainless Steel Bolts of Grade A4-70
(st) = nut thread stripping
(br) = bolt body breaking
(bent) = bolt had bent but not failed
(ok) = the bolt sustained no damage or insignificant deformation

Flush end plate connections: measurements of deformation after failure

The following tests are presented in the planned logical order, not the numerical order in which they took place.

BB = Black bolts. SS = Stainless steel bolts, $\Delta L = 30mm$

No.	Test type	Location	Plate def. (mm)	Bolt deformation			
				Top Row		Bottom Row	
				ΔL (mm)	$\varepsilon = \frac{\Delta L}{L_0}$ (%)	ΔL (mm)	$\varepsilon = \frac{\Delta L}{L_0}$ (%)
T5	Static; BB; Flush end plate						
		Row 1	0	1 (st)	3.3	1 (st)	3.3
		Row 2	0.5	1 (st)	3.3	1 (st)	3.3
		Row 3	1	1 (st)	3.3	1.5 (st)	5
		Row 4	1	1.5 (st)	5	1 (st)	3.3
		Row 5	0	1.5 (st)	5	4 (fr)	13
		Average		1.2	4.0	1.7	5.6
		Standard deviation		0.3	0.9	1.3	4.2
				Note: ▪ Bolts failed through thread stripping with very little elongation. ▪ One bolt fractured, elongating approximately 4 mm in the process.			
	Bottom flange buckling		1.5	Note: The bottom flange of the beam stub buckled so that the deformation was similar on both sides of the web.			
T6	Static; SS; Flush end plate						
		Row 1	2.5	14 (br)	47	14 (br)	47
		Row 2	5	14 (br)	47	14 (br)	47
		Row 3	6	14 (br)	47	14 (br)	47
		Row 4	5	13 (br)	43	14 (br)	47
		Row 5	1.5	2 (ok)	6.7	2.5 (ok)	8.3
		Average		11.4	38.1	11.7	39.3
		Standard deviation		5.3	17.7	5.1	17.3
				Note: ▪ The first 4 rows of bolts all failed through bolt body breaking. ▪ The bolts from the bottom row did not fail.			
	Bottom flange buckling		4.0	Note: The bottom flange of the beam stub buckled so that the deformation is similar on both sides of the web.			

T8	Dynamic; BB; Flush end plate						
		Row 1	0	1 (st)	3.3	1 (st)	3.3
		Row 2	0.5	0.5 (st)	1.7	1 (st)	3.3
		Row 3	1	1 (st)	3.3	1 (st)	3.3
		Row 4	1	0.5 (st)	1.7	0.5 (st)	1.7
		Row 5	0	1 (st)	3.3	4 (fr)	13
		Average		0.8	2.7	1.5	4.9
		Standard deviation		0.3	0.9	1.4	4.6
				Note: ▪ Bolts failed through thread stripping with very little elongation. ▪ One bolt fractured, elongating approximately 4 mm in the process. ▪ A distinctive feature of this test was that the column was completely separated from the beam stub at the end of the failure process.			
	Bottom flange buckling		0	Note: No buckling of bottom flange			
T9	Dynamic; SS; Flush end plate; *In progress*						
		Row 1	2.5	14 (br)	47	14 (br)	47
		Row 2	5	14 (br)	47	14 (br)	47
		Row 3	6	14 (br)	47	14 (br)	47
		Row 4	5	13 (br)	43	14 (br)	47
		Row 5	1.5	2 (ok)	6.7	2.5 (ok)	8.3
		Average		11.4	38.1	11.7	39.3
		Standard deviation		5.3	17.7	5.1	17.3
	Bottom flange buckling		6.5	Note: Buckling of the bottom flange is significant only on one side of the web giving a maximum deformation of approximately 6.5mm.			

BB = M12 Black Bolts of Grade 8.8
SS = M12 Stainless Steel Bolts of Grade A4-70
(st) = nut thread stripping
(br) = bolt body breaking
(bent) = bolt had bent but not failed
(ok) = the bolt sustained no damage or insignificant deformation

B.4 Experimental data from bolt tests

Table B.1. Experimental data from carbon steel and stainless steel bolts tensile tests

Test	Bolt type	Displacement rate (mm/min)	Average engineering strain rate (s^{-1})	Ultimate load (kN)	Dynamic Increase Factor	Energy absorbed (kJ)
1	Stainless Steel	2	0.001	76.04		1.074
2		2	0.001	74.26		1.144
3		2	0.001	74.15		1.145
4		2	0.001	74.58		1.148
5		2	0.001	74.18		1.146
11		2	0.001	75.49		1.118
12		2	0.001	75.76		1.130
13		2	0.001	77.45		1.144
		Average static:		75.24		1.131
14		20	0.01	73.83	0.98	0.931
15		200	0.1	74.94	1.00	0.850
24		2000	0.86	77.82	1.03	0.817
6	Carbon Steel	2	0.001	79.08		0.402
7		2	0.001	79.89		0.522
8		2	0.001	79.29		0.577
9		2	0.001	78.67		0.397
10		2	0.001	80.01		0.439
16		2	0.001	80.88		0.559
17		2	0.001	76.58		0.377
18		2	0.001	77.63		0.527
		Average static:		79.01		0.475
19		20	0.01	79.21	1.00	0.339
20		200	-	79.27	1.00	-
21 R20		200	0.1	81.83	1.04	0.543
25		2000	0.81	84.52	1.07	0.478

Table B.2. Experimental data from steel coupon tests

Test	Specimen	Yield stress (N/mm^2)	Yield strain (mm/mm)	Ultimate stress (N/mm^2)	Ultimate strain (mm/mm)	Strain at fracture
1	F1	380	-	506	-	0.2444
2	F1	407	-	527	-	0.2222
3	F1	406	-	527	-	0.2000
4	F1	385	-	516	-	0.2111
11	W1	419	0.002174	508	0.147390	0.2222
Average:		394	Average:	519		
14	F2	447	0.002255	531	0.171480	0.2889
15	F2	448	0.002237	534	0.173650	0.2889
16	F2	452	0.002257	532		0.2778
17	F2	435	0.006380	532	0.168720	0.2778
13	W2	420	0.002080	529	0.171740	0.2667
Average:		445	Average:	532		
7	12mm	400	-	570	-	0.2667
8	12mm	416	-	554	-	0.2333
Average:		408	Average:	562		

Table B.3. Dynamic increase factor for ultimate strength for all stainless steel samples tested

Displacement Rate (mm/minute)	Average Plastic Strain Rate (mm/mm/second)	Ultimate Strength (N/mm^2)	Dynamic Increase Factor
10	0.00567	729.13	1.10
10	0.00567	692.56	1.04
10	0.00567	713.72	1.07
100	0.0567	718.98	1.08
100	0.0567	710.24	1.07
200	0.110	754.12	1.13
500	0.270	769.72	1.16
500	0.270	718.82	1.08
750	0.407	752.07	1.13
750	0.400	734.53	1.10
1,000	0.550	743.46	1.12
1,000	0.583	773.33	1.16
5,000	1.067	772.39	1.16
5,000	1.233	728.97	1.10
10,000	1.167	766.05	1.15
50,000	1.500	754.61	1.13
100,000	1.134	779.03	1.17
100,000	1.267	725.87	1.09
100,000	1.167	759.33	1.14

Table B.4. Dynamic increase factor for ultimate strength for all carbon steel samples tested with one nut

Displacement Rate (mm/minute)	Average Plastic Strain Rate (mm/mm/second)	Ultimate Strength (N/mm^2)	Dynamic Increase Factor
10	0.00567	720.55	1.03
10	0.00567	711.80	1.02
10	0.00567	727.05	1.04
10	0.00567	718.48	1.03
75	0.00400	692.89	1.00
100	0.0567	741.87	1.06
100	0.0567	742.55	1.06
125	0.0667	704.36	1.01
150	0.0800	724.81	1.04
500	0.270	735.77	1.05
1,000	0.533	734.39	1.05
1,000	0.533	715.10	1.02
5,000	1.267	733.75	1.05
10,000	1.200	720.28	1.03
50,000	1.400	716.77	1.03
100,000	1.300	746.38	1.07
100,000	1.267	733.12	1.05

Table B.5. Experimental results for carbon steel bolts tested with two nuts

Displacement Rate (mm/minute)	Average Elastic Strain Rate (mm/mm/s)	Yield Strength (N/mm^2)	Average Plastic Strain Rate (mm/mm/s)	Ultimate Strength (N/mm^2)	Deformation at Ultimate Strength (%)	Deformation Prior to Failure (%)
10	0.00567	626.66	0.00567	729.35	10.49	18.72
20	0.011	648.09	0.011	742.97	10.65	19.91
30	0.0166	632.68	0.0166	728.27	10.65	18.69
100	0.0567	646.09	0.0567	720.41	10.05	18.24
300	0.163	596.92	0.167	740.9	10.33	17.69
500	0.273	600.48	0.283	725.19	10.34	17.21
1,000	0.533	599.81	0.583	736.44	9.88	16.65
5,000	1.4	586.61	1.133	759.87	10.91	16.34
10,000	1.567	533.83	1.233	759.76	9.7	14.35
100,000	1.533	648.33	1.133	754.17	11.48	17.59

Appendix C

C.1 Abaqus input for S355 steel coupon model

In order to model the full behaviour of S355 steel with Abaqus, elastic, plastic, damage and fracture behaviours must be defined. Table C 1 provides the minimum number of values needed to model this behaviour in a quasi-static and high rate loading scenario. There is no single unique set of values for $\left(\varepsilon_{D,0}^{pl}, \bar{u}^{pl}, D_{max}\right)$ that define the damage and fracture behaviour of S355 steel. Several different sets may be found that result in acceptable results. The plastic behaviour described by the graph is inputted as discreet set of points $\{(\sigma, \varepsilon^{pl}, \dot{\varepsilon})\}$.

Table C 1: Abaqus input values modelling the quasi-static behaviour of S355 steel

Density	$\rho = 7.8 \cdot 10^{-9}\ tonnes/mm^3$		
Elastic behaviour	$E = 200000\ MPa$		$v = 0.3$
Damage	$\varepsilon_{D,0}^{pl} = 0.24$	$Triaxiality = 0.33$	$\dot{\varepsilon}_0 = 0.00047$
Displacement at failure	$\bar{u}^{pl} = 2.4$	Maximum element degradation	$D_{max} = 0.3$
Plastic behaviour	True stress versus true plastic strain described by graph below		
	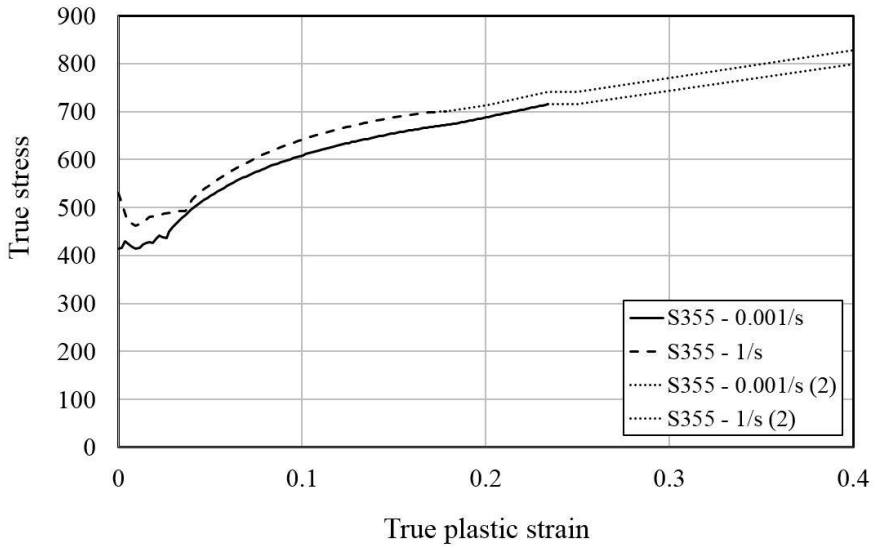		

Figure C 1 shows how the elastic behaviour is defined in Abaqus/Standard. Figure C 2 shows some points from the set $\{(\sigma, \varepsilon^{pl}, \dot{\varepsilon})\}$, which is used to define the plastic behaviour. This set is used by combining two sets $\{(\sigma, \varepsilon^{pl}, 0.001s^{-1})\}$ and $\{(\sigma, \varepsilon^{pl}, 1s^{-1})\}$ with the Malvar-Crawford DIFs to allow prediction of $(\sigma, \varepsilon^{pl})$ for a wider range of $\dot{\varepsilon} = [0.001\ s^{-1}, 100\ s^{-1}\ ]$.

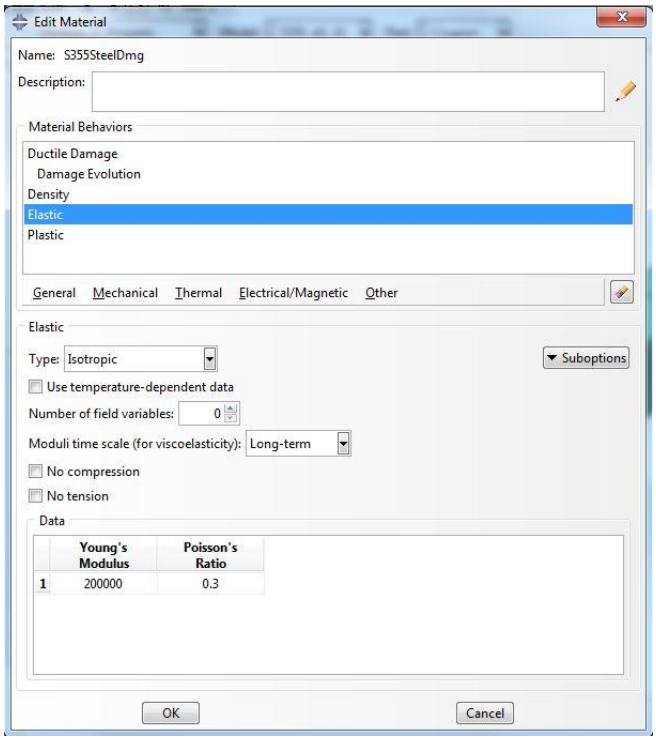

Figure C 1: Defining elastic behaviour of S355 steel

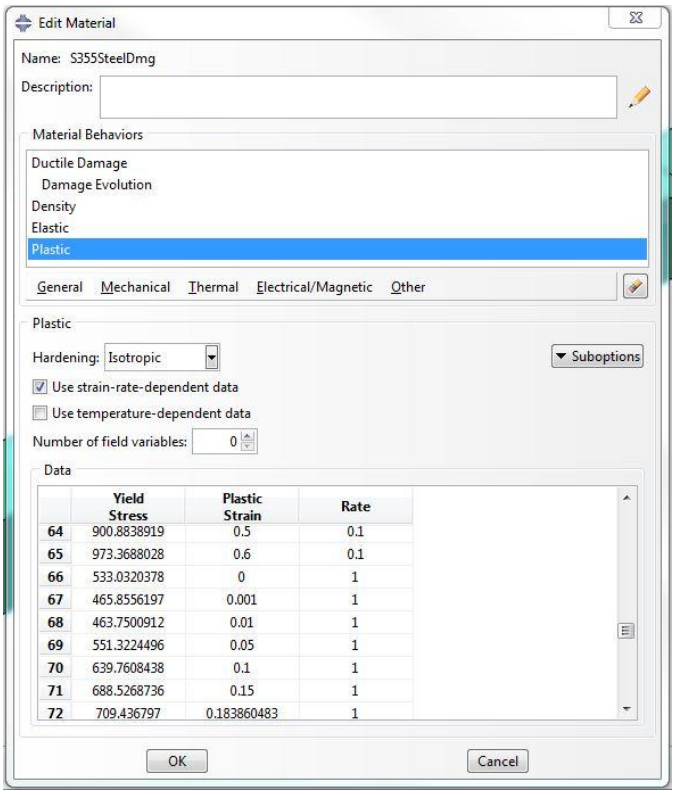

Figure C 2: Defining plastic behaviour of S355 steel

Figure C 3 shows the set $\{(\varepsilon_{D,0}^{pl}, \eta, D_{max})\}$ used to define the damage and fracture of S355 steel for different strain rates. This set was found to give acceptable results for tests where $\dot{\varepsilon}_1 \cong 0.00047\ s^{-1}$ and $\dot{\varepsilon}_2 \cong 1$. Figure C 3 shows damage evolution defined as linear and the value of $\bar{u}^{pl}$ is 2.4mm where the elements used in the model were of an approximate global size of 1mm.

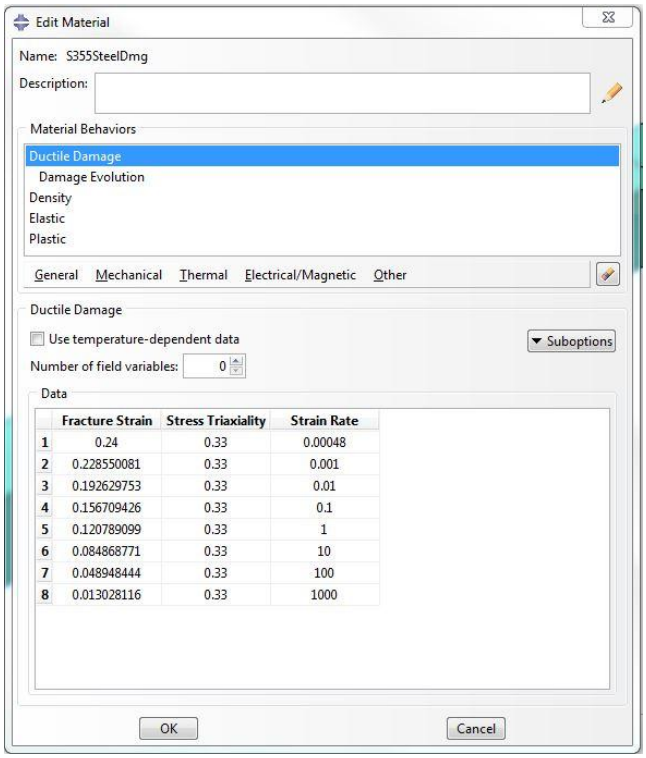

Figure C 3: Defining fracture strain for S355 steel

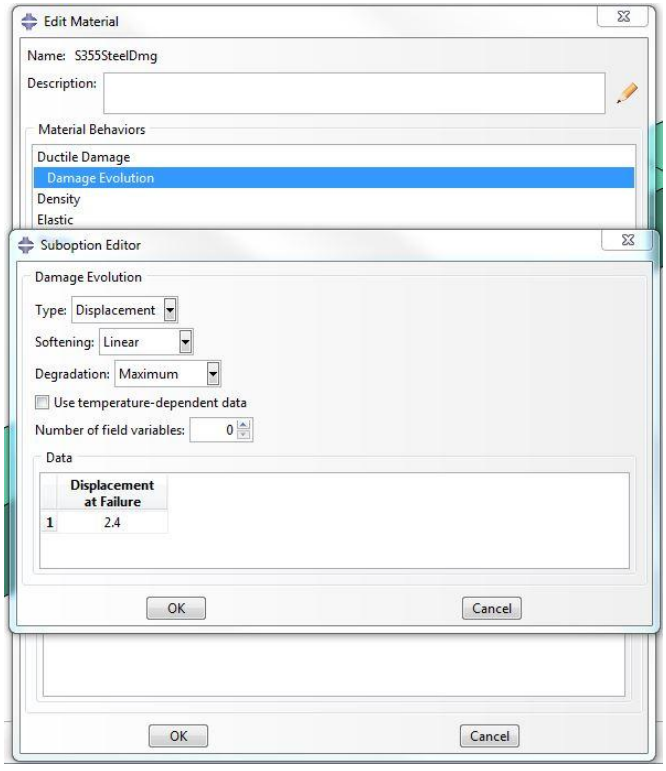

Figure C 4: Defining damage evolution for S355 steel

Figure C 5 shows the window used for defining the element type used in modelling the S355 steel coupon under dynamic loading. The element library used was "Explicit" since the model is used for dynamic loading. The family is "3D stress", the geometric order is "linear" and the element uses "reduced integration". Element deletion was turned on and the maximum degradation D_{max} was set as 0.3. This is not the only possible value, values of 0.2 or 0.4 for example would yield satisfactory results. But the value of 0.3 was found to work best with the set of values defined for damage and fracture.

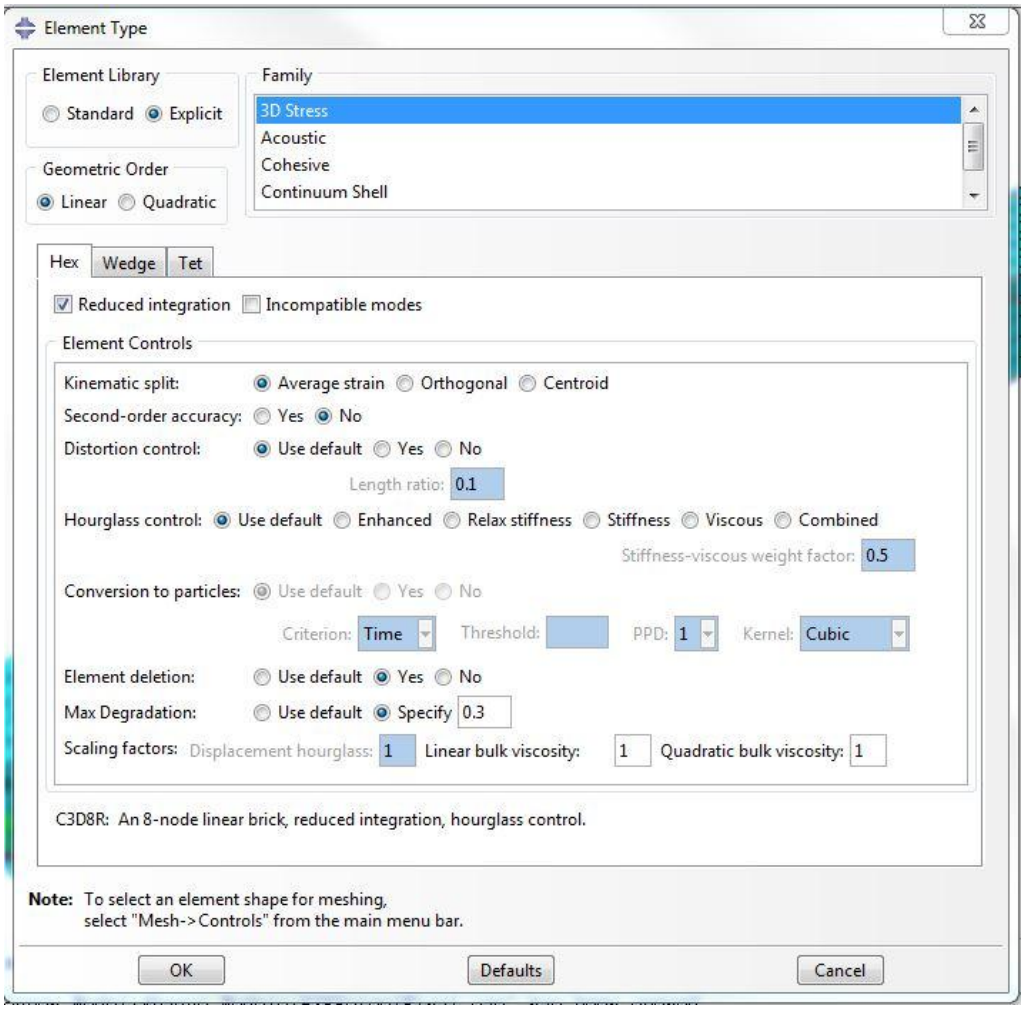

Figure C 5: Defining element type for S355 steel

C.2 Abaqus input for A4-70 stainless steel bolt

In order to model the full behaviour of A4-70 stainless steel with Abaqus, elastic, plastic, damage and fracture behaviours must be defined. Table C 2 provides the minimum number of values needed to model this behaviour in a quasi-static scenario. There is no single unique set of values for $\left(\varepsilon_{D,0}^{pl}, \bar{u}^{pl}, D_{max}\right)$ that define the damage and fracture behaviour of A4-70 steel. Several different sets may be found that result in acceptable results. The plastic behaviour described by the graph is inputted as a discreet set of points $\{(\sigma, \varepsilon^{pl}, \dot{\varepsilon})\}$.

Table C 2: Abaqus input values modelling the quasi-static and dynamic behaviour of A4-70 stainless steel

Density	$\rho = 7.8 \cdot 10^{-9}\ tonnes/mm^3$		
Elastic behaviour	$E = 200000\ MPa$		$v = 0.3$
Damage	$\varepsilon_{D,0}^{pl}$	$Triaxiality$	$\dot{\varepsilon}_0$
	1	0.33	0.00111
	0.866048	0.33	0.005
	0.804358	0.33	0.01
	0.661118	0.33	0.05
	0.599428	0.33	0.1
	0.456188	0.33	0.5
	0.394498	0.33	1
	0.332808	0.33	2
	0.271118	0.33	4
	0.251258	0.33	5
	0.235031	0.33	6
	0.221312	0.33	7
	0.209428	0.33	8
	0.189568	0.33	10
Displacement at failure	$\bar{u}^{pl} = 0.8$	Maximum element degradation	$D_{max} = 0.4$
Plastic behaviour	True stress versus true plastic strain described by graph below		
Johnson-Cook parameters	$C = 0.0067$		$\dot{\varepsilon}_0 = 0.00111$

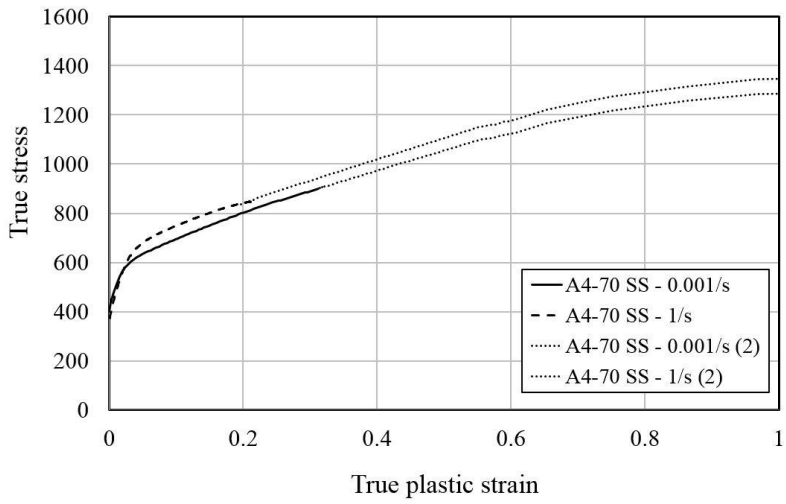

Figure C 6 shows some points from the set $\{(\sigma, \varepsilon^{pl})\}$, which is used to define the plastic behaviour. The plastic behaviour is defined by combining the set $\{(\sigma, \varepsilon^{pl}, 0.0011s^{-1})\}$ with the Johnson-Cook test-calibrated C of 0.0067 and reference strain rate $\dot{\varepsilon}_0$ of 0.0011 to allow prediction of $(\sigma, \varepsilon^{pl})$ for a wider range of $\dot{\varepsilon}$.

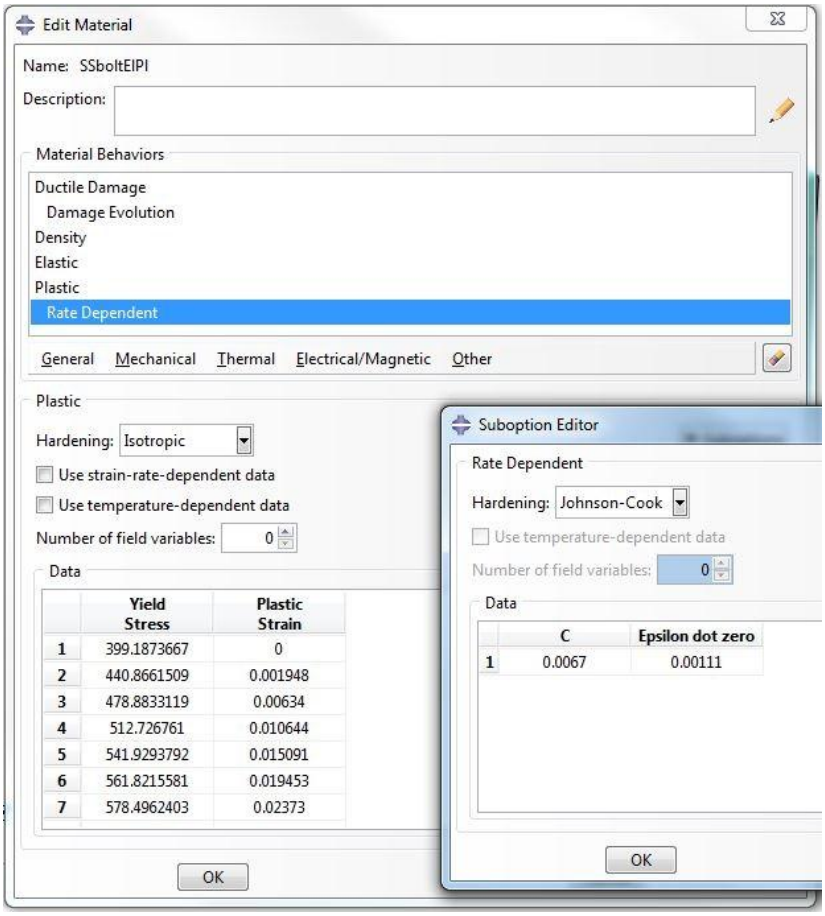

Figure C 6: Defining plastic behaviour for A4-70 stainless steel

Figure C 7 shows the set $\{(\varepsilon_{D,0}^{pl}, \eta, D_{max})\}$ used to define the damage and fracture of A4-70 stainless steel for different strain rates. This set was found to give acceptable results for tests where $\dot{\varepsilon}_1 \cong 0.00111\ s^{-1}$ and $\dot{\varepsilon}_2 \cong 1\ s^{-1}$. Figure C 8 shows damage evolution defined as linear and the value of $\bar{u}^{pl}$ is 0.8mm where the elements used in the model were of an approximate global size of 1mm.

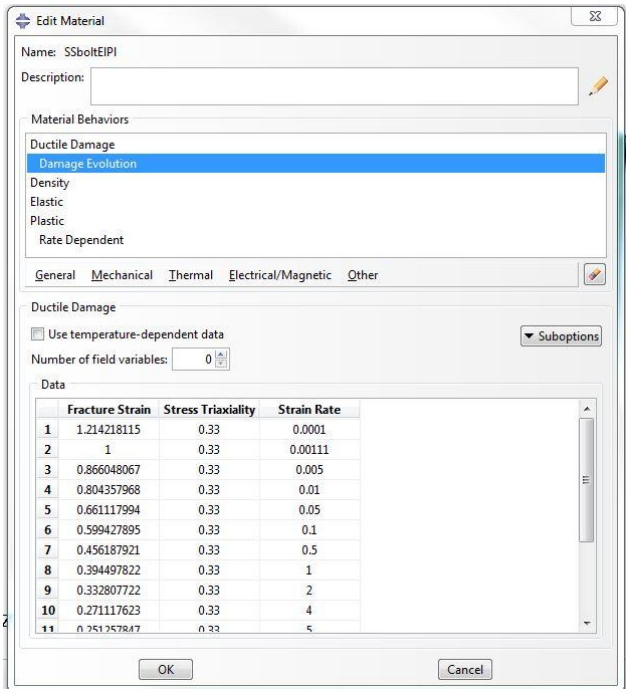

Figure C 7: Defining fracture strain for A4-70 stainless steel

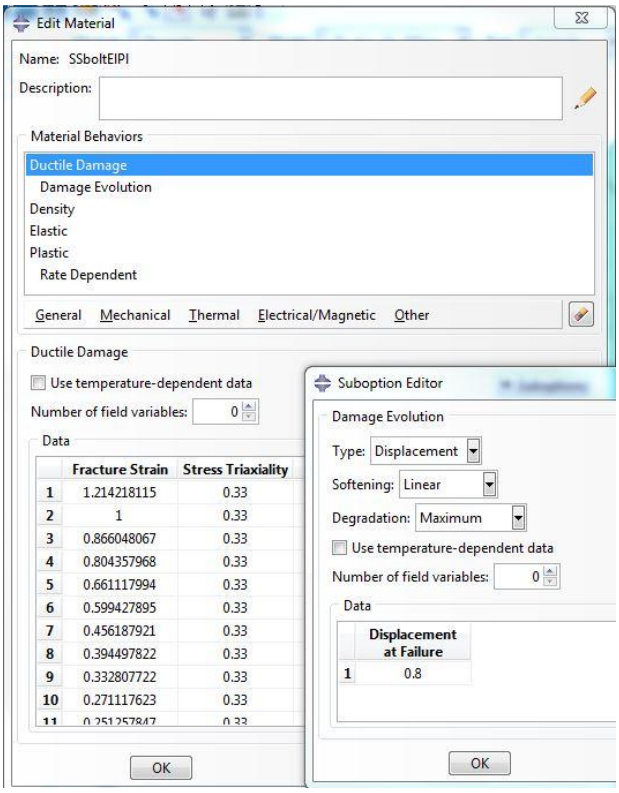

Figure C 8: Defining damage evolution for A4-70 stainless steel

Figure C 9 shows the window used for defining the element type used in modelling the A4-70 stainless steel bolt under dynamic loading. The element library used was "Explicit" since the model is used for dynamic loading. The family is "3D stress", the geometric order is "linear" and the element uses "reduced integration". Element deletion was turned on and the maximum degradation D_{max} was set as 0.4. This is not the only possible value, values of 0.3 or 0.5 for example would yield satisfactory results. But the value of 0.4 was found to work best with the set of values defined for damage and fracture.

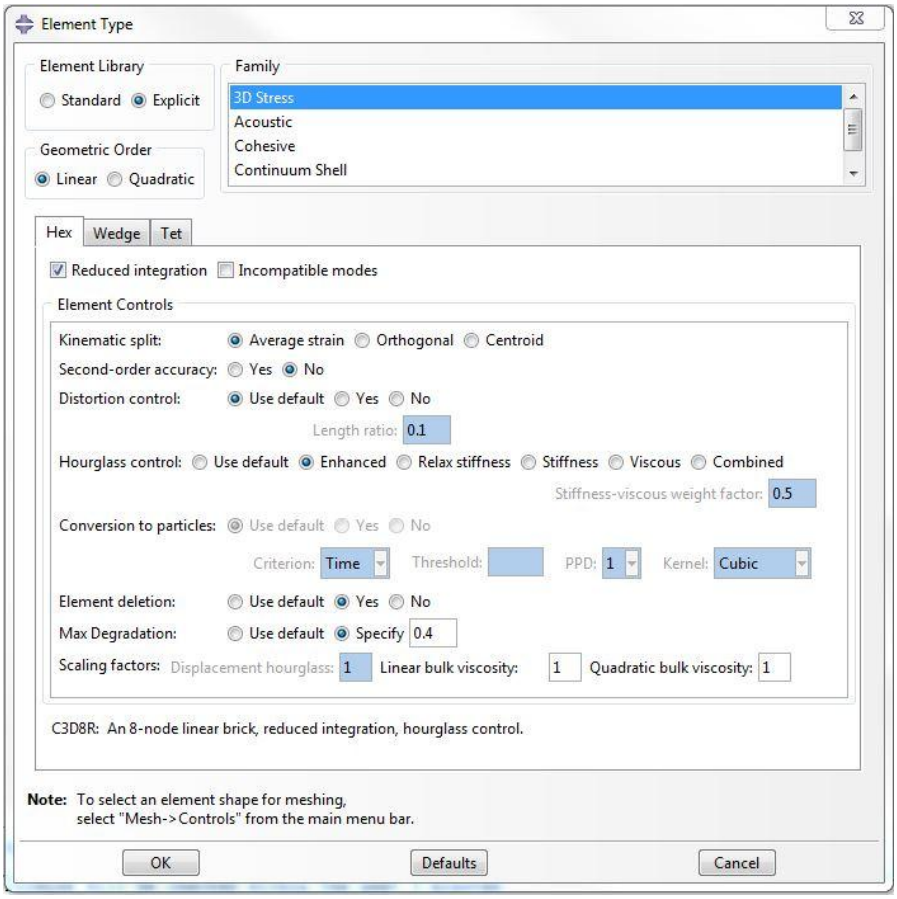

Figure C 9: Defining element type for stainless steel

C.3 Abaqus input for connector representing stainless bolt

For a detailed description of connector modelling refer to Section 4.7.5.

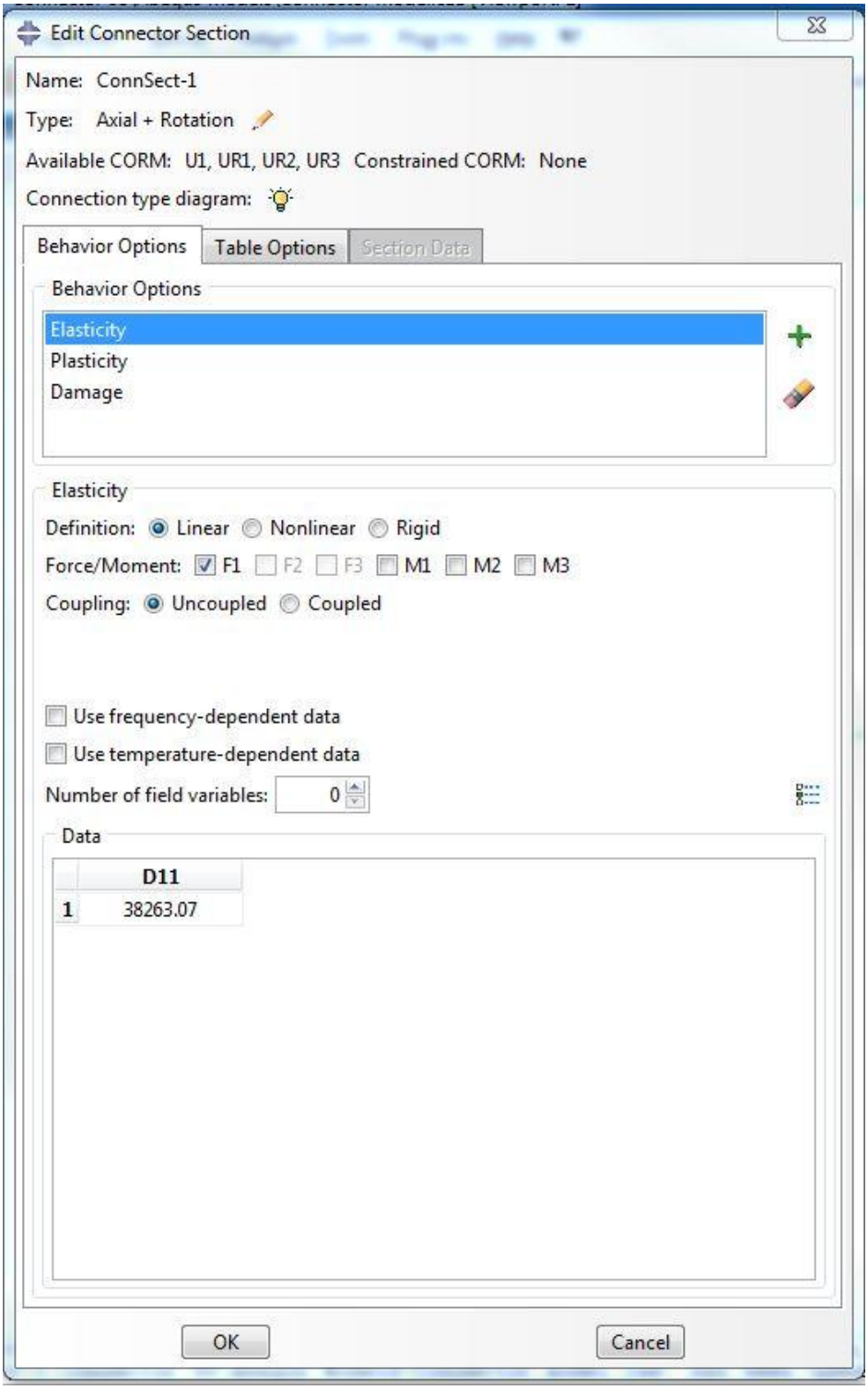

Figure C 10: Defining elastic behaviour for connector elements representing stainless steel bolts

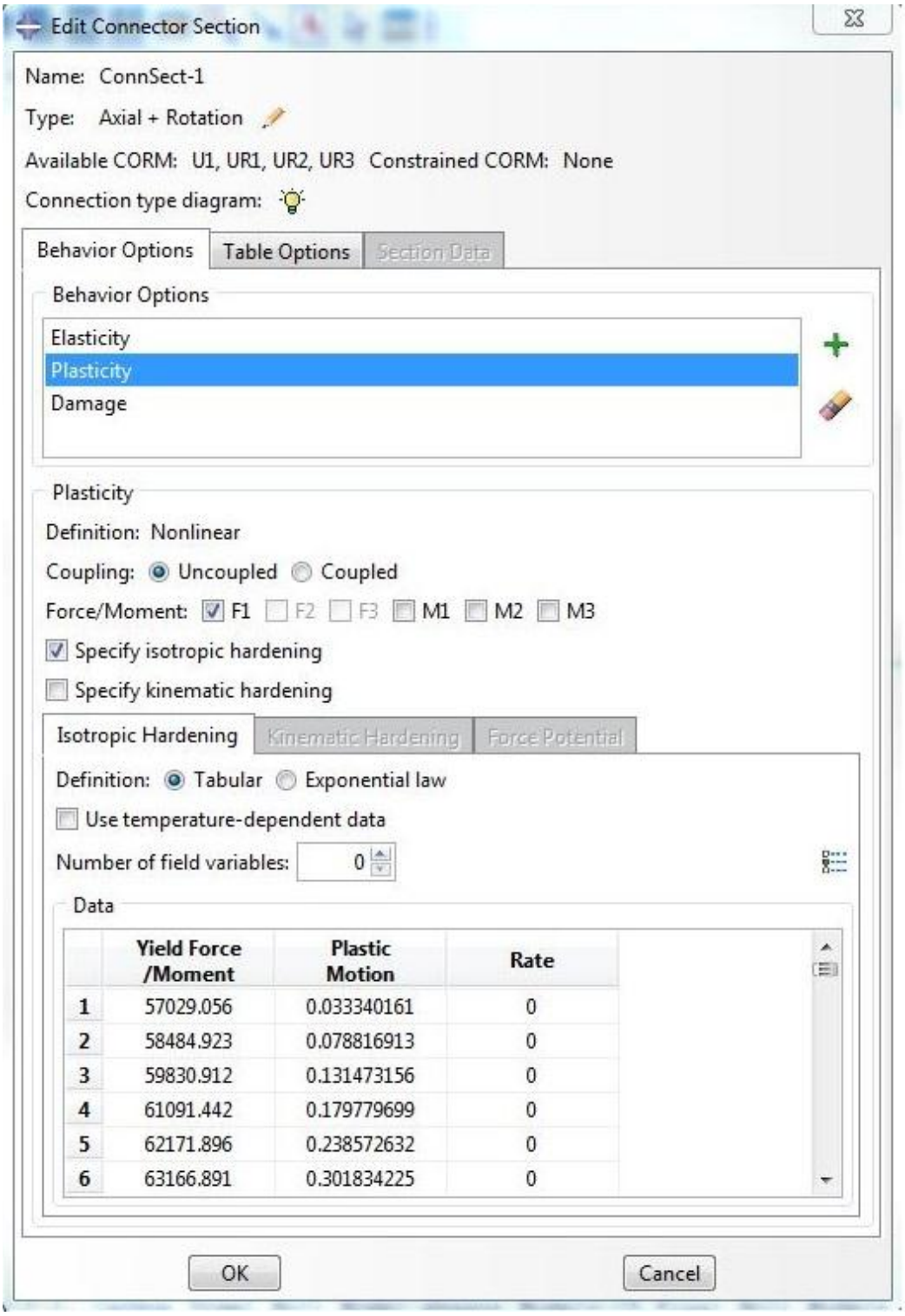

Figure C 11: Defining plastic behaviour for connector elements representing stainless steel bolts

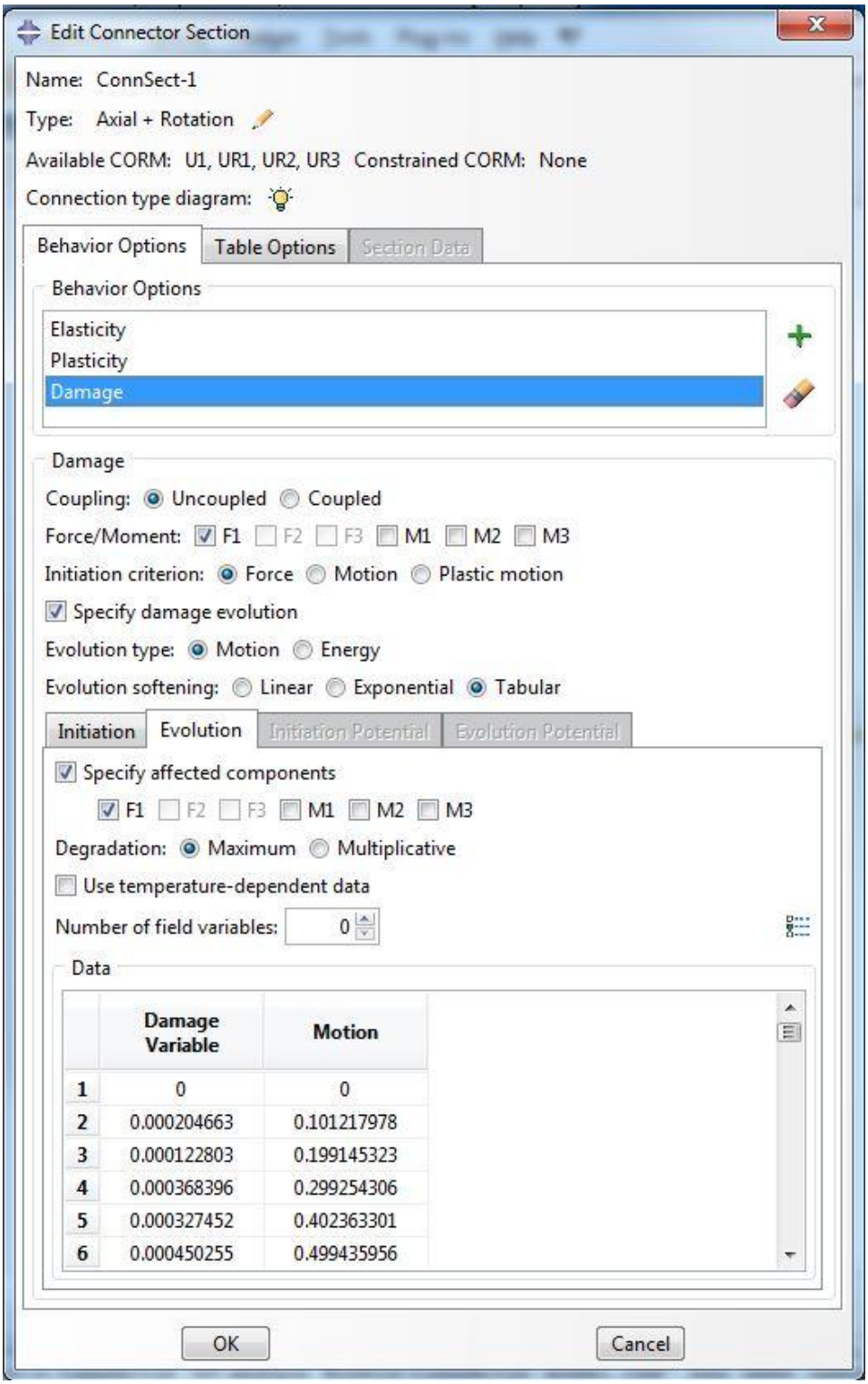

Figure C 12: Defining damage behaviour for connector elements representing stainless steel bolts

Appendix D

From material test the engineering stress-strain curve is obtained easily and is shown on Figure D 1 in dark blue. Using Equations (4.6) and (4.7) the true stress-strain curve is obtained as shown in dark red. However, this does not accurately describe the full behaviour of a 1mm (assumed 1mm) element in the neck. These elements undergo a degree of *transformation* from austenite to martensite followed soon by a degree of *damage* before *fracture*. Rusinek et al. (2015) give a material model that describes this transformation behaviour for AISI 304 stainless steel, shown in purple. However, since A40-70 has a greater nickel (Ni) content it has a higher flow stress. A good estimate is obtained by adding 54 N/mm^2 to give the light blue curve. By extending the slope of the original true stress-strain curve and further trial and error, the actual true stress-strain curve is obtained as it was used as Abaqus input for A4-70 stainless steel, shown by the orange curve.

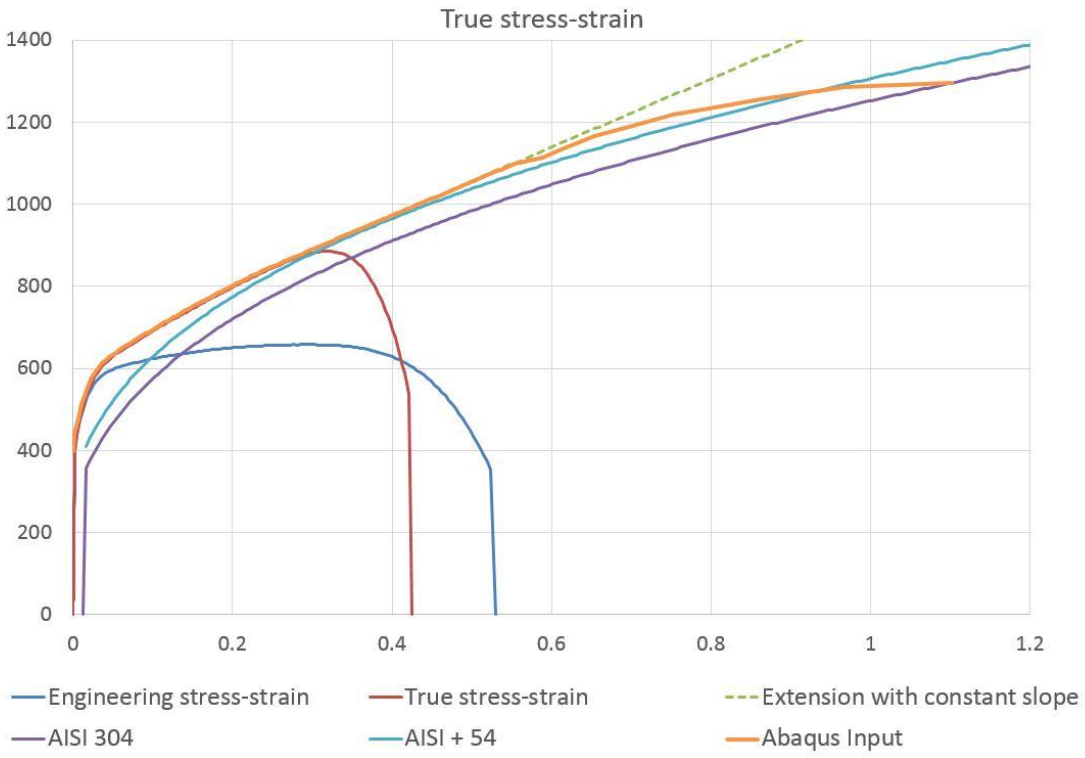

Figure D 1: Estimating true stress-strain curve for A4-70 using advanced Rusinek-Klepaczko (RK) material model for AISI 304 published by Rusinek et al. (2015)

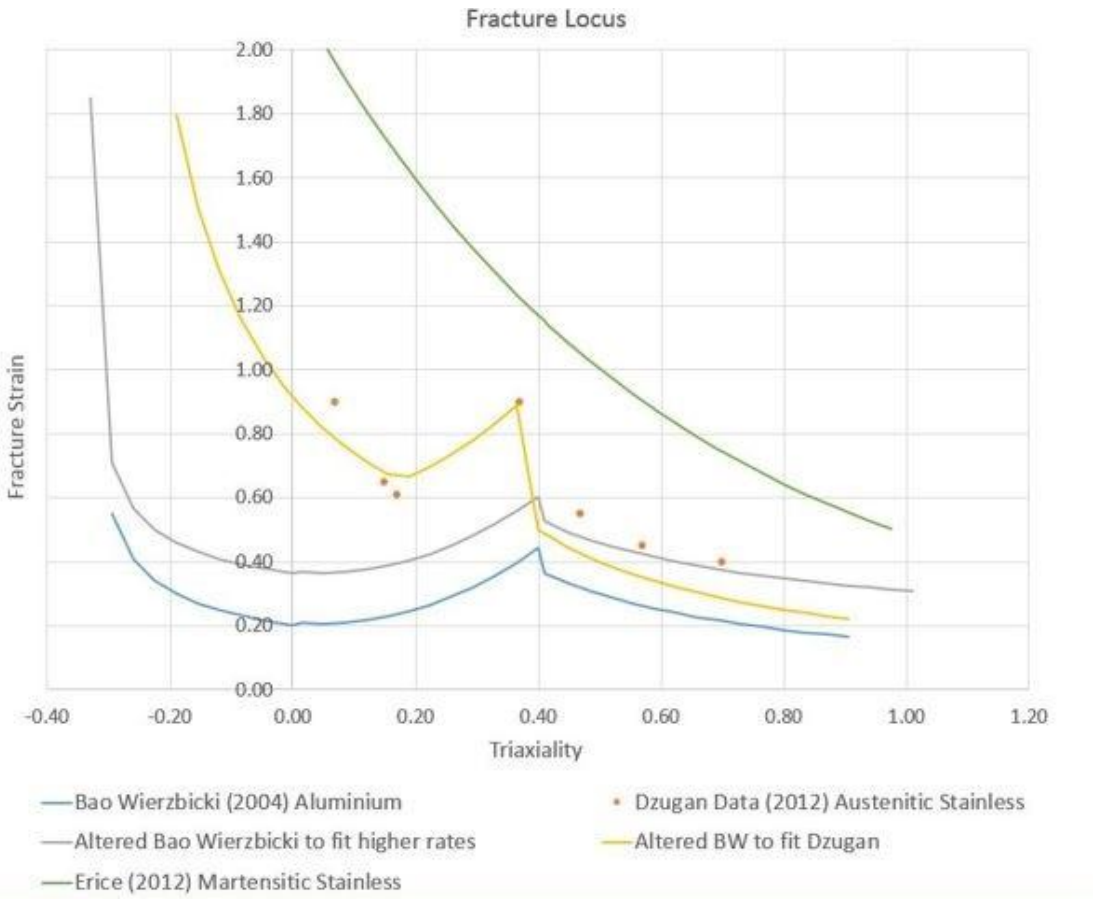

Figure D 2: Estimating fracture locus using functions found by Bao-Wierzbicki (2004) for aluminium and data points for stainless steel published by Dzugan et al. (2012)

List of References

Al-Jabri, K.S., Burgess, I.W. & Plank, R.J., 2005. Spring-stiffness model for flexible end-plate bare-steel joints in fire. *Journal of Constructional Steel Research*, 61(12), pp.1672–1691. Available at: http://www.sciencedirect.com/science/article/pii/S0143974X05000817 [Accessed March 16, 2015].

Alexander, E.M., 1977. Analysis and Design of Threaded Assemblies. *SAE Technical Paper 770420*.

Baddoo, N.R., 2002. *Structural Design of Stainless Steel (P291)*, The Steel Construction Institute.

Bao, Y. & Wierzbicki, T., 2004. On fracture locus in the equivalent strain and stress triaxiality space. *International Journal of Mechanical Sciences*, 46(1), pp.81–98.

BCSA, 2010. *National Structural Steelwork Specification for Building Construction 5th Ed.*,

Bickford, J.H., 2007. *Introduction to the Design and Behavior of Bolted Joints, Fourth Edition: Non-Gasketed Joints: v. 1* 4th ed., CRC Press.

Byfield, M.P., 2006. Behaviour and Design of Commercial Multistory Buildings Subjected to Blast. *J. Perform. Constr. Facil.*, 20(SPECIAL ISSUE: Mitigating the Potential for Progressive Disproportionate Structural Collapse), pp.324–329. Available at: http://dx.doi.org/10.1061/(ASCE)0887-3828(2006)20:4(324).

Carper, K.L. & Smilowitz, R., 2006. Special issue: Mitigating the Potential for Progressive Disproportionate Structural Collapse. *J. Perform. Constr. Facil.*, 20(4), pp.305–427.

CEN, 2005. *BS EN 1993-1-8:2005 Eurocode 3: Design of steel structures - Part 1-8: Design of Joints*, European Committee for Standardization (CEN).

Department for Communities and Local Government, 2013. *The Building Regulations: Approved Document A*,

Dossett, J.L. & Boyer, H.E., 2006. *Practical heat treating*, ASM International.

Dzugan, J. et al., 2012. Identification of Ductile Damage Parameters for Austenitic Steel.

In *International Scholarly and Scientific Research & Innovation. World Academy of Science, Engineering and Technology*.

Edwards, K., 2015. *Investigation into the tensile strength of stainless steel and ordinary grade 8.8 mild steel bolts*,

El-Tawil, S., Li, H., Kunnath, S., 2014. Computational Simulation of Gravity-Induced Progressive Collapse of Steel-Frame Buildings: Current Trends and Future Research Needs. *J. Struct. Eng.*, 140(SPECIAL ISSUE: Computational Simulation in Structural Engineering). Available at: http://ascelibrary.org/doi/abs/10.1061/%2528ASCE%2529ST.1943-541X.0000897.

Fang, C. et al., 2013. Modeling of semi-rigid beam-to-column steel joints under extreme loading. *Frontiers of Structural and Civil Engineering*, 7(3), pp.245–263. Available at: http://dx.doi.org/10.1007/s11709-013-0215-9.

FEMA, 2002. *World Trade Center Building Performance Study*. *FEMA 403.*, Washington, DC.

Fransplass, H., Langseth, M. & Hopperstad, O.S., 2013. Numerical study of the tensile behaviour of threaded steel fasteners at elevated rates of strain. *International Journal of Impact Engineering*, 54(0), pp.19–30. Available at: http://www.sciencedirect.com/science/article/pii/S0734743X12001984.

Grimsmo, E.L. et al., 2015. An experimental study of static and dynamic behaviour of bolted end-plate joints of steel. *International Journal of Impact Engineering*, 85, pp.132–145. Available at: http://www.sciencedirect.com/science/article/pii/S0734743X15001554 [Accessed October 15, 2015].

Hillerborg, A., Modeer, M. & Petersson, P.E., 1976. Analysis of crack formation and crack growth in concrete by means of fracture mechanics and finite elements. *Cement and Concrete Research*, 6, pp.773–782.

Institution of Structural Engineers, 2002. *Safety in tall buildings and other buildings with large occupancy*, London, United Kingdom.

Izzuddin, B.A. et al., 2008. Progressive collapse of multi-storey buildings due to sudden column loss — Part I: Simplified assessment framework. *Engineering Structures*, 30(5), pp.1308–1318. Available at:

http://www.sciencedirect.com/science/article/pii/S0141029607002805.

Johnson, G.R. & Cook, W.H., 1983. A constitutive model and data for metals subjected to large strains, high strain rates and high temperatures. *Proc. 7th int. symp. on ballistics*, p.7.

Johnson, G.R. & Cook, W.H., 1985. Fracture characteristics of three metals subjected to various strains, strain rates, temperatures and pressures. *Engineering Fracture Mechanics*, 21(1), pp.31–48. Available at: http://www.sciencedirect.com/science/article/pii/0013794485900529.

Kuhlmann, U. et al., 2009. *Robust structures by joint ductility*, European Commission, Research Fund for Coal and Steel Unit, Brussels.

Kyawthetlatt, 2013. BCC and FCC structures.

Lemaitre, J., 1985. A Continuous Damage Mechanics Model for Ductile Fracture. *Journal of Engineering Materials and Technology*, 107(1), pp.83–89. Available at: http://dx.doi.org/10.1115/1.3225775.

Lew, H.S. et al., 2013. Performance of Steel Moment Connections under a Column Removal Scenario. I: Experiments. *J. Struct. Eng.*, 139(1), pp.98–107.

de Lima, L.R.O. et al., 2004. Experimental evaluation of extended endplate beam-to-column joints subjected to bending and axial force. *Engineering Structures*, 26(10), pp.1333–1347. Available at: http://www.sciencedirect.com/science/article/pii/S014102960400121X [Accessed May 6, 2015].

Malvar, L.J., 1998. Review of Static and Dynamic Properties of Steel Reinforcing Bars. *Materials Journal*, 95(5), pp.609–616.

Meyers, M.A., 1994. *Dynamic Behaviour of Materials* 1st ed., Wiley-Interscience.

Meyers, M.A. & Chawla, K.K., 2008. *Mechanical Behavior of Materials* 2nd ed., Cambridge University Press.

Mouritz, A.P., 1994. Failure mechanisms of mild steel bolts under different tensile loading rates. *Int J Impact Eng*, 15(3), p.14.

Munoz-Garcia, E., Davison, J.B. & Tyas, A., 2005. Analysis of the response of structural

bolts subjected to rapid rates of loading. *4th European Conference on Steel and Composite Structures, Eurosteel 2005*, C(4.10), pp.147–154.

National Commission on Terrorist Attacks, 2004. *The 9/11 Commission Report*,

NIST NCSTAR 1, 2005. *Final report on the collapse of the World Trade Center Towers*,

Ribeiro, J., Santiago, A., Rigueiro, C., et al., 2015. Analytical model for the response of T-stub joint component under impact loading. *Journal of Constructional Steel Research*, 106, pp.23–34. Available at: http://www.sciencedirect.com/science/article/pii/S0143974X14003241 [Accessed March 15, 2015].

Ribeiro, J. et al., 2016. Numerical assessment of T-stub component subjected to impact loading. *Engineering Structures*, 106, pp.450–460. Available at: http://www.sciencedirect.com/science/article/pii/S0141029615006811 [Accessed November 20, 2015].

Ribeiro, J., Santiago, A. & Rigueiro, C., 2015. Numerical assessment of beam-to-column steel joints subjected to impact loading. In *Eigth International Conference on Advances in Steel Structures*.

Rusinek, A. et al., 2015. Experimental characterisation and modelling of the thermo-viscoplastic behaviour of steel AISI 304 within wide ranges of strain rate at room temperature.

Sadek, F. et al., 2010. *An Experimental and Computational Study of Steel Moment Connections under a Column Removal Scenario*, National Institute of Standards and Technology (NIST).

Sadek, F., 2005. *Baseline Structural Performance and Aircraft Impact Damage Analysis of the World Trade Center Towers. Federal Building and Fire Safety Investigation of the World Trade Center Disaster (NIST NCSTAR 1-2)*,

Sadek, F. et al., 2013. Performance of Steel Moment Connections under a Column Removal Scenario. II: Analysis. *J. Struct. Eng.*, 139(1), pp.108–119.

Sadek, F. et al., 2011. Testing and Analysis of Steel and Concrete Beam-Column Assemblies under a Column Removal Scenario. *J. Struct. Eng.*, 137(SPECIAL ISSUE: Commemorating 10 Years of Research since 9/11), pp.881–892.

Del Savio, A.A. et al., 2009. Generalised component-based model for beam-to-column connections including axial versus moment interaction. *Journal of Constructional Steel Research*, 65(8–9), pp.1876–1895. Available at: http://www.sciencedirect.com/science/article/pii/S0143974X09000534 [Accessed March 16, 2015].

SCI/BCSA, 2013. *Joints in steel construction: Moment-resisting joints to Eurocode 3 (P398)*, The Steel Construction Institute and The British Constructional Steelwork Association.

SCI/BCSA, 1995. *Joints in steel construction: Moment Connections*, The British Constructional Steelwork Association/The Steel Construction Institute.

SCI/EuroInox, 2006. *Design manual for structural stainless steel* 3rd ed., Euro Inox and The Steel Construction Institute.

Shyam-Sunder, S., 2005. *Federal Building and Fire Safety Investigation of the World Trade Center Disaster: Final Report of the National Construction Safety Team on the Collapses of the World Trade Center Towers (NIST NCSTAR 1)*,

Simulia, 2015a. *Abaqus/CAE User's Guide*,

Simulia, 2015b. *Abaqus Analysis User's Guide*,

Simulia, 2015c. *Getting Started with Abaqus: Interactive Edition*,

Smith, P., Byfield, M.P. & Goode, D., 2010. Building Robustness Research during World War II. *J. Perform. Constr. Facil.*, 24(6), pp.529–535.

Sopwith, D.G., 1948. The Distribution of Load in Screw Threads. *Proceedings of the Institution of Mechanical Engineers*, 159(1), pp.373–383. Available at: http://pme.sagepub.com/content/159/1/373.abstract.

Stoddart, E.P., 2012. *Development of Component-based Connection Modelling for Steel Framed Structures Subjected to Blast or Progressive Collapse*. Southampton: University of Southampton.

Stoddart, E.P. et al., 2013. Strain rate dependent component based connection modelling for use in non-linear dynamic progressive collapse analysis. *Engineering Structures*, 55(0), pp.35–43. Available at: http://www.sciencedirect.com/science/article/pii/S0141029612002854.

Totten, G.E., 2006. *Steel Heat Treatment: Metallurgy and Technologies*, CRC Press.

Tyas, A. et al., 2012. A Methodology for Combined Rotation-Extension Testing of Simple Steel Beam to Column Joints at High Rates of Loading. *Experimental Mechanics*, 52(8), pp.1097–1109.

Vlassis, A.G. et al., 2008. Progressive collapse of multi-storey buildings due to sudden column loss—Part II: Application. *Engineering Structures*, 30(5), pp.1424–1438. Available at: http://www.sciencedirect.com/science/article/pii/S0141029607003239.

Yu, H. et al., 2009. Development of a yield-line model for endplate connections in fire. *Journal of Constructional Steel Research*, 65(6), pp.1279–1289. Available at: http://www.sciencedirect.com/science/article/pii/S0143974X08002824 [Accessed March 15, 2015].

Zaera, R. et al., 2012. A constitutive model for analyzing martensite formation in austenitic steels deforming at high strain rates. *International Journal of Plasticity*, 29, pp.77–101.